

Abstract

Planets are not Points: The Profound Effect of Planetary Structure on Exoplanet System Architectures

Tiger C. Lu

2025

The quantity and quality of astronomical data has advanced to the point in which truly detailed and nuanced theoretical models are necessary. In the field of exoplanetary dynamics, it has become increasingly clear that we must account for the effects of planetary structure when considering the dynamics of the system. In other words, Planets are not Points. This dissertation details my contributions to the field of exoplanet dynamics, split into three subcategories:

- Part I (Chapters 2 - 3): Numerical Methods & the N-Body Problem. These chapters discusses the numerical methods I have developed to study the analytically unsolvable N-Body problem, and details their implementation into the popular open-source software REBOUND.
- Part II (Chapters 4 - 5): Spin-Orbit Dynamics. These chapters explore my work into the complex interplay between a planet's spin and it's motion, driven by tidal forces. I present an origin story for the large obliquity of the planet Uranus, and I show that such large obliquity can also explain the anomalously low density of the super-puff planet HIP-41378 f.
- Part III (Chapter 6). Coupled Planetary Structure and Dynamical Evolution. This chapter details my work into self-consistent evolution of a planet's interior structure and the system's dynamical evolution. I present a case study of the intriguing HAT-P-11 system, a dynamical puzzle that can only be explained via truly self-consistent evolution.

Planets are not Points: The Profound Effect of Planetary Structure
on Exoplanet System Architectures

A Dissertation
Presented to the Faculty of the Graduate School
of
Yale University
in Candidacy for the Degree of
Doctor of Philosophy

by
Tiger C. Lu

Dissertation Director: Malena Rice

May 2025

Copyright © 2025 by Tiger C. Lu
All rights reserved.

Contents

1	Introduction	1
1.1	Background	2
1.2	The Gravitational N-Body Problem	3
1.2.1	Analytic Theory	4
1.2.2	Numerical Methods	5
1.3	The Diversity of Exoplanetary Systems	7
1.3.1	Eccentric and Misaligned Orbits	7
1.3.2	Hot Jupiters	7
1.3.3	Resonant Chains	8
1.4	Planetary Structure	9
1.4.1	Planetary Shape	9
1.4.2	Tidal Friction	10
1.5	Thesis Overview	11
I	Numerical Methods & The N-body Problem	12
2	TRACE: a code for Time-Reversible Astrophysical Close Encounters	13
2.1	Introduction	14
2.2	Equations of Motion of the Planetary N-Body Problem	17
2.2.1	Constructing Hamiltonian Maps	17
2.2.2	The Wisdom–Holman Map	18
2.3	Hybrid Integrators	20
2.3.1	Planet-Planet close encounters	21
2.3.2	Pericenter Approach	22
2.3.3	The TRACE Maps	23
2.4	The TRACE Code	26
2.4.1	Switching Scheme	26
2.4.2	Switching Functions	29

2.4.3	Collisions	32
2.4.4	Additional Forces	32
2.5	Performance Tests	33
2.5.1	Chaotic Exchange Orbit	33
2.5.2	Highly Eccentric Orbits	34
2.5.3	Violent Systems	35
2.5.4	Accretion of the Moon	38
2.5.5	ZLK Cycles	42
2.6	Potential Improvements	45
2.6.1	Pairwise Reversibility	45
2.6.2	Adaptive Timestepping	45
2.7	Conclusion	46
2.8	Appendix: Democratic Heliocentric Coordinates	48
2.9	Appendix: Other Pericenter Switching Functions	48
2.10	Appendix: Symplecticity of TRACE	49
2.10.1	Symplecticity of variable timestep maps	50
3	Self-Consistent Spin, Tidal and Dynamical Equations of Motion	52
3.1	Introduction	53
3.2	Equilibrium Tide Theory	55
3.3	Equations of Motion	58
3.4	Implementation	61
3.4.1	Spin, Structure and Tidal Parameters	61
3.4.2	Dynamics	62
3.4.3	Spin Axis Evolution	62
3.5	Test Cases	63
3.5.1	Pseudo-Synchronization of Hot Jupiters	63
3.5.2	Obliquity-Driven Sculpting of Exoplanetary Systems	65
3.5.3	Exploring the ZLK effect	67
3.6	Summary	69
3.7	Acknowledgements	70
3.8	Appendix: Secular Orbit Evolution Equations	70
3.9	Appendix: Exploration of Numerical Differences	71
II	Spin-Orbit Dynamics	76
4	Tilting Uranus via Secular Spin-Orbit Resonance with Planet 9	77
4.1	Introduction	78
4.2	Precessional Frequencies	80

4.3	Spin-Orbit Resonance	82
4.3.1	First Order Spin Axis Equation of Motion	82
4.3.2	Cassini States	84
4.3.3	Resonant Capture	86
4.3.4	Spin Axis Equation of Motion	86
4.4	Nodal Evolution Modeling	87
4.4.1	Laplace-Lagrange Secular Theory	88
4.4.2	Effect of Planet Nine	89
4.4.3	Numerical Simulations	90
4.5	Results of N-Body Simulations	92
4.5.1	Solar System Model	92
4.5.2	Axial Precession Rate Discrepancy	97
4.5.3	The Latest Planet Nine Parameters	100
4.5.4	Stochastic Scattering	100
4.6	Discussion	102
4.7	Acknowledgments	104
5	Oblique Exorings Masquerading as a Puffy Planet	105
5.1	Introduction	106
5.2	Architecture and Stability of the HIP-41378 System	108
5.2.1	Formation via Convergent Migration	109
5.3	Transiting Planetary Rings	111
5.3.1	Ring Extent	111
5.3.2	Ring Orientation	111
5.3.3	Transit Depth	112
5.3.4	Detection in ingress/egress	113
5.4	Secular Spin-Orbit Resonance	115
5.4.1	Spin Axis Precession	116
5.4.2	Nodal Precession	116
5.4.3	Cassini States and Resonance Capture	117
5.5	The Obliquity of HIP-41378f	118
5.5.1	Spin Equilibria	118
5.5.2	Migration-Driven Frequency Evolution	119
5.5.3	Migration Simulations	121
5.5.4	The Effect of a Massive Moon	126
5.6	Other Super-Puffs	128
5.7	Conclusion	130
5.8	Acknowledgements	131

III	Coupled Planetary Structure and Dynamical Evolution	132
6	The Dynamical History of the HAT-P-11 System	133
6.1	Introduction	134
6.2	Planet-Planet Scattering	136
6.2.1	Theoretical Background	137
6.2.2	N-Body Simulations	138
6.3	ZLK Migration	143
6.3.1	ZLK Oscillations	145
6.3.2	Tidal Friction	147
6.3.3	Radius Evolution	150
6.3.4	N-body simulations	154
6.3.5	Simulation Results	156
6.4	Conclusions	159
6.5	Acknowledgements	161
6.6	Appendix: Self-Consistent Spin, Tidal and Dynamical Equations of Motion	162
6.7	Appendix: Orbital Parameter Definitions	162
7	Conclusion	164
7.1	Summary	165
7.2	The Search for Planet Nine	165
7.3	The James Webb Space Telescope	165
7.4	GAIA Data Release 4	166
7.5	Towards a Unified Theory of System Formation	167
7.6	Final Thoughts	168
	Bibliography	169

Acknowledgments

"Frodo wouldn't have got far without Sam."
– Frodo Baggins

Planetary systems meaningfully evolve over the course of billions of years: far beyond the scope of human civilization, an individual lifetime, or a Ph.D. thesis. As dynamicists, we are entrusted with the monumental task of reconstructing the long and complex history of a planetary system through fleeting snapshots in time. I would like to think that we have done a wonderful job of it. In a similar vein, I hope that this Acknowledgments section serves as an illuminating window into a five year Ph.D. journey: the ups & downs, the hopes & dreams, the laughs and tears. It has not been easy, and I have many people to thank.

I consider myself the luckiest astronomer in the world to have had the privilege of working under my adviser, Gregory Laughlin. Greg's guidance and mentorship have made me the scientist I am today and I have never doubted that he has had my back, under any condition and any context. It really has been a pleasure.

I am proud to also call Malena Rice my adviser. **Far** more importantly, she is my academic big sister, my trusted confidant and my rock in turbulent times. She is the very first person to hear any news I receive, good or bad, and I truly don't know how I would have navigated the last two years without her genuine, unconditional support. It is a rare privilege to be the first Ph.D. student of someone you are lucky enough to call one of your best friends, and I do not take that honor lightly – I will strive every day to live up to it. She is the best thing that has ever happened to the Yale Astronomy Department, and words cannot express how grateful I am for her.

This Ph.D. journey does not happen without Konstantin Batygin. As a burnt-out senior undergrad at Caltech who was unsure if grad school was something I wanted to pursue, it was a conversation with Konstantin that re-ignited my excitement for science. I was not a strong applicant out of undergrad, and it was his letter of recommendation that got me into Yale. Thank you for taking a chance on me. I hope I've made you proud.

If I have seen further, it is by standing on the shoulders of giants – or rather Sarah Millholland, a long-time collaborator whose work is the foundation upon which this thesis is built. So much of my success is owed to her – in a long and uncertain postdoc application process, every position I had success in was one which Sarah

wrote me a letter of recommendation. Thank you for being my academic big sister and my biggest advocate. I still remember going to my first ever conference specifically to meet you. In hindsight, it was one of the best decisions I've ever made.

I am endlessly grateful for the kind and infinitely patient mentorship of Gongjie Li, who served as my primary research advisor for the first-author paper that I am most proud of. Her encouragement and thoughtful feedback has given me not only great physical intuition, but the art and craft of independent research and approaching complex problems with creativity and rigor. I attribute much of my growth as a scholar to her steadfast belief in my potential. Thank you for sticking with me.

[Mardling & Lin \(2002\)](#) was a seminal paper that I read in my second year of grad school. When you read this thesis, it will quickly become apparent how important this work was to my own research. Fast forward a few years, and I am incredibly fortunate to call Rosemary Mardling and Douglas Lin collaborators, mentors, friends, and two of the sharpest minds I've ever met. Always meet your heroes.

In a similar vein, my formative years as an astronomer were shaped by the REBOUND package. It was my introduction to planetary dynamics, and I remember seeing the names Hanno Rein, David Hernandez and Dan Tamayo omnipresent in the papers and documentation that described REBOUND. It is surreal, then, to see my name next to theirs' today as co-authors. I am proud to have contributed to this amazing project, and I hope that the name "Tiger Lu" will one day inspire the same feeling in a budding undergrad.

I am grateful for the many senior astronomers I have had the pleasure of meeting over the course of my Ph.D. studies. I would especially like to thank Smadar Naoz and Fei Dai, who went above and beyond the call of duty for me. Thank you for the hospitality, kindness, and belief in my ability as a scientist – UCLA and the University of Hawai'i both truly felt like home when I visited. I would also like to thank Songhu Wang, Cristobal Petrovich, Josh Winn, Matt Holman, Dave Charbonneau, Ruth Murray-Clay, Richard Zeebe, Burkhard Militzer, Terese Hansen, Erin Flowers, Guðmundur Stefánsson, Antoine Petit, Simon Albrecht, Timothy Brandt, Anthony Piro, Shreyas Vissapragada, Anne-Marie Madigan, Dong Lai, Jane Huang, Ji-Wei Xie, and Sharon Wang.

I am also grateful to senior astronomers closer to home, in the Yale Astronomy department. I would like to thank the members of my dissertation committee:

Greg Laughlin, Malena Rice, Frank van den Bosch, and Dan Tamayo. I thank Héctor Arce for spirited running chats in the hall, Frank van den Bosch for the most well-taught class in grad school, Marla Geha for inviting me into the Warrior Scholar Program, and Priya Natarajan for generous support in the uncertain final year of my Ph.D. The behind-the-scenes support at Yale is just as important, and I would like to thank Robyn Lisone and Teena Griggs for being the best administrative staff in the world. Thank you for the patience, the little chats in the halls, and the secret Krabby Patties.

I'm lucky to have found myself in a wonderfully vibrant department filled with so many smiling faces. Yasmeen Asali has been my greatest supporter and a truly amazing friend. Thank you for all the Jitterbus trips, the office meltdowns, the gentle bullying – thank you for everything. That "three person group chat with a weird name" featuring Konstantin Gerbig and Sebastian Monzon – thank you for all the memes, the Mario Kart showdowns, the Bonchon depression sessions. Through it all, I know you've had my back. I want to thank Josephine Baggen for being a genuine ray of sunshine and positivity that has never failed to brighten my day, Chloe Neufeld for exact opposite vibes that somehow manage to achieve the same effect on my mood, Shashank Dattathri for giving me a target to aspire to in the gym, and Juliëtte Hilhorst for her steadfast wholesomeness through the confusion. In my final year I was lucky to have been graced with the presence of Quang Tran and Prathik Gandhi, who have been wonderful mentors and sympathetic ears through all the trials and tribulations of a final-year graduate student. I'm grateful to have shared these years with Garrett Levine, Chris Lindsay, Isa Medlock, Isabella Trierweiler, Tim Miller, Lily Zhao, Kaustav Mitra, Antonio Porras, Colin Burke, Erin Kado-Fong, Aritra Ghosh, Imad Pasha, Juan Guerra, and Michael Keim. We got really lucky, guys. I'll never take this department for granted.

Astronomy is full of so many brilliant young minds, and I am fortunate enough to call many of them my friends. I would especially like to thank Yubo Su, the first astronomy friend I made in grad school. Conferences are scary for the typical quiet little astronomer but are made exponentially easier the more people you know, and I am comforted each time I get on a plane knowing Yubo awaits on the other end. I'd like thank Ben Cassese, my oldest friend in astronomy, and now officially a collaborator. What could be better than writing a paper with an old friend? I'm also grateful for Briley Lewis, who, chance met one day on the road during a phase of my Ph.D I can best describe as "floundering", told me that my competence would be "exponential". I don't think either of us realized it at the time, but that short conversation changed the course of my career –

there is always hope. I'm grateful for Michael Poon, Dang Pham, Mark Dodici, Garrett Brown, Max Goldberg, Sam Yee, Janosz Dewberry, J.J. Zanazzi, Arcelia Hermosillo Ruiz, Qier An, Theron Carmichael, Nick Saunders, Elina Zhang, Rena Lee, Rebecca Zhang, Denys Melchor, Grant Weldon, Thea Faridani, Isabel Angelo, Zoë de Beurs, Caleb Lammers, Jared Siegel, Akash Gupta, Brandon Radzom, Tom Wagg, Aizhan Akhmetzhanova, Chengcheng Xin, Hyerin Cho, Brianna Zawadski, Daniel Yahalom, Kangrou Guo, Sally Jiang, Chris O'Connor, Rixin Li, Winter Parts, and Hanna Adamski. I would also like to give a very special shoutout to Yurou Nina Liu – it has been a joy to watch you grow as a scientist! I would expect to see many of these names at the forefront of the field in the coming years.

Running always has and always will be a constant fixture in my life, and for me it's the people who make it special. During this phase of my life, these people were the New Haven Road Runners. I will emphasize that this section, more than any other, is a non-exhaustive list lest this Acknowledgments section balloon further out of control than it already has. First and foremost, Lizzie Mundell-Perkins has been the big sister I never had. Who would have thought that accidentally kudos'ing your debut marathon all those years ago would have led to such a beautiful friendship? Kidan Kidane was my best friend through her final years in New Haven, and I'm deeply grateful for the role she played in it all. New Haven didn't feel like home until I started running with you two. You are the best training partners I have ever had – thank you for the countless miles and smiles. I am proud to have worked under President Josephine Jayworth for the past four years, and to have helped her create this wonderful and special community. She's been a great number one. I also want to thank Aziza Chigatayeva for making New Haven a less lonely place when I needed it the most – I'm not sure you quite realized just how much I needed it. I thank Tim Cannata for always being a compassionate and steady presence, Andie Condie & Max Storms for all the laughter in my final year, Laura Addison for sometimes scaring the living daylights out of me, Cara DeAngelis for genuinely being the kindest & most wholesome human being alive, and Matthew Lynch for supporting me wherever either of us are in this vast world. I'd also like to thank Dante Hatem, Jordy Mazza, Jake Jayworth, Mason Rouches, Mady Neufeld, Mattie Webb, Kolja Hildenbrand, Katie Wojnowski, Katherine Manansala, Omar Radwan, Lexi Cafiero, Garrett Allington, Elle Nye, Cait Jokubaitis, Allie Konrad, Michael Minopoli, Miche Palmer, Stefanie Gillson, Kristen Gregory, Crossan Cooper, Zachary Haas, Yoon Lee, Dana Scott, Phoebe Liu and Bruce Ma. There's a reason my first tattoo is our elm leaf. How lucky I am to have something that makes saying goodbye so hard.

Friends are forever, whether a thousand miles away or at your doorstep. I will

forever be grateful for Claire Hu, who has been there for me for everything and anything with no hesitation or judgement. I'm thankful for Lia Xia, who has always shown me, in her special way, how much she cares – including flying across the country for your friend's public thesis defense! I'll always fondly remember swapping unhinged grad school memes with Miriam Sun, laughing at the endless source of unintentional entertainment provided by Rachel Lin, and the unwavering loyalty I've learned to always expect from James Park. I am so thankful for my ability to show up on Catherine Day's doorstep with a day's notice, and for an impromptu mountain run with Pippa Richter that has blossomed into a wonderful friendship. My heart fills with pride when I see my old Caltech cross country teammates still killing it five years down the track: Simon Ricci, Mooly Croteau, Michelle Marasigan, Julen Lujambio, David Fager, and Skye Reese. I'm thankful for Sara Shi, Eilleen Zhang, Chorizo Tran, Katie Chiu, Annie Chen, Jenny Lin, Bijan Mazaheri, Jemma Tan, Victor Chen, Steve Guo, Connor Soohoo, Akshay Gowrishankar, Vincent Zhu, Steven Chang, and Alison Carranza. I'd especially like to thank Tanvi Gupta, who has had to hear more about spin-orbit dynamics and tidal theory than any normal human being should have to stomach in a lifetime. I hope you know how much it meant to me.

I would like to specifically thank everyone who went out of their way for me in what I like to call my "Postdoc World Tour", a two-month period where I couchsurfed my way across the US in <5 day increments. So, to Sara, Nick, Miriam, Julen, Simon, Lia, Rachel, Arcelia, Mooly, Michelle, Lizzie, Malena, Rebecca, Jemma, Hanna, Pippa, Gongjie, Catherine, Yubo, DJ, Katherine, and Ben: you were oases of peace in the chaos. Thank you for giving me something to look forward to beyond yet another talk. It was so good to see your smiling faces!

This fall, I will start a new appointment as a Flatiron Research Fellow at the Center for Computational Astrophysics (CCA) in New York City. I am brimming with excitement for this new adventure, and I feel incredibly fortunate to have been given this opportunity. I'd like to thank Phil Armitage, Megan Bedell, Will Farr, Yan-Fei Jiang, Julianne Dalcanton, Michael Palumbo, Wenrui Xu, Linn Erikson, Thomas Pfeil, Ryan Rubenzahl, Jared Goldberg, Brent Tan, Aida Behmard, Yu Wang, Sabina Sagynbayeva and especially Jiayin Dong for the warm welcome shown to me in all my CCA visits over the past year. While it was by no means an easy decision to spend the next three years of my life here, you made it a choice that felt right beyond any doubt when I made it. Let's drink some kombucha!

An extra special shoutout goes to Winston, who has been my steadfast companion through many dangers. I've seen the edges of the world in these last five years,

from the windswept peaks of New Zealand to the charming canals of Leiden to the blue skies of sunny Pasadena, and Winston has been by my side through all of it. It wouldn't have been possible without you, buddy.

Last, but certainly not least. The unconditional support of my family to chase my dreams is not something I take lightly. I'm grateful for my Aunt and Uncle, Janice & Michael Ye, for always opening their home in Boston to me. And my cousins: Hayley & Colby Ye, as well as Mary Decker, my sister-in-law, for their curiosity, for their hospitality, and their unshakeable faith in my ability to succeed. I'm lucky enough to have one grandparent with me, and even without understanding astronomy, his excitement for my success has been contagious. As for the other three, I know they would be proud of me, and I carry that with me always. Finally, I thank my parents, Min Lu and Julia Chen. No matter what these past five years have thrown at me, their belief in me has never wavered. Even from across the vast Pacific ocean, their love has always been clear. I'm a lucky guy.

I've never felt as loved and supported as I have in these final months before they add "Dr." to the front of my name. To everyone who has been a part of the journey, big or small, thank you from the bottom of my heart. It has truly meant the world to me.

for my parents

List of Figures

1.1	Progress of N-Body Simulations over the years	6
1.2	Example of a bizarre exoplanet system architecture	8
1.3	Schematic representation of the planetary structure effects	9
2.1	Flowchart of the TRACE algorithm	27
2.2	Comparison between TRACE, MERCURIUS and WHFAST for the chaotic exchange problem	34
2.3	A comparison of TRACE, MERCURIUS, BS and WHFAST for a Sun-Jupiter-Saturn system where Saturn has been given a high eccentricity . . .	36
2.4	Statistics on an ensemble of 500 three-body scattering simulations, comparing the performance of TRACE, MERCURIUS, IAS15 and BS. . .	39
2.5	Cumulative distribution functions of the orbital elements for scattering simulations with TRACE, MERCURIUS, IAS15 and BS	40
2.6	Efficiency plot comparing TRACE, MERCURIUS, IAS15, and BS for a large- N accretion problem without considering collisions	42
2.7	Simulations results from a lunar accretion problem including 1000 particles	43
2.8	A comparison of IAS15 (green), TRACE (blue), and WHFAST in both Jacobi (gold) and DH (gold dashed) coordinates for ZLK oscillations	44
3.1	Schematic representation of the additional parameters, dynamical variables and forces needed to shift from a point particle framework to one in which the bodies are endowed with structure	60
3.2	A comparison between the numerical results of our REBOUNDx simulations and analytic predictions	64
3.3	A comparison between ML19 (left) and our results (right)	66
3.4	Results of the simulation demonstrating the ZLK mechanism with a Neptune-like planet	69
3.5	Schematic depiction of the topology of Colombo's top, along with the locations of the Cassini States	73

3.6	Scatterplots of spin axis positions for a small cutaway of Figure 3.3	75
4.1	Schematic view of spin-axis precession	81
4.2	Schematic view of nodal recession	83
4.3	Level curves of the spin axis Hamiltonian, with the Cassini state equilibrium points labeled	85
4.4	Result of a simple evolution of the ratio $ \alpha/g $	86
4.5	The evolution of the four outer planets as described by Lagrange-Laplace secular theory	89
4.6	Planet Nine's forcing frequency on Uranus as a function of semi-major axis	91
4.7	Examples of Uranus and Neptune's semi-major axis evolution for three stability cases	94
4.8	Summary of results of our N-Body simulations	95
4.9	Spin axis evolution for one of our simulations	96
4.10	A closer look at two instances where the obliquity of Uranus exceeds 90°	98
4.11	Summary of results of simulations with updated parameters from Brown & Batygin (2021)	101
4.12	400 self-consistent REBOUND simulations of Planet 9's dynamical migration	103
5.1	Cumulative distribution of unstable configurations of the HIP-41378 f system	110
5.2	Fraction of ϕ ring orientations capable of reproducing the transit depth of HIP-41378 f	113
5.3	Comparison of transit lightcurves of a flat planet and a planet with an inclined ring system	114
5.4	Analysis of precession rates in the HIP-41378 system	120
5.5	A fiducial case of the dynamical evolution of the HIP-41378 system	123
5.6	Population-level statistics of our migration simulations	125
5.7	Exploration of how a massive moon enhances spin precession rate	127
5.8	Frequency analysis of five multi-planet super-puff systems	129
6.1	Schematic view of one possible orbital architecture of the HAT-P-11 system	136
6.2	Example three-body scattering results	141
6.3	Results from our ensemble of three-body scattering simulations . .	142
6.4	Results from an ensemble of four-planet scattering simulations . .	144
6.5	Comparison of precessions from the ZLK effect to general relativity and tides	149

6.6	A simply prescription for radius evolution as a function of tidal luminosity	153
6.7	Results from a population synthesis of fully self-consistent ZLK simulations	156
6.8	Fiducial ZLK migration of HAT-P-11 b	157

List of Tables

5.1	Relevant physical and orbital parameters of the planets in the HIP-41378 f system	107
6.1	Parameters of the HAT-P-11 System	135
6.2	Relevant input parameters and output values of the REBOUND simulation shown in Figure 6.8	159

Chapter 1

Introduction

"It's a dangerous business, Frodo, going out your door. You step onto the road, and if you don't keep your feet, there's no knowing where you might be swept off to."

– Bilbo Baggins

1.1 Background

The incredible diversity of exoplanet systems discovered over the past two decades has illuminated the shortcomings of our understanding of planetary system formation. For millenia, our own solar system was the sole data point that guided our theoretical models. Generally, this paradigm of small rocky planets close in and gas giants further out, all on circular orbits, was successfully reproduced and thought to be well understood. Exoplanets, on the other hand, are seen in a wide configuration of bizarre orbits that exist in significant tension with our understanding of the solar system's formation. Astronomy as a field has since scrambled to paint a new picture of planetary system formation, one that could reconcile these strange worlds with theoretical understanding.

Today, the consensus of the field is that gravitational interactions between pairs of planets are the culprit behind many anomalous systems that we see. The interactions can be gentle and occur over millions or billions of years without compromising the long-term stability of the system. They can also be violent, and in this case may result in planets colliding or being fully ejected from the spheres of influence of their host stars. Taken together, these effects are known as dynamical sculpting, and the field of *planetary dynamics* encompasses the study of planetary motion as a consequence of interactions between stars, planets, and minor bodies. Planetary dynamics has blossomed into a rich and complex field; and has offered compelling origins for many of the bizarre systems seen in the observational data.

Upon first glance, it seems a reasonable assumption to ignore a planet's actual physical extent when analyzing its motion. Space is vast, and the distance between bodies dwarfs the size of these bodies. From this scale, planets appear little more than points. However, in recent years it has become clear that this approximation is often insufficient. The only way to explain some of the phenomena we see in nature is to account for effects such as a planet's spin, flattening due to rotation, or heating in the deep interior from tidal forces. The most brilliant minds in the field have made tremendous strides in developing simple, elegant models that have made predictions with truly astounding foresight. For instance, Peale et al. (1979) asserted that Jupiter's moon Io should have a molten surface from intense volcanism driven by tidal heating due to its close proximity to Jupiter, a prediction that was verified by the Voyager probe just days later. With cutting-edge instruments such as JWST that have launched in past few years, observational evidence to verify these models for exoplanetary systems is now within our grasp. It truly is an exciting time to study exoplanets.

In this thesis, I detail my own contributions to the field of planetary dynamics. I approach this topic from a computational and theoretical perspective. I have actively developed novel numeric tools and directly applied them to a wide range

of dynamical topics. Simultaneously, I am closely connected to the observational data. Anomalies in the data, from population-level trends to specific strange systems, have guided my theoretical explorations. This Introduction serves to lay crucial groundwork to interpret my results and place them in the greater context of the field. In Section 1.2 I discuss some of the challenges in studying planetary motion. In Section 1.3 I provide context on some of the most bizarre exoplanetary systems known to date. In Section 1.4 I explicitly map out the effect of planetary structure on system dynamics. Finally, in Section 1.5 I give an overview of the structure of this thesis.

1.2 The Gravitational N-Body Problem

The gravitational N -Body problem is simple in concept, but surprisingly difficult in execution. The problem is defined as such: given the initial positions and velocities of N bodies, predict their new positions and velocities at some arbitrary point in time under the influence of gravity. At first glance, this does not seem like a difficult problem – the differential equations governing the motion of bodies under the influence of gravity are relatively simple. If we make the simplifying assumption that planets are points, the dynamics of the system are completely described by the following equation:

$$\ddot{\mathbf{d}}_i = \sum_{j \neq i}^N \frac{G(m_i + m_j)}{d_{ij}^3} \mathbf{d}_{ij}. \quad (1.1)$$

where \mathbf{d}_i is the position vector and m_i the mass, associated with the i th particle of the system.

If $N = 2$, we call this problem the Kepler problem. In this case we are in luck – this problem is exactly solved (Goldstein et al., 2002). The solution is fairly intuitive and straightforward: in the Kepler problem, the two bodies move about each other on so-called *Keplerian orbits*. The specific orbit can be uniquely and completely described with just six numbers, called the orbital elements (Murray & Dermott, 2000):

- a , the semimajor axis. This describes the size of the orbit, essentially the average distance between the two bodies.
- e , the eccentricity. This describes how circular the orbit is. If $e = 0$, the orbit is perfectly circular. If $e \sim 1$, the orbit is a very stretched out ellipse.
- i , the inclination. This is an angle that describes how tilted the planet's orbit is, relative to some reference plane. In this thesis, i will typically describe the

angle between the plane defined by the star’s spin axis and the orbit of the planet.

- Ω , the longitude of ascending node. This angle describes the horizontal orientation of the orbit.
- ω , the argument of periapsis. This indicates the direction the orbit points.
- f , the true anomaly. This shows where the orbiting object is along its path at a specific time.

This result is obviously limited in scope, but nonetheless provides powerful intuition for most planetary systems where the central star is typically massive enough to dominate the system’s dynamics. To zeroth order, a set of Keplerian orbits that ignore the contributions of the other planets can indeed describe the dynamics of a multi-planet system.

If $N = 3$, the problem becomes vastly more complex. This is the famous three-body problem, and technically an exact analytic solution exists. [Sundman \(1913\)](#) proved that the problem could be exactly solved in the form of a power series. Unfortunately, this solution is completely infeasible – for astronomical contexts, the exact analytic solution would need to include upwards of $10^{8000000}$ terms ([Belorizky, 1930](#)). Thus, an exact analytic solution to the N -body problem eludes us in practice.

1.2.1 Analytic Theory

While not the main focus of this dissertation, it would be remiss not to mention the tremendous progress made by analytic theorists with pen and paper to develop highly nuanced analytic approximations of the N -body problem that offer incredible physical intuition.

An often reasonable assumption in planetary dynamics is that the central star is the dominant contribution to the motion of its planets. In this case, a powerful approximation is to consider the effect of the other planets as small deviations from the path which would otherwise be completely dictated by the star’s influence. The addition of extra terms to describe these minor perturbations are known as the *disturbing function*, often expressed as a series expansion in orbital elements (e.g. [Kaula, 1962](#)). The disturbing function can be made arbitrarily nuanced with consideration of additional higher-order terms with corresponding increasing mathematical complexity. However, the problem can be made tractable by realizing for certain problems, only certain terms in the disturbing function are relevant over long timescales. Averaging out the appropriate inconsequential

terms is the gate and key to understanding a number of relevant problems in planetary dynamics, and this builds the foundation of so-called *secular theory*.

The term “secular” arises from the Latin word *saeculum*, which means century ([Murray & Dermott, 2000](#)). Secular theory therefore describes the motion of planetary systems on timescales far longer than an orbit. One can think of secular theory as modeling a planet not as a point mass traveling around its star in an orbit, but rather “smearing out” the motion of the planet into a wire. Secular theory thus predicts the stretching and squeezing of the wire as a planet’s orbit oscillates in eccentricity and inclination. Great strides have been made in solar system science with secular theory, for which a fantastic review is provided by [Laskar \(2012\)](#). In brief, an elegant solution for the motion of the planets was derived by [Lagrange \(1778\)](#) and [Laplace \(1784\)](#), where periodic oscillations in eccentricity and inclination in a planet’s orbit are driven by a sum of forcing terms from all other companions in the system. Lagrange-Laplace secular theory has been improved upon by numerous authors since (e.g. [Brouwer & van Woerkm, 1950](#); [Wisdom, 1985](#); [Laskar et al., 2004](#)) and has delivered numerous deep insights into the dynamical nature of the solar system (e.g. [Ward, 1974](#); [Morbidelli & Henrard, 1991](#); [Hinnov, 2018](#)).

1.2.2 Numerical Methods

Analytic theory is a powerful tool for building physical intuition, but is an inherently limited framework. Most significantly, analytic theory cannot probe chaos, or the extreme sensitivity of physical systems to minute changes in initial conditions. In addition, by nature of the averaging schemes used to analyze the disturbing function, it is nearly impossible to study problems that involve rapid change of the system on timescales less than an orbit such as violent planet-planet scattering. The best way to study these systems is by numerically and approximately integrating the equations of motion, for which an in-depth review is given by ([Hairer et al., 2006](#)). Much of the work discussed in this thesis is based upon numerical integration methods, so I provide a brief overview of numerical integration in the field of planetary dynamics.

The practice of numerical integration has existed since time immemorial. For instance, ancient Babylonians used numerical techniques to predict Jupiter’s trajectory across the night sky ([Ossendrijver, 2016](#)). Over the course of millennia, these methods have been greatly refined in both speed and accuracy. Algorithms such as Runge-Kutta and Bulirsch-Stoer ([Press et al., 2002](#)) are flexible, accurate and fast enough to efficiently analyze the motion of virtually any system on timescales of millions of years. Today, the gold standard for numerical integration of astrophysical systems is IAS15 ([Rein & Spiegel, 2015](#)), based on the algorithm of [Everhart](#)

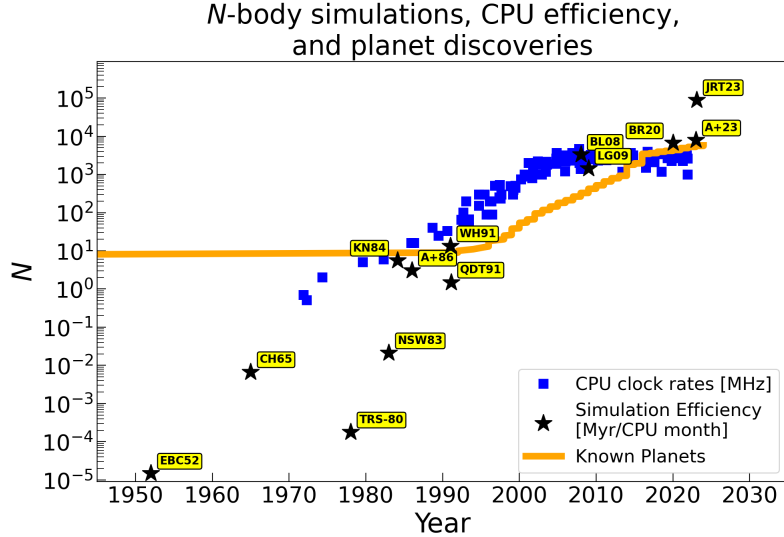


Figure 1.1. Progress made in the efficiency of N -Body simulations over the past century. Starred points are significant simulations in the literature. Figure credits to [Sam Hadden](#).

(1985). IAS15 achieves theoretically optimal error growth over time, and systematic errors in the algorithm are kept well below machine precision. These are powerful tools to accurately study the dynamical evolution of arbitrary systems – indeed, in many cases they are the only available tools.

Numerical methods always come with a fundamental trade-off. Typically, this trade-off is between speed and accuracy – the more accurate an integration, the greater the computational cost. However, certain schemes are able to maintain both high speed and accuracy, so long as certain assumptions are met. [Wisdom & Holman \(1991\)](#) developed a revolutionary scheme with incredible speed and accuracy in the limit of a dominant central mass – again, typically a reasonable assumption for planetary systems where the mass of the star dwarfs all other bodies. The “Wisdom-Holman” scheme allows for accurate integration of planetary systems on timescales of *billions* of years. The scheme has been vastly improved upon since its inception – in fact, the most recent edition, WHFAST512 ([Jahaveri et al., 2023](#)), allows for solar system integrations over five billion years in just over a day. Figure 1.1 summarizes the progress made over the past century in numerical simulations, as both computer hardware and computational methods have tremendously improved.

Many of the numerical methods described in this section, including Bulirsh-Stoer, IAS15, and WHFAST512, are included in the popular open-source REBOUND software package ([Rein & Liu, 2012](#)). A great deal of this thesis work was performed with the tools included in REBOUND, which has served as an invaluable tool for the astronomy community as a whole.

1.3 The Diversity of Exoplanetary Systems

Armed now with the tools necessary to study planetary motion, in this section I motivate the need for such study by providing several examples of observed exoplanetary system configurations that can only be explained via dynamical sculpting. These are but a few illustrative examples – the diversity of exoplanetary systems is vast, and in nearly all of them some dynamical process is critically at play.

1.3.1 Eccentric and Misaligned Orbits

The eight planets of our solar system travel about the Sun on near-circular ($e \sim 0$) and aligned ($i \sim 0^\circ$) orbits. Any deviation from the paradigm is curious, and represents a dynamical puzzle that must be solved – and indeed, we see many such dynamical puzzles in the exoplanet population. Figure 1.2 is an example of one such strange system. Planets such as HD 80606b (Naef et al., 2001) are seen on extremely eccentric orbits that resemble long-period comets more than the planets of our solar system. A growing population of polar planets that orbit perpendicular to the orientation of their host stars (Albrecht et al., 2021) has been discovered in recent years, a trend which has not yet been fully understood. In fact, some peculiar systems such as HAT-P-11 (Yee et al., 2018) and 14 Herculis (Bardalez Gagliuffi et al., 2021) host multiple planets that are both eccentric and misaligned. It is believed that these strange orbits are imprints of a dynamically violent past – close encounters between pairs of planets result in scattering one or both planets from well-behaved circular orbits to the eccentric misaligned orbits we observe. Formation theories must be able to account for such systems, and understanding the process of planet-planet scattering is critical to this end.

1.3.2 Hot Jupiters

The origin of hot Jupiters is the oldest mystery in exoplanet science. The very first exoplanet to be discovered, 51 Pegasi b (Mayor & Queloz, 1995), was a gas giant on a four day orbit – if placed in our solar system, it would sit well within Mercury’s orbit. Over the years around 500 such “hot Jupiter” planets have been discovered, which stand in stark contrast with our understanding of the solar system – there are obviously no gas giant planets within the orbit of Mercury. In fact, their existence lies in tension with planet formation theory in general. Planets are believed to form from the gas and dust of the primordial circumstellar disks that surround young stars. This close to the host star, there does not exist sufficient material to form gas giant planets (Dawson & Johnson, 2018). Hence, these hot Jupiter

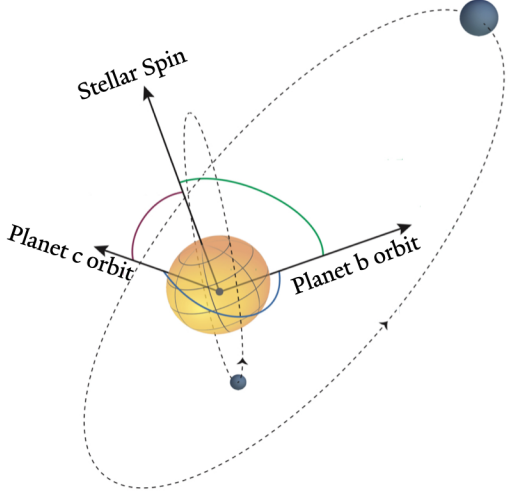


Figure 1.2. An example of a bizarre exoplanet system configuration, which hosts two planets that are both eccentric and misaligned. This stands in stark contrast with our own solar system, which hosts eight planets on circular and aligned orbits. It is believed that dynamical processes such as planet-planet scattering are responsible for generating such strange systems. Figure adapted from [Lu et al. \(2024a\)](#).

planets are believed to have formed significantly further from their host stars, and migrated to their present-day locations – typically driven by perturbations from a nearby stellar companion ([Naoz et al., 2012](#)).

1.3.3 Resonant Chains

A surprising fraction of multi-planet systems are found in or near mean-motion resonances, where pairs of successive planets have orbital periods in near-integer ratios (e.g. [Petrovich et al., 2013](#)). The most striking of these systems are the so-called “resonant chains”, which consist of systems in which each successive pair of planets is in a mean motion resonance. Resonant chain systems such as TRAPPIST-1 ([Gillon et al., 2017](#)), TOI-1136 ([Dai et al., 2023](#)) and HD 110067 ([Lammers & Winn, 2024a](#)) have each garnered immense interest upon their discoveries. Such systems naively are unexpected, since there is no reason to expect planets to end up in neat integer period ratios. Even more intriguingly, these systems are often compact and typically dynamically unstable – numerical simulations show compact resonant chains violently ejecting many of their planets far within the expected system lifetimes. It has been shown that planetary migration, driven by interactions with the primordial circumstellar disk (e.g. [Tamayo et al., 2017](#)), can both preferentially deliver multi-planet systems into resonant chain configurations and ensure their

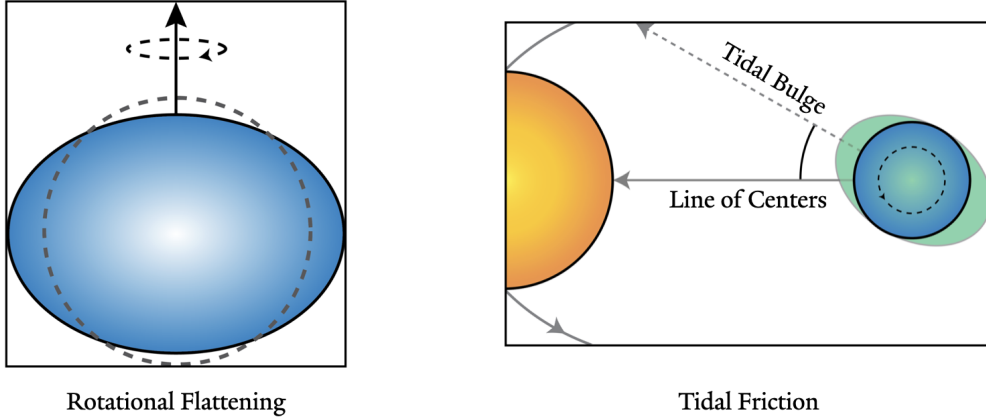


Figure 1.3. Schematic representation of the planetary structure effects that are considered in this dissertation. I discuss deformation from a perfect sphere arising from rotation or tidal perturbations, and tidal dissipation that arises from friction within a planet.

long-term stability.

1.4 Planetary Structure

So far we have discussed planetary motion in the context of Equation 1.1 only. But planets are not points, and in many relevant astrophysical cases this approximation becomes insufficient. For the purposes of this thesis work, two aspects of planetary structure are important: the planet's shape, and tidal friction. These are schematically depicted in Figure 1.3.

1.4.1 Planetary Shape

A perfectly spherical planet has the external gravitational potential of a pure point particle. However, planets are not perfect spheres. The gravitational potential V at some point x associated with a planet of arbitrary shape can be expressed as a volume integral:

$$V(x) = - \iiint \frac{G}{|x - r|} dm(r) \quad (1.2)$$

This expression naturally may encompass infinite complexity. For the purposes of this thesis, I concern myself with only the first-order simplest effects. First and foremost, planets spin. A spinning planet that is not perfectly rigid will deform and flatten along its poles. In response to rotation, a planet will become *oblate*. A similar deformation also occurs in response to gravitational perturbations from

a companion, be it a host star or a satellite. The gravitational force experienced on the side of the planet closer to the perturber in question is greater than the force experienced on the far side. This imbalance also works to stretch the planet along the line connecting the centers of the planet and its perturber. The resulting oblateness is called the *tidal bulge*. To describe the potential arising from this deformation, Equation (1.2) can be expanded in Legendre Polynomials, assuming the deformations are spherically symmetric:

$$V(r, \theta) \sim -\frac{GM}{r} - J_2 \frac{GMa^2}{r^3} \frac{3\cos^2\theta - 1}{2} \quad (1.3)$$

where r, θ are the standard spherical coordinates, a the planet's equatorial radius, and J_2 the gravitational harmonic of degree two that describes the quadrupole-order deviation from a perfectly spherical potential.

1.4.2 Tidal Friction

Consider a planet spinning at some rate Ω , perturbed by a satellite orbiting with mean motion n , where $\Omega \neq n$. The satellite would like to raise a tidal bulge on the planet that points directly along the line of centers connecting the two bodies. However, planets are dissipative. Particle elements in the planet are carried along by the planet's rotation, and cannot instantaneously deform to assume the equilibrium position of pointing exactly along the line of centers. Hence, if $\Omega > n$ the tidal bulge leads the line of centers, and if $\Omega < n$ it lags. The result of this is a tidal torque, which transfers angular momentum between the planet's spin and the orbit of the satellite. Tidal interactions profoundly influence the long-term evolution of planetary systems, and it is necessary to invoke orbital evolution driven by tidal torques to explain many phenomena seen in exoplanetary systems. For instance, hot Jupiters (as discussed in Section 1.3.2) are believed to have migrated to their present-day configurations. Typically, this involves tidal forces that slowly shrink the planet's orbit over long timescales. In fact, we have caught some hot Jupiters in the very act of this – for instance, the hot Jupiter WASP-12b has been observed to have a decaying orbit which has been attributed to tides (Yee et al., 2020).

Of course, this simple tale is not the full story. In reality, the specific response of a planet to a tidal perturber is an extremely complex function of interior structure. This is the study of *dynamical tides*, and many authors have contributed this framework over the years (e.g. Mardling, 1995; Lai, 1997). The framework that I have described is the *equilibrium tide* framework, which is elegant in its simplicity and in many cases is a very good approximation. An in-depth review of equilibrium tide theory is given in Chapter 3.

1.5 Thesis Overview

My thesis research can be divided into three distinct parts:

1. **Part I** details my contributions to numerical orbital methods. Chapter 2 describes the design and implementation of a novel hybrid integrator, TRACE, specifically designed for fast and accurate integrations of violent planet-planet scattering. Chapter 3 outlines the implementation of self-consistent equations of motion detailing the evolution of planetary spin and dynamics under the influence of tidal forces. Both of these tools are included in the open-source REBOUND framework.
2. **Part II** discusses two compelling investigations into spin-orbit coupling, the complex interplay between planetary structure and motion. In Chapter 4 I present a novel hypothesis to explain Uranus' large obliquity, driven by the outward migration of the putative Planet Nine. In Chapter 5 I comprehensively analyze the dynamical history of the HIP-41378 system, and show that large planetary obliquity can ultimately masquerade as unusually puffy and low-density planets.
3. **Part III** explores my most recent and planned future work of self-consistent coupled planetary structure and dynamical evolution. Chapter 6 is a detailed case study of the dynamical history of the HAT-P-11 system, an intriguing system which presents a dynamical puzzle that is solved only if planetary structure evolution is accounted for in conjunction with the dynamics.

Part I

Numerical Methods & The N-body Problem

Chapter 2

TRACE: a code for Time-Reversible Astrophysical Close Encounters

"I find the great thing in this world is not so much where we stand, as in what direction we are moving."
– Oliver Wendell Holmes

Adapted From:

Lu, T., Hernandez, D. & Rein, H. 2024, Monthly Notices of the Royal Astronomical Society, Volume 533, Issue 3, pp.3708-3723

Abstract

We present TRACE, an almost time-reversible hybrid integrator for the planetary N -body problem. Like hybrid symplectic integrators, TRACE can resolve close encounters between particles while retaining many of the accuracy and speed advantages of a fixed timestep symplectic method such the Wisdom–Holman map. TRACE switches methods time-reversibly during close encounters following the prescription of Hernandez & Dehnen. In this paper we describe the derivation and implementation of TRACE and study its performance for a variety of astrophysical systems. In all our test cases TRACE is at least as accurate and fast as the hybrid symplectic integrator MERCURIUS. In many cases TRACE’s performance is vastly superior to that of MERCURIUS. In test cases with planet-planet close encounters, TRACE is as accurate as MERCURIUS with a 12x speedup. If close encounters with the central star are considered, TRACE achieves good error performance while MERCURIUS fails to give qualitatively correct results. In ensemble tests of violent scattering systems, TRACE matches the high-accuracy IAS15 while providing a 15x speed-up. In large N systems simulating lunar accretion, TRACE qualitatively gives the same results as IAS15 but at a 41x speedup. We also discuss some cases such as von Zeipel-Lidov-Kozai cycles where hybrid integrators perform poorly and provide some guidance on which integrator to use for which system. TRACE is freely available within the REBOUND package.

2.1 Introduction

The N -body problem is one of the most fundamental problems in astronomy. Conceptually, it is a seemingly simple problem: given the initial positions and velocities of N particles, can we predict their state at some arbitrary time in the past or future? In most astronomical contexts, the inter-particle forces are given by Newton’s laws of gravitation (Newton, 1687). Advancements in our understanding of the N -body problem have shed light on topics as varied as the long-term secular behavior of the solar system (Laplace, 1775; Lagrange, 1778), the large-scale structure of the universe (Lemson & Virgo Consortium, 2006), and the dynamics of globular clusters (Heggie & Hut, 2003), to name but a few.

Despite its conceptual simplicity, solving the N -body problem is extremely difficult. The two-body problem is exactly solved (Bernoulli, 1775). However, it is well known that for $N \geq 3$ the N -body problem admits no practical general analytic solution¹, with solutions either only valid in the limit of certain simplifying assumptions (Poincaré, 1890) or slow to the point of being completely infeasible in

¹Newton implies that the N -body problem is in general unsolvable in his original manuscript.

practice (Sundman, 1913; Qiu-Dong, 1990). With these constraints of both accuracy and computation time, to study the N -body problem we must turn to numerical methods of approximation.

Of particular interest to astronomers is the planetary N -body problem, which is characterized by a dominant central "star" orbited by many smaller "planets". Wisdom & Holman (1991)² developed an efficient, accurate and widely used integrator for the planetary N -body problem by treating the effects of other planets in the system as perturbations to the dominant Keplerian motion. Improvements on this "Wisdom–Holman" method over the years are described in Saha & Tremaine (1992, 1994); Wisdom et al. (1996); Laskar & Robutel (2001); Hernandez & Bertschinger (2015); Rein & Tamayo (2015); Hernandez (2016); Wisdom (2018); Rein et al. (2019a); Jahaveri et al. (2023). The Wisdom–Holman method is an example of a symplectic method, from which many of its desirable characteristics can be attributed to. Symplectic integrators solve Hamiltonian systems, and are hugely advantageous because they exactly conserve phase space volumes and Poincaré invariants (Yoshida, 1993; Hairer et al., 2006). Due to these constraints, they boast impressive energy error performance over millions of dynamical timescales of a system, whereas conventional integrators may exhibit significant failures after only a few. Given that the dynamics of most astrophysical systems are governed by Hamiltonians (as far as gravity is concerned), symplectic integrators are ideal for their study. The Wisdom–Holman scheme allowed for feasible computation of the evolution of planetary systems on Gyr timescales, and its speed and efficiency have made insights into computationally demanding topics such as the stability of planetary systems (Holman & Wisdom, 1993; Holman & Wiegert, 1999) and the precise orbital and obliquity evolution of solar system planets (Touma & Wisdom, 1993; Laskar et al., 2004, 2011) possible.

Wisdom–Holman integrators have become mainstays in celestial dynamics, but this is not to say they are without their drawbacks. One such shortcoming is inflexibility: usually symplectic methods use a constant timestep which cannot be adapted if relevant timescales in the problem change. Focusing on the Wisdom–Holman method in particular, it fails when the underlying assumption of a dominant Keplerian orbit is challenged. This occurs primarily when there is a close encounter between two pairs of bodies and inter-particle forces dominate instead. In practice, this means Wisdom–Holman integrators are only effective for problems where all planets maintain stable Keplerian orbits for the duration of the simulation. There are a few ways to circumvent this issue. We will focus on the method of hybrid symplectic integrators. Schemes such as MERCURY/MERCIUS (Chambers, 1999; Rein et al., 2019b) and modified SYMBA (Duncan et al., 1998;

²Kinoshita et al. (1991) developed a similar integrator independently.

(Levison & Duncan, 2000) are able to achieve acceptable levels of accuracy while retaining many of the long-term error and speed benefits of the Wisdom–Holman map in uses cases when the traditional map fails. This is achieved by using maps utilizing more flexible conventional (but non-symplectic) integrators such as Bulirsch–Stoer (Press et al., 2002) or IAS15 (Rein & Spiegel, 2015) upon close encounters, switching between integration methods based on some predetermined switching function. Hybrid symplectic integrators have allowed for study of topics such as planetary/lunar accretion (Canup, 2004; Raymond et al., 2006), the dynamical history of our solar system (Morbidelli et al., 2005; Tsiganis et al., 2005; Gomes et al., 2005), and the imprint of instabilities on the demographics of exoplanetary systems (Chatterjee et al., 2008; Ford & Rasio, 2008; Lissauer et al., 2011), all topics involving regimes where the Wisdom–Holman method breaks down but are simultaneously too computationally demanding for conventional integrators. The hybrid integrators listed are symplectic, which come with advantages and disadvantages. Maintaining symplecticity ensures good long-term error performance, but also carries with it much of the inflexibility described before. This primarily manifests in the choice of switching function, which in practice can often be restrictive or cumbersome.

In this work, we take an alternative approach to constructing a hybrid integrator. Our integrator is not symplectic, but instead is time-reversible. While the breadth of study and literature on time-reversible integration methods is small in comparison to that of symplectic methods (Hut et al., 1995; Hairer et al., 2006, 2009; Dehnen, 2017; Hernandez & Bertschinger, 2018; Boekholt et al., 2023), in principle an exactly time-reversible scheme shares many of the long-term beneficial error properties as a symplectic integrator. While many time-reversible schemes have proven computationally infeasible for practical purposes, in the recent work of Hernandez & Dehnen (2023) a simple time-reversible algorithm was developed with comparable error and computational performance to symplectic methods.

Based on the ideas of Hernandez & Dehnen (2023) we present TRACE, an almost time-reversible hybrid integrator for the planetary N -body problem. TRACE is not exactly symplectic — see Appendix 2.10 for an analysis. The TRACE algorithm and switching scheme is conceptually simple, flexible and easy to modify. It is capable of accurately integrating close encounters between any pair of bodies in the planetary N -body problem, including the central star. We have tested TRACE on a variety of realistic astrophysical systems. We have further developed switching functions beyond those discussed in Hernandez & Dehnen (2023), performed statistical tests on ensembles of chaotic scattering systems, and tested the performance limits of our code on large N systems. In all cases, TRACE matches or exceeds the accuracy of previous hybrid integrators such as MERCURIUS, and admits speedups of up to 13x. TRACE is publicly available in the REBOUND N -body

package (Rein & Liu, 2012). The structure for this paper is as follows. In Section 2.2 we provide background on the construction of integrators for the planetary N -body problem. In Section 2.3 we discuss the current hybrid integration techniques currently available and derive the TRACE equations of motion. In Section 2.4 we discuss the TRACE switching scheme. In Section 2.5 evaluate TRACE’s performance on realistic astrophysical systems one might encounter including highly eccentric orbits, planet-planet scattering and planetesimal accretion. In Section 2.6 we discuss potential improvements to the TRACE algorithm. In Section 2.7 we draw our conclusions, and provide specific guidelines for when TRACE should be used over other integrators.

2.2 Equations of Motion of the Planetary N-Body Problem

In this section we introduce the equations of motion used for the planetary N -body problem, and review the construction and benefits of the Wisdom–Holman map.

2.2.1 Constructing Hamiltonian Maps

We will first provide a brief overview of constructing maps for conservative Hamiltonian systems in general. Consider some system governed by the Hamiltonian \mathcal{H} . Denote the state of the system in canonical coordinates by the vector $z = (q, p)$. Hamilton’s equations dictate the time-evolution of z ,

$$\frac{dz}{dt} = \{z, \mathcal{H}\}, \quad (2.1)$$

Where t is time. The *Lie operator* $\hat{\mathcal{H}}$ is defined $\hat{\mathcal{H}}z \equiv \{z, \mathcal{H}\}$. We can thus rewrite Equation (2.1),

$$\frac{dz}{dt} = \hat{\mathcal{H}}z, \quad (2.2)$$

This differential equation admits the solution,

$$z(t + h) = e^{h\hat{\mathcal{H}}}z(t), \quad (2.3)$$

Here h is referred to as the time step and $e^{h\hat{\mathcal{H}}}$ is defined as the *propogator* or *map*³. While this is indeed an exact solution for the problem, in many cases this is difficult to solve and impractical. One useful path forward is operator splitting: in many

³Explicitly, the propagator is defined by the Taylor series $e^{\hat{\mathcal{H}}} \equiv \sum_{n=0}^{\infty} \frac{\hat{\mathcal{H}}^n}{n!}$

Hamiltonian systems, we may decompose \mathcal{H} into the sum of sub-Hamiltonians, each corresponding to some component of the motion. A simple scheme is to split the potential and kinetic components,

$$\mathcal{H} = T(p) + V(q). \quad (2.4)$$

In practice, these sub-Hamiltonians are often significantly simpler to solve, and in many cases admit analytic solutions where the full Hamiltonian does not. The idea behind operator splitting is that the true equation of motion may be approximated by first evolving the system under T , and then V . Maps may be constructed through different splittings and applications of the individual propagators over various timesteps. Splitting schemes are not exact solutions, but are often the only viable way to study such systems. The error in a splitting scheme can be analyzed via the Baker-Campbell-Hausdorff (BCH) formula ([Campbell, 1897](#); [Baker, 1905](#); [Hausdorff, 1906](#); [Hairer et al., 2006](#)). For propagators \hat{A} , \hat{B} , and \hat{C} satisfying $\hat{C} = \hat{A} + \hat{B}$, the local error in the canonical coordinates over one step of the splitting scheme can be expressed as,

$$\begin{aligned} \text{Error} &= \left(e^{h\hat{C}} - e^{h\hat{A}} e^{h\hat{B}} \right) z \\ &= \frac{h^2}{2} [\hat{A}, \hat{B}] z + O(h^3), \end{aligned} \quad (2.5)$$

where $[\hat{A}, \hat{B}] \equiv \hat{A}\hat{B} - \hat{B}\hat{A}$ is the commutator. Higher order terms in h depend on a series of nested commutators, so the error in a splitting scheme arises from pairs of propagators not commuting. For instance, the well-known leapfrog method is given $e^{h\hat{\mathcal{H}}} \approx e^{\frac{h}{2}\hat{T}} e^{h\hat{V}} e^{\frac{h}{2}\hat{T}}$. By using the convenient symmetric form of the BCH formula, we can calculate the error in one timestep of leapfrog,

$$\begin{aligned} \text{Leapfrog Error} &= \left(e^{h\hat{\mathcal{H}}} - e^{\frac{h}{2}\hat{T}} e^{h\hat{V}} e^{\frac{h}{2}\hat{T}} \right) z \\ &= \frac{h^3}{24} \left([\hat{V}, [\hat{V}, \hat{T}]] - 2[\hat{T}, [\hat{T}, \hat{V}]] \right) z + O(h^5). \end{aligned} \quad (2.6)$$

Note that symmetry ensures no even powers of h survive in this expansion. Errors that depend higher power of h are preferable as the timestep is generally small.

2.2.2 The Wisdom–Holman Map

The planetary N -body problem considers a system of N planets with a dominant central mass. The central mass is denoted with subscript 0, and the other planets

$1, 2, \dots, N$. The well-known Hamiltonian of the system may be written,

$$\mathcal{H} = \sum_{0 \leq i} \frac{p_i^2}{2m_i} - G \sum_{0 \leq i < j} \frac{m_i m_j}{|\mathbf{q}_i - \mathbf{q}_j|}, \quad (2.7)$$

with \mathbf{q}, \mathbf{p} the canonical coordinates/momenta and \mathbf{m} the masses. We make an important note at this point: this is the **only** Hamiltonian considered in this work. We will rewrite this Hamiltonian many times for convenience, but all will be exactly equal to Equation (2.7).

Of course, the full N -body Hamiltonian is very difficult to numerically solve. The brilliance of the Wisdom–Holman map is in its clever splitting of the Hamiltonian into a dominant and a much smaller part which may be considered a perturbation. Specifically, the gravity of the Sun is considered the dominant part and the influence of the other planets in the system are considered perturbations. In this sense, the Wisdom–Holman map approximates the planetary N -body problem into N individual Kepler problems, one for each planet. It is clear why this is effective upon inspection of the BCH formula. If the Hamiltonian is split into two parts $\mathcal{H} = \mathcal{H}_1 + \mathcal{H}_2$ such that $\mathcal{H}_2 = \epsilon \mathcal{H}_1$ with $\epsilon \ll 1$, then the local error over one timestep will scale as $O(\epsilon h^3)$, in comparison with $O(h^3)$ as in standard leapfrog (Wisdom & Holman, 1991; Tremaine, 2023). This allows Wisdom–Holman integrators to take comparatively large timesteps while maintaining small errors. The resulting speed and accuracy has allowed for long-term integrations of planetary systems on timescales comparable to the age of the solar system.

We will make use of democratic heliocentric coordinates (DHC) \mathbf{Q}_i and momenta \mathbf{P}_i . For more in-depth discussion of this coordinate system see Duncan et al. (1998); Hernandez & Dehnen (2017); Rein & Tamayo (2019), as well as Appendix 2.8. Note that the Wisdom–Holman map was originally derived in Jacobi coordinates instead of DHC - we use the DHC coordinate system because it can effectively deal with orbit crossings. Our state vector is thus defined:

$$\mathbf{z}_i \equiv (\mathbf{Q}_i, \mathbf{P}_i). \quad (2.8)$$

The advantage of DHC is that it allows us to rewrite eq. (2.7) as a sum of four

terms, each with a clear physical interpretation,

$$\mathcal{H} = \underbrace{\frac{P_0^2}{2m_{\text{tot}}}}_{\mathcal{H}_0} + \underbrace{\frac{1}{2m_0} \left(\sum_{i \neq 0} P_i \right)^2}_{\mathcal{H}_J} - \underbrace{\sum_{0 < i < j} \frac{Gm_i m_j}{Q_{ij}}}_{\mathcal{H}_I} + \underbrace{\sum_{i > 0} \left(\frac{P_i^2}{2m_i} - \frac{Gm_0 m_i}{Q_i} \right)}_{\mathcal{H}_K}. \quad (2.9)$$

We use underbraces to mark the sub-Hamiltonians for clarity. Here \mathcal{H}_0 describes the motion of the center of mass, \mathcal{H}_J is called the jump term and describes the barycentric motion of the star, \mathcal{H}_I describes planet-planet interactions, \mathcal{H}_K the pure Keplerian motion of the planets around the central body. $m_{\text{tot}} = \sum_{i=0}^N m_i$ is the total mass of the system), and $Q_{ij} \equiv Q_i - Q_j$. In DHC, the splitting of the Wisdom–Holman map is given by the following composition, which uses the splitting in (2.9):

$$M = e^{\frac{h}{2}\hat{\mathcal{H}}_I} e^{\frac{h}{2}\hat{\mathcal{H}}_J} e^{h\hat{\mathcal{H}}_0} e^{h\hat{\mathcal{H}}_K} e^{\frac{h}{2}\hat{\mathcal{H}}_I} e^{\frac{h}{2}\hat{\mathcal{H}}_J}. \quad (2.10)$$

Each of the sub-Hamiltonians $\mathcal{H}_0, \mathcal{H}_J, \mathcal{H}_I$ and \mathcal{H}_K may individually be solved analytically. The equations of motion governed by $\mathcal{H}_0, \mathcal{H}_J$ and \mathcal{H}_I are trivially solved, while \mathcal{H}_K corresponds to Kepler’s equations which can be solved with a Kepler solver ([Danby, 1992](#)).

2.3 Hybrid Integrators

There are a variety of relevant and interesting situations in many astrophysical systems where the assumptions underlying the Wisdom–Holman integrator break down. As mentioned previously, more conventional integrators are better equipped to handle these failure cases, but lose the long-term error benefits of Wisdom–Holman.

Ideally, we would like to use the Wisdom–Holman scheme when possible to leverage its considerable speed advantages, and use a more conventional, flexible integrator when the assumptions inherent to the Wisdom–Holman map break down in the interest of accuracy. This is the idea behind hybrid integrators. In this section, we will enumerate various situations where the Wisdom–Holman map fails, and discuss the existing solutions. At the end, we will introduce our map

TRACE, which is capable of effectively handling all such pitfalls.

2.3.1 Planet-Planet close encounters

If two planets undergo a close encounter, \mathcal{H}_I will dominate over \mathcal{H}_K . The Wisdom–Holman scheme breaks down here. A solution was proposed by Chambers (1999) in their code MERCURY by smoothly moving terms from the interaction term to the Kepler term. This ensures that \mathcal{H}_K is always the dominant term in the Hamiltonian. A modified version of this scheme is implemented in REBOUND in the form of the hybrid symplectic integrator MERCURIUS (Rein et al., 2019b). While \mathcal{H}_K no longer exactly corresponds to Kepler’s equation and cannot be analytically solved, it is possible to approximate accurately and efficiently with a more conventional integration techniques. MERCURY uses a Bulirsch-Stoer scheme while MERCURIUS uses IAS15, an adaptive-timestep 15th-order non symplectic integrator that serves as the default integrator in REBOUND. Explicitly, the MERCURIUS map is obtained by splitting eq. (2.7), for use in map (2.10), in the following way,

$$\begin{aligned} \mathcal{H} = & \underbrace{\frac{P_0^2}{2m_{\text{tot}}} + \frac{1}{2m_0} \left(\sum_{i \neq 0} P_i \right)^2}_{\mathcal{H}_0} \\ & - \underbrace{\sum_{0 < i < j} \frac{Gm_i m_j}{Q_{ij}} [1 - K(Q_{ij})]}_{\mathcal{H}_I} \\ & + \underbrace{\sum_{i > 0} \left(\frac{P_i^2}{2m_i} - \frac{Gm_0 m_i}{Q_i} \right)}_{\mathcal{H}_K} - \sum_{0 < i < j} \frac{Gm_i m_j}{Q_{ij}} K(Q_{ij}). \end{aligned} \quad (2.11)$$

Note that this is exactly equal to Equation (2.9) as the terms with $K(Q_{ij})$ cancel, but we have redefined the sub-Hamiltonians that affect the splitting scheme Equation (2.10). Here, the center of mass and jump terms remain the same as those of the Wisdom–Holman map. Meanwhile, the Kepler and interaction terms are now modulated by the switching function $K(Q_{ij})$, a mathematically smooth scalar function that is purely a function of the pairwise distance between the two bodies in question and takes values $\in [0, 1]$. MERCURIUS offers several built-in switching functions, but all smoothly switch from $K = 1$ at close encounters to $K = 0$ very far from an encounter. Note that for $K = 0$, the standard Wisdom–Holman map is

recovered.

2.3.2 Pericenter Approach

The Wisdom–Holman map in DHC encounters issues for massive particles on orbits with very close pericentric distances⁴. This is because \mathcal{H}_K does not exactly represent a Keplerian orbit, since it incorporates a nonphysical central gravitating mass — \mathcal{H}_J must be incorporated as well to correct. Hence, when \mathcal{H}_J becomes very large during close pericenter approaches the Wisdom–Holman method fails as well (Duncan et al., 1998; Rauch & Holman, 1999). In principle, it is possible to avoid this issue by resolving the pericenter with a small enough timestep (Wisdom, 2015). However, since Wisdom–Holman uses a fixed timestep this worst-case timestep must be applied to the entire problem which comes at a significant computational cost. Neither MERCURY nor MERICRIUS allow for close pericenter approaches.

There are two approaches that one can take to resolve this issue. Levison & Duncan (2000) propose a solution in which entails smoothly moving terms from the jump term to the Kepler term upon a close encounter with the central body. Explicitly, their map is obtained by splitting (2.7), for use in map (2.10), in the following way,

$$\begin{aligned} \mathcal{H} = & \underbrace{\frac{P_0^2}{2m_{\text{tot}}} - \sum_{0 < i < j} \underbrace{\frac{Gm_i m_j}{Q_{ij}}}_{\mathcal{H}_I}}_{\mathcal{H}_0} \\ & + \underbrace{\frac{1}{2m_0} \left(\sum_{i \neq 0} P_i \right)^2 (1 - F(Q))}_{\mathcal{H}_J} \\ & + \underbrace{\sum_{i > 0} \left(\frac{P_i^2}{2m_i} - \frac{Gm_0 m_i}{Q_i} \right)}_{\mathcal{H}_K} + \underbrace{\frac{1}{2m_0} \left(\sum_{i \neq 0} P_i \right)^2 F(Q)}. \end{aligned} \quad (2.12)$$

Compared to the classic Wisdom–Holman map the center of mass and interaction terms do not change. The jump and Kepler terms are modulated by F , again a mathematically smooth function taking values $\in [0, 1]$ of all particles' heliocentric distances, with $F = 1$ very close to the central body and $F = 0$ very far from it.

⁴In Jacobi coordinates, Wisdom–Holman can integrate arbitrarily eccentric orbits as long as the interaction term is 0. For more discussion see (Duncan et al., 1998)

Hernandez & Dehnen (2023) expand on this method by using a discrete binary switching function for F . Again, note that the Wisdom–Holman map is recovered in the case of $F = 0$. Note also that $F(Q)$ is a function of all particles' pericenter distance, in contrast to $K(Q_{ij})$ in MERCURY/MERCIUS. This is because when any particle undergoes a pericenter passage, the jump term must be shifted to the Kepler term. As the jump term is a function of all P_i in the system, this means the Kepler term of the particle is now coupled to every other particle in the system — see Equation (2.22) — and cannot be independently integrated. Since we only need to integrate \mathcal{H}_K with the conventional integrator and stay within the DHC coordinate system, we denote this as the PARTIAL PERI approach.

We have found in our testing (see Section 2.5) that this solution, although not failing, achieves less than desirable results for some cases such as massive bodies on very eccentric orbits due to numerical instabilities. Therefore, we present and find good success with an alternative approach. In this approach, when a close approach with the central star is detected we abandon DHC coordinates entirely and perform our integration in the inertial frame. Explicitly, if $F(Q) = 0$ we integrate the standard Wisdom–Holman map in DHC coordinates, Equation (2.9). If $F(Q) = 1$, we convert our system back to the inertial frame and integrate Equation (2.1) with a conventional integrator. This approach completely sidesteps all issues with the DHC splitting for close pericenter approaches. We will show below that this approach is slightly slower than the Levison & Duncan (2000) and Hernandez & Dehnen (2023) method, since we are now including all interaction terms in the more complex \mathcal{H} , but well worth the trade off in accuracy. Since we are completely switching integration schemes, we denote this as the FULL PERI approach.

2.3.3 The TRACE Maps

We combine the above concepts from Chambers (1999), Levison & Duncan (2000), Hernandez & Dehnen (2023) as well as our new FULL PERI switching criteria to derive the TRACE map. TRACE can work in two regimes depending on the state of the system: in DHC coordinates, and in inertial Cartesian coordinates (hereafter, simply referred to as "inertial"). The evolution in each of these regimes is described

by the following splittings of (2.7), for use in map (2.10), respectively:

$$\mathcal{H} = \underbrace{\frac{P_0^2}{2m_{\text{tot}}} + \frac{1}{2m_0} \left(\sum_{i \neq 0} P_i \right)^2 \left[1 - C \Big|_{t_n} \right]}_{\mathcal{H}_0} - \underbrace{\sum_{0 < i < j} \frac{Gm_i m_j}{Q_{ij}} \left[1 - \mathcal{K}_{ij} \Big|_{t_n} \right]}_{\mathcal{H}_I} \\ + \underbrace{\sum_{i > 0} \left(\frac{P_i^2}{2m_i} - \frac{Gm_0 m_i}{Q_i} \right) - \sum_{0 < i < j} \frac{Gm_i m_j}{Q_{ij}} \mathcal{K}_{ij} \Big|_{t_n} + \frac{1}{2m_0} \left(\sum_{i \neq 0} P_i \right)^2 C \Big|_{t_n}}_{\mathcal{H}_K}, \quad (2.13)$$

and,

$$\mathcal{H} = \underbrace{\sum_i \frac{p_i^2}{2m_i} - G \sum_{0 \leq i < j} \frac{m_i m_j}{|\mathbf{q}_i - \mathbf{q}_j|}}_{\mathcal{H}_K}, \quad (2.14)$$

where $\mathcal{H}_0 = \mathcal{H}_I = \mathcal{H}_L = 0$. Here \mathcal{K} and C are the splitting functions for planet-planet and planet-star encounters, respectively. There is a major difference in writing Eq. (2.13) compared with Eqs. (2.11) and (2.12): the functions C and \mathcal{K}_{ij} are no longer smooth functions of the phase space, but are instead modified Heaviside functions, in which their value is allowed to be 0 and 1 only and updated immediately before a timestep only: we have denoted the Heaviside functions with $C \Big|_{t_n}$ and $\mathcal{K}_{ij} \Big|_{t_n}$. t_n indicates the n th discrete time sampled by the integrator, or the simulation time immediately pre-timestep. To reduce clutter, we will drop the t_n superscript for the remainder of the paper with the understanding that all \mathcal{K}_{ij} and C are evaluated only at $t = t_n$.

[Hernandez & Dehnen \(2023\)](#) demonstrated that velocity-dependent switching functions are viable for such time-reversible, but not symplectic codes, and in this work we show that these switching functions can actually depend on higher derivatives of position. Hence, we will add a dependence on $Q^{(x)}$ to show that arbitrary derivatives of Q may be accounted for in both switching functions. In this section, for brevity we will use the shorthands $\mathcal{K}(Q_{ij}^{(x)}) \equiv \mathcal{K}_{ij}$ and $C(Q^{(x)}) \equiv C$. $\mathcal{K}_{ij} = 1$ if there is a planet-planet close encounter between planets i and j , and $\mathcal{K}_{ij} = 0$ otherwise. Similarly, $C = 1$ if there is any close encounter with the central body, and $C = 0$ otherwise.

We work in DHC coordinates whenever there is no close encounter with the central body $C = 0$, or if the PARTIAL PERI prescription is used. We only work in the inertial frame if there is both a close pericenter approach ($C = 1$) and we are using the FULL PERI prescription.

Note that our splitting functions are discrete rather than smooth. Discrete switching functions were analyzed in [Hernandez \(2019\)](#), and found to generally perform inaccurately in the long term when compared to continuous, smooth switching functions (as seen in MERCURIUS and SyMBA). However, we will see that with the reversible switching scheme of [Hernandez & Dehnen \(2023\)](#) that we have implemented, the discrete switching function has comparable error performance to the continuous case, in contrast to the results of [Hernandez \(2019\)](#). This allows us to leverage the conceptually simpler discrete switching function. We describe our switching algorithm in depth in the following section.

We may use Hamilton's equations to derive the equations of motion associated with the components $\mathcal{H}_0, \mathcal{H}_J, \mathcal{H}_I, \mathcal{H}_K$ that make up \mathcal{H} . For the CoM step,

$$\dot{Q}_0 = \frac{\mathbf{P}_0}{m_{\text{tot}}}, \quad (2.15)$$

$$\dot{V}_0 = 0. \quad (2.16)$$

For the jump step,

$$\dot{Q}_i = \frac{\partial \mathcal{H}_J}{\partial \mathbf{P}_i} = \frac{1}{m_0} \left(\sum_{k>0} \mathbf{P}_k \right) [1 - C], \quad (2.17)$$

$$\dot{V}_i = -\frac{1}{m_i} \frac{\partial \mathcal{H}_J}{\partial Q_i} = 0. \quad (2.18)$$

For the interaction step,

$$Q_i = 0, \quad (2.19)$$

$$\dot{V}_i = -G \sum_{j \neq i, j \neq 0} \frac{m_j}{Q_{ij}^3} Q_{ij} [1 - \mathcal{K}_{ij}]. \quad (2.20)$$

And finally for the Kepler step \mathcal{H}_K ,

$$\dot{Q}_i = \frac{1}{m_0} \left(\sum_{k>0} \mathbf{P}_k \right) C + V_i, \quad (2.21)$$

$$\dot{V}_i = -\frac{Gm_0}{Q_i^3} Q_i - \sum_{j \neq i, j \neq 0} \left(\frac{Gm_j}{Q_{ij}^3} Q_{ij} \right) \mathcal{K}_{ij}. \quad (2.22)$$

Here $V_i \equiv \mathbf{P}_i/m_i$ are the heliocentric velocities. For $C = \forall(i, j) \mathcal{K}_{ij} = 0$, all components of \mathcal{H} admit analytic solutions. \mathcal{H}_K is the only nontrivial equation of motion,

and is solved with the fast Kepler solver used by `WHFAST`. In the case of $C = 1$ or $\mathcal{K} = 1$, \mathcal{H}_K becomes non-integrable and is solved with the BS implementation in `REBOUND`, which was first implemented in Lu et al. (2023). In the $0 < C < 1$ and $0 < \mathcal{K} < 1$ regimes \mathcal{H}_J and \mathcal{H}_I also become non-integrable, respectively. The discrete switching function completely avoids this regime — in this scheme only \mathcal{H}_K will be non-integrable and computationally expensive to solve. The equations of motion associated with $\mathcal{H}_{\text{Inertial}}$ are significantly more complex, and are always expensive to solve. We always require the use of a conventional integrator such as BS or `IAS15` to solve the equations in the inertial frame.

2.4 The TRACE Code

2.4.1 Switching Scheme

As previously mentioned, the computational benefits of the discrete switching function typically come with the trade-off of poor error performance. The time-reversible algorithm presented by Hernandez & Dehnen (2023) sidesteps this issue by changing integrators reversibly upon a close encounter, and achieves better error performance with reduced computational cost and conceptual simplicity. In this section we provide a brief summary of the algorithm, and describe our specific switching functions.

Figure 2.1 schematically walks through the switching algorithm. Let us define each of these terms for the TRACE map specifically:

- M_1 is the map used when there is no pericenter approach. In other words, $C = 0$, but we may have some pairs of $\mathcal{K}_{ij} = 1$. Explicitly, this map is obtained by splitting (2.7), for use in map (2.10), in the following way:

$$\begin{aligned} \mathcal{H} = & \underbrace{\frac{P_0^2}{2m_{\text{tot}}} + \frac{1}{2m_0} \left(\sum_{i \neq 0} P_i \right)^2}_{\mathcal{H}_0} - \underbrace{\sum_{0 < i < j} \frac{Gm_i m_j}{Q_{ij}} [1 - \mathcal{K}_{ij}]}_{\mathcal{H}_I} \\ & + \underbrace{\sum_{i > 0} \left(\frac{P_i^2}{2m_i} - \frac{Gm_0 m_i}{Q_i} \right) - \sum_{0 < i < j} \frac{Gm_i m_j}{Q_{ij}} \mathcal{K}_{ij}}_{\mathcal{H}_K}. \end{aligned} \quad (2.23)$$

The jump step is applied to all particles, while the interaction step is applied to particle pairs for which $\mathcal{K}_{ij} = 0$. For particles i that are not undergoing

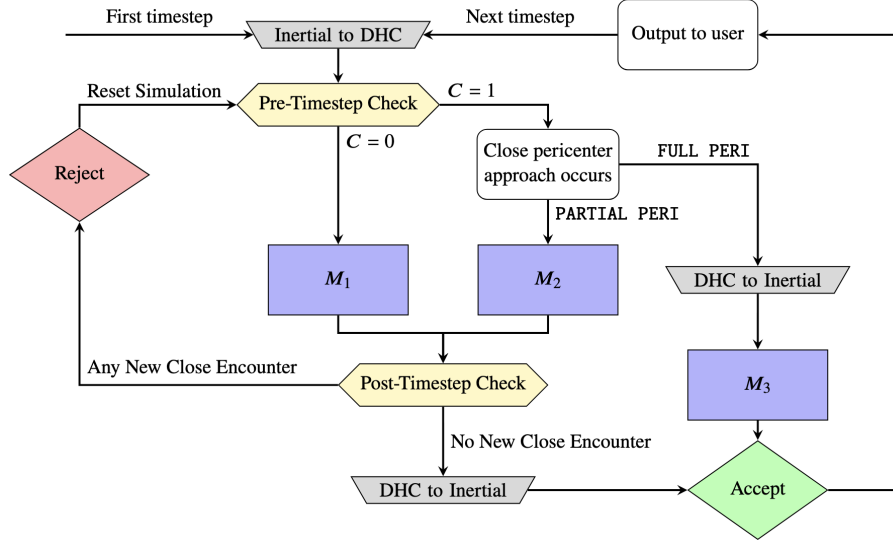


Figure 2.1. Flowchart of the TRACE algorithm. Grey trapezoids correspond to shifting reference frames. Yellow hexagons correspond to checking the planet-planet and pericenter close encounter conditions. The red diamond corresponds to step rejections that result in resetting the simulation to the pre-timestep conditions. The green diamond represents a step acceptance. Blue rectangles correspond to advancements of the simulation with the various maps M_1, M_2, M_3 . A *New Close Encounter* is defined as either any \mathcal{K}_{ij} or C_i which was previously evaluated as 0 now evaluated as 1.

any planet-planet close encounters ($K_{ij} = 0$ for all j) the Kepler step is solved with the WHFAST Kepler solver. Otherwise, BS is used.

- M_2 is the map used when there is a close pericenter approach ($C = 1$), and we are using the PARTIAL PERI prescription. Explicitly, this map is obtained by splitting (2.7), for use in map (2.10), in the following way,

$$\begin{aligned} \mathcal{H} = & \underbrace{\frac{P_0^2}{2m_{\text{tot}}} - \sum_{0 < i < j} \frac{Gm_i m_j}{Q_{ij}} [1 - \mathcal{K}_{ij}]}_{\mathcal{H}_0} \\ & + \underbrace{\sum_{i>0} \left(\frac{P_i^2}{2m_i} - \frac{Gm_0 m_i}{Q_i} \right) - \sum_{0 < i < j} \frac{Gm_i m_j}{Q_{ij}} \mathcal{K}_{ij} + \frac{1}{2m_0} \left(\sum_{i \neq 0} P_i \right)^2}_{\mathcal{H}_K}. \end{aligned} \quad (2.24)$$

$\mathcal{H}_J = 0$, while the interaction step is applied to particle pairs for which $\mathcal{K}_{ij} = 0$ as previously. The Kepler step for all particles is integrated using BS.

- M_3 is the map used when there is a close pericenter approach ($C = 1$), and we are using the FULL PERI prescription. Explicitly:

$$\mathcal{H} = \underbrace{\sum_i \frac{p_i^2}{2m_i} - G \sum_{0 \leq i < j} \frac{m_i m_j}{|\mathbf{q}_i - \mathbf{q}_j|}}_{\mathcal{H}_K}. \quad (2.25)$$

The DHC coordinates are abandoned here, and we simply integrate as in eq. (2.14). TRACE offers two options for this map: BS and IAS15. To differentiate these two options we denote them FULL BS and FULL IAS15.

We will now describe the switching algorithm in detail. By default, TRACE uses the FULL BS pericenter prescription.

1. The system is first converted from inertial coordinates to DHC. Note that all the coordinate conversions occur "under the hood" - the user inputs coordinates in the inertial frame, and will always receive output in the inertial frame as well.
2. At the beginning of each timestep, we evaluate C and all \mathcal{K}_{ij} .
 - (a) If $C = 0$, this means no particles are currently undergoing pericenter passage. We use M_1 .
 - (b) If $C = 1$, there is a particle undergoing a pericenter passage.
 - i. If PARTIAL PERI is being used, use map M_2 .
 - ii. If FULL PERI is being used, first convert back to inertial coordinates, then use map M_3 . We are not performing any splitting here, so there is no need to do a post-timestep check. We always accept the step.
3. After executing M_1 or M_2 , the conditions C and K_{ij} are re-evaluated for each particle.
 - (a) If no particle pair that initially has $\mathcal{K}_{ij} = 0$ becomes $\mathcal{K}_{ij} = 1$, **and** C does not go from 0 to 1, this means no close encounters of any sort have been introduced in the new step. We **accept** this step. Note that we do not concern ourselves with a particle pair with $\mathcal{K}_{ij} = 1$ initially going to $\mathcal{K}_{ij} = 0$ or C going from 1 to 0, as this corresponds to a particle leaving the close encounter regime.

- (b) Otherwise, a particle has entered a close encounter of some sort in the previous step. We **reject** the step, reset the simulation and perform a new step where the pre-encounter step now takes into account the updated \mathcal{K}_{ij} 's and C . The logic for the operators in this new step follow the first bullet point, accounting for the new values of \mathcal{K}_{ij} and C in this new step.
4. If needed (in the case of M_1 or M_2 being accepted), we convert from DHC to Inertial coordinates.

Note that for a step with the efficient map M_1 to be accepted, it must satisfy $\mathcal{K}_{ij} = 0$ and $C = 0$ both before and after the step. This ensures the time-reversibility of our algorithm - integrating in either time direction will result in the same switching between maps. In practice, very few steps will need to be rejected, typically of order a few percent or less. But as we will see in the following section, the rejection of these few spurious steps results in very good long-term error performance, and the fact that so few steps need to be redone is a worthwhile trade-off.

We note that this algorithm is only almost perfectly time reversible. This is due to inconsistent or ambiguous cases that our algorithm cannot detect. For more discussion on this topic, see [Hernandez & Dehnen \(2023\)](#). We also note that even if the algorithm itself were to be perfectly time-reversible, floating-point precision and secular drift from Bulirsch-Stoer also render the algorithm not exactly time-reversible.

2.4.2 Switching Functions

In this section we describe the switching functions $\mathcal{K}(Q_{ij}^{(x)})$ and $C(Q^{(x)})$. In principle any user-defined switching function that does not depend on the sign of time (for instance, a dependence on V^n with odd n) may be used - we will focus on the two switching functions used in our tests that are responsible for our algorithm's computational efficiency and are included in TRACE by default.

Planet-Planet Close Encounter Condition

The default switching condition is designed to detect close encounters at the beginning, end and during a timestep in a time-reversible way, making use only of the positions and momenta available at each time step. Our algorithm approximates particle motion mid-timestep as straight line motion, so some close encounters may be missed – however, we have found it to be effective in the vast majority of

cases. Explicitly, the switching function which detects a close encounter between particles i and j , $\mathcal{K}_{ij}(Q_{ij}^{(x)})$, can be written:

$$\mathcal{K}(Q_{ij}^{(x)}) = \begin{cases} 1 & \text{for } Q_{\min} < a_H R_{\text{crit}} \\ 0 & \text{otherwise.} \end{cases} \quad (2.26)$$

On the right-hand side, a_H is a constant that may be set by the user ($a_H = 3$ by default) and R_{crit} is the maximum of a modified Hill radius criteria between the two bodies,

$$R_{\text{crit}} = \max\left(Q_i \sqrt[3]{m_i/3m_0}, Q_j \sqrt[3]{m_j/3m_0}\right), \quad (2.27)$$

which is the Hill radius where heliocentric distance replaces the traditional semi-major axis. The logic behind using the modified Hill radius condition is due to unbound particles: the Hill radius only has meaning for Keplerian orbits, and thus will not appropriately flag a close encounter between a pair of unbound planets. While less physically meaningful than the Hill radius, our criterion achieves good results across the board, and is much better for systems where particles become unbound, and the traditional Hill radius definition fails.

Q_{\min} represents the minimum distance between particles over the range $t \in [t_n - \frac{h}{2}, t_n + \frac{h}{2}]$. We use a similar first-order estimate in time to the one described in Hernandez & Dehnen (2024)⁵, section 3.1.1, to calculate Q_{\min} . To ensure time-reversibility, we must check in the two time directions by switching the sign of velocity. The minimum will occur in the d time direction, where $d = \pm 1$, and $d = 1$ is forwards time and $d = -1$ is backwards time. d satisfies $d(Q_{ij} \cdot V_{ij}) < 0$. In the rare case $Q_{ij} \cdot V_{ij} = 0$, Q_{\min} is given at present, with $Q_{\min} = Q_{ij}$. Otherwise, Q_{\min} occurs at $t = t_n + dt_{\min}$, with $t_{\min} \equiv -d(Q_{ij} \cdot V_{ij})/V_{ij}^2$ (so that $t_{\min} > 0$). Then we have,

$$Q_{\min} = \begin{cases} \sqrt{Q_{ij}^2 - (Q_{ij} \cdot V_{ij})^2/V_{ij}^2} & \text{for } t_{\min} < h/2, \text{ and} \\ \sqrt{Q_{ij}^2 + hd(Q_{ij} \cdot V_{ij}) + h^2V_{ij}^2/4} & \text{for } t_{\min} \geq h/2. \end{cases} \quad (2.28)$$

This is a similar switching function to the one used in MERCURIUS. There are four key differences: first, our switching function is discrete, while the MERCURIUS switching function is smooth. Secondly, MERCURIUS uses the standard Hill radius definition while ours is modified. Third, MERCURIUS includes a more robust encounter prediction algorithm. In the MERCURIUS algorithm the particles are as-

⁵Hernandez & Dehnen (2024) have a typo in their section 3.1.1. Rather than $r_{\min} = \sqrt{q^2 + 2h_i p \cdot q + p^2 + h_i^2}$, it should read $r_{\min} = \sqrt{q^2 + 2h_i p \cdot q + p^2 h_i^2}$.

sumed to undergo Keplerian trajectories, rather than the straight lines used in TRACE. Due to the structure of the MERCURIUS integrator, it is feasible to perform a Kepler step "for free" computationally, but this is impossible for TRACE, so we resort to more simplified trajectories. **This is the only advantage MERCURIUS has over TRACE.** Finally, MERCURIUS calculates the switching radius at the beginning of the integration for each pair of particles, which them remains fixed for the duration of the simulation. This is necessary to maintain the symplectic nature of MERCURIUS, but has the unfortunate side result of the switching radius becoming less physically meaningful if the planet's semimajor axis changes over the course of the integration. However, changing the switching function does not impact reversibility, so this is not an issue for TRACE. To our knowledge, this is the first switching function for a hybrid integrator which **can** depend on the current state of the system, a novel result which greatly improves the flexibility of TRACE.

Pericenter Condition

The recent work of Pham et al. (2024) introduced a new adaptive timestep criterion for the IAS15 integrator. We use their result to inform our default choice of the pericenter switching. We first define,

$$\tau_{\text{PRS},i} \equiv \sqrt{\frac{2Q_i^{(2)}Q_i^{(2)}}{Q_i^{(3)}Q_i^{(3)} + Q_i^{(2)}Q_i^{(4)}}}, \quad (2.29)$$

where $Q_i^{(j)}$ is the magnitude of the j th derivative of heliocentric position of the i th particle. These higher order derivatives are approximated using a finite differencing method, the details of which are enumerated in Everhart (1985); Rein & Spiegel (2015). The necessity of calculating the higher-order derivatives does introduce some additional computational overhead, but this is not too significant and we judged that the robustness of this condition justifies this additional overhead. Then, our switching condition is given,

$$C(Q^{(x)}) = \begin{cases} 1 & \text{for } h > \eta \cdot \min_{i>1}(\tau_{\text{PRS},i}) \\ 0 & \text{otherwise.} \end{cases} \quad (2.30)$$

Where we have found that $\eta = 1$ gives good results in our testing, and is hence set as the default value. Note that this condition is a minimum over all non-central bodies in the system. Thus if any body is flagged for pericenter approach, the entire simulation will be integrated with BS or IAS15.

A note about our switching criteria follows. TRACE is a second order method. Defining the exact trajectory as $z(t)$, the TRACE trajectory as $\tilde{z}_t(t)$, and the initial

conditions $z(0)$, TRACE’s local error is,

$$\tilde{z}_t(h) = z(h) + O(h^3). \quad (2.31)$$

The switching functions in this section can only be considered approximately physical due to this fact. By contrast, the orbit for a higher order method (like IAS15) is,

$$\tilde{z}_h(h) = z(h) + O(h^{n+1}), \quad (2.32)$$

with n a larger integer like 15. For such higher order methods, the switching functions are more physical, representing time and length scales mimicking the orbits more closely. Regardless, our switching criteria work well in all tested problems.

These are the default pericenter switching conditions used in TRACE, but we have implemented a few others as well. See Appendix 2.9 for details on these alternatives.

2.4.3 Collisions

Collisions and mergers constitute irreversible steps. Thus TRACE cannot possibly be time reversible when collisions occur. TRACE handles collisions by enforcing a step acceptance: if a collision is detected mid-timestep, the step is automatically accepted regardless of either switching condition. TRACE is compatible with the standard REBOUND collision modules.

2.4.4 Additional Forces

In many astrophysical systems it may be advantageous to consider extra dissipative forces which cannot be modelled through pure N -body gravitational interactions such as tides or radiation forces. It is very easy to add these additional forces to REBOUND using REBOUNDx (Tamayo et al., 2020a), a library of additional physics that can be added to a REBOUND simulation.

We briefly comment on the efficacy of using a time-reversible integrator such as TRACE for the dynamics of the system if non-reversible forces are implemented. First, the extra forces do not necessarily need to be Hamiltonian — we can insert additional operators symmetrically in Equation (2.10). These extra forces, as long as they are relatively small, do not compromise the long-term accuracy of a symplectic method as shown in Tamayo et al. (2020a). Similarly, Hairer et al. (2006) show that time-reversible methods are not compromised by small non-Hamiltonian perturbations.

2.5 Performance Tests

In this section, we apply TRACE to a number of realistic astrophysical systems and compare its performance against other integrators available in REBOUND⁶. All the tests are performed using their C implementations. In all of our comparisons with IAS15, we use the new adaptive timestep criterion described by Pham et al. (2024). Unless otherwise specified, TRACE uses the FULL BS pericenter approach prescription for all our tests in this section.

2.5.1 Chaotic Exchange Orbit

We first investigate the case of a chaotic exchange orbit in the restricted coplanar three-body problem. The particular problem we have chosen includes a Sun-like star, a Jupiter-like planet on a circular orbit at its present-day semimajor axis, and a zero mass test particle. It has been studied in depth by a number of works including Wisdom (2017), Dehnen & Hernandez (2017), Hernandez (2019) and Hernandez & Dehnen (2023). In the circular restricted three-body problem, the only conserved quantity is the Jacobi constant C_J (Murray & Dermott, 2000; Tremaine, 2023). For the initial value of C_J we have selected in our tests, the test particle's orbit is exchanged between the primary and the secondary, undergoing multiple close encounters with the secondary. It can also never escape the system, making this problem an excellent test of body-body close encounters. Figure 2.2 shows the results of our test. We integrate the system for 5000 orbits of the secondary, using a timestep of $h = 8$ days. We use a hill radius switching criteria of $a_H = 4.84$ ⁷. Once every 10 years, the Jacobi constant error is calculated. We compare TRACE to MERCURIUS and WHFast. As expected, WHFAST fails to resolve the close encounters with the secondary at all, and the error is immediately catastrophic. MERCURIUS and TRACE are both able to resolve the close encounters, and both display very good error performance over the entire integration with no secular drift. The performance of both integrators are comparable, staying well below 1 percent for the duration of the simulation. Comparing the runtimes of the two hybrid integrators: TRACE took 3.26 seconds while MERCURIUS took 39.7 seconds, a 12x speedup.

⁶<https://github.com/hannorein/rebound>

⁷This value is selected for a direct comparison with MERCURIUS, which includes a hidden factor of 1.21 in the source code.

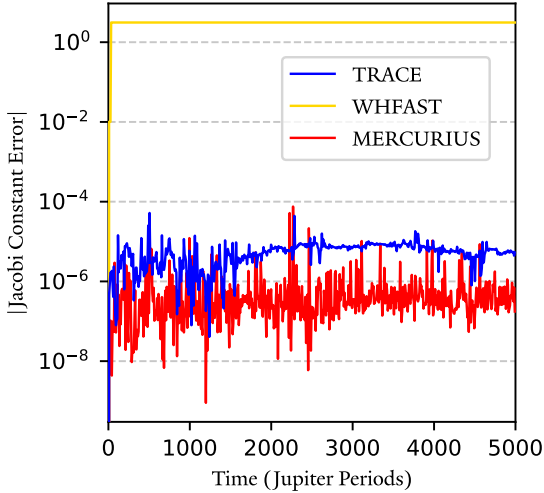


Figure 2.2. A comparison between TRACE, MERCURIUS and WHFAST for the chaotic exchange problem. With a timestep of $h = 8$ days, the system is integrated for 5000 orbits of the primary with Jacobi constant error recorded every 100 years. WHFAST immediately fails, while TRACE and MERCURIUS both show comparable good error performance with no secular drift. TRACE represents a $9.4x$ speedup over MERCURIUS for this problem. The mean error for TRACE and MERCURIUS are 5.72×10^{-6} and 3.01×10^{-6} , respectively.

2.5.2 Highly Eccentric Orbits

To evaluate TRACE’s capabilities in resolving close encounters with the central body, we consider a two-planet system consisting of the Sun, Jupiter and Saturn. However, here Saturn’s eccentricity is set to a various extremely high values, while its inclination is set to $\pi/2$ with respect to the orbit of Jupiter. With this setup, Saturn never has a close encounter with Jupiter, but does approach very close to the Sun.

This problem was first introduced in [Levison & Duncan \(2000\)](#) and revisited by [Wisdom \(2017\)](#); [Hernandez & Dehnen \(2023\)](#). We present the results of a number of tests we have performed on this system. First, we set $e = 0.99$ for Saturn and integrated the system for 300 Saturn orbits, using a timestep of $h = 0.15$ years. This is approximately 1/80th the period of Jupiter, the shortest orbital period of the system, so naively one might expect this to be an appropriate timestep for the Wisdom–Holman map. However, of course in reality this is not the case, as pericenter is not resolved. In the first panel of Figure 2.3, we compare the performance of WHFAST, MERCURIUS, BS and TRACE. The absolute value of the relative energy error, defined as $(E - E_{\text{init}})/E_{\text{init}}$, is output at the end of every timestep. We see that once again WHFAST immediately fails catastrophically, while MERCURIUS also fails to resolve the close encounters with the host star and the energy error rapidly

exceeds 10^{-1} . TRACE keeps the energy error well under 10^{-4} for the entire duration of the simulation, with no appreciable secular drift. BS does better than any of the splitting schemes, but secular drift is visible, which is expected of non-symplectic or non-reversible schemes. We also test WHFAST with a smaller timesteps which resolves the pericenter, to show that in principle it is possible to achieve similar results with the pure Wisdom–Holman map. The timestep necessary to resolve the pericenter for an eccentric orbit is related to the "effective period at pericenter" (Wisdom, 2015; Hernandez et al., 2022),

$$\tau_f = 2\pi \sqrt{\frac{(1-e)^3}{1+e} \frac{a^3}{Gm_0}}, \quad (2.33)$$

where a, e are the eccentricity and semimajor axis of the orbit. We test WHFAST with a timestep of $\tau_f/50$. This timestep is chosen to achieve a close match with TRACE's performance. We refer to this tests as WHFAST Resolved. We see that it is possible to reach similar levels of energy error with TRACE with pure Wisdom–Holman. However, we can see from the bottom panel of Figure 2.3 that there are vast computational costs to picking such a small timestep, and that TRACE achieves similar error performance much faster.

In the second panel of Figure 2.3, we perform similar simulations, but we now set the initial eccentricity of Saturn to various values up to 0.9999. These values were selected for comparison with Figure 1 of Levison & Duncan (2000) and Figure 8 of Hernandez & Dehnen (2023). For each simulation, we plot the maximum energy error reached over the entire runtime. WHFAST and MERCURIUS perform similarly, with at least 10^{-1} energy error in all cases and reaching errors significantly greater than unity for the highly eccentric systems. TRACE again keeps the error around 10^{-3} , and in fact shows consistent performance across all eccentricities. We see that even with much smaller timesteps WHFAST Resolved still performs badly at high eccentricities, while also having significantly slower compute time. The power of the pericenter switching condition allows TRACE to resolve extremely eccentric orbits with far more reasonable timesteps.

2.5.3 Violent Systems

We envision violent systems to be one of the most relevant and powerful applications of TRACE. A violent system is one which undergoes significant dynamical instability, triggered by close encounters between planets. This can result in planets being ejected from the system, or being scattered onto orbits with high eccentricity and/or inclination. Planet-planet scattering almost certainly plays a role in sculpting the demographics of exoplanetary systems (Nagasawa & Ida, 2011). Such systems are obvious applications for hybrid integrators, as for the vast

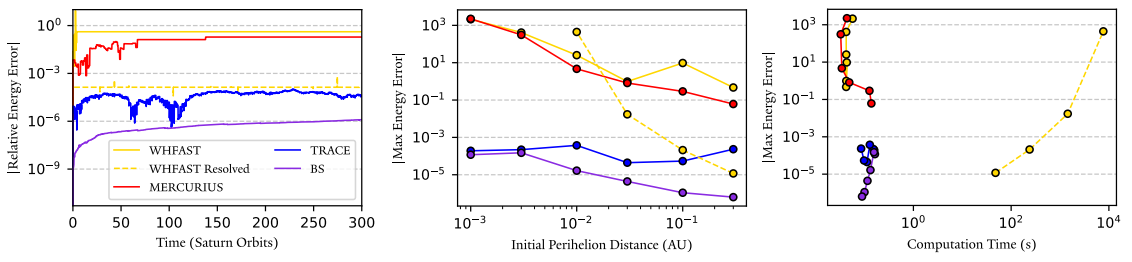


Figure 2.3. A comparison of TRACE, MERCURIUS, BS and WHFAST for a Sun-Jupiter-Saturn system where Saturn has been given a high eccentricity. The first subplot shows the absolute value in the energy error over 300 orbits of Saturn, for a case where $e = 0.99$. MERCURIUS and WHFAST are both unable to resolve the close encounter with the Sun and the error quickly reaches or exceeds unity. TRACE keeps the error less than 10^{-3} with no secular drift. WHFAST Resolved, which are simply WHFAST with much smaller timesteps, is also plotted in dotted lines. It achieves similar error performance to TRACE, but requires significantly more time. The middle subplot compares the maximum error of six such systems with varying eccentricity for Saturn, plotted as a function of initial perihelion distance (the orbit slightly evolves over the course of the simulations). All MERCURIUS and WHFAST simulations perform worse as the eccentricity increases, while TRACE is consistently better. The bottom plot shows the same data points as the middle subplot, but now plotted on an efficiency cost vs. maximum energy error plot. We see that while WHFAST Resolved can in principle keep up with TRACE in error performance for relatively low eccentricities, this comes at a vast computation cost. TRACE performs comparably to BS from a computation cost standpoint.

majority of the simulation the planets are well separated and Wisdom–Holman is sufficient to accurately integrate the system. While close encounters in these systems represent a relatively small fraction of the total runtime, it is crucial to handle them with a conventional integrator to avoid catastrophic error. **MERCIUS** is ineffective for many violent systems. While it can handle planet–planet close encounters well in most cases planets will be scattered onto highly eccentric orbits which leads to the pericenter approach not being resolved. In this section we will show that **TRACE** can handle these systems both quickly and accurately.

Let us consider a system of three Jupiter-mass planets orbiting a Sun-like star. Chambers et al. (1996) showed that such a system will essentially always exhibit dynamical instability if their initial separations are less than 10 mutual Hill radii. To induce rapid dynamical instability in our system, we place the first planet at $a_1 = 5$ au and space the other two 3 mutual Hill radii out from the planet immediately interior. The eccentricity of each planet is set to 0.05, and the inclinations are set to $1^\circ, 2^\circ, 3^\circ$ from the inner to outer planet. All other orbital angles are set to 0. We remove any particles which pass beyond 10^4 au of the central star, using the `exit_max_distance` condition in REBOUND. Each time a particle is removed from the simulation, we reset to the center of mass frame of the system to avoid CoM and particle drift (which, left unchecked, would trigger the exit condition for all particles). We account for the lost energy associated with removing a particle from the system and the transformation back to the new center of mass by using REBOUND’s built in `track_energy_offset` feature. We consider collisions as well, using the built-in REBOUND collision modules `REB_COLLISION_DIRECT` for collision detection and `reb_collision_resolve_merge` for collision resolution. Collisions are flagged when any pair of particles overlap radii, and are resolved by merging the two colliding particles into one (conserving mass, momentum, and volume, but not energy).

This is a highly chaotic system, so comparing the performance of integrators for a single system is essentially meaningless - the slight numerical differences ensure that we are very quickly working with entirely different systems. Instead, we take a statistical approach by considering an ensemble of such systems. The setup of our analysis is as follows. We have run 500 instances of the system as described above, but have displaced the x -coordinate of the outermost planet by a random amount between -10^{-12} and 10^{-12} au. We run each of these 500 instances with the following integrators: **TRACE**, **MERCIUS**, **BS**, and **IAS15**. Each system is integrated forward in time for 10^7 years (which is roughly 9×10^5 initial orbits of the innermost planet). For **TRACE** and **MERCIUS** we set the initial timestep equal to 0.221 years. We arrive at this value from a conservation of energy argument. The smallest possible dynamical timescale at the end of this problem is the scenario where one planet is left on a close-in orbit and the other two are completely ejected. We

calculate the orbital period of this close-in orbit and set our timestep to 1/15th of this value. IAS15 and BS are adaptive-timestep integrators - their initial timesteps are taken to be $2\pi \times 10^{-3}$ years.

Figure 2.4 shows the statistical results from our ensemble. The upper subplot displays the number planets in the system that survive over the course of the 10^7 year integration. The distributions of TRACE, BS and IAS15 match each other very well, with the vast majority of systems ejecting one planet and retaining two. MERCURIUS, on the other hand, differs significantly in these statistics, with a more even split between one- and two- planet systems. The middle subplot displays the distribution of energy error at the end of the simulations of TRACE, BS and MERCURIUS. As expected IAS15 performs very well, with a distribution centered around 10^{-11} , and as such is omitted from the plot for clarity. MERCURIUS, also as expected, performs very poorly, with a median error very close to unity. Pure BS in general performs better than either hybrid integrator, with a median error of approximately 10^{-4} . TRACE represents a significant improvement over MERCURIUS, with a median error of $10^{-1.49}$ compared to $10^{-0.14}$. The largest TRACE error is $10^{-0.28}$, and the largest MERCURIUS error is $10^{0.44}$. In the bottom subplot, we show histograms of the total runtime of simulations. For clarity, we only show the lower end of the IAS15 results - this distribution is centered on 26 minutes. The TRACE has a significant speed advantage over both BS and IAS15. This advantage grows the more particles are added to the system, as can be seen in the next section.

Of particular interest to those seeking to use TRACE on large ensembles of chaotic systems is the question of how well TRACE is able to reproduce the demographics of orbital elements on a statistical level. We investigate this in Figure 2.5. For this phase we consider only our simulations where two planets survive, as the other three cases do not have sufficient representation to perform robust statistical analysis on. We have plotted the cumulative distributions of eccentricity and inclination for the inner (P1) and outer (P2) planets for all simulations in which two planets survive, for each integrator. By eye, TRACE, BS and IAS15 appear quite similar.

In summary, TRACE reproduces the results of IAS15 quite well on a statistical level, with an almost 20x speedup. This is in stark contrast to MERCURIUS, which qualitatively fails to reproduce the IAS15 statistics. In the preparation of this manuscript, [Lu et al. \(2024a\)](#) used TRACE for a similar ensemble of violent scattering systems, with excellent error performance as well.

2.5.4 Accretion of the Moon

As a test of TRACE's ability to integrate systems with a very large number of particles, we study the accretion of the moon from an impact disk generated by

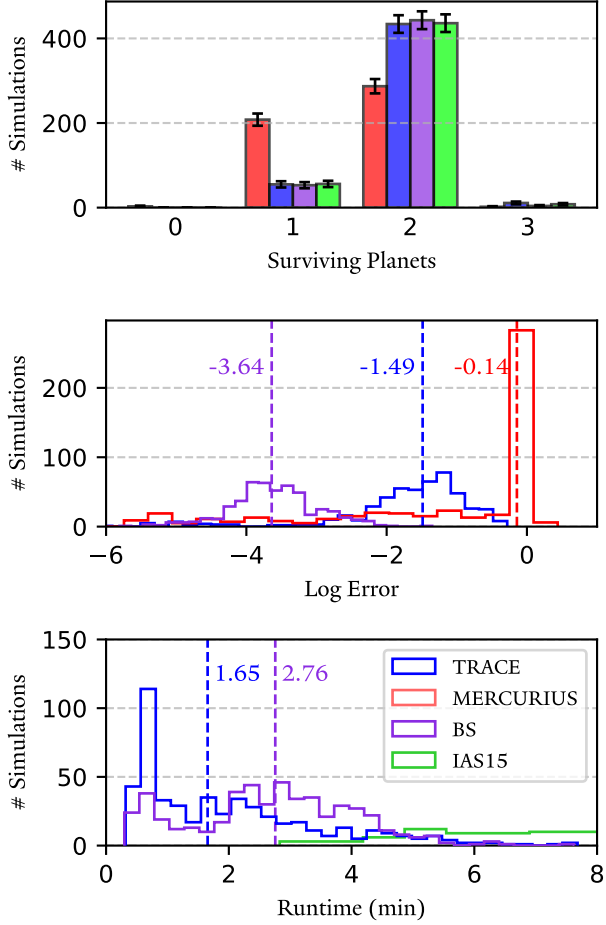


Figure 2.4. Statistics on an ensemble of 500 three-body scattering simulations, comparing the performance of TRACE, MERCURIUS, IAS15 and BS. The top subplot shows the final number of planets surviving at the end of the 10^7 year integration. MERCURIUS is the obvious outlier, while TRACE replicates the statistics of IAS15 best. Poisson error bars are shown. The middle subplot shows histograms of the final energy errors, as well as the median values. IAS15 is not shown for clarity, but its distribution is centered around 10^{-11} . TRACE represents a significant improvement over MERCURIUS, with the largest TRACE error being $10^{-0.28}$. The bottom subplot shows histograms of the runtimes. MERCURIUS is very fast due to the number of systems that eject too many planets. TRACE and BS both significantly improve on the IAS15 runtime, with TRACE having a small advantage over BS. The median runtimes of TRACE and BS are plotted in dotted lines. TRACE has a 1.67x speed advantage over BS and a 15.56x speed advantage over IAS15. Since MERCURIUS performs very poorly in this system we elect not to display its runtime on the bottom subplot to reduce clutter — it is very fast, but due to poor error performance should not be used for such systems.

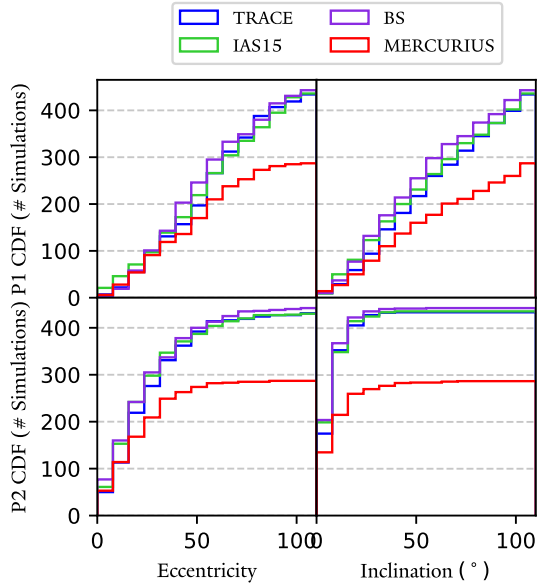


Figure 2.5. Cumulative distribution functions for the two-planet systems with all four integrators. The top row are the distributions for the inner planet, and the bottom row the distributions for the outer planet. We plot eccentricities in the left column and inclinations in the right. TRACE, BS, and IAS15 show very similar distributions, while it is clear that MERCURIUS underpredicts two-planet systems.

a giant impact via direct N -body simulations. This problem has been studied by [Ida et al. \(1997\)](#); [Duncan et al. \(1998\)](#); [Kokubo et al. \(2000\)](#) among others.

We present results from a simulation in the spirit of these studies. While our exact initial conditions do not match these studies, the final results are not sensitive to the precise initial conditions. Our simulation includes 10^3 disk particles around an Earth-mass planet. The units of this simulation are the same as the study of [Duncan et al. \(1998\)](#): mass in Earth masses, Roche radius, and $G = 1$ (so a particle exactly at Earth's Roche radius has an orbital period of 2π). The initial masses are randomly drawn from a power law distribution $\propto m^{-1}$ between $m = 3.2 \times 10^{-7}$ and $m = 3.2 \times 10^{-4}$. The total initial mass of the disk in our simulation is approximately four lunar masses. As in [Kokubo et al. \(2000\)](#), the density of the disk particles is $\rho_p = 3.3 \text{ g cm}^{-3}$, while the density of the Earth is taken as $\rho_E = 5.5 \text{ g cm}^{-3}$. Therefore, the radius of each disk particle is given by $r = (m/M_E)^{1/3}(\rho_p/\rho_E)^{-1/3}R_E$. In these units, $R_E = 1/2.9$. The semimajor axes of the disk particles are drawn from a power law distribution $\propto a^{-1}$ between $a = R_E$ and $a = 1.5$. The eccentricities, inclinations, and other orbital angles (Ω, ω, f) are drawn from uniform distributions between $\{0, 0.95\}, \{0^\circ, 50^\circ\}$ and $\{0^\circ, 360^\circ\}$, respectively. Unlike [Duncan et al. \(1998\)](#), we do not remove initially Earth-crossing orbits as our method can handle highly eccentric orbits well.

We first do not consider collisions, and simply integrate the system with TRACE, MERCURIUS, IAS15, and BS for 6π time units. In this particular system while disk particles do get very eccentric, they have such low mass that error associated with a large jump term may not be significant. We thus also investigate the performance of TRACE using three prescriptions: the default FULL BS pericenter prescription, PARTIAL PERT, as well as completely turning off pericenter switching. The results are plotted in Figure 2.6 on an efficiency diagram. We see that TRACE, BS and IAS15 all have very good error performance and high compute times. The poor computational performance of TRACE makes sense in this context: with so many particles we approach the limit of there being a pericenter close encounter every timestep - so TRACE essentially becomes BS with more overhead in this case. MERCURIUS is just as slow as the other three integrators, but performs worse due to failing to resolve pericenter approaches. Note, however, that despite failing to resolve pericenter approaches the error is still relatively good (around 10^{-3}), as stated earlier. The reason for the slightly better performance of MERCURIUS compared to the non-pericenter TRACE prescriptions is due to MERCURIUS having a more robust encounter prediction routine, as described in Section 2.4. TRACE with no pericenter switching detected 77299 close encounters, while MERCURIUS detected 137520. TRACE Partial and TRACE with no pericenter switching achieve similar accuracy to MERCURIUS, but significantly faster. TRACE Partial has a 6.2x speed advantage over MERCURIUS, and a TRACE with no pericenter switching at all has a 41.1x advantage. We conclude that for large N systems where the particles are relatively small, TRACE with full pericenter switching offers no advantage over BS or IAS15. But if we relax pericenter switching requirements, TRACE offers comparable (relatively good) error performance to MERCURIUS with a vastly improved runtime.

We now perform the same simulation, but integrate 10^3 time units and turn collisions on with the same prescription as Section 2.5.3. Figure 2.7 shows the results of our simulation using TRACE Partial. The left hand subplot shows the number of particles in the simulation as a function of time. While a direct comparison should not be made with the results of [Ida et al. \(1997\)](#) and [Duncan et al. \(1998\)](#) due to the slightly different initial conditions, qualitatively all four integrators match their results (and each other) well – see Figure 9 in [Duncan et al. \(1998\)](#). The right hand plots show snapshots of our TRACE simulation (blue) and IAS15 simulation (green) at the simulation’s start (shared between the two simulations, plotted in black), 60 time units and at the end. The location of the particles think is plotted in cylindrical coordinates (r, z) centered on Earth in units of Roche radius. These may be compared to Figures 2 – 4 in [Ida et al. \(1997\)](#), and again are qualitatively similar. Both final results for TRACE and IAS15 in the bottom right panel shows one large body just within the Roche radii. This is in good agreement with the results of [Ida et al. \(1997\)](#) and [Kokubo et al. \(2000\)](#).

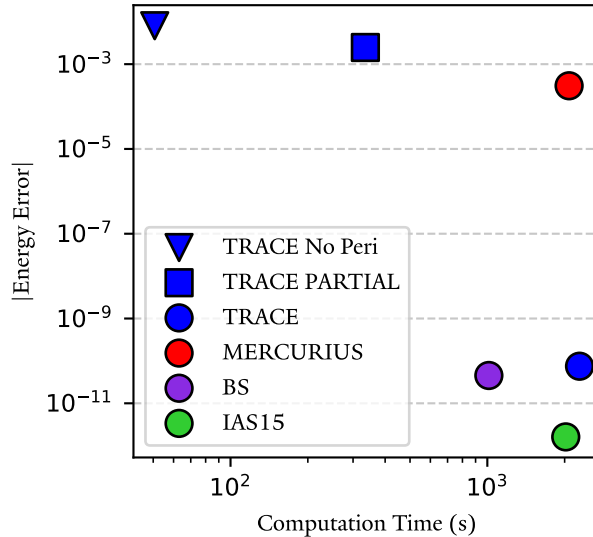


Figure 2.6. Efficiency plot of various integrators for the large- N accretion problem without considering collisions. TRACE, BS and IAS15 all perform very well from an error standpoint, but are quite slow. MERCURIUS is just as slow, but is far less accurate. TRACE Partial and TRACE no Peri offer much fast alternatives while maintaining roughly the accuracy of MERCURIUS.

The differences in our simulations can be attributed to differences in the initial conditions and integration methodology. The runtimes for the simulations are 7.06, 46.87, 90.13, and 65.98 seconds for TRACE, MERCURIUS, BS and IAS15, respectively. TRACE improves on the runtime of MERCURIUS, BS and IAS15 by 6.60x, 12.80x and 9.30x, respectively.

We conclude that once again TRACE offers enormous computational benefits while maintaining acceptable levels of accuracy for large N systems with collisions, qualitatively reproducing the results of IAS15.

2.5.5 ZLK Cycles

The von Zeipel-Lidov-Kozai (ZLK) effect has been a well-studied phenomenon of great interest and wide application since its discovery (von Zeipel, 1910; Lidov, 1962; Kozai, 1962; Naoz, 2016). In a hierarchical three-body system, a highly inclined outer perturber can induce significant coupled eccentricity and inclination oscillations in the orbit of the inner body. Similarly to Section 2.5.2 Wisdom-Holman methods are in principle capable of accurately integrating the system. However, a worst-case timestep that accurately resolves the pericenter passage during high-eccentricity epochs must be applied over the length of the simulation, meaning that in practice it is actually faster to use adaptive-timestep higher order

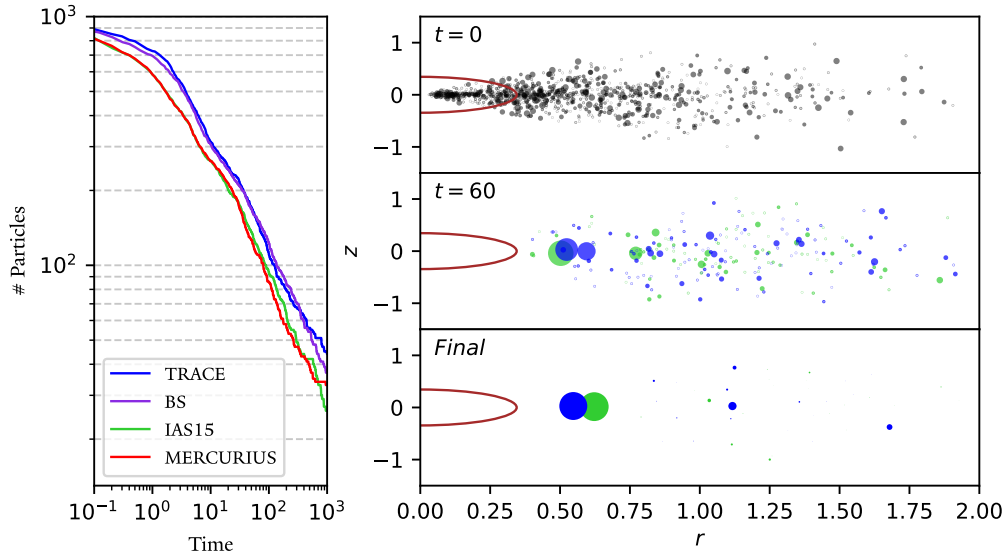


Figure 2.7. Results from a lunar accretion problem involving 1000 particles, accounting for collisions. We compare results from TRACE, MERCURIUS, IAS15 and BS. The left subplot shows the total number of bodies in the simulation as a function of time. All three integrators show good agreement. The right subplots show snapshots of the simulation at $t = 0, 60$ time units and the end of the simulation, for both TRACE (blue) and IAS15 (green). The positions of the planetesimals are plotted in cylindrical coordinates, and the size of each point in the graph corresponds to the planetesimal's mass. The physical radius of Earth is depicted in brown. We see that a roughly lunar-mass object (~ 0.9 lunar masses in both simulations) forms at just within the Earth's Roche limit. Note also that many disk particles are initialized within the physical radius of Earth. In many previous works these particles would need to be removed due to poor resolution of pericenter passage — a significant advantage of TRACE is in the accurate handling of such particles.

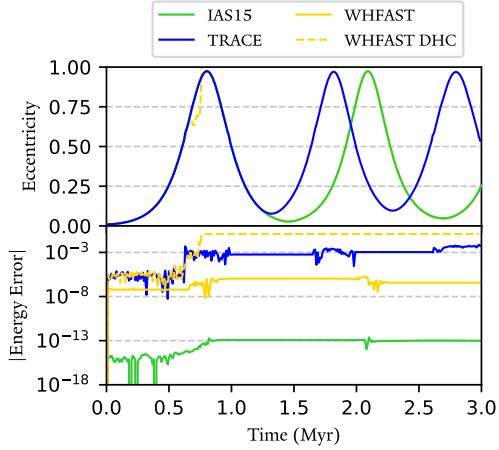


Figure 2.8. A comparison of IAS15 (green), TRACE (blue), and WHFAST in both Jacobi (gold) and DH (gold dashed) coordinates for ZLK oscillations. The upper subplot shows eccentricity evolution, and the bottom subplot depicts energy error over time. The eccentricity evolution of IAS15 and WHFAST in Jacobi coordinates are identical at this scale – their curves appear identical. WHFAST in Jacobi coordinates outperforms TRACE in both error and computation performance. TRACE gives qualitatively different results than IAS15 and WHFAST.

integrators such as IAS15. This would initially seem to be a good use case for TRACE, but we will show in this section that other integrators perform better.

We first consider a prototypical system in which ZLK oscillations are expected to occur. The initial values of our fiducial system are slightly modified from Figure 16 of Naoz (2016). In our test, we consider a Neptune-mass planet initially orbiting a $0.32 M_{\odot}$ star with $a_1 = 2$ au and $e_1 = 0.01$. The perturber is a $10 M_J$ brown dwarf orbiting the primary with $a_2 = 50$ au, $e_2 = 0.52$ and $i_2 = 80^\circ$. We integrate this system with IAS15, WHFAST and TRACE. For TRACE, we use a timestep equal to 1/20 the initial orbital period of the planet. Figure 2.8 plots the eccentricity evolution of the inner planet and the energy error over two ZLK cycles.

The runtimes for TRACE, WHFAST and IAS15 are 19.63, 7.47, and 284.98 seconds, respectively. We see that while TRACE maintains an acceptable level of error in this problem, WHFAST actually outperforms it in both speed and computation time. The reason for this has to do with the choice of splitting scheme and coordinates. By default, WHFAST is implemented in Jacobi coordinates. This differs from DHC used by TRACE in that \mathcal{H}_K does exactly represent a Keplerian orbit. Hence, in Jacobi coordinates Wisdom–Holman methods are able to accurately integrate arbitrarily eccentric orbits without the need to choose an extremely small timestep to resolve pericenter approach. We demonstrate this by also plotting an implementation of WHFAST in DHC in dotted lines, with the same timestep. We see that this scheme

fails at relatively low eccentricity, and the planet is quickly ejected from the system.

We emphasize that this is not exactly a failure case for TRACE, as it is working as intended. Rather, this should be seen as a strength of the Wisdom–Holman method for the specific case of a highly eccentric innermost planet. We conclude that for such systems, TRACE is unsuitable: if one desires extremely high accuracy IAS15 should be used, and if moderate accuracy with high speed is required then WHFAST outperforms TRACE and should be used instead.

2.6 Potential Improvements

In this section, we list two potential improvements to TRACE that are not currently implemented.

2.6.1 Pairwise Reversibility

Currently, upon rejection of a timestep, TRACE will reset the entire simulation to the initial state and re-integrate all particles. This is unavoidable for close encounters with the central body, since the TRACE map entails moving the entire \mathcal{H}_I to \mathcal{H}_K , which would couple the equations of motions of all the particles and necessitates solving them all with BS. However, this in principle can be avoided for planet-planet close encounters, since moving \mathcal{H}_I to \mathcal{H}_K is only a function of the positions and velocities of the two bodies undergoing a close encounter. Hence we should only need to redo the interaction steps for the non-close encounter particles, without needing to recalculate the relatively expensive Kepler step.

In practice this is only a time save for step rejections, which for the majority of simulations are a comparatively small fraction of the total steps taken in the simulation, so the actual computational benefit is insignificant. We have hence elected to not include pairwise reversibility in this iteration of TRACE.

2.6.2 Adaptive Timestepping

[Hernandez & Dehnen \(2023\)](#) showed that reversibly switching between timesteps using the same switching scheme is feasible. Notably, [Hernandez & Dehnen \(2024\)](#) were able to reversibly adapt the timestep of a SYMBA-like algorithm to great effect. Their implementation used different timesteps for different "shells" of increasing distance from the host star. The difficulty of a more flexible scheme valid for a wider array of astrophysical systems precluded its inclusion into TRACE. In principle, the global timestep of TRACE should be able to be adapted reversibly, which would result in performance gains.

2.7 Conclusion

We present TRACE, a time-reversible hybrid integrator capable of efficiently and accurately resolving any type of close encounter in the planetary N -body problem. TRACE matches or improves upon the error performance of current hybrid integrators such as MERCURIUS with a conceptually simpler switching scheme and a significant speedup (up to 14x for certain problems). TRACE is freely available as part of the REBOUND package at <https://github.com/hannorein/rebound>⁸. It is available in both C and Python. From our testing, TRACE is superior to MERCURIUS in all cases. We anticipate TRACE having a myriad of useful applications including violent scattering systems, large N systems, and systems with highly eccentric orbits.

While TRACE shows excellent performance, there are clear avenues of improvement such as pairwise-reversibility and adapting the global timestep, both of which could lead to significant speedups. The fact that TRACE is almost completely reversible lends itself to significantly more flexibility than symplectic integrators such as MERCURIUS, in particular with our choices of switching functions. We did not deeply explore potential switching functions - rather, we aimed to select safe defaults for the user. In principle, these switching functions could be any arbitrary function of particle positions and velocities and further exploration may lead to better results.

It is instructive to directly compare and discuss the advantages TRACE has over MERCURIUS, the current hybrid integrator implemented in REBOUND. First, TRACE is significantly faster than MERCURIUS in many cases. There is some minor benefit from the simpler switching function. However, the vast majority of the speedup comes from the use of BS for close encounters in the case of TRACE, instead of IAS15 for MERCURIUS. While IAS15 indeed is significantly more accurate than BS, for hybrid integrators the error is dominated by error associated with operator splitting (see Section 2.2.1). This greatly overshadows the difference in error between IAS15 and BS, so our choice of BS over IAS15 provides significant speed benefits with negligible accuracy tradeoff. Secondly, TRACE is able to resolve close encounters with the central body, unlike MERCURIUS which can only handle close encounters between pairs of planets. This allows TRACE to effectively integrate highly eccentric orbits which MERCURIUS fails at. Finally, ignoring finite floating point precision, TRACE is exactly time-reversible while MERCURIUS is symplectic. The almost time-reversible nature of TRACE means that it has good long-term error conservation properties as we have shown in this work. The fact that TRACE

⁸Extensive documentation and example notebooks are available at <https://rebound.readthedocs.io>

is not symplectic affords it several flexibility advantages over MERCURIUS, which is demonstrated most prominently in the switching function. To maintain the symplectic nature of MERCURIUS, the switching distance is set at the beginning of the simulation and cannot change. If the system significantly changes this criteria may become unphysical - for instance, if a planet moves outward over the course of the simulation close encounters will be underpredicted. TRACE does not face this issue, and can adjust the switching criteria as a function of the state of the simulation such that it always remains a physically meaningful quantity. This has the further advantage that we can implement TRACE such that each timestep only depends on the inertial particle coordinates, but not pre-calculated per-particle parameters such as switching radii. This makes adding/removing/colliding/merging particles during a simulation much easier. Given that TRACE performs strictly better than MERCURIUS, the MERCURIUS integrator will be deprecated in the near future.

Finally, we discuss specific use cases for TRACE. We must emphasize that by virtue of being a hybrid integrator TRACE has limited use cases. In the vast majority of cases, REBOUND users are encouraged to use WHFAST for the planetary N -body problem when there are no close encounters, or IAS15 for a wider variety of problems where high accuracy is paramount. We recommend TRACE for cases of the planetary N -body problem where close encounters do occur, be it with the central star or between pairs of planets, and where only moderate accuracy is required but fast computation is desired. For instance, in large ensembles of chaotic systems exact accuracy in each individual system is not required to recover macroscopic quantities on a statistical or population level - and very large ensembles benefit greatly from the speedups afforded by TRACE.

Acknowledgements

We thank the reviewer Antoine Petit for helpful comments that greatly improved the manuscript. We thank Yasmeen Asali, Walter Dehnen, Shigeru Ida, Gregory Laughlin, Rosemary Mardling and J. Sebastian Monzon for enlightening discussions. This work has benefited from use of the Grace computing cluster at the Yale Center for Research Computing (YCRC). Some results in this work make use of the colormaps in the CMasher package ([van der Velden, 2020](#)).

2.8 Appendix: Democratic Heliocentric Coordinates

TRACE uses the Democratic Heliocentric Coordinates introduced by [Duncan et al. \(1998\)](#). These coordinates are also used by MERCURIUS, and are given by,

$$\mathbf{Q}_i = \begin{cases} \mathbf{q}_i - \mathbf{q}_0 & \text{for } i \neq 0 \\ \frac{1}{m_{\text{tot}}} \sum_{j=0}^{N-1} m_j \mathbf{q}_j & \text{for } i = 0. \end{cases} \quad (2.34)$$

The corresponding conjugate momenta are given:

$$\mathbf{P}_i = \begin{cases} \mathbf{p}_i - \frac{m_i}{m_{\text{tot}}} \sum_{j=0}^{N-1} \mathbf{p}_j & \text{for } i \neq 0 \\ \sum_{j=0}^{N-1} \mathbf{p}_j & \text{for } i = 0. \end{cases} \quad (2.35)$$

2.9 Appendix: Other Pericenter Switching Functions

In this Appendix we describe some alternative prescriptions for our pericenter switching condition that are also included with TRACE.

Effective Period at Pericenter

[Wisdom \(2015\)](#) demonstrated that the Wisdom–Holman method is able to integrate arbitrarily eccentric orbits, so long as the timestep chosen does not exceed 1/16th of the effective period at pericenter, or $2\pi/\dot{f}|_{\text{pericenter}}$ where f is the true anomaly. We use this result to informs another possible choice of pericenter switching condition:

$$P_i = \frac{2\pi}{\dot{f}_i} - a_p h, \quad (2.36)$$

where

$$\dot{f}_i = \frac{|\mathbf{Q}_i \times \mathbf{v}_i|}{Q_i^2}. \quad (2.37)$$

a_p is a constant that may be set by the user. [Wisdom \(2015\)](#) recommends $a_p = 17$. The full switching condition condition is given by

$$C(Q^{(x)}) = \begin{cases} 1 & \text{for } \min_{i>0} P_i < 0 \\ 0 & \text{otherwise.} \end{cases} \quad (2.38)$$

While powerful, this condition is incomplete - it is only meaningful for bound Keplerian orbits. For unbound orbits, this condition does not trigger.

Heliocentric Distance

The most simple prescription one can use is simple heliocentric distance from the star, and can be written,

$$C(Q^{(x)}) = \begin{cases} 1 & \text{for } \min_{i>0} [Q_i < a_p] < 0 \\ 0 & \text{otherwise.} \end{cases} \quad (2.39)$$

The choice of a_p is not intuitive, depends on the scale of the system, and may require some experimentation. However, if a suitable value is found for a particular system, this condition offers the most easily understood pericenter switching condition.

None

It is also possible to turn off pericenter switching as a whole, which may be desirable for some problems. In this case, TRACE essentially becomes a faster version of MERCURIUS.

2.10 Appendix: Symplecticity of TRACE

In this Appendix we demonstrate that although TRACE is composed of maps that are both symplectic and reversible, switching between them renders TRACE itself not exactly symplectic. Assume we have symplectic and reversible maps M_1 and M_2 and we'd like to switch between them. z_i is defined as the mapped phase space and z is the initial state: $z_i = M_i z$. By definition of symplecticity, it follows that,

$$\Omega = J_i^T \Omega J_i, \quad (2.40)$$

where Ω is an antisymmetric matrix,

$$\Omega = \begin{bmatrix} 0 & -1 \\ 1 & 0 \end{bmatrix}, \quad (2.41)$$

and J_i is the Jacobian matrix, $J_i = \partial z_i / \partial z$ for $i = 1$ and 2. Let's switch according to some binary scalar function $F(z)$, taking values 0 or 1, in a way that is non-reversible. We merely want to prove that switching between two symplectic maps is not symplectic, without concern for reversibility. Denote a map that switches between M_1 and M_2 as M_3 :

$$z_3 = M_3 z = (M_1 F(z) + M_2 (1 - F(z))) z, \quad (2.42)$$

Note that this map behaves differently from the algorithm behind the TRACE code; in the code's case, F is set before and after a global timestep (a modified Heaviside function), but here F can vary within a step. We return to this difference shortly. The Jacobian of this map is,

$$J_3 = \frac{\partial z_3}{\partial z} = J_1 F(z) + J_2 (1 - F(z)) + (z_1 - z_2) \frac{\partial F}{\partial z}. \quad (2.43)$$

$\partial F / \partial z$ is not finite everywhere and thus M_3 is not canonical (symplectic) everywhere. Because a modified Heaviside map has similar discontinuous F behavior, it follows that the algorithm behind the TRACE code is also nonsymplectic. Given what we have just shown, we can argue that we can switch between two symplectic methods in a nearly symplectic way, but experimentally such an algorithm often shows poor error performance. Establishing near time-reversibility, as TRACE does, is crucial for good error performance in switching between the two symplectic maps discretely.

2.10.1 Symplecticity of variable timestep maps

In fact, we can also show that symplectic maps with variable timesteps also lose exact symplecticity. We illustrate this as follows. Write a general map as,

$$\begin{aligned} q_1 &= a(z, h) \\ p_1 &= b(z, h), \end{aligned} \quad (2.44)$$

where we assume for the time being that h is a constant parameter. We can form the Jacobian of (2.44), and insert in the condition (2.40). The constraint so that map (2.44) is symplectic is,

$$\partial_q a \partial_p b - \partial_q b \partial_p a = 1, \quad (2.45)$$

which is simply the requirement that the determinant of the Jacobian matrix be 1. Now, assume h is no longer a constant parameter; e.g.,

$$\begin{aligned} q_1 &= a(z, h(z)) \\ p_1 &= b(z, h(z)). \end{aligned} \quad (2.46)$$

We take the Jacobian of map (2.46), again insert into (2.40), and use the new constraint (2.45). We are left with the following constraint, assuming $a \neq b$:

$$\partial_q h \partial_p b \partial_p a - \partial_p h \partial_q a \partial_q b = 0. \quad (2.47)$$

Only special $h(z)$ satisfying Eq. (2.47), depending on the specific map functions a and b , constitute symplectic maps. It would be interesting to construct such functions to test this constraint.

Chapter 3

Self-Consistent Spin, Tidal and Dynamical Equations of Motion

"Measure what is measurable, and make measurable what is not so."
– Galileo

Adapted From:

*Lu. T., Rein, H., Tamayo, D., Hadden, S., Mardling, R., Millholland, S. & Laughlin, G.
2023, The Astrophysical Journal, Volume 948, Issue 1, pp.11*

Abstract

We have introduced self-consistent spin, tidal and dynamical equations of motion into REBOUNDx, a library of additional effects for the popular N -body integrator REBOUND. The equations of motion used are derived from the constant time lag approximation to the equilibrium tide model of tidal friction. These effects will allow the study of a variety of systems where the full dynamical picture cannot be encapsulated by point particle dynamics. We provide several test cases and benchmark the code's performance against analytic predictions. The open-source code is available in the most recent release of REBOUNDx.

3.1 Introduction

For a myriad of interesting astrophysical systems - including but not limited to close-in binaries, hot Jupiters, ultra-short period planets (USPs), and resonant chains - the dynamics of a planet's spin axis yield crucial insight regarding the state of the system. In general the spin axis has profound implications for climate and habitability - the rotation rate and obliquity of a planet greatly influences climate stability via effects on heat flux and radiative balance (Spiegel et al., 2009). In the specific case of the systems enumerated above, *spin-orbit coupling* cannot be ignored - the dynamics of the system are impacted by the dynamics of the spin vector, and vice versa. In these cases separately computing the dynamics of the system and the evolution of the spin axes is insufficient - a self-consistent framework is required to fully capture the dynamics of both the system and the spin axes.

The *equilibrium tide* model of tidal friction was first described by Darwin (1879), and has been expanded upon by many authors (Alexander, 1973; Hut, 1980, 1981; Eggleton et al., 1998; Mardling & Lin, 2002). In the Darwin model, a star or planet possesses a tidal bulge which lags by a constant small time interval from the orientation it would have in the absence of dissipation. The equations of motion governing the spin axis of each body depend on the body's quadrupole moment and the tidal forces acting on the quadrupole deformation, both of which in turn depend on the magnitude and direction of the spin vector.

A plethora of results that draw on the equilibrium tide model have been reported over the past century and a half. Enumerating a few examples relevant to the present discussion, Goldreich & Soter (1966) constrained the internal dissipation of the solar system planets based on secular orbital observations. Wu & Murray (2003) invoked von Zeipel-Lidov-Kozai (ZLK) cycles and tidal friction to explain the highly eccentric orbit of HD 80606b (Naef et al., 2001). Fabrycky

& Tremaine (2007) investigated the evolution and orbital distributions of binary stars using the same mechanism of ZLK cycles and tidal friction, and showed it to greatly enhance the population of binary stars on short-period orbits. Mardling (2007) showed that for co-planar multi-planet systems at tidal fixed points such as HD 209458b (Charbonneau et al., 2000), eccentricity measurements yield incredible insights into the planet’s internal structure. This approach was also applied by Batygin et al. (2009) to the HAT-P-13 system (Bakos et al., 2009), and generalized to inclined systems by Mardling (2010). The above studies all utilized orbit-averaged secular expressions. While significant insight can indeed be drawn from this analytic approach, they are inherently less flexible than N -body simulations, and the orbit-averaging disallows analysis of resonant scenarios.

Hence, in recent years the development of N -body codes which self-consistently consider the evolution of both the spin and dynamical evolution of the system using instantaneous tidal deformation forces has been a priority. To provide a few excellent examples of such codes: Millholland & Laughlin (2019) used an N -body code to show that secular resonance-driven spin-orbit coupling arising during disk-driven migration is able to generate and maintain large obliquities in many of the exoplanets discovered during the course of the Kepler Mission (Borucki et al., 2010). The resulting obliquity-driven tidal dissipation provides an evolutionary mechanism that can explain the overabundance of planets just wide of mean-motion resonance. Bolmont et al. (2015) have modified the hybrid symplectic integrator Mercury (Chambers, 1999) to consistently track the spin evolution in their package Mercury-T. They used this code to draw insights regarding the habitability of the Kepler-62 system (Borucki et al., 2013) and showed the two planets in the systems habitable zone are likely to differ greatly in both obliquity and spin rate, with natural consequences for their habitability. Kreyche et al. (2021) further expanded upon this framework with SMERCURY-T, providing a framework that can self-consistently track the orbit and spin evolution of bodies in a multi-planet system under tidal influences from all bodies. Chen et al. (2021) present their independent consistent symplectic integrator package as well, GRIT. They have applied it to the Trappist-1 system (Gillon et al., 2017) and demonstrated that the differences in transit-timing variations could reach up to a few minutes over decade-long measurement baselines, and that strong planetary perturbations could push the outer Trappist-1 planets out of synchronized states.

In this work we present our implementation of self-consistent equations of spin, tidal and dynamical equations of motion in the REBOUNDx framework. REBOUND (Rein & Liu, 2012) is a widely adopted open-source N -body integrator package. REBOUNDx (Tamayo et al., 2020a) is an associated library of routines that permits the flexible addition of additional physics to REBOUND simulations. Examples of such additions include exponential growth and damping of orbits, radiation forces,

and post-Newtonian corrections. While an implementation of equilibrium tide theory is included in REBOUNDx (Baronett et al., 2022), this specific prescription does not evolve the spin axes of the bodies and hence is valid only for cases where spin-orbit coupling is negligible. This work introduces self-consistent equations of motion which are aware of the structure of each particle into the REBOUNDx package. While similar codes (mentioned previously) exist our framework provides unique advantages by virtue of its inclusion in REBOUNDx, including a variety of other rigorously-tested effects already present. These new effects in conjunction with the existing framework will provide many avenues of exploration.

The structure of the paper is as follows: in Section 3.2 we describe the equilibrium tide model we have implemented, the approximations used and the reasoning behind our choices. In Section 3.3 we explicitly describe the coupled equations of motion and additional physical parameters needed to describe systems in the equilibrium tide model. In Section 3.4 we detail how our code fits into the REBOUNDx framework - readers not interested in the details of the background physics of equilibrium tide theory can skip to this section. In Section 3.5 we apply the code to a few interesting test cases, and verify its accuracy with analytic results.

3.2 Equilibrium Tide Theory

The *equilibrium tide* model was first described by Darwin (1879). In this model, a perturbed body assumes the shape it would have in hydrostatic equilibrium with the time-varying gravitational potential of the system. Darwin (1879) expanded the gravitational potential of the perturbing body as a sum of Legendre polynomials. In the presence of internal dissipation, the body assumes a tidal deformation that is slightly misaligned with the line of centers connecting the two bodies. Each component contribution is associated with a frequency-dependent phase lag ϵ_v , where v is the frequency at which that component is forced.

The precise frequency dependence of the phase lag components is a complex function of internal structure, and hence extremely difficult to constrain. This has necessitated further approximations, for which two primary schools of thought have emerged - the *constant time lag* model (CTL) and *constant phase lag* (CPL). These prescriptions differ in their treatment of the phase lag components. We will briefly describe each approach.

The CTL approach directly follows from Darwin (1879) in the limit of a viscoelastic body. Alexander (1973) was the first to evaluate the Darwin (1879) framework in this regime: each tidal component ϵ_l is directly proportional to the l th forcing frequency. This is equivalent to a fixed time lag τ between the tidal bulge and the line of centers between the two bodies, and τ is the constant of propor-

tionality relating ϵ_l and the relevant tidal forcing frequency. [Hut \(1981\)](#) provided a novel re-derivation by approximating the tidal bulge as two point masses on the surface of the body, and through energy & angular momentum conservation arguments present orbit-averaged expressions for the evolution of the orbital elements and spin rate. [Eggleton et al. \(1998\)](#), hereafter EKH) expands upon the [Hut \(1981\)](#) framework by considering the distortion of the shape of a fluid planet to quadrupole order, in the presence of its own rotation Ω and a tidal perturber. They then assumed that the rate of loss of tidal energy is directly proportional to the square of the rate of change of the shape (in the rotating frame), with the constant of proportionality being a dissipation constant σ intrinsic to the interior structure of each body. This dissipation constant is related to the time lag τ (also intrinsic to each body) via

$$\tau = \frac{3\sigma r^5}{4G} k_L, \quad (3.1)$$

where r is the body's radius and k_L its tidal Love number (parameterizing degree of central concentration - typically denoted k_2 , but k_L here to reduce confusion with other subscripts¹). Both the [Hut \(1981\)](#) and [EKH](#) prescriptions have the advantage of introducing no discontinuities for low tidal frequencies, and makes no assumptions regarding eccentricity. While the [Hut \(1981\)](#) framework assumes low obliquity, [EKH](#) is valid for any orientation of the spin axis. This is the approach we have implemented.

We briefly summarize the alternative school of thought, the CPL approach. The CPL approach parameterizes the tidal response via the specific dissipation function Q defined in [Goldreich \(1963\)](#). Today this quantity is commonly referred to as the tidal quality factor:

$$Q^{-1} \equiv \frac{1}{2\pi E_0} \oint \left(-\frac{dE}{dt} \right) dt, \quad (3.2)$$

where E_0 is the peak energy stored in the orbit during a tidal cycle, and $\oint \frac{dE}{dt} dt$ is the energy dissipated over a complete cycle. Via analogy to the simple harmonic oscillator ([MacDonald, 1964](#); [Greenberg, 2009](#)), Q may be related to a component of phase lag ϵ via

$$Q^{-1} = \tan 2\epsilon. \quad (3.3)$$

In principle, Q is a function of the frequency and amplitude of the tidal perturbation. However, laboratory and field experiments showed that for a variety of

¹Not to be confused with the *apsidal motion constant*, notably denoted k in many of the cited works and is equal to half the tidal Love number

solid materials Q varies weakly, if at all, with frequency (Knopoff & MacDonald, 1958; Knopoff, 1964). Therefore, in the CPL prescription introduced by Goldreich & Soter (1966), all tidal components are misaligned with the line of centers by the same angle ϵ . This approximation reproduces the behavior of Earth and solid planets well, and is the prescription that has been widely adopted by the exoplanet community. While appealing in its simplicity, the CPL model poorly represents fluid bodies (whose Q varies directly with frequency, see Knopoff 1964) and is only accurate to first order in eccentricity (Goldreich, 1963). In addition, this model results in discontinuities when the tidal forcing frequency is close to zero (Heller et al., 2011).

Other excellent reviews contrasting the CTL and CPL approaches and the merits/drawbacks of either are Greenberg (2009), Leconte et al. (2010), Mardling (2010) and Heller et al. (2011). Given the previously listed disadvantages of the CPL model, we implement the CTL prescription of EKH in this work. As the CPL prescription and parameterization of a Q intrinsic to each planet has been adopted by the exoplanet community at large, for ease of use and intuition it is tempting to utilize some sort of hybrid approach. For instance, Mardling & Lin (2002) present a fully self-consistent framework in the CTL regime, but implement Q with the assumption that Q can be expressed as some function of τ . Such formulations are powerful in their accessibility. However, it is very important to note that these approaches are only valid in certain limiting cases - in general, there is no simple relation between Q and τ . In some cases of interest such a relation is possible (Leconte et al., 2010): for $Q \gg 1$ and a synchronized circular orbit, the eccentric annual tide with frequency n (mean motion) dominates. In this case, we can write

$$Q^{-1} \sim 2\epsilon \sim 2n\tau. \quad (3.4)$$

This is the assumption made in works including Mardling & Lin (2002), Wu & Murray (2003) and Millholland & Laughlin (2019) to reconcile the tidal quality factor Q with the CTL model. We emphasize again that use of the EKH prescription is advantageous in that it makes no assumptions about the orbit of a tidal perturber (and hence is valid not just for satellite-primary tides, but for satellite-satellite tides as well). The user may appeal to this relation to set τ from a known value of Q , with the understanding that it is strictly valid only in the case of a synchronized circular orbit.

We recognize the contributions over the past decade by many authors (Ogilvie & Lin, 2004; Efroimsky & Williams, 2009; Ferraz-Mello, 2013; Correia et al., 2014; Storch & Lai, 2014; Boué et al., 2019; Teyssandier et al., 2019; Vick et al., 2019, among others) in the development of more complex tidal formalisms. These tidal models more extensively account for the rheologies of the body, and may

indeed yield more accurate and nuanced results than the equilibrium tide model. Implementing such models consistently into an N -body integrator is certainly an avenue worth pursuing in the future. Given the present-day uncertainty around the precise interior compositions of exoplanets, the equilibrium tide model is elegant and powerful in its simplicity, and while exact quantitative details may differ it is more than sufficient to draw powerful qualitative insights.

3.3 Equations of Motion

In this section, we explicitly describe the self-consistent spin, tidal and dynamical equations of motion of the EKH we implement into REBOUNDx. These equations of motion represent an extension of the equilibrium tide theory already implemented in REBOUNDx by Baronett et al. (2022), which assumed the framework of Hut (1981) but assumed no evolution of the spin axes.

First, we list the parameters (set and fixed at the beginning of a simulation) and dynamical variables (set and evolved over time) associated with each body. For point particle dynamics, the only parameter that is required is the mass m , while the necessary dynamical variable is the vector distance \mathbf{d} between each pair of bodies. Additional parameters and dynamical variables are required to describe dynamics beyond point particles. The parameters are, for each body: a radius r , the fully dimensional moment of inertia² I , the Love number k_L , and the dissipation constant σ . The additional dynamical variables are, for each body, the three components of the spin vector $\Omega_x, \Omega_y, \Omega_z$ (parameterizing both the magnitude and direction of rotation). The equation of motion describing the relative vector separation $\dot{\mathbf{d}} \equiv \mathbf{d}_1 - \mathbf{d}_2$ between two bodies (denoted 1 and 2) is given

$$\ddot{\mathbf{d}} = \mathbf{f}_g + \mathbf{f}_{\text{QD}}^{(1,2)} + \mathbf{f}_{\text{QD}}^{(2,1)} + \mathbf{f}_{\text{TF}}^{(1,2)} + \mathbf{f}_{\text{TF}}^{(2,1)}. \quad (3.5)$$

Explicitly, these forces are the familiar point particle gravitational acceleration:

$$\mathbf{f}_g = -\frac{G(m_1 + m_2)}{d^3} \mathbf{d}. \quad (3.6)$$

The acceleration due to the quadrupole moment of body 1, accounting for both its

²While not directly used in the code, the dimensionless moment of inertia $C \equiv I/mr^2$ is a useful quantity that will be referenced later in the paper.

spin distortion and tidal distortion produced by body 2:

$$\mathbf{f}_{\text{QD}}^{(1,2)} = r_1^5 k_{L,1} \left(1 + \frac{m_2}{m_1} \right) \cdot \left[\frac{5(\Omega_1 \cdot \mathbf{d})^2 \mathbf{d}}{2d^7} - \frac{\Omega_1^2 \mathbf{d}}{2d^5} - \frac{(\Omega_1 \cdot \mathbf{d}) \Omega_1}{d^5} - \frac{6Gm_2 \mathbf{d}}{d^8} \right], \quad (3.7)$$

with an equivalent expression for the acceleration due to the quadrupole moment of body 2, $\mathbf{f}_{\text{QD}}^{(2,1)}$. Furthermore, the acceleration due to the tidal damping of body 1 is:

$$\mathbf{f}_{\text{TF}}^{(1,2)} = - \frac{9\sigma_1 k_{L,1}^2 r_1^{10}}{2d^{10}} \left(m_2 + \frac{m_2^2}{m_1} \right) \cdot [3\mathbf{d}(\mathbf{d} \cdot \dot{\mathbf{d}}) + (\mathbf{d} \times \dot{\mathbf{d}} - \Omega_1 d^2) \times \mathbf{d}], \quad (3.8)$$

and again an equivalent expression for the tidal damping of body 2. The addition of dissipative tidal forces into a symplectic scheme is not a concern with the operator-splitting methods applied by REBOUND - for an in-depth analysis see Tamayo et al. (2020a). For a schematic representation of the relevant forces, see Figure 3.1.

The evolution of the spin vector of body 1 can be derived via matching torques on the orbit and the extended body in concordance with conservation of angular momentum, and is described by the differential equation

$$I_1 \dot{\Omega}_1 = - \left(\frac{m_1 m_2}{m_1 + m_2} \right) \mathbf{d} \times (\mathbf{f}_{\text{QD}}^{(1,2)} + \mathbf{f}_{\text{TF}}^{(1,2)}), \quad (3.9)$$

with an equivalent expression for the evolution of body 2's spin vector. This framework may be extended to any number of bodies. We note here one subtlety that is not considered - each body reacts only in response to the tides it itself raises. For example, in a three-body system in which all three bodies are endowed with structure, body 2 reacts not only to the tides it raises on body 1 (which our code does consider), but also to the tides raised on body 1 by body 3. While these effects are expected to be minor for most systems, further work must certainly be done for a more complete picture that includes these non-pairwise accelerations.

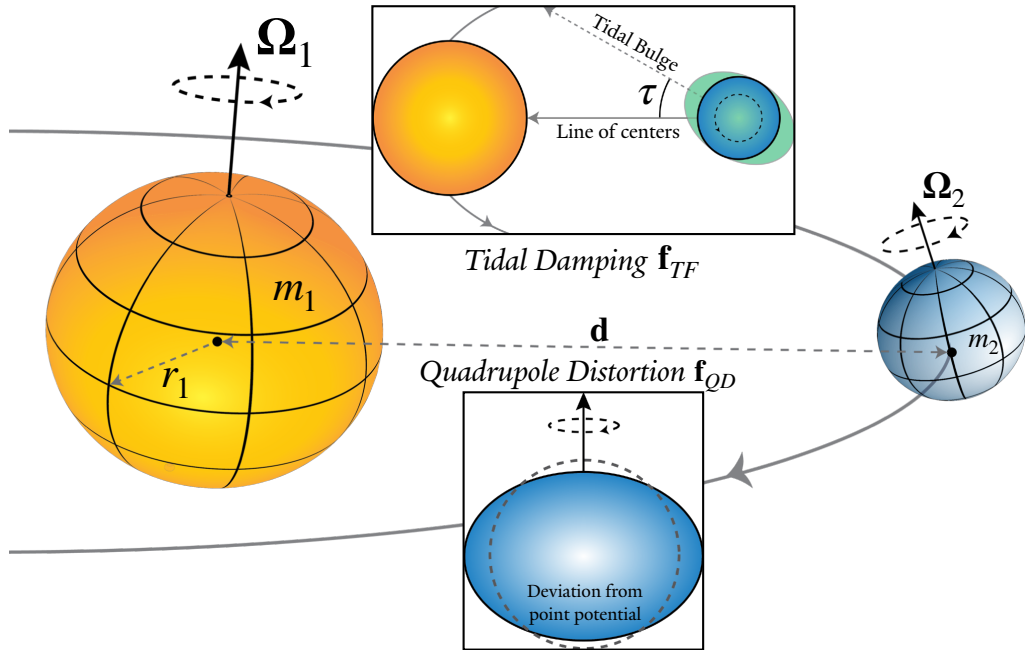


Figure 3.1. Schematic representation of the additional parameters, dynamical variables and forces needed to shift from a point particle framework to one in which the bodies are endowed with structure. Each body is parameterized by a mass m , a radius r , a spin vector Ω , a Love number k_L , and a dissipation constant σ (directly related to the time lag τ via Equation 3.1), with the bodies separated by a separation vector \mathbf{d} . The additional forces to be considered are the quadrupole distortion force \mathbf{f}_{QD} due to each body shape's deviation from a perfect sphere, and the tidal damping force \mathbf{f}_{TF} arising from the dissipation of energy via tidal friction. Not pictured is the planet's obliquity θ , defined as the angle between the spin axis and its orbit normal.

3.4 Implementation

In this section we describe the implementation of the previously described self-consistent spin, tidal and dynamical equations of motion in REBOUNDx³.

3.4.1 Spin, Structure and Tidal Parameters

To turn on the additional forces for a given body, the following parameters & dynamical variables must be set to finite values: the radius r , the Love Number k_L , the dissipation constant τ , the moment of inertia I , and the spin vector components $\Omega_x, \Omega_y, \Omega_z$.

- If k_L and all of $\Omega_x, \Omega_y, \Omega_z$ are set, the body will generate quadrupole distortion forces. If τ is also set, the body will generate tidal damping forces as well.
- If I and all of $\Omega_x, \Omega_y, \Omega_z$ are set, the evolution of the body's spin axis will be tracked. Note that the evolution of the spin axis depends solely on $\mathbf{f}_{\text{QD}} + \mathbf{f}_{\text{TF}}$ - in other words, both k_L and σ should be set as well to observe any interesting dynamics of the spin vector; otherwise, the spin axis will remain stationary.

If none of these are set, the body will be treated as a point particle. Explicitly, it will raise tides on other bodies endowed with structure, and its own motion will be affected both by the associated quadrupole and tidal forces. However, it itself will generate neither.

The framework of EKH we have adopted parameterizes the magnitude of the tidal force via the dissipation constant σ with units of mass⁻¹length⁻²time⁻¹. σ has a complex dependence on internal structure and we recognize that heuristic estimates of such a parameter will be unreliable and that few, if any, will have good intuition for reasonable values of σ . For this reason, leveraging that Equation 3.1 relating τ and σ is always valid, the user-facing tidal parameter is chosen to be τ . The selected value of τ is converted "under the hood" to the corresponding value of σ for use in the equations of motion. It is worth noting that while direct measurements of Q and k_L exist for planets and satellites in the solar system (Lainey et al., 2009; Lainey, 2016; Lainey et al., 2017), no such measurements exist for τ . Hence, for many practical uses of the code the relation of Equation 3.4 must be invoked to set τ from measured values. There are no built-in warnings for when this approximation is valid - it is left to the user's judgement to use this conversion as seen fit.

³Detailed documentation is available at reboundx.readthedocs.io.

3.4.2 Dynamics

The forces applied to each body are calculated in a pairwise manner. For a given pair of bodies, at each timestep the REBOUNDx parameters of each are checked to assess which forces it will generate. The relevant accelerations are then applied to each body, scaled to their relative masses. For example, in a system of two bodies 1 and 2, for the quadrupole distortion force generated by body 1 $\mathbf{f}_{\text{QD}}^{(1,2)}$: body 1 will experience the acceleration $m_2/(m_1 + m_2) \cdot \mathbf{f}_{\text{QD}}^{(1,2)}$, while body 2 will experience the acceleration $m_1/(m_1 + m_2) \cdot (-\mathbf{f}_{\text{QD}}^{(1,2)})$.

The additional forces implemented are compatible with different integrators, and may also be used in conjunction with any of the other implemented effects in the REBOUNDx library. The package supports a mix of point particles and bodies with internal structure in one simulation.

3.4.3 Spin Axis Evolution

The spin vectors of each body are tracked using REBOUND's built-in coupled ODE structure. This is a new feature that was added in REBOUND version 3.19. It allows the user to integrate any arbitrary set of ordinary differential equation structure in parallel with the main N-body integration⁴.

Each set of ODEs can use the current dynamical state of the N-body simulation in their right-hand side equation. Similarly, the current state of a user provided ODE can be used in calculating additional forces for the N-body particles.

The user provided ODEs are integrated with an adaptive Gragg-Bulirsch-Stoer (BS) integrator and a default tolerance parameters of 10^{-5} . If BS is also used for the integration of the N-body equations of motion, then everything is simply treated as one big coupled set of ordinary differential equations with one adaptive timestep.

It is also possible to integrate arbitrary ODEs in conjunction with other REBOUND integrators such as IAS15 and WHFast. These integrators are typically more accurate and faster for integrations of planetary systems. In that case, only the user-defined ODEs are integrated with BS after a successful N-body integration step. BS still uses an adaptive timestep, but it also makes sure to synchronize its timesteps to that of the N-body integration. This type of switching back and forth between N-body and user-provided ODEs will lead to an error. However, if the timescales involved in the user-defined ODEs are much longer than the timestep of the N-body integration then this will be a small error (Tamayo et al., 2020a). This is typically the case for evolution of spin vectors.

⁴More information on this API can be found at https://rebound.readthedocs.io/en/latest/ipython_examples/IntegratingArbitraryODEs/.

To initialize the ODE structure associated with tracking the spin vectors, the user needs to call the `rebx_spin_initialize_ode` function after all relevant REBOUNDx parameters have been set. This function sets up the ODE which tracks the spin vector evolution of every body with a valid moment of inertia I and spin vector $[\Omega_x, \Omega_y, \Omega_z]$. The spin vector REBOUNDx parameters $\Omega_x, \Omega_y, \Omega_z$ are updated before and after each ODE timestep - this means the user can pull the relevant real-time values of the spin axis by looking up the REBOUNDx parameters, without accessing the ODE framework itself.

At the moment, our implementation assumes there is a constant number of particles, and a constant number of particles for which we have to track the spin evolution.

3.5 Test Cases

3.5.1 Pseudo-Synchronization of Hot Jupiters

A simple test of the code is a comparison with secular orbit-averaged analytic predictions. We use the analytic orbital evolution equations of [Leconte et al. \(2010\)](#), which are the orbital evolution equations derived by [Hut \(1981\)](#) extended to arbitrary obliquity and is equivalent to the [EKH](#) framework. These equations describe a system of two mutually orbiting extended bodies, and describe the evolution of the semimajor axis, eccentricity, spin rate and obliquity of each body. The explicit expressions are given in Appendix 3.8.

We perform a basic test integration illustrating the spin-down and circularization of a generic hot Jupiter orbiting a Sun-like star with both the REBOUNDx numerical simulations and a numerical integration of the analytic equations of [Leconte et al. \(2010\)](#), shown in the left subplot of Figure 3.2. The initial conditions of the simulation are: $m_* = 1M_\odot, r_* = 1R_\odot, m_p = 1M_J, r_p = 1R_J, a = 4.072 \times 10^{-2}$ AU, $e = 0.01, k_{L,*} = 0.07, \tau_* = 4.12 \times 10^{-4}$ s, $C_* = 0.07, \Omega_* = 27$ days, $\theta_* = 0, k_{L,p} = 0.3, \tau_p = 4.12$ s, $C_p = 0.3, \Omega_p = 0.5$ days, $\theta_p = 30^\circ$. We used the symplectic WHFast integrator ([Rein & Tamayo, 2015](#)) with a timestep of one tenth the initial orbital period. This is the same test case used by [Millholland & Laughlin \(2019\)](#) to test the accuracy of their numeric code, and we see very close agreement between numeric and analytic results as they do.

One of the most notable predictions of the constant time lag model (noted upon both by [Hut 1981](#) and [Leconte et al. 2010](#)) is rapid evolution towards a pseudo-synchronous state. More specifically, for typical hot Jupiter-like parameters, the planetary obliquity is quickly damped to zero while the spin rate evolves toward

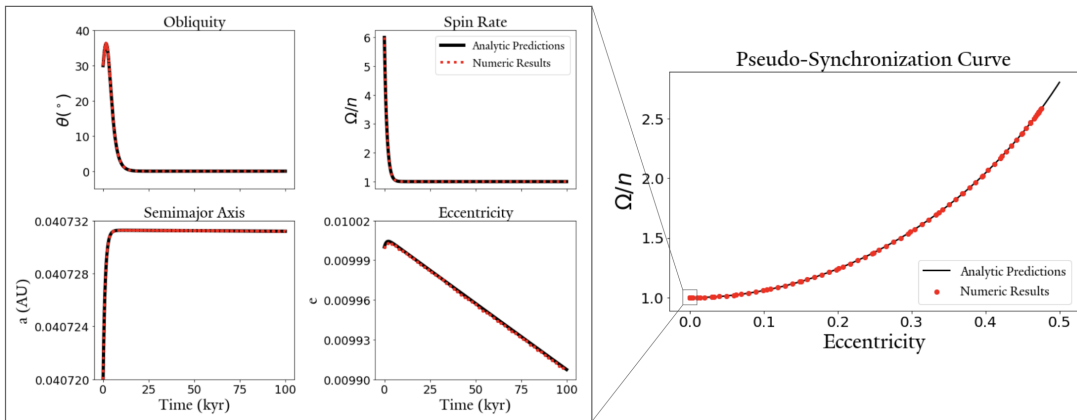


Figure 3.2. A comparison between the numerical results of our REBOUNDx simulations and analytic predictions using the framework of Leconte et al. (2010). The right subplot shows the end state of 80 numerical simulations of hot Jupiters initialized at varying eccentricities settling to their equilibrium pseudo-synchronous spin values, as well as the analytic prediction of these values given by Equation 3.10. Each simulation lands on the pseudo-synchronization curve and there is excellent agreement. The left subplot shows the evolution of the obliquity, spin rate, semimajor axis, and eccentricity of a specific hot Jupiter (corresponding to the lowest eccentricity case in the right subplot), where the black line represents the analytic predictions and the red dots represent our numeric results. The spin rate rapidly synchronizes and the obliquity is driven to zero. Again, there is excellent agreement between the analytic and numeric results.

an equilibrium value given by

$$\frac{\Omega_{eq}}{n} = \frac{1 + \frac{15}{2}e^2 + \frac{45}{8}e^4 + \frac{5}{16}e^6}{\left(1 + 3e^2 + \frac{3}{8}e^4\right)\left(1 - e^2\right)^{3/2}}. \quad (3.10)$$

To verify this prediction with our numeric code, we have run 80 additional simulations. The initial eccentricity of each of these additional simulations varied from 0.01 to 0.8, with all other parameters kept identical. Each simulation is advanced for 1 Myr and their final spin rates are reported on the right subplot of Figure 3.2, as well as the analytically predicted equilibrium rotation values given by Equation 3.10. We see excellent agreement and the "pseudo-synchronization" curve described in both [Hut \(1981\)](#) and [Leconte et al. \(2010\)](#) is well reproduced. The earlier simple test integration corresponds to the lowest-eccentricity example.

3.5.2 Obliquity-Driven Sculpting of Exoplanetary Systems

An interesting result from the Kepler Mission ([Borucki et al., 2010](#)) is the statistical excess of planet pairs just wide of first-order mean-motion resonances ([Lissauer et al., 2011](#); [Petrovich et al., 2013](#); [Fabrycky et al., 2014](#)). [Millholland & Laughlin \(2019\)](#), hereafter ML19 postulate that obliquity tides could be a viable explanation; large axial tilts created by secular spin-orbit resonance spin-orbit coupling drain orbital energy to heat. Specifically, ML19 used an independent N -body code to demonstrate that convergent migration and resonant interaction precipitated by capture into a mean-motion resonance is capable of generating and maintaining large obliquities over long periods, and argue that this mechanism is common in the compact, near-coplanar system typical of the *Kepler* multis. In the test case used by ML19, two planets are initialized around a star just wide of the 3:2 MMR. Both planets initially experience inward, convergent orbital migration, which is switched off after 2 Myr. See Figure 3.3 for the dynamical evolution of the system: as the planets are captured into the 3:2 MMR, the inner planet is kicked to $> 50^\circ$ obliquity, which is maintained indefinitely. While this particular simulation is associated with a specific set of parameters (see ML19 for details), no fine-tuning is done and the qualitative behavior of the system is independent of slight changes in initial parameters.

We reproduce the results of the ML19 simulation - Figure 3.3 compares our two results. Our simulation is initialized in the same initial state as the ML19 simulation. The dynamics of the system use the WHFast integrator with a timestep of 0.159×10^{-4} yrs - this is roughly 0.1 times the inner planet's initial orbital period. The inward migration is modelled with the `modify_orbits_forces` implementation ([Kostov et al., 2016a](#); [Tamayo et al., 2020a](#)) in REBOUNDx: the τ_a parameter

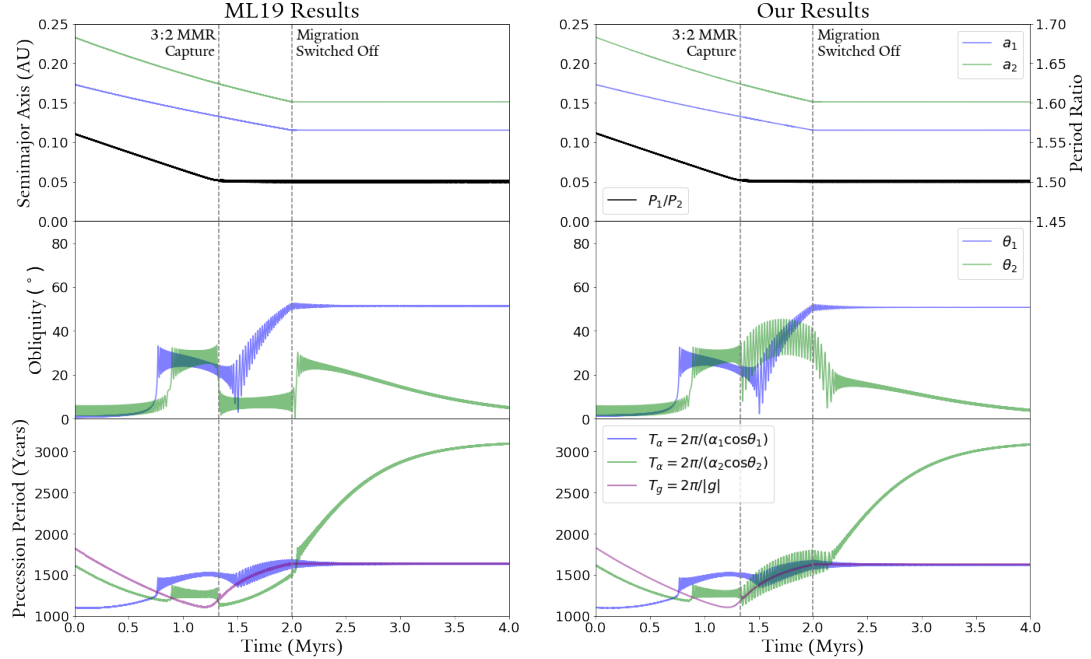


Figure 3.3. A comparison between [ML19](#) (left) and our results (right). The top subplot shows the semimajor axis evolution of both planets as they migrate inward and are caught into the 3:2 MMR. The blue points correspond to the inner planet, the green points to the outer planet, and the black line to their period ratios. The middle subplot shows the resulting obliquity evolution of the system. The dynamics of the system are identical - while the spin evolution differs the final state of the system is very similar. The bottom subplot shows the evolution of the relevant precessional frequencies of the system: the axial precession and nodal recession periods (see Appendix 3.9 for details).

(describing the rate of migration) is set to -5×10^6 years and -4.54×10^6 years for the inner and outer planet, respectively (as in [ML19](#)).

The qualitative end state behavior of the system - namely, the generation and maintenance of a high-obliquity state for the inner planet - is well reproduced. The quantitative differences in the evolution of the system are expected outcomes of the different implementations of the spin-orbit coupling framework used. While our framework is that of [EKH](#), [ML19](#) uses that of [Mardling & Lin \(2002\)](#) - these frameworks are equivalent with the assumption $Q^{-1} = 2\epsilon = 2n\tau$. [ML19](#) uses an initial $Q = 10^4$ for both planets - this is equivalent to $\sigma_1 \sim 8.76 \times 10^{14}$ and $\sigma_2 \sim 1.36 \times 10^{15}$. In addition, $Q = 10^6$ is used for the central star - we assume this is the tidal quality factor associated with the forcing frequency of the inner planet (though qualitatively there is no difference for the particular problem), so $\sigma_* \sim 3.15 \times 10^3$ - all σ values are given in the default REBOUND units⁵. Otherwise,

⁵The default REBOUND units are M_\odot , AU, yr/ 2π as measures of mass, distance, and time, respectively - this selection yields $G = 1$.

the physical parameters and initial conditions were identical to [ML19](#). In terms of system evolution, there are three differences between our framework and [ML19](#): **i)** [ML19](#) assumes the planets do not raise tides on the star, or one another - the only tidal effects considered are the star raising tides on the planets. Our framework assumes each interacting pair raises tides upon one another. **ii)** [ML19](#) does not employ the force splitting we have used (described in Section 3.4.2). **iii)** [ML19](#) use a Bulirsch-Stoer integrator with a similar timestep to ours and an accuracy parameter of 10^{-13} . These differences are expected to be minor and indeed do not affect the qualitative final state of the system significantly. A more in-depth dicussion regarding the evolutionary differences in the two codes may be found in Appendix 3.9.

3.5.3 Exploring the ZLK effect

It was shown by [Lidov \(1962\)](#) and [Kozai \(1962\)](#) that in a hierarchical three-body system characterized by a significant misalignment between the relative inclinations of the inner and outer orbits, there may be high-amplitude coupled oscillations in the eccentricity and inclination of the inner orbit. Commonly known as the Kozai-Lidov effect, the initial discovery of this mechanism by [von Zeipel \(1910\)](#) has been pointed out by [Ito & Ohtsuka \(2019\)](#) who hence advocate referring to this effect as the von Zeipel-Lidov-Kozai (ZLK) effect, which we adopt here. This mechanism has since been greatly expanded upon and is well studied - for an in-depth review, see [Naoz \(2016\)](#) and references within. Of particular relevance to this work is the effect of tidal friction when considered in conjunction with ZLK cycles. This was notably explored by [Wu & Murray \(2003\)](#) regarding the orbit of HD 80606b and [Fabrycky & Tremaine \(2007\)](#) to explain the overabundance of short-period binary stars.

The ZLK mechanism, coupled with tidal friction, has often been invoked to explain the unusual orbits of hot Jupiters and other close-in exoplanets. As the planet approaches periastron during the high-eccentricity epoch of a ZLK cycle, tidal dissipation becomes very significant and the planet's semi-major axis shrinks. Eventually, the ZLK cycles are damped out by tidal or general relativistic precessions ([Einstein, 1916](#)). The characteristic period of a ZLK cycle is given ([Fabrycky & Tremaine, 2007](#)):

$$\tau_{ZLK} = \frac{2P_c^2}{3\pi P_p} \frac{m_* + m_p + m_c}{m_c} (1 - e_c^2)^{3/2}, \quad (3.11)$$

where quantities subscripted with $*$, c , p correspond to the central body, an outer perturber, and the planet respectively. Recall that the axial precession rate, α , scales as a_p^{-3} . We define the ZKL frequency $g_{ZLK} \equiv 2\pi/\tau_{ZKL}$ (in this section the traditional

g will be denoted g_{orbit} for clarity). As the orbit of the planet shrinks g_{ZLK}/α will pass through unity, the criterion for resonance capture/kick. The effects of such a resonant crossing on the planet's obliquity⁶ have yet to be explored.

We explore the obliquity evolution of a generic Neptune-like planet in a binary star system experiencing ZKL oscillations. For concreteness, we initialize the initial conditions of the simulation to fiducial values. These are $m_* = m_c = 1.0 \text{ M}_\odot$, $r_* = R_\odot$, $k_{L,*} = 0.01$, $C_* = 0.07$, $m_p = 1 \text{ M}_N$, $r_p = R_N$, $a_p = 2 \text{ AU}$, $e_p = 0.01$, $k_{L,p} = 0.4$, $C_p = 0.25$, $a_c = 50 \text{ AU}$, $e_c = 0.7$, $i_c - i_p = 80^\circ$. In terms of the dissipation parameter, we adopt the approximation $Q = (2\epsilon)^{-1} = (2n\tau)^{-1}$ with initial fiducial values $Q_* = 10^6$ and $Q_p = 3 \times 10^5$. The spins of central star and planet are initialized with spin periods of $\Omega_* = 4.6$ days and $\Omega_p = 1$ day, both with 0 obliquity. The outer perturber is considered a point particle. We incorporate general relativistic precession via the "gr_full" implementation in REBOUNDx (Newhall et al., 1983; Tamayo et al., 2020a). While the WHFast integrator was used for the two previous examples and in general has the fastest performance, in this case the high-eccentricity pericenter approaches inherent to a ZLK cycle would force WHFast to apply the worst-case timestep over the entire integration at great cost to performance. For this reason, here we use the IAS15 adaptive-timestep high-order integrator (Rein & Spiegel, 2015). We use an initial timestep of $dt = 5 \times 10^{-2}$ years.

The results of this simulation are shown in Figure 3.4, where we plot various quantities associated with the system's planet. Before 6 Myr, we see the standard ZLK oscillations. During the high-eccentricity epochs of each ZLK cycle, the planet experiences very quick nodal recession and the resulting crossings between $\alpha \cos \theta$ and g_{orbit} results in several obliquity kicks in both directions. At 6.2 Myr, the semimajor axis rapidly shrinks, which motivates a rapid decrease in g_{kozai} and increase in $\alpha \cos \theta$. When the two frequencies cross, the obliquity experiences a large kick downward as is damped to near zero, where it remains indefinitely. While the specific parameters of this simulation are given and changing these parameters does significantly alter the evolution of the system, this damping of obliquity at the crossing of g_{kozai} and $\alpha \cos \theta$ is robust regardless of the specific parameters selected. We therefore conclude that planets which invoke ZLK cycles to explain their present orbits are expected to have negligible obliquity. This conclusion is particularly relevant given JWST observations of planets such as HD80606b expected in the near-future (Kataria et al., 2021), which may be able to constrain the obliquity of the planet.

⁶Obliquity here refers to the angle between the planet's orbit normal and its spin axis. This is not to be confused with the angle between the star's spin axis and the planet's orbit normal, another common designation known as *stellar* obliquity.

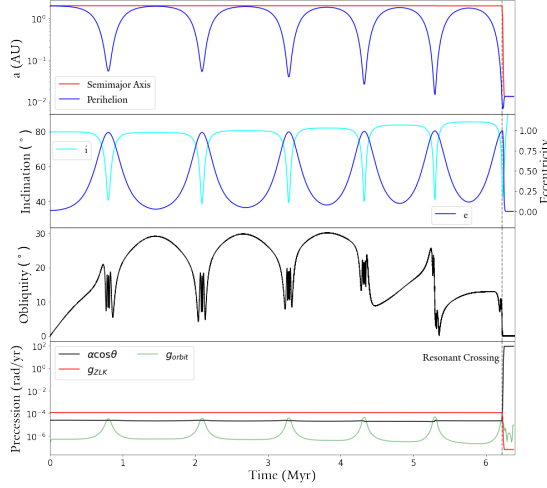


Figure 3.4. Results of the simulation demonstrating the ZLK mechanism with a fiducial Neptune-like planet. The top subplot shows the evolution of the planet’s semimajor axis (red) and perihelion (blue). The second subplot shows the planet’s eccentricity (blue) and mutual inclination between planet and perturber (aqua). The third subplot shows the obliquity of the planet, again defined as the angle between its orbit normal and spin axis. The bottom subplot shows the evolution of the three relevant precessional frequencies: $\alpha \cos \theta$, g_{ZLK} , and g_{orbit} . The gray dotted line spanning all four subplots denotes the point at which g_{ZLK} crosses $\alpha \cos \theta$.

3.6 Summary

In this work, we presented self-consistent spin, tidal and dynamical equations of motion integrated into the REBOUNDx framework (Tamayo et al., 2020a), as an improvement over the point-particle dynamics that REBOUND (Rein & Liu, 2012) was previously restricted to. The equations of motion used are those derived in the constant time lag approximation of the equilibrium tide model by Eggleton et al. (1998). The framework is set up such that these additional forces may be easily turned on or off, and such that a mix of bodies with structure and point particles may coexist in a REBOUND simulation. Extensive documentation and example Jupyter notebooks are available reboundx.readthedocs.io.

We provide several interesting test cases and verify the results of the code against both analytic predictions (Leconte et al., 2010) and previous work (Mill-holland & Laughlin, 2019). We also apply the code to a fiducial system undergoing von Zeipel-Lidov-Kozai oscillations and show that these systems are expected to damp down to near zero obliquity at the conclusion of the oscillation period. These are just a few examples of the myriad applications of this framework. We anticipate our code to have wide-reaching applications to systems in resonant chains such as Trappist-1 (Gillon et al., 2017; Luger et al., 2017; Tamayo et al., 2017; Agol

et al., 2021) and TOI-1136 (Dai et al., 2021), mis/aligned systems (Rice et al., 2021; Rice et al., 2023), ultra-short period planets (Millholland & Spalding, 2020; Dai et al., 2021), and the general phase-space evolution of exoplanet obliquities (Su & Lai, 2022) to name a few. We hope this extension to REBOUNDx will provide a useful avenue in the study of exoplanet dynamics as a whole.

3.7 Acknowledgements

We thank Malena Rice, Alexander Heger, David Hernandez, Konstantin Batygin, Konstantin Gerbig and Tanvi Gupta for invaluable insight, discussion, and feedback. We also thank the anonymous reviewer for helpful comments that greatly improved the manuscript.

3.8 Appendix: Secular Orbit Evolution Equations

The secular, orbit-averaged equations governing the evolution of the semimajor axis, eccentricity, spin rate and obliquity of each body for a system of two mutually orbiting extended bodies are (Leconte et al., 2010):

$$\frac{da}{dt} = \frac{4a^2}{Gm_1m_2} \sum_{i=1}^2 K_i \left[N(e)x_i \frac{\Omega_i}{n} - N_a(e) \right], \quad (3.12)$$

$$\frac{de}{dt} = \frac{11ae}{Gm_1m_2} \sum_{i=1}^2 K_i \left[\omega_e(e)x_i \frac{\Omega_i}{n} - \frac{18}{11}N_e(e) \right], \quad (3.13)$$

$$\frac{d\Omega_i}{dt} = -\frac{K_i}{I_i n} \left[(1 + x_i^2)\omega(e) \frac{\Omega_i}{n} - 2x_i N(e) \right], \quad (3.14)$$

$$\frac{d\theta_i}{dt} = \frac{K_i \sin \theta_i}{I_i \Omega_i n} \left[(x_i - \eta_i) \omega(e) \frac{\Omega_i}{n} - 2N(e) \right], \quad (3.15)$$

where $x_i = \cos \theta_i$, $N(e)$, $N_a(e)$, $N_e(e)$, $\omega(e)$, $\omega_e(e)$ are the functions of eccentricity:

$$N(e) = \frac{1 + \frac{15}{2}e^2 + \frac{45}{8}e^4 + \frac{5}{16}e^6}{(1 - e^2)^6}, \quad (3.16)$$

$$N_a(e) = \frac{1 + \frac{31}{2}e^2 + \frac{255}{8}e^4 + \frac{185}{16}e^6 + \frac{25}{64}e^8}{(1 - e^2)^{15/2}}, \quad (3.17)$$

$$N_e(e) = \frac{1 + \frac{15}{4}e^2 + \frac{15}{8}e^4 + \frac{5}{64}e^6}{(1 - e^2)^{13/2}}, \quad (3.18)$$

$$\omega(e) = \frac{1 + 3e^2 + \frac{3}{8}e^4}{(1 - e^2)^{9/2}}, \quad (3.19)$$

$$\omega_e(e) = \frac{1 + \frac{3}{2}e^2 + \frac{1}{8}e^4}{(1 - e^2)^5}, \quad (3.20)$$

K_i is defined as⁷

$$K_i = 3k_{L,i}\tau_i \left(\frac{Gm_i^2}{r_i}\right) \left(\frac{m_j}{m_i}\right)^2 \left(\frac{r_i}{a}\right)^6 n^2, \quad (3.21)$$

and η is the ratio of rotational to orbital angular momentum

$$\eta_i = \frac{m_i + m_j}{m_i m_j} \frac{I_i \Omega_i}{a^2 n \sqrt{1 - e^2}}. \quad (3.22)$$

3.9 Appendix: Exploration of Numerical Differences

In Section 3.5.2, we benchmarked our results against the independent N -body code of ML19. We performed an integration on the same fiducial system they do, and while the outputs qualitatively match, the quantitative evolution significantly differs and merits exploration. Ultimately, these difference arise from sensitive dependence on the precise location of the spin axis. In this appendix we examine these differences in greater detail.

To understand these results it will be necessary to first provide a brief review of the process of secular spin-orbit resonance and the dynamics of the spin axis (for more in-depth reviews, see Ward & Hamilton 2004, Millholland & Batygin 2019, Su & Lai 2020, Lu & Laughlin 2022, as well as ML19 itself). We must first define two relevant dynamical quantities. The first is the *axial precession* period T_α , defined as the period at which the planet's spin axis precesses about its orbit normal due to torques from the host star and the planet's own rotation:

$$T_\alpha \equiv \frac{2\pi}{\alpha \cos \theta}, \quad (3.23)$$

where α is the precessional constant, which is given (in the absence of satellites)

⁷The k used in Leconte et al. (2010) is the tidal Love number rather than the apsidal motion constant described by Hut (1981).

by (Ward & Hamilton, 2004; Millholland & Laughlin, 2019):

$$\alpha = \frac{1}{2} \frac{M_*}{m} \left(\frac{r}{a} \right)^3 \frac{k_L}{C} \Omega. \quad (3.24)$$

Where M_* is the mass of the host star, m is the planet mass, r is the planet radius, and a is the semimajor axis. The second relevant period is the *nodal recession* period, the period at which the planet's orbit regresses about the invariant plane of the system. This period is given by $T_g = 2\pi/|g|$, where the nodal recession rate g is the rate of change of the longitude of ascending node of the planet's orbit, Ω_{node} . The nodal recession rate arises from torques contributed by the other planets in the system. In a two-planet system, assuming negligible stellar oblateness the nodes of both planets regress at the same rate. For the comparison with ML19, these periods are plotted on the bottom subplots of Figure 3.3.

The behavior of the spin vector is best understood in a frame of reference rotating along with the planet's orbital recession g , with x -axis aligned with the ascending node and z -axis along the orbit normal. To interpret our results, we first rotate our simulations into the invariant frame, with z -axis aligned with the total angular momentum of the system and x -axis aligned with the line of nodes. We transform from the invariant frame of the system to this frame via the transformation

$$\hat{\Omega}^* = A \hat{\Omega}, \quad (3.25)$$

where $\hat{\Omega}^*$ is the unit spin axis in the frame that rotates with planet, $\hat{\Omega}$ is the unit spin axis in the invariant plane, and A is the time-dependent rotation matrix

$$A = \begin{bmatrix} \cos \Omega_{node} & \sin \Omega_{node} & 0 \\ -\cos i \sin \Omega_{node} & \cos i \cos \Omega_{node} & \sin i \\ \sin i \sin \Omega_{node} & -\sin i \cos \Omega_{node} & \cos i \end{bmatrix}, \quad (3.26)$$

In this frame, the trajectories of the unit spin vector trace out a family of parabolae - the exact landscape of spin-axis phase-space trajectories depends on the ratio $|g|/\alpha$. For the seminal work of Colombo (1966), this phase-space landscape of the spin axis is known as "Colombo's Top" (see also Peale 1969, Ward 1975, Henrard & Murigande 1987 and Su & Lai 2020). In this frame of reference, the equilibrium states of the spin axis appear stationary. These equilibrium positions are known as "Cassini States", and depending on the exact value of $|g|/\alpha$ there are either two or four Cassini States. If $|g|/\alpha$ is below a critical value $(|g|/\alpha)_{crit}$, all four Cassini states exist. At $(|g|/\alpha)_{crit}$, Cassini States 1 and 4 merge and disappear - above $(|g|/\alpha)_{crit}$

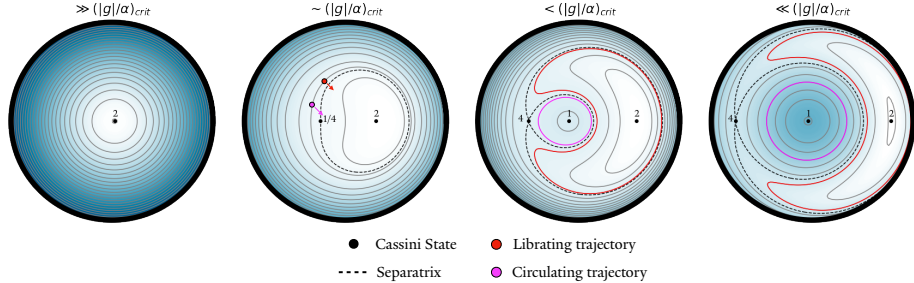


Figure 3.5. Schematic depiction of the topology of Colombo’s top for various values of $|g|/\alpha$, along with the locations of the Cassini States. The red and pink dots/lines represent two initially similar spin states that, through a process of resonant kick and capture, ultimately end up on significantly different trajectories. This illustrates the sensitivity of the spin-axis evolution on the instantaneous phase at the time of resonant capture/kick.

only Cassini States 2 and 3 exist. The critical value is a function of inclination i :

$$(|g|/\alpha)_{crit} = (\sin^{2/3} i + \cos^{2/3} i)^{-3/2} \sim 1 \text{ for small } i. \quad (3.27)$$

Figure 3.5 shows the topology of Colombo’s Top for various values of the ratio $|g|/\alpha$, as well as the location of the Cassini States (Cassini State 3 corresponds to a retrograde spin state and is not shown). Cassini States 1 and 2 are stable equilibria and adjacent trajectories will librate or circulate about them. Cassini State 4, on the other hand, lies on the separatrix and is unstable.

Typically, two resonant mechanisms are invoked to explain high-obliquity states. Both are relevant to our current study. The first of these is resonant capture, and is motivated by the evolution of the topology of Colombo’s Top as the ratio $|g|/\alpha$ decreases. If $|g|/\alpha$ approaches and crosses unity from above slowly enough to preserve the adiabatic criterion, a spin axis that begins on a low-obliquity state will follow Cassini State 2 as it evolves to high obliquity. The second of these mechanisms is a resonant kick. This may occur in a few ways, but for the case in interest this occurs upon rapid change of the ratio $|g|/\alpha$ such that the adiabatic criterion is not preserved. While resonant capture is characterized by movement of the trajectory itself, in a resonant kick the spin axis jumps from one trajectory to another.

Figure 3.5 also overplots a demonstration of the sensitive dependence on the precise instantaneous location of the spin axis, invoking both resonant mechanisms. On the second subplot, two spin axis instances on the same trajectory are shown - the two instances will have very similar obliquities but different phase angles. If at the time shown both are given a small resonant kick, given their proximity to the separatrix they will be kicked onto trajectories in two different regimes - the red point is kicked onto a trajectory librating about Cassini State 2,

while the pink point is kicked onto one circulating about Cassini State 1. As the system evolves as a consequence of the changing $|g|/\alpha$, the librating red trajectory is excited to higher and higher obliquity, while the pink trajectory does not change appreciably.

To more closely investigate the differences in our codes, Figure 3.6 zooms in on a time slice of the simulation shown in Figure 3.3 where the first significant deviation between the two results occurs (1.2 Myr to 1.7 Myr). The scatter plots show a polar view of the spin axis location, while the inset plots show the evolution of $|g|/\alpha$. Analysis of Figure 3.6 clearly shows the mechanism described earlier in Figure 3.5: at roughly 1.3 Myr a small kick is seen in the evolution of $|g|/\alpha$. This causes the spin axis to jump to a nearby trajectory - for planet 2, the slight difference in the spin axis position at the moment of the kick is enough to knock the spin axes onto what will become trajectories on diverging evolutions. The differences in evolution between our results and ML19 can be understood then as slight deviation in the physics from implementation differences resulting in significant differences due to the probabilistic nature of the resonant capture/kick process (for more review on the probabilistic nature of resonance, see Henrard (1982); Saillenfest et al. (2021a)).

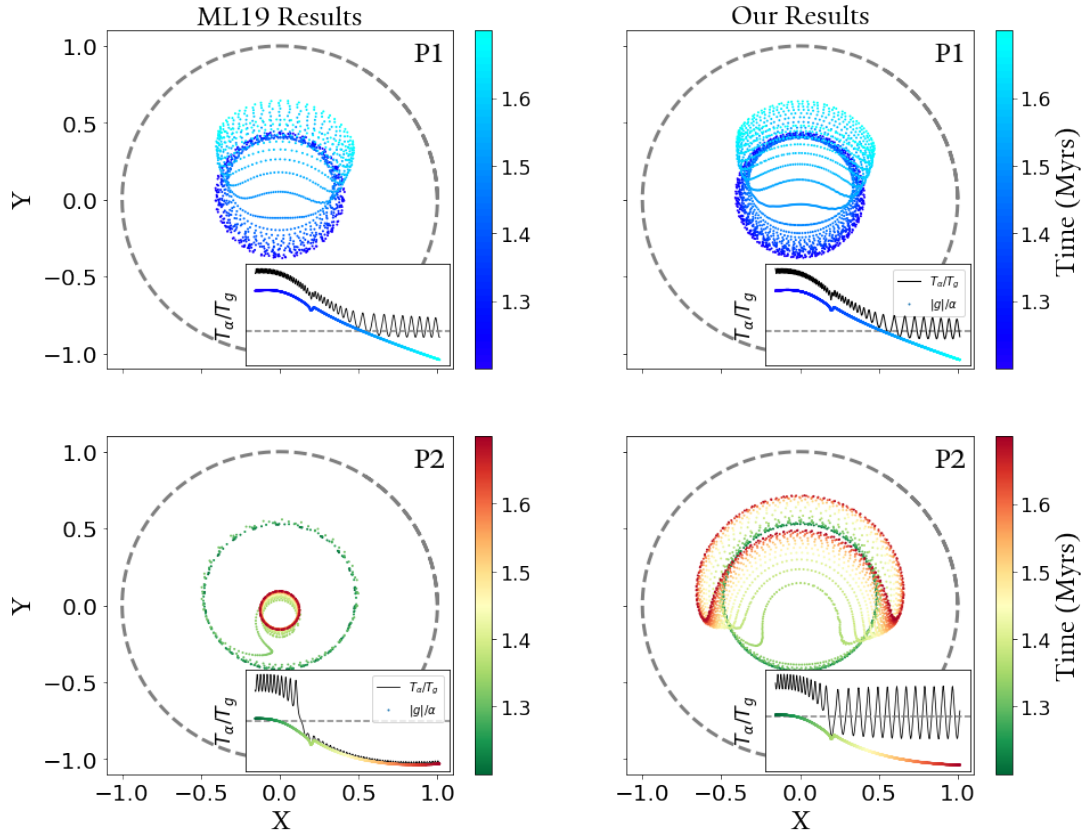


Figure 3.6. Scatterplots of the spin axis positions for the smaller time slice (from 1.2 to 1.7 Myr). The left column are results from [ML19](#), while the right column are our results. The plots with the blue colorbar (first row) correspond to planet 1, while the plots with a green-red colorbar (second row) correspond to planet 2. Each subplot shows the position of the unit spin vector in the XY plane (recall the z-axis is aligned with the planet's orbit normal) over time. Each subplot also shows an inset plot with three lines. The line with the same colorbar as the scatterplot represents the evolution of the ratio $|g|/\alpha$. The black line represents the ratio T_α/T_g , which is equivalent to $|g|/\alpha \cos \theta$. The dashed grey line marks unity for clarity.

Part II

Spin-Orbit Dynamics

Chapter 4

Tilting Uranus via Secular Spin-Orbit Resonance with Planet 9

"Be extremely subtle, even to the point of formlessness. Be extremely mysterious, even to the point of soundlessness. Thereby you can be the director of the opponent's fate."

– Sun Tzu

Adapted From:

Lu, T. & Laughlin, G. 2022, The Planetary Science Journal, Volume 3, Issue 9, pp.13

Abstract

Uranus' startlingly large obliquity of 98° has yet to admit a satisfactory explanation. The most widely accepted hypothesis involving a giant impactor that tipped Uranus onto its side encounters several difficulties with regards to the Uranus' spin rate and its prograde satellite system. An obliquity increase that was driven by capture of Uranus into a secular spin-orbit resonance remains a possible alternative hypothesis that avoids many of the issues associated with a giant impact. We propose that secular spin-orbit resonance could have excited Uranus' obliquity to its present day value if it was driven by the outward migration of an as-yet undetected outer Solar System body commonly known as Planet Nine. We draw support for our hypothesis from an analysis of 123 N-body simulations with varying parameters for Planet Nine and its migration. We find that in multiple instances, a simulated Planet Nine drives Uranus' obliquity past 98° , with a significant number falling within 10% of this value. We note a significant caveat to our results in that a much faster than present-day spin-axis precession rate for Uranus is required in all cases for it to reach high obliquities. We conclude that while it was in principle possible for Planet Nine (if it exists) to have been responsible for Uranus' obliquity, the feasibility of such a result hinges on Uranus' primordial precession rate.

4.1 Introduction

The large obliquity of Uranus is a puzzle. Conservation of angular momentum in the primordial Solar System naively suggests that as primordial gas giant planets accrete from the planetary disk, their axial tilts should be driven to zero. In reality, however, the Solar System's gas giants span a range of obliquities, with Uranus being most extreme with $\theta = 98.7^\circ$. The prevailing and best-studied theory posits that some type of giant impact was responsible - likely a $1\text{-}3 M_E$ body impacting the primordial Uranus, simultaneously generating the large axial tilt and spurring the formation of its satellite system ([Harris & Ward, 1982](#); [Benz et al., 1989](#); [Slattery et al., 1992](#); [Izidoro et al., 2015](#); [Kegerreis et al., 2018, 2019](#); [Reinhardt et al., 2020](#); [Ida et al., 2020](#); [Rogoszinski & Hamilton, 2021](#)). The theory has significant merit and giant impacts are indeed both feasible and capable of explaining much of Uranus' present-day configuration. In a few aspects, however, it encounters difficulties. [Rogoszinski & Hamilton \(2021\)](#) present an in-depth discussion of both the merits and drawbacks of the giant impact hypothesis. An immediate issue lies in the near-match between the spin rates of Uranus and Neptune. Both Uranus and Neptune spin significantly slower (with $T_U \sim 17.2$ hours and $T_N \sim 16.1$ hours)

than their break-up speeds, which would naively be expected for an accreting gas giant (Machida et al., 2008; Batygin, 2018; Bryan et al., 2018; Dong et al., 2021; Dittmann, 2021). A giant impact would likely change a planet's spin rate - however, Rogoszinski & Hamilton (2021) show that the impactors required to explain both Uranus' and Neptune's obliquities ($\theta_N \sim 30^\circ$) are unlikely to spin both planets down similarly. In addition, the prograde Uranian satellite system at first glance appears incompatible with a giant impact. Morbidelli et al. (2012) argues that given a single impactor the system would be expected to have a retrograde orbit. To account for the observed prograde orbit, Uranus would either require an initially large obliquity (on the order of $\sim 10^\circ$) or multiple impactors. Furthermore, impactors that are sufficiently large to explain the axial tilt of Uranus (greater than $1 M_E$) are expected to produce disks that exceed the total mass of the Uranian satellite system by an order of magnitude (Kegerreis et al., 2018; Reinhardt et al., 2020). A possible solution has been offered by Ida et al. (2020), who show that the incongruity in impact-generated disks can be reconciled if the evolution of a water-vapor disk is taken into account. By assuming ice-dominated compositions for both Uranus and its impactor, Uranus' present-day satellite system is reproduced.

We investigate an alternative explanation of Uranus' large axial tilt by positing the capture and subsequent evolution of the planet in secular spin-orbit resonance. The resonant capture mechanism is slow enough to preserve both the structure of the planet's satellite system and its spin rate (Goldreich, 1965), which circumvents many of the problems with the giant impact theory. Furthermore, the process is potentially responsible for Jupiter's 3° (Ward & Canup, 2006; Vokrouhlický & Nesvorný, 2015) and Saturn's 27° (Ward & Hamilton, 2004; Hamilton & Ward, 2004) obliquities; plausibility in these instances is supported by the near-match between Jupiter's and Saturn's spin precession frequencies and the contributing nodal regression frequencies driven by Uranus and Neptune, respectively. Recently, however, Saillenfest et al. (2021a,b) have argued that early resonance with Neptune is incompatible with the fast tidal migration of Titan, and suggest that a later entry to the resonance driven by nodal precession evolution stemming from Titan's migration is responsible for Saturn's obliquity. A similar process, driven by the migration of the Galilean satellites, may excite Jupiter's currently small obliquity to larger values in the future (Saillenfest et al., 2020).

Uranus' current spin precession frequency is far too slow to be a near-match for any mode of secular forcing provided by the present-day Solar System. Significant work has thus been done to explore past Uranian evolutionary pathways which would result in a closer match. Millholland & Batygin (2019) studied the effect of an evolving circumstellar disk on the obliquities of both Uranus and Neptune, and concluded that disk-induced spin-orbit resonance is unlikely to be the cause of their axial tilts. Boué & Laskar (2010) posit that Uranus' current obliquity is

possible if Uranus had an additional large moon present in the past - however, this moon would require a mass of up to 1% the mass of Uranus and would have needed to be dispensed with after the resonance's action was complete. The study of [Rogoszinski & Hamilton \(2021\)](#) posited a circumplanetary disk that increased the Uranian spin precession frequency, and was able to account for obliquities of up to 70°. More recently, [Rogoszinski & Hamilton \(2021\)](#) investigated the effect of Neptune's migration on a primordial Uranus placed between Jupiter and Saturn. They concluded that 90° obliquities are achievable, but only on unrealistic timescales; 40° tilts are obtainable upon more reasonable timescales. In all cases, however, impacts must be invoked to subsequently drive the obliquity to the present-day value of 98°.

The review of [Batygin et al. \(2019\)](#) summarizes the development of the hypothesis that the observed orbital alignment of long-period trans-Neptunian objects is maintained by the presence of an as-yet undetected ($5 - 10 M_E$) body (known as Planet Nine) in the outer reaches of the Solar System. The dynamical effect that such a body, if present, would exert on Uranus thus merits investigation. In this article, we examine the effect that dynamical evolution (in the form of outward migration) of Planet Nine would have on Uranian spin axis, and we find that under certain conditions, a Planet Nine could have generated the dramatic spin-orbit misalignment that constitutes Uranus' most uniquely defining feature.

The paper is structured as follows. In Section 4.2, we outline the relevant values of axial precession and nodal regression. In Section 4.3, we use these quantities to discuss the physics involved in the process of secular spin-orbit resonance, and introduce the equation of motion that dictates the evolution of the spin axis. In Section 4.4, we describe our procedure for modeling the evolution of the Uranian node. We also discuss how we model the dynamical evolution of Planet Nine and its effect on the Uranian orbital evolution. In Section 4.5, we report the resulting obliquities we are able to achieve, and we discuss and draw conclusions in Section 4.6.

4.2 Precessional Frequencies

In the presence of torques from a host star and a satellite system, a planet's spin axis will precess about its orbit normal ([Goldreich, 1965](#)) with period (given low orbital eccentricity)

$$T_\alpha = \frac{2\pi}{|\alpha \cos \theta|}, \quad (4.1)$$

where θ is defined as the planet's obliquity, or the angle between the spin axis and orbit normal, and α is defined as the *precessional constant*. Figure 4.1 provides a

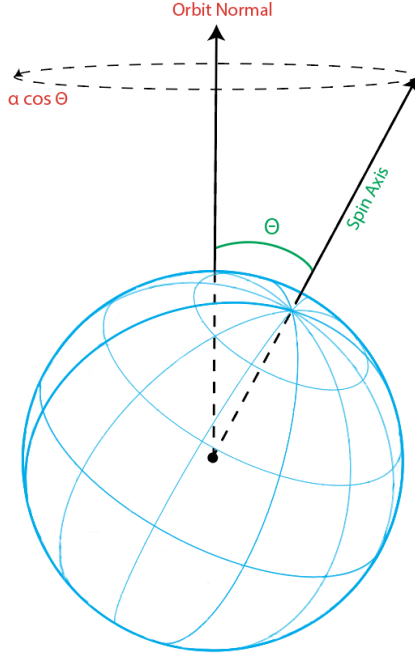


Figure 4.1. Torques associated with the host star and satellite system cause the spin axis to precess about the orbit normal with frequency $\alpha \cos \theta$.

schematic representation.

The precessional constant parameterizes the rate at which the spin axis precesses about the orbit normal. In the case where the satellite system exhibits prograde orbits in the equatorial plane (as is the case for the Uranian system), it is given by (Tremaine, 1991; French et al., 1993; Rogoszinski & Hamilton, 2021)

$$\alpha = \frac{3n^2}{2\omega} \frac{J_2 + q}{\lambda + l}, \quad (4.2)$$

where ω is the planet's spin frequency, n its orbital mean motion about the host star, J_2 is the quadrupole moment of the planet's gravitational field, and λ is its moment of inertia normalized by $M_p R_p^2$. The quantities q and l account for elements of the planet's satellite system or circumplanetary disk, with q being the effective quadrupole coefficient and l the angular momentum normalized by $M_p R_p^2 \omega$. For a satellite system (Tremaine, 1991; French et al., 1993; Ward & Hamilton, 2004;

Rogoszinski & Hamilton, 2021) one has

$$q \equiv \frac{1}{2} \sum_i \left(\frac{M_i}{M_p} \right) \left(\frac{a_i}{R_p} \right)^2 \quad (4.3)$$

$$l \equiv \frac{1}{M_p R_p^2 \omega} \sum_i M_i a_i^2 n_i,$$

with the sum running over all i satellites, and where M_i, a_i, n_i are the mass, semi-major axis and mean motion, respectively, of each satellite.

Considering the major satellites of Uranus, from Equations 4.2 and 4.3, we can calculate the present-day value of α for Uranus. Using $J_2 = 3.343 \times 10^{-3}$ (Dermott & Jupp, 1984) and $\lambda = 0.225$ (Yoder, 1995), we find that $\alpha = 0.045$ arcseconds/yr. At its current $\theta = 98^\circ$ obliquity, Uranus' axial precession period is $T_\alpha = 169$ Myr.

Simultaneously, in the presence of torques from neighboring planets and other large bodies, the orbital plane of a planet will recess about the normal to the invariant plane of the system (the plane perpendicular to the system's overall angular momentum vector). The period of recession is given by $T_g = 2\pi/|g|$, with $g = \dot{\Omega}$, where Ω is the longitude of the ascending node. Figure 4.2 shows a schematic view of the motion.

4.3 Spin-Orbit Resonance

Secular spin-orbit resonance trapping has repeatedly been shown to be a possible mechanism for generating substantial planetary obliquities. The dynamics of the phenomenon are well-studied (Peale, 1969), and its action has been shown to be plausibly responsible for Jupiter's 3° (Ward & Canup, 2006) and Saturn's 26.7° (Ward & Hamilton, 2004; Hamilton & Ward, 2004; Saillenfest et al., 2021b,a) axial tilts. Exciting obliquities via secular spin-orbit resonance has been shown to be self-consistent with the orbital migrations of Uranus and Neptune predicted by the Nice Model (Vokrouhlický & Nesvorný, 2015).

4.3.1 First Order Spin Axis Equation of Motion

To a first order of approximation, resonant motion of a planet's spin axis can be exhibited with the restrictive assumption of constant I, α and g . In a coordinate frame rotating with angular frequency g centered on the orbit normal (which we will call the "rotating frame"), the equation of motion can be approximated

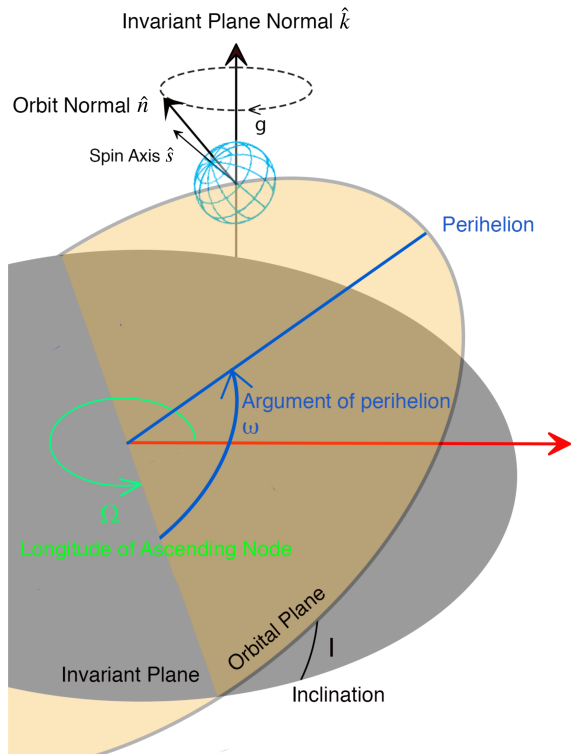


Figure 4.2. Torques associated with perturbing planets cause the inclined orbit of a planet (with normal \hat{n}) to recess about the invariant plane normal \hat{k} , at a rate of $g = \dot{\Omega}$. The planet's spin axis \hat{s} is also shown. Not shown on this figure is the longitude of periapsis ω , defined as $\omega = \Omega + \omega$

(Tremaine, 1991; Ward & Hamilton, 2004)

$$\frac{d\hat{s}^*}{dt} = \alpha (\hat{s}^* \cdot \hat{n}) (\hat{s}^* \times \hat{n}) + g(\hat{s}^* \times \hat{k}), \quad (4.4)$$

where $\hat{s}^*, \hat{n}, \hat{k}$ are the unit vectors pointing in the direction of the spin axis, orbit normal, and invariant plane normal, respectively. The superscript * notation on the unit spin vector is to differentiate the spin vector defined here in the rotating frame as opposed to in the invariant plane of the system, which will be defined later.

4.3.2 Cassini States

The spin axis may be defined in terms of two angles - the obliquity θ , previously defined, and the *precession angle* ψ , which is defined as the angle between the projections of \hat{s} and \hat{k} onto the plane perpendicular to \hat{n} . These angles can be related to the position of the unit spin vector in Cartesian coordinates Morbidelli (2002)

$$\hat{s}_x = \sin \theta \sin \psi, \hat{s}_y = \sin \theta \cos \psi, \hat{s}_z = \cos \theta \quad (4.5)$$

The Hamiltonian that governs the motion of the spin axis is well known (Morbidelli, 2002). In Cartesian coordinates (in the rotating frame),

$$\begin{aligned} \mathcal{H} = & \frac{\alpha}{2} \left(1 - \frac{1}{2}x^2 - \frac{1}{2}y^2 \right)^2 + \frac{\cos(I)}{2} g(x^2 + y^2) \\ & - \frac{\sin(I)}{2} gx \sqrt{4 - x^2 - y^2}, \end{aligned} \quad (4.6)$$

where I is the planet's inclination, and the Cartesian coordinates x and y can be expressed in terms of the obliquity and precession angle

$$x = 2 \sin \frac{\theta}{2} \cos \psi, y = 2 \sin \frac{\theta}{2} \sin \psi \quad (4.7)$$

For a full derivation, see Millholland & Batygin (2019). The motion of the spin vector is confined to the level curves (curves of constant energy) of the Hamiltonian. As the ratio α/g evolves, so do the locations of the level curves. At a critical value,

$$(\alpha/g)_{crit} = - \left(\sin^{2/3} I + \cos^{2/3} I \right)^{3/2}, \quad (4.8)$$

a separatrix appears and additional equilibrium points emerge (Ward & Hamilton, 2004; Fabrycky et al., 2007). See Figure 4.3 for a plot of the level curves of

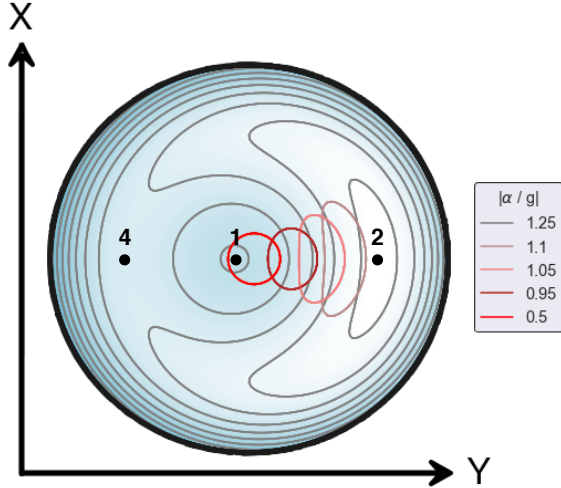


Figure 4.3. Level curves of the spin axis Hamiltonian (in black) with $\alpha/g = 1.25 > (\alpha/g)_{crit}$, with the Cassini state equilibrium points labeled (Cassini State 3 corresponds to a retrograde spin state and is not shown). Spin axis trajectories are confined to these level curves. The colored lines tracks the evolution of one such trajectory as the ratio $|\alpha/g|$ changes - note how the curve begins as a circulating trajectory and evolves into a librating one.

the Hamiltonian in the rotating frame of the planet at $\alpha/g > (\alpha/g)_{crit}$ (the necessary criterion for resonant capture, see Section 4.3.3). The equilibrium points at the extrema of the Hamiltonian are known as *Cassini states*, and correspond to configurations such that in the invariant frame, (Colombo, 1966; Peale, 1969)

- \hat{s}, \hat{n} and \hat{k} are coplanar
- \hat{s} and \hat{n} precess about \hat{k} at the same rate.

Clearly, in the rotating frame centered on the orbit normal, the spin axis position appears stationary. Four such equilibrium points exist: states 1, 2 and 4 are shown on Figure 4.3, while state 3 is retrograde and thus projects into the downward-facing hemisphere. For a pair of values of α/g and inclination I , the obliquities θ_c of the corresponding Cassini states are given by (Ward & Hamilton, 2004)

$$\frac{\alpha}{g} \cos \theta_c \sin \theta_c + \sin(\theta_c - I) = 0. \quad (4.9)$$

For $\alpha/g < (\alpha/g)_{crit}$ states 1 and 4 do not exist (Ward & Hamilton, 2004), so we consider motions of the spin axis about Cassini State 2. Figure 4.3 shows that for trajectories that lie close to Cassini state 2, the spin axis will librate in a banana-like trajectory about the equilibrium, rather than circulating the origin.

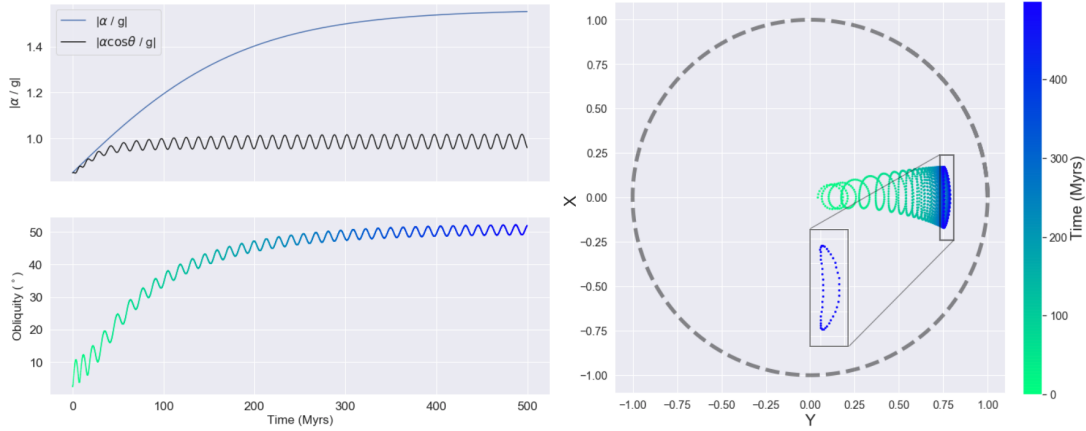


Figure 4.4. Result of a simple evolution of the ratio $|\alpha/g|$, obtained via integration of Equation 4.4. The upper left plot displays the evolution of $|\alpha/g|$ imposed on this simulation - note that the ratio $|\alpha \cos \theta/g|$ saturates at unity. The bottom left plot shows the resulting obliquity evolution. The right plot shows the location of the spin axis over the evolution period. We have zoomed in on one libration timescale to explicitly show the banana-like libration motion the spin axis exhibits when captured into resonance.

4.3.3 Resonant Capture

If the ratio α/g changes slowly enough, the phase space area enclosed by a trajectory remains constant. This is known as the *adiabatic criterion* and is satisfied if the rate of change in α/g is much slower than a libration timescale (Millholland & Batygin, 2019). As the ratio $|\alpha/g|$ increases, Cassini state 2 will move outward and an orbital trajectory trapped in resonance will be forced to larger and larger obliquities. This evolution is overplotted in Figure 4.3.

If the adiabatic condition is satisfied, resonant capture occurs when the ratio $|\alpha \cos \theta/g|$ approaches unity from *below*. At low obliquities, this is equivalent to the condition that $|\alpha/g|$ approach unity from below. By contrast, a passage through unity from the opposite direction leads to an impulsive, potentially large kick to the obliquity, without capture into resonance (Ward & Hamilton, 2004). If resonance capture occurs, the ratio T_g/T_α oscillates around an average value of unity and large increases in obliquity can occur. Figure 4.4 shows an example evolution of the ratio $|\alpha/g|$ and the resultant obliquity evolution.

4.3.4 Spin Axis Equation of Motion

In reality, a planet's orbital inclination is not constant, the orbit is eccentric, and the value of α can vary with time. The simple equation of motion in this event no longer gives an accurate picture. In the invariant plane of the solar system, the orbital inclination and longitude of ascending node may be decomposed into

more than one harmonic. The motion of the unit spin axis \hat{s} in this regime is given by (Ward, 1979; Hamilton & Ward, 2004):

$$\begin{bmatrix} \dot{s}_x \\ \dot{s}_y \\ \dot{s}_z \end{bmatrix} = \frac{\alpha(s_x p \xi - s_y q \xi + s_z \eta)}{(1 - e^2)^{3/2}} \begin{bmatrix} s_y \eta + s_z q \xi \\ s_z p \xi - s_x \eta \\ -s_x q \xi - s_y p \xi \end{bmatrix}, \quad (4.10)$$

which in turn draws on functions of the planet's orbital elements

$$\begin{aligned} p &= 2 \sin\left(\frac{I}{2}\right) \sin \Omega \\ q &= 2 \sin\left(\frac{I}{2}\right) \cos \Omega \\ \xi &\equiv \sqrt{1 - \frac{1}{4}(p^2 + q^2)} \\ \eta &\equiv 1 - \frac{1}{2}(p^2 + q^2), \end{aligned} \quad (4.11)$$

where e is eccentricity, I is inclination, ω is the longitude of periapsis and Ω the longitude of ascending node. To see librations we must transform back into the frame of the planet's orbit via (Ward, 1974)

$$\hat{s}^* = A \hat{s}, \quad (4.12)$$

where \hat{s}^* is the unit spin axis in the frame that rotates with the angular momentum vector of the planetary orbit, \hat{s} is the unit spin axis in the invariant plane, and A is the time-dependent rotation matrix

$$A = \begin{bmatrix} \cos \Omega & \sin \Omega & 0 \\ -\cos I \sin \Omega & \cos I \cos \Omega & \sin I \\ \sin I \sin \Omega & -\sin I \cos \Omega & \cos I \end{bmatrix}, \quad (4.13)$$

where $\Omega(t)$ and $I(t)$ vary in time.

4.4 Nodal Evolution Modeling

Approaches of escalating complexity can be employed to model the evolution of the Uranian nodal precession, g in response to perturbations from the other bodies of the Solar System.

4.4.1 Laplace-Lagrange Secular Theory

Short of full numerical simulations that track the Uranian node, significant physical intuition can be gained from the linear approximation provided by Laplace-Lagrange secular theory. Secular theory describes the orbital motion of planetary orbits as an averaged approximation of their long term motions. Terms in the gravitational disturbing function that include the mean longitude are ignored in this approximation, as they vary relatively rapidly and in the long term average to zero. In the late 1700s, it was determined that to lowest order, the time dependence of the eccentricities e (Laplace, 1775) and the inclinations I (Lagrange, 1778) of a planetary system with k bodies are described by a system of first-order linear differential equations:

$$\frac{d}{dt} \begin{bmatrix} z_1 \\ \vdots \\ z_k \\ \zeta_1 \\ \vdots \\ \zeta_k \end{bmatrix} = \sqrt{-1} \begin{bmatrix} A_k & 0_k \\ 0_k & B_k \end{bmatrix} \begin{bmatrix} z_1 \\ \vdots \\ z_k \\ \zeta_1 \\ \vdots \\ \zeta_k \end{bmatrix}. \quad (4.14)$$

which was applied to the motion of the solar system planets by Laplace (1784) (for an in-depth review of the development of Laplace-Lagrange secular theory, see (Laskar, 2013)). Here $z \equiv e \exp \sqrt{-1}\omega$ and $\zeta \equiv 2 \sin(I/2) \exp \sqrt{-1}\Omega$. A_k and B_k are $k \times k$ matrices whose elements depend solely on the masses and semi-major axes of the k planets, and 0_k denotes the $k \times k$ zero matrix. At this level of approximation, the time evolution of z_i and ζ_i is given as a sum of sinusoidal contributions

$$\begin{aligned} z_i &= \sum_{j=1}^k \alpha_{ij} e^{\sqrt{-1}\gamma_j t} \\ \zeta_i &= \sum_{j=1}^k \beta_{ij} e^{\sqrt{-1}\delta_j t}, \end{aligned} \quad (4.15)$$

where the quantities δ_j , α_{ij} , γ_j , β_{ij} are the eigenvalues and eigenvectors of the A_k and B_k matrices, respectively. The i and j indices range from 1 to k and represent each planet in the system. Of particular interest to our analysis is the quantity δ_j , which determines the "forcing frequency" at which the j th body perturbs Ω .

A slightly modified version of the foregoing theory that is specific to the Solar System (and which partially accounts for additional Jupiter-Saturn interactions)

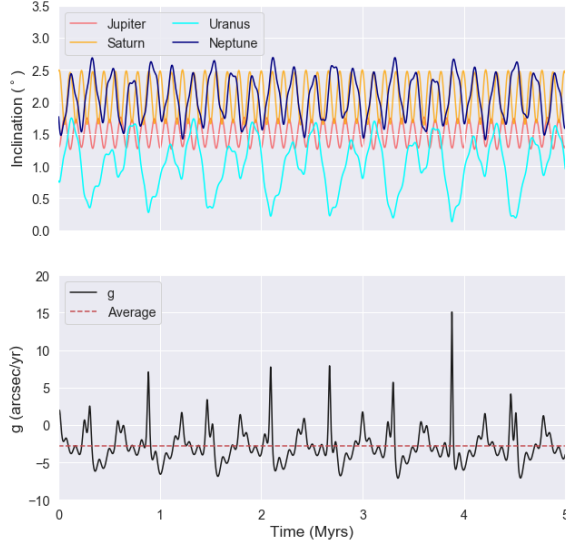


Figure 4.5. The evolution of the four outer planets as described by the secular theory of Laplace (1784). The upper plot shows the evolution of inclination of all four outer planets - note the complex yet semi-periodic behavior. The bottom plot shows the evolution of g , the rate of change of Uranus's node position.

was developed by Brouwer & van Woerkom (1950), and was notably reprinted in (Murray & Dermott, 2000).

Given the time evolution of z_i and ζ_i , the orbital elements (see Equation 4.11) including Ω can be recovered. Figure 4.5 shows the inclination evolution of the four outer planets implied by secular theory, as well as the evolution of the Uranian g .

4.4.2 Effect of Planet Nine

Planet Nine is a hypothesized body in the outer Solar System whose existence has been inferred from the apparent apsidal confinement of long-period trans-Neptunian objects (Batygin & Brown, 2016). For a more detailed review of the evidence for Planet Nine, see (Batygin et al., 2019). The most recent Markov Chain Monte Carlo simulations (Brown & Batygin, 2021) give Planet Nine's best-fit orbital parameters:

$$\begin{aligned} m_9 &= 6.9_{-1.6}^{+2.6} M_E \\ a_9 &= 460.7_{-103.3}^{+178.8} \text{ AU} \\ e_9 &= 0.3_{-0.1}^{+0.1} \\ i_9 &= 15.6_{-5.4}^{+5.2} \text{ }^\circ. \end{aligned} \tag{4.16}$$

In contrast, however, the recent study by [Batygin & Brown \(2021\)](#) suggests that a more eccentric and more distant Planet Nine may be required.

In situ formation of Planet Nine is believed to be unlikely ([Kenyon & Bromley, 2016](#)), and discussion has settled on two preferred possibilities for its origin. One possibility is that it formed alongside the four giant planets and subsequently migrated outward to a much more distant orbit ([Thommes et al., 1999](#); [Brasser et al., 2012](#); [Izidoro et al., 2015](#); [Bromley & Kenyon, 2016](#); [Li & Adams, 2016](#); [Eriksson et al., 2018](#)). A second possibility is that it was captured from a passing star within the Solar System's stellar birth aggregate ([Li & Adams, 2016](#); [Mustill et al., 2016](#); [Parker et al., 2017](#)). If this second scenario holds, there would be no plausible connection to the Uranian obliquity, so we focus on long-distance outward migration of Planet Nine as an assumed formation pathway. The parameters given in Equation 4.16 assume a prior involving Planet Nine's origin and eventual ejection from the Jupiter-Saturn region.

[Batygin et al. \(2019\)](#) proposed a two-step migration process: First, Jupiter or Saturn scatter Planet Nine onto a temporary high-eccentricity orbit, which was then circularized via gravitational perturbations from nearby stars in the cluster. It should be stressed, however, that this is an unlikely scenario - the probability of a Planet Nine-sized body settling between 100 and 5000 AU due to stellar perturbations is no more than a few percent ([Bailey & Fabrycky, 2019](#)). A more likely alternative involves circularization via dynamical friction with a circumstellar disk. With a gaseous disk, [Bromley & Kenyon \(2016\)](#) were able to reproduce orbits similar to that of Planet Nine post-scattering, with a preference towards very slowly decaying disks (with dissipation timescales on the order of 10 Myr). Subsequently, numerical simulations of [Carrera et al. \(2017\)](#) were used to suggest that a 60–130 M_E planetesimal disk formed beyond 100 AU as a consequence of the streaming instability. [Eriksson et al. \(2018\)](#) found that a 10 M_E planet scattered into such a disk from the vicinity of Neptune's orbit has a 20–30% chance of reproducing a Planet Nine-like orbit.

As Planet Nine moves outward in its putative migratory trajectory, the magnitude of its perturbations on the Uranian Ω steadily diminish (see Figure 4.6). The rate of change of the Uranian node, g , thus decreases with time. In the event that the precession factor, α , remains constant, this provides a pathway for resonance capture as the ratio $|\alpha/g|$ evolves to reach unity.

4.4.3 Numerical Simulations

The Laplace-Lagrange theory assumes constant semi-major axes for all planets, and additionally fails in the limit of significant short-period terms ([Camargo et al., 2018](#)), so a migrating Planet Nine cannot be modelled in this framework. We

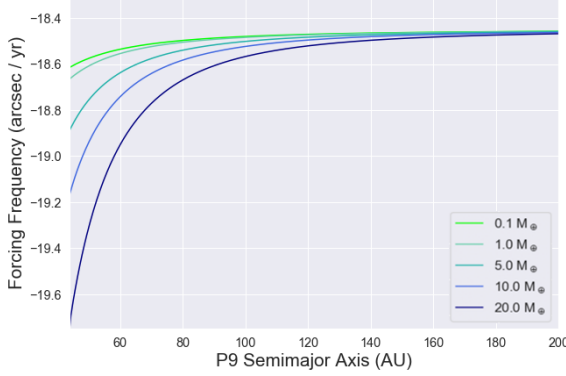


Figure 4.6. Planet Nine’s forcing frequency on Uranus as a function of semi-major axis. Each line corresponds to a Planet Nine of varying mass (in Earth masses). Note that the forcing frequency does not go to zero even as Planet Nine’s mass does - this is because each eigenfrequency does not correspond one-to-one with a planet, but rather is simply dominated by a given body.

instead turn to full N-body integrations that employ the REBOUND package (Rein & Liu, 2012) with the adaptive high-order IAS15 integrator (Rein & Spiegel, 2015). We incorporated orbit-averaged physical forces to simulate the outward migration of Planet Nine using the *modify_orbits_forces* implementation (Kostov et al., 2016b) in the REBOUNDx package (Tamayo et al., 2020a).

An overview of our modeling procedure is as follows. A REBOUND simulation is initialized with the Sun and the four outer planets in their present-day configuration, with orbital element values from the NASA HORIZONS database. Planet Nine is then initialized in its starting position. Free parameters associated with Planet Nine include its mass, its eccentricity, and its inclination. We set the initial semi-major axis and τ_a (which parameterizes the migration rate as seen in Kostov et al. (2016b)) constant. The system as thus specified is in the frame of the ecliptic. We then determine the invariant plane of the Solar System with Planet Nine accounted for, via the method outlined by Souami & Souchay (2012). The normal vector to the invariant plane is

$$\hat{L}_{tot} = \sum_{j=1}^N m_j \hat{r}_j \times \hat{v}_j, \quad (4.17)$$

where m_j, r_j, v_j are the mass, barycentric position, and barycentric velocity of the j th body, respectively. We recalculate the inclination of each planet in the invariant frame by taking the angle between \hat{L}_{tot} and the planet’s own orbital angular momentum vector. Each simulation is then integrated forward for 10^8 years. The results of the REBOUND simulation (namely, values for the Uranian inclination, eccentricity, Ω , and ω) are used to construct time evolutions of the orbital elements

$e(t)$, $p(t)$, $q(t)$. The orbital elements at each timestep are then passed into the spin axis equation of motion (eq. 4.10) to track the motion of the spin axis. The rate of nodal regression $g = \dot{\Omega}$ is itself not used as an input to our spin vector equation of motion, but is useful for illustrative purposes - this quantity is calculated numerically from the value of $\Omega(t)$ recovered at each timestep. In each case, Uranus' spin axis is initialized with an obliquity of 2.5° . This value is arbitrarily chosen, but any small initial tilt should yield similar results. We test each REBOUND simulation with various values of α linearly spaced between 0.005 and 6 arcseconds / yr and track the results.

4.5 Results of N-Body Simulations

In this section we present selected results from our N-body simulations. For a compiled list of all our simulation results as well as the source code used, see www.github.com/tigerchenlu98/tilting-uranus. Throughout all of our simulations, the magnitude of the spin vector differs from unity by less than one part in 10^5 .

4.5.1 Solar System Model

We now examine simulations of a Solar System dynamical model that includes Jupiter, Saturn, Uranus, Neptune, and Planet Nine. To save computation time the terrestrial planets were not included, as their effects are negligible. For each simulation, we initialize Planet Nine at 40 AU. The τ_a parameter, as seen in Kostov et al. (2016b), parameterizes the rate of change in the system. The evolution of Planet Nine's semi-major axis is given by

$$a = a_0 e^{t/\tau_a}, \quad (4.18)$$

In practice, perturbative influences from the other planets lead to slightly more complex realized semi-major axis evolution and hence a non-deterministic final a . We set $\tau_a = 4 \times 10^7$ years for each of our simulations - for this value, the semi-major axis progresses through 2.5 e-folding timescales. We emphasize that our choice of initial a and τ_a do not reflect Planet Nine's true initial position or migratory trajectory - recall that Planet Nine is believed to have originated with the giant planets. Rather, the value of 40 AU is picked to encapsulate as much of the evolutionary trajectory as possible, without sacrificing the stability of the simulation. As the effect of Planet Nine on the Uranian Ω only increases for smaller semi-major axis (per secular theory), bringing Planet Nine's initial position closer in would serve to bring the ratio α/g down, which favors resonant capture.

Therefore, in principle any smaller initial a_9 and any τ_a satisfying the adiabatic criterion should yield similar or larger obliquities than our simulations. We also emphasize that the given migration scheme does not represent the most accurate physical evolutionary pathway of Planet 9's semimajor axis. In reality, Planet 9's outward migration was likely not smooth and its expansion rate likely decreased with time. We will discuss a more realistic migration scheme in Section 4.5.4 - for now, the simple exponential model of semimajor axis growth is selected for ease of use and is sufficient to draw first-order conclusions, given that as long as the evolution remains within the adiabatic limit the precise evolution of the semimajor axis should not significantly impact the dynamics.

Given the uncertainty regarding Planet Nine's orbital parameters, we first analyze results drawn from a wide range of possible orbits

$$\begin{aligned} m_9 &= 5 - 10 M_E \\ a_9 &= 400 - 800 \text{ AU} \\ e_9 &= 0.2 - 0.5 \\ i_9 &= 15^\circ - 25^\circ. \end{aligned} \tag{4.19}$$

where m_9, e_9, i_9 are the initial mass, eccentricity and inclination of Planet Nine in the frame of the ecliptic, respectively. With the context from the wide distribution, we then more closely examine the narrow parameter range suggested by the recent Brown & Batygin (2021) study.

Using draws from the wider range of parameters, we performed a total of 48 dynamical simulations, using the values

$$\begin{aligned} m_9 &\in \{5 M_E, 7 M_E, 10 M_E\} \\ e_9 &\in \{0.3, 0.4, 0.5, 0.6\} \\ i_9 &\in \{15^\circ, 20^\circ, 25^\circ, 30^\circ\}. \end{aligned} \tag{4.20}$$

Of these 48 simulations, nine resulted in one or more of Uranus, Neptune, or Planet Nine being ejected from the Solar System. These cases are beyond the scope of this paper and are not analyzed further. The remaining 39 simulations exhibit a range of dynamical stability for the orbits of Uranus and Neptune (Jupiter and Saturn remain stable in all cases). We classify them into three categories - *stable*, *slightly unstable*, and *significantly unstable*. Each is defined below (see Figure 4.7 for examples of each case).

- *Stable* simulations: the semi-major axes of Uranus and Neptune do not diverge from within 10% of their initial values for the duration of the run.

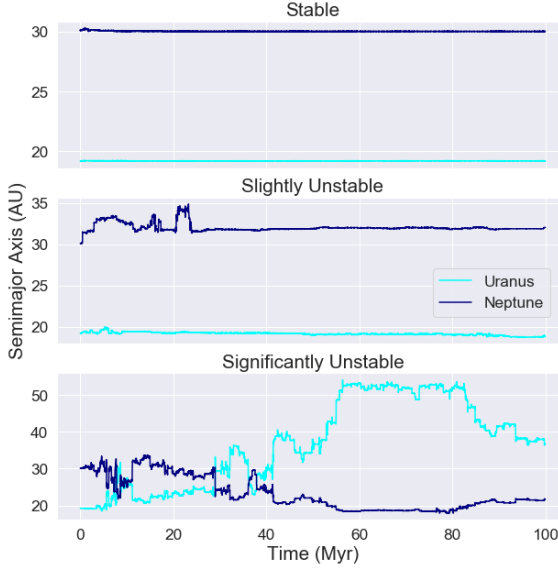


Figure 4.7. Examples of Uranus and Neptune's semi-major axis evolution for the three stability cases we have defined. The stable case was produced by a Planet Nine with $m_9 = 5 M_E$, $e_9 = 0.4$, $i_9 = 30^\circ$, the slightly unstable case with $m_9 = 5 M_E$, $e_9 = 0.6$, $i_9 = 20^\circ$, and the unstable case with $m_9 = 7 M_E$, $e_9 = 0.4$, $i_9 = 15^\circ$.

Eighteen of the simulations produced stable outcomes by this measure.

- *Slightly unstable* simulations: the semi-major axes of Uranus and/or Neptune diverge by more than 10% from their initial values, but return to within this threshold by the end of the run. Four simulations are slightly unstable.
- *Significantly unstable* simulations: the semi-major axes of Uranus or Neptune differ more than 10% from their initial values at the end of the run. Seventeen simulations are significantly unstable.

Figure 4.8 summarizes results from our simulations. The format is as follows - each grid cell represents the most stable simulation for an eccentricity/inclination value pair. If two simulations with comparable stability existed for an eccentricity/inclination pairing, the one with the higher maximum obliquity obtained was chosen. Of these simulations, the highest maximum obliquity achieved was 105.6° , while the lowest maximum obliquity was 75.9° . The average maximum obliquity reached is 94.7% . $13/16$, or 81.3% , reach a maximum obliquity within 5% of Uranus' present day obliquity of 98° or higher, while $6/16$ reach a maximum obliquity greater than 98° . It must be stressed that these high obliquities are reached only with high Uranian precession rates - the associated ramifications will be discussed further in Section 4.5.2.

Summary of Most Stable Simulations

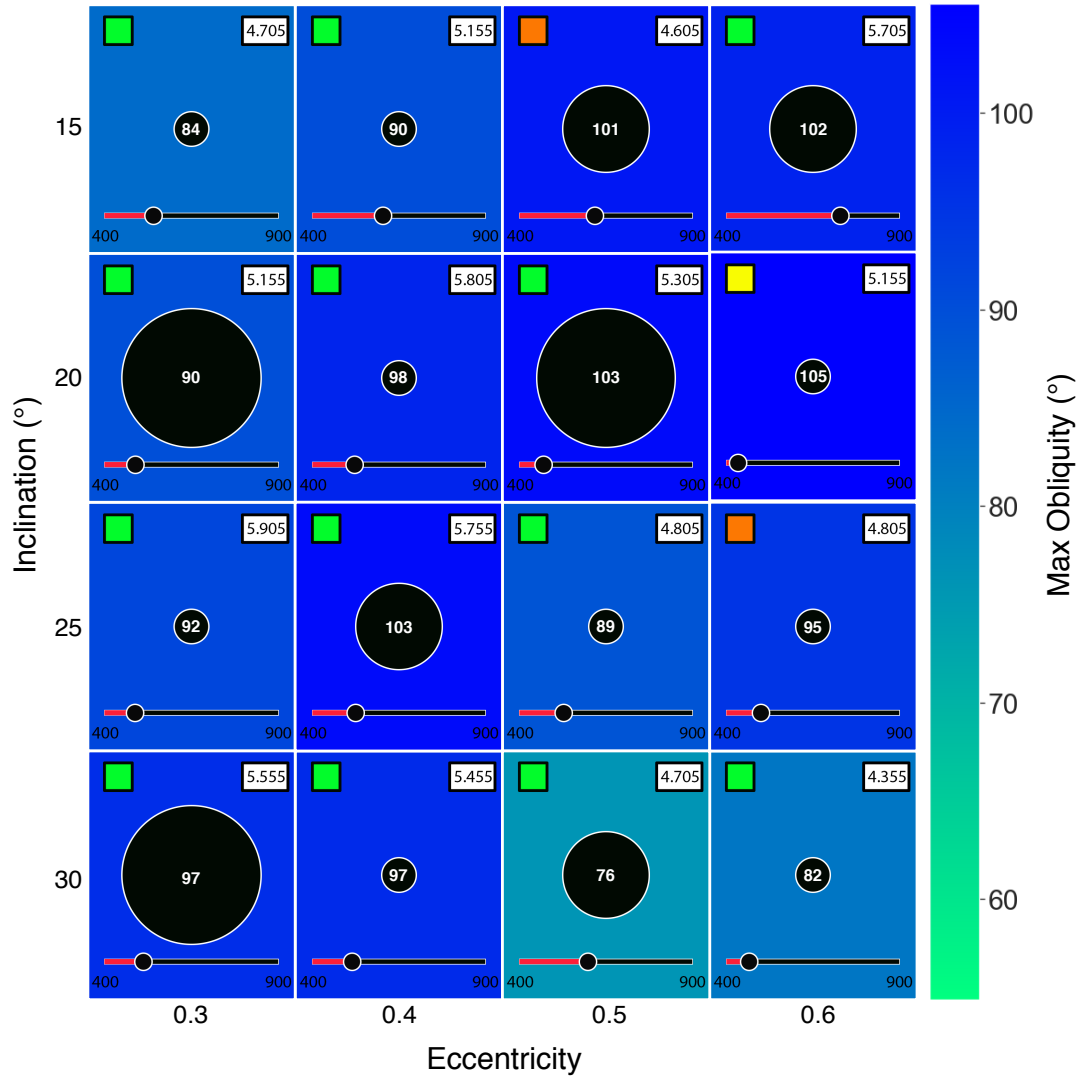


Figure 4.8. Summary of results of our simulations. Each grid cell contains the most stable result for that eccentricity/inclination pairing. The background color of each grid cell shows the maximum obliquity reached (see colorbar on the right). The size of the central black dot represents the mass of Planet Nine used in that run - small for $5 M_E$, medium for $7 M_E$, and large for $10 M_E$. The number inside each black dot is the maximum obliquity reached to the nearest degree. The colored square on the upper left hand corner of each grid cell represents the stability of that run - green for stable, yellow for slightly unstable, and orange for significantly unstable. The number in the upper right hand corner of each cell is the value of α used to achieve the maximum obliquity, in arcseconds/year. The slider at the bottom of each cell represents the final semi-major axis of Planet Nine, on a scale from 400 - 900 AU. Three boxes in this plot show yellow or orange stability - this indicates there was no perfectly stable run associated with that cell and the best alternative was selected.

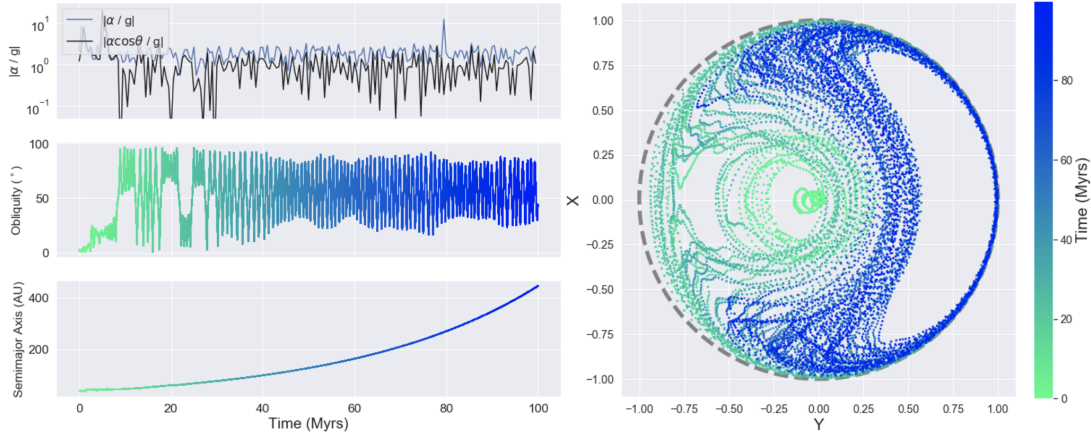


Figure 4.9. Spin axis evolution for one of our simulations. *Top:* the evolution of $|g|$ (top), the ratio $|\alpha/g|$ (second), obliquity in degrees (third), and Planet Nine’s semi-major axis in AU (bottom). The dotted red line in the topmost subfigure marks $|\alpha/g| = 1$. *Bottom:* the evolution of Uranus’ spin axis, as calculated with Equation 4.10 with $\alpha = 5.305$ arcsec/yr. A maximum obliquity of 103.46° is achieved, with Planet Nine’s final semi-major axis at 445.4 AU. Note the resonance kicks when the ratio $|\alpha/g|$ crosses unity quickly, and the subsequent resonance capture when the long-term average slowly crosses unity from below.

We now take a closer look at one of the simulations. Figure 4.9 shows the spin-axis evolution of one of our simulations, as well as the obliquity evolution and Planet Nine’s migration trajectory. In this model, we used $m_9 = 10 M_E$, $e_9 = 0.5$ and $i_9 = 20^\circ$. Planet Nine’s final semi-major axis is 445.39, and we used $\alpha = 5.305$ arcsec/yr to achieve the maximum obliquity value of 103.49° . Here, we see examples of resonance kicks in both directions (in the 10-30 Myr range) before the spin axis is then captured into resonance and we see the characteristic banana-like librations.

A natural question that arises from these simulations concerns our resonance argument: namely, how Uranus achieves obliquities greater than 90° . From Equation 4.1, as the planet’s obliquity reaches 90° its axial precession rate tends to 0, breaking the resonance (Rogoszinski & Hamilton, 2021). However, many of our simulations show maximum obliquities greater than 90° . Quillen et al. (2018) explored a different resonant argument including mean motion terms capable of exciting obliquities above 90° - this resonant argument is insensitive to orbital inclination and requires multiple additional planets. We need not appeal to another resonant argument, however - our results can be explained either via obliquity kicks or the amplitude of libration during resonant capture. The simulation shown in Figure 4.9 is a good illustration of both these cases, as it includes instances of $> 90^\circ$ obliquity due to both an obliquity kick and during resonance itself. In Figure

4.10, we have zoomed in on a sample of a kick (a), and a resonant libration (b). In (a), note how after the rapid obliquity increase the spin axis fully circulates about the planet, which shows that the spin-axis has not been captured into resonance, and that a rapid kick was responsible for the increase in obliquity. Resonant kicks, which do not satisfy the adiabatic criterion, face no comparable constraint to Equation 4.1 and thus are capable of exciting obliquities beyond 90° . In (b), the characteristic banana-like shape of libration is clearly visible - an indication that resonance capture has occurred. Note that obliquities above 90° are achieved only at the maximum amplitude of libration, indicating that the libration itself is about a spin-axis position corresponding to an obliquity $\theta < 90^\circ$ hence, there is no contradiction with Equation 4.1. The maximum excursions in ψ and θ from equilibrium over one libration period are related, and can be expressed (Hamilton & Ward, 2004):

$$\Delta\psi = \sqrt{\tan \theta / \sin i} \Delta\theta \quad (4.21)$$

4.5.2 Axial Precession Rate Discrepancy

While we have found that Planet Nine is capable of tilting Uranus up to 98° , there is a caveat to our results - in all cases we require a value of α significantly higher than the present day value. Uranus' current day α is 0.045 arcsec/yr , two orders of magnitude less than the smallest value used in our simulations. The mechanism of α enhancement has, in the past, been investigated as an attractive avenue for tilting Uranus. Boué & Laskar (2010) proposed enhancing the Uranian α with an additional moon, and were able to excite Uranus' obliquity to present day values. This moon, however, would have needed to be very large, with a mass of $0.01 M_U$ and a semi-major axis of $50 R_U$. For reference Uranus' most distant present-day satellite is Oberon with a semi-major axis of $23 R_U$, and its most massive satellite is Titania with $m = 4.06 \times 10^{-5} M_U$. This hypothetical moon would raise Uranus' precessional constant to $\alpha = 10.58 \text{ arcsec/yr}$; however, its size and the fact that it would need to be disposed of at some point raise significant issues with this theory. Rogoszinski & Hamilton (2021), who proposed a circumplanetary disk to enhance α , were able to tilt Uranus up to 70 degrees. In this scenario an impact would still be necessary to reach Uranus' present day obliquity - our simulations have the advantage of requiring no impact at all.

The effect of a circumplanetary disk on a planet's precession rate is well known. For a circumplanetary disk with mass m_{cp} , outer radius r_{cp} within the Laplace radius of the planet, and surface density profile $\Sigma_{cp}(r) = \Sigma_{cp,0}(r/R_p)^{-\gamma}$ (Millholland

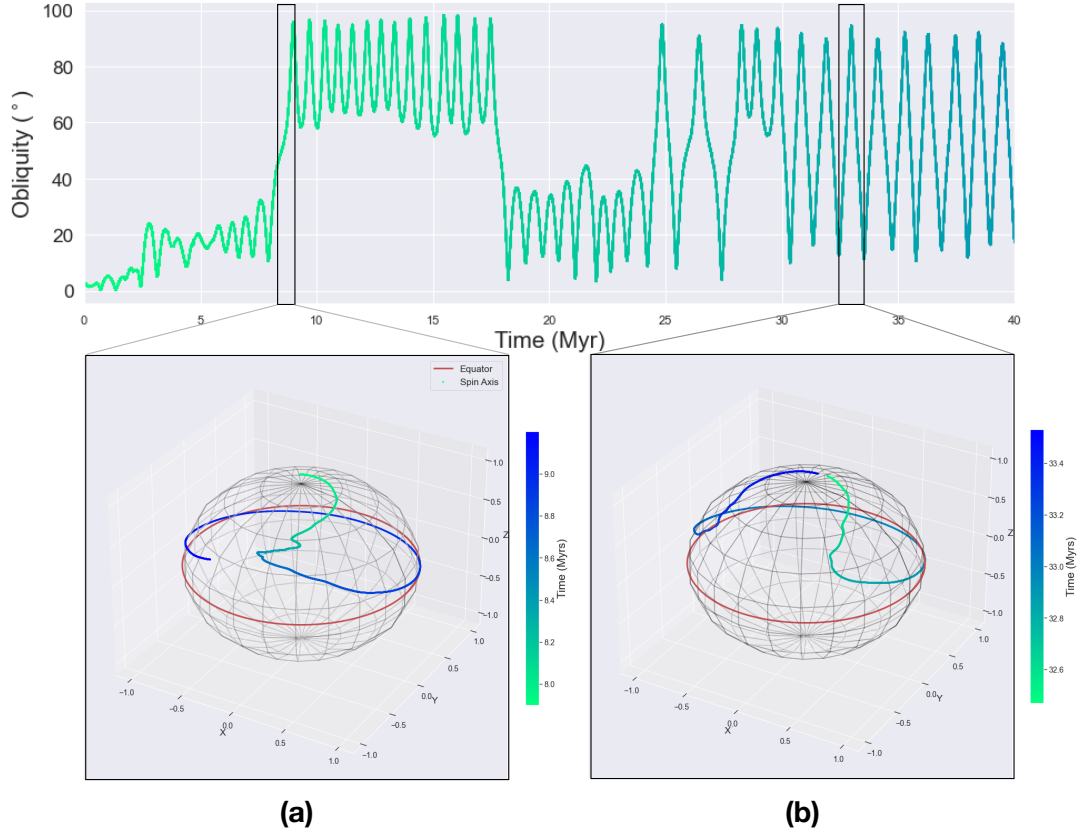


Figure 4.10. A closer look at two instances where the obliquity of Uranus exceeds 90° . The top plot shows the first 40 Myr of the obliquity time evolution from Figure 4.9. Both bottom figures show 3-D scatterplots of Uranus' spin axis in the designated time slices. The red great circle represents the projection of Uranus' orbit plane onto the unit sphere, and marks the point at which the obliquity of Uranus exceeds 90° . In (a), we see an example of an obliquity kick, as the spin axis continues to circulate after the increase in obliquity. In (b), the spin axis is shown in resonance, with the characteristic banana-like libration clearly visible.

& Batygin, 2019)

$$q \equiv \frac{1}{2} \left(\frac{2-\gamma}{4-\gamma} \right) \left(\frac{m_{cp}}{M_p} \right) \left(\frac{r_{cp}}{R_p} \right)^2 \quad (4.22)$$

$$l \equiv \left(\frac{2-\gamma}{5/2-\gamma} \right) \left(\frac{m_{cp}}{M_p R_p^2 \omega} \right) \left(GM_p r_{cp} \right)^{1/2},$$

These values are inserted into Equation 4.2 to calculate the corresponding Uranian α . It is thus useful to assess the feasibility of our results in the context of a circumplanetary disk. Szulágyi et al. (2018) performed radiative hydrodynamic simulations to estimate a reasonable initial mass for the Uranian circumplanetary disk of $\sim 7.4 \times 10^{-4} M_U$. Using this value and taking a fiducial value for the circumplanetary disk radius of $r_{cp} = 54 R_U$ based on the Laplace radius (Rogoszinski & Hamilton, 2021), we arrive at $\alpha = 1.06 \text{ arcsec/yr}$. However, Szulágyi et al. (2018) shows that the circumplanetary disk is not a closed system but rather is continuously fed mass by the circumstellar disk at a rate of $2 \times 10^{-3} M_U/\text{yr}$. Given this, a larger disk of $m_{cp} = 2.9 \times 10^{-3} M_U$ and $r_{cp} = 75 R_U$ can reasonably be assumed, which is sufficient to give $\alpha = 6 \text{ arcsec/yr}$, which encompasses the range of all our simulations. (Rogoszinski & Hamilton, 2021) argue that the traditional Laplace radius of a planet is potentially enhanced by a factor of four in the presence of a circumplanetary disk, so this larger required radius is reasonable and fits within the potential Laplace radius of the planet. These values consider a constant surface density disk - for a disk with surface density gradient $\gamma = 3/4$ (Canup & Ward, 2002; Millholland & Batygin, 2019), a disk mass of $m_{cp} = 4.1 \times 10^{-3} M_U$ is required.

Our brief circumplanetary disk analysis oversimplifies a deep and richly complex field. Mamajek et al. (2012) estimate that the lifetime of a circumplanetary disk at Uranus' present-day orbit is of order 10 Myr - a timeframe in modest tension with the durations of our simulations. The possibility of dips in the circumplanetary disk's surface density near the Laplace radius and detachment from the ecliptic plane at high obliquities have also been noted by Rogoszinski & Hamilton (2021) and Tremaine & Davis (2014), respectively - the latter scenario is of particular concern, as detachment from the ecliptic would shrink the rate of precession and potentially break the resonance. Neither of these effects are considered in this argument. Finally, we also do not consider the effect of Uranus accreting from the circumplanetary disk over time - as Uranus accretes matter and gains angular momentum, from Equation (4.2) all else being equal the axial precession rate α will decrease (Rogoszinski & Hamilton, 2021). This works against the increase of $|\alpha/g|$ - resonance capture will occur more slowly. If we are to account for accretion from the circumplanetary disk, we would expect longer timescales to reach

the obliquities in this paper, dependant on the rate of accretion from the disk. We emphasize that we are agnostic with regards to the means of this necessary precessional frequency enhancement and offer this discussion of the effect of circumplanetary disks to provide an order-of-magnitude feasibility analysis for one of several viable options.

4.5.3 The Latest Planet Nine Parameters

We now present results from a set of simulations more closely analyzing the parameter space predicted by [Brown & Batygin \(2021\)](#) (see Equation 4.16). Again, we initialize each REBOUND simulations with the four outer planets, and Planet Nine at 40 AU. We set $\tau_a = 4.09 \times 10^7$ years and integrate for 10^8 years. This in principle gives

$$a_f = a_i e^{t_{max}/\tau_a} = 460 \text{ AU}, \quad (4.23)$$

though again effects of the other bodies in the system make the true final semi-major axis ultimately unpredictable. We ran 75 simulations with the values

$$\begin{aligned} m_9 &\in \{4.9 M_E, 6.2 M_E, 8.4 M_E\} \\ e_9 &\in \{0.20, 0.25, 0.30, 0.35, 0.40\} \\ i_9 &\in \{11^\circ, 13^\circ, 16^\circ, 18^\circ, 21^\circ\}. \end{aligned} \quad (4.24)$$

Two of these simulations resulted in a body being ejected and were not considered in our analysis. Of the remaining 73, 53 were stable, 8 were slightly unstable, and 12 were significantly unstable. Figure 4.11 summarizes these results in the same format as Figure 4.8. On the whole, maximum obliquities tend to be lower than the more general case; nevertheless, 10/25 (or 40%) of the simulations reach a maximum obliquity within 10% of Uranus' present day value. This round of simulations favors the most massive $m_9 = 8.4 M_E$ case.

4.5.4 Stochastic Scattering

As a brief caveat, note that simple exponential migration as we have modelled does not necessarily represent the most physically accurate pathway for Planet Nine's current orbit. Rather, as a typical TNO is scattered outwards its perihelion distance is coupled to Neptune and remains constant, while the semimajor axis grows stochastically. For such a stochastic system, the dynamics of semimajor axis evolution may be described by a conventional diffusion equation, where the

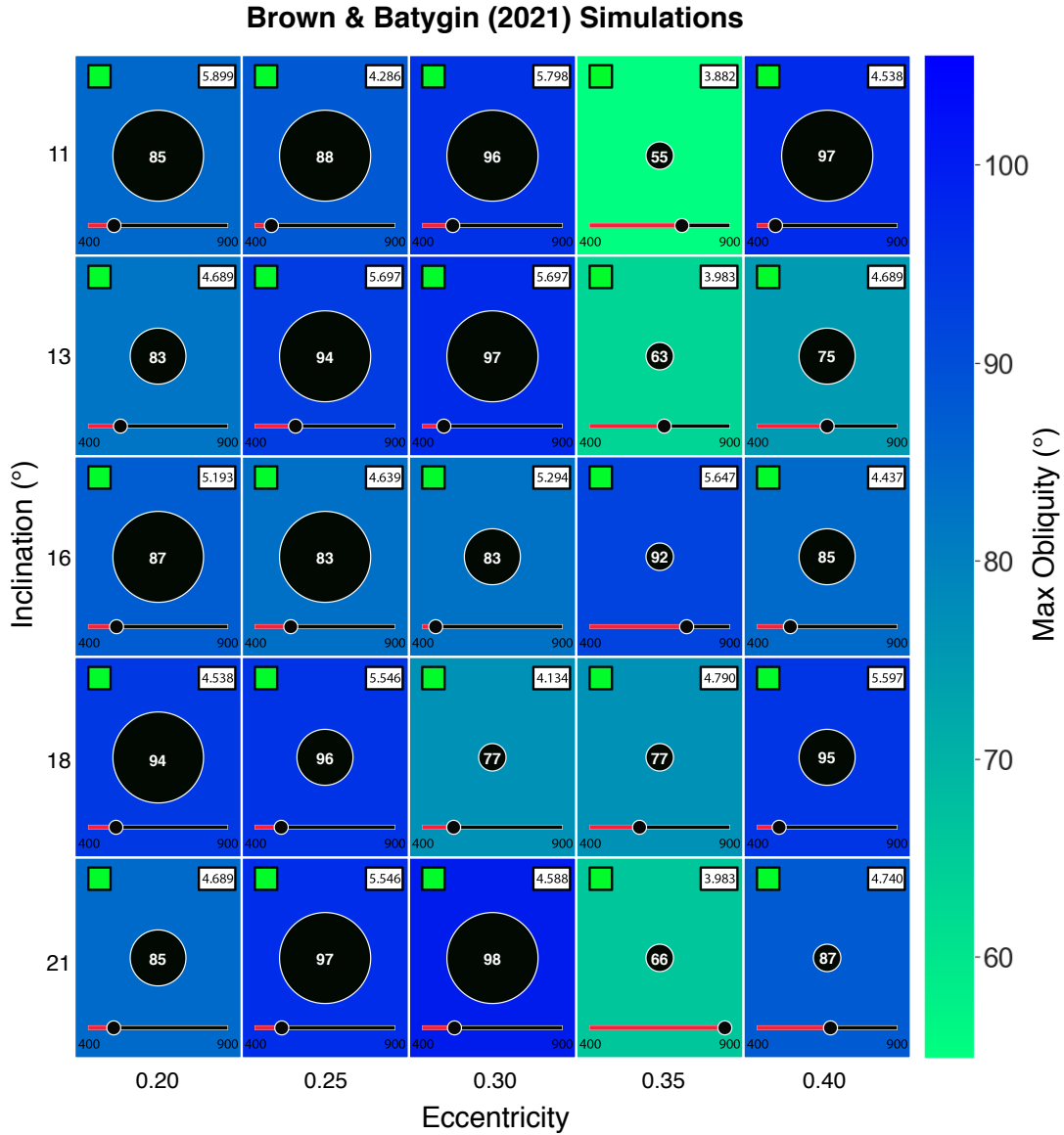


Figure 4.11. Summary of results of our most stable simulations with the updated parameters from Brown & Batygin (2021). Quantities are as described in Figure 4.8, with the exception of mass - a small central circle for $m_9 = 4.9 M_E$, a medium one for $m_9 = 6.2 M_E$, and a large one for $m_9 = 8.4 M_E$.

relevant physics are encapsulated by the diffusion coefficient (Batygin et al., 2021)

$$\mathcal{D}_a = \frac{8}{5\pi} \frac{m_p \sqrt{GM_\odot a_p}}{M_\odot} \exp\left[-\frac{1}{2}\left(\frac{q}{a_p}\right)^2\right]. \quad (4.25)$$

Here m_p, a_p are the mass and semimajor axis of the coupled planet (for a typical TNO this is Neptune - in the case of Planet 9's migration Saturn is more appropriate) and q is the perihelion of Planet Nine.

As previously mentioned Bromley & Kenyon (2016); Li & Adams (2016); Eriksen et al. (2018), the issue of Planet 9's migration is a difficult one. We have performed a suite of numerical simulations as our own brief analysis of the issue. Figure 4.12 shows the results of 400 REBOUND simulations integrated over 10 Myr. Each simulation is initialized as follows - the four giant planets in their present-day configuration, and Planet 9 initialized at 40 AU with a perihelion of 25 AU ($e_9 = 0.375$) and a random phase. No additional forces are imposed - the resulting migration of Planet 9 is fully self-consistent and arises purely from perturbations from the other planets. The shaded region of the plot represents the analytic solution of Batygin et al. (2021): in time t the expected scattering is $\pm \sqrt{\mathcal{D}_a t}$. For the vast majority of simulations, the numeric results are in good agreement with the analytic prediction. The large excursions from the norm are the cases relevant to our study: these would be the pathways resulting in a Planet 9 which would match present-day parameters. It is clear that an instability which would both match Planet 9's present-day configuration and occur on a timescale slow enough to enter secular-spin orbit resonance is very difficult to reproduce. For this reason, a fully self-consistent picture of Planet 9's migration and its effect on the Uranian spin axis is beyond the scope of this paper. We note that these large excursions need not be in conflict with Uranus' large present-day obliquity - we can imagine a scenario where Planet 9 diffuses in the "standard" smooth migration regime sufficiently long to excite Uranus' obliquity, and then subsequently enters the regime of large excursions to place it at its present-day location.

4.6 Discussion

We have computed an array of simulations spanning Planet Nine's parameter space that are capable of exciting Uranus' obliquity to very high values. From the set of simulations encompassing the most general Planet Nine parameter space from Batygin et al. (2019), 81.2% are able to reach or exceed within 10% of the present-day value of 98°. We also present an array of simulations more closely examining the parameter space given by the most recent Markov Chain Monte Carlo analysis (Brown & Batygin, 2021), and find that 40% of these simulations are

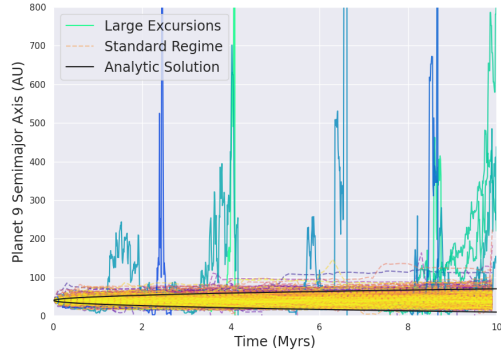


Figure 4.12. 400 self-consistent REBOUND simulations of Planet 9’s dynamical migration. Each line corresponds to one simulation - in each one, Planet 9 is initialized with a random phase. The yellow-purple lines represent pathways which do not deviate far from the expected analytic solution (in black), while the blue-green lines represent pathways which show large excursions from the mean.

able to reach within 10% of Uranus’ present day obliquity. Given our results, we conclude that it is possible to tilt Uranus over via a spin-orbit resonance mechanism driven by Planet Nine’s outward migration. The feasibility of this scenario is not as straightforward. While we are, in several cases, able to tilt Uranus to 98° , we require an axial precession rate α two orders of magnitude greater than Uranus’ present day $\alpha = 0.045 \text{ arcsec/yr}$, and a few times larger than the disk sizes favored by the hydrodynamic simulations of Szulágyi et al. (2018). We also imposed a smooth exponential migration scheme, with is not the most realistic migration pathway for Planet 9. The feasibility of our results thus depends on the probability of a more robust α enhancement, perhaps through larger circumplanetary disks (Rogoszinski & Hamilton, 2021) or a primordial moon (Boué & Laskar, 2010) - more work in assessing the potential for Uranus’ primordial precession rate, as well as Planet 9’s precise migration history, will be vital in assessing our hypothesis.

This work only considers simulations which resulted in reproducing the Solar System as it stands today, and heavily favored systems that exhibited a high degree of stability. In fact, we did produce several unstable simulations which were able to drive extremely high obliquities (up to a maximum of 134.16°), but were rejected due to a high degree of instability or even the ejection of a planet. Of course reproducing the Solar System’s current state is paramount, but instability does not necessarily preclude this possibility. In fact, the Nice model (Tsiganis et al., 2005; Gomes et al., 2005; Morbidelli et al., 2005) both reproduces the present day Solar System and predicts migration in each of the giant planets, with some models admitting the possibility of a planet’s ejection (Batygin et al., 2011). Vokrouhlický & Nesvorný (2015) have shown that the outward migration predicted by the Nice

model is consistent with Jupiter and Saturn’s present day axial tilts. [Rogoszinski & Hamilton \(2021\)](#) have taken significant strides in investigating Uranus’ obliquity evolution within the context of planetary migration (in their case, Neptune) - further work in placing Planet Nine’s migration in this greater framework has the potential to yield interesting results, both in general and applied to Uranus’ axial tilt.

The implication that planetary migration can induce high obliquity in other planets of the system is an intriguing one. Most notably, the fact that we are able to tilt Uranus to such an extent raises the question of Neptune’s 30° obliquity and if Planet Nine’s migration could be responsible as well. More broadly, obliquity plays an important role in assessing the viability of an exoplanet’s habitability, and direct measurement has proven difficult ([Shan & Li, 2018](#)). With the recent detection of a circumplanetary disk by [Benisty et al. \(2021\)](#), it seems feasible that more robust estimates of exoplanet α values may be forthcoming.

4.7 Acknowledgments

We thank Konstantin Batygin, Garrett Levine, Harrison Souchereau, Tanvi Gupta and our colleagues at the Yale Exoplanet Journal Club for useful feedback and discussions. We also thank the anonymous reviewers for helpful comments that greatly improved the manuscript. T.L would like to thank the Yale Center for Research Computing (YCRC) for valuable support and resources over the course of the project.

Chapter 5

Oblique Exorings Masquerading as a Puffy Planet

"Vision is the art of seeing things invisible."
– Jonathan Swift

Adapted From:

Lu. T., Li, G., Cassese, B. & Lin, D. 2025, The Astrophysical Journal, Volume 980, Issue 1, pp.14

Abstract

The super-puff HIP-41378 f represents a fascinating puzzle due to its anomalously low density on a far-out orbit in contrast with other known super-puffs. In this work, we explore the hypothesis that HIP-41378 f is not in fact a low-density planet, but rather hosts an opaque ring system. We analyze the dynamical history of the system, and show that convergent migration is necessary to explain the system's long-term stability. We then show that this same migration process plausibly captures HIP-41378 f into spin-orbit resonance and excites the planetary obliquity to high values. This tilts the surrounding ring and is a plausible explanation for the large transit depth. In the end, we also briefly comment on the likelihood of other super-puff planets being in high-obliquity states. We show that the existence of a tilted extensive ring around a high obliquity planet can serve as an explanation for puffy planets, particularly in multi-planetary systems at far distances from their host stars.

5.1 Introduction

In recent years, a class of planets with extremely low densities has emerged. These planets, the so-called "super-puffs" (Lee & Chiang, 2016), have masses a few times greater than Earth's and radii in excess of Neptune's, resulting in densities of $\rho < 0.3 \text{ g/cm}^{-3}$. Standard thermal evolution models (e.g. Rogers et al., 2011; Batygin & Stevenson, 2013; Lopez & Fortney, 2014) have been seriously challenged to reproduce these super-puffs, often requiring envelope mass fractions well in excess of 20% which lies in tension with standard core accretion models of planet formation.

A number of explanations have been put forth to explain these anomalous planets. Lee & Chiang (2016) posit that super-puffs form in the outskirts of the circumstellar disk where it is easier to accrete large amounts of material, and migrated to their present-day locations. Tidal inflation is another possibility – Millholland (2019); Millholland et al. (2020) demonstrated that tidal heating is sufficient to inflate planets with more standard envelope mass-fractions of 1–10%. The question of planetary inflation is perhaps best studied in hot Jupiters, where the hot Jupiter radius anomaly remains an open question (e.g. Fortney et al., 2021). While the exact mechanism responsible for this inflation is uncertain (e.g. Fabrycky et al., 2007; Batygin & Stevenson, 2010; Leconte et al., 2010; Tremblin et al., 2017), there is a clear trend linking radius inflation and effective temperature (Laughlin et al., 2011) which indicates inflation relies on the super-puff in question orbiting close-in to its host star. Most discovered super-puffs do indeed have the requisite

Planet	Mass (M_E)	Radius (R_E)	ρ (g/cm 3)	Orbital Period (days)
b	6.89 ± 0.88	2.595 ± 0.036	2.17 ± 0.28	$15.57208 \pm 2 \times 10^{-5}$
c	4.4 ± 1.1	2.727 ± 0.060	1.19 ± 0.30	$31.70603 \pm 6 \times 10^{-5}$
d	< 4.6	3.54 ± 0.06	< 0.56	$278.3618 \pm 5 \times 10^{-4}$
e	12 ± 5	4.92 ± 0.09	0.55 ± 0.23	369 ± 10
f	12 ± 3	9.2 ± 0.1	0.09 ± 0.023	$542.07975 \pm 1.4 \times 10^{-4}$

Table 5.1. Relevant physical and orbital parameters of the planets in the HIP-41378 f system, as reported in [Santerne et al. \(2019\)](#).

close-in orbit. However, this trend was broken with the discovery of the HIP-41378 system by [Vanderburg et al. \(2016\)](#). The outermost planet, HIP-41378 f, was found to be a super-puff by [Santerne et al. \(2019\)](#), and this presents an intriguing mystery. HIP-41378 f exhibits an extremely low density of $\rho \sim 0.09$ g/cm $^{-3}$ yet orbits its host star with a period of 542 days, well beyond the orbit of Earth. The relevant physical and orbital parameters of the system are provided in Table 5.1. [Belkovski et al. \(2022\)](#) showed that no reasonable interior structure consistent with standard formation theory is capable of reproducing the anomalous density of HIP-41378 f, and conclude that the planet’s low density is incompatible with the traditional methods of inflation.

Given the difficulty of creating such a low-density planet far from its host star, an appealing explanation is that the planet is not actually an extremely low density planet and only appears to be due to some obscuring effect masquerading as a large radius in the transit lightcurve. One explanation is atmospheric hazes and a dusty outflowing atmosphere ([Wang & Dai, 2019](#)). The most popular hypothesis, which we explore in this work, is the existence of an opaque planetary ring system around the planet ([Akinsanmi et al., 2020](#)). While there has to date not been a direct detection of a exoplanetary ring system, there is some evidence to support this hypothesis – [Ohno & Fortney \(2022\)](#) demonstrate that the presence of planetary rings or hazes results in a featureless transmission spectrum, which was observed by [Alam et al. \(2022\)](#). They also conclude that planetary rings are long-term stable around planets only if $T_{eq} < 300$ K, which rules out the majority of super-puffs but is consistent with HIP-41378 f’s equilibrium temperature of 294 K.

A crucial piece of the exoring hypothesis is planetary obliquity – for a ring system to be visible in the transit lightcurve the planet must have a nonzero planetary obliquity, lest the rings be viewed edge-on and therefore contribute nothing to the transit depth (e.g. [Barnes & Fortney, 2004](#)). [Saillenfest et al. \(2023\)](#) proposed a formation mechanism involving a migrating exomoon which consistently explains the planetary obliquity and formation of the ring system. [Harada et al.](#)

(2023) showed that such large moons are tidally and dynamically stable around HIP-41378 f. In this work we explore an alternative dynamical history of the HIP-41378 system. We show that the system was likely delivered to its present-day orbital configuration via convergent migration, and that excited planetary obliquity sufficient to reproduce the observed transit depth is a natural consequence of this migration. The structure of this paper is as follows. In Section 5.2 we discuss the architecture of the HIP-41378 system, and show that it is unstable unless convergent migration occurred in its past. In Section 5.3 we describe the extent and configuration of a realistic planetary ring system around HIP-41378 f, and the resulting impact on the transit lightcurve as a function of ring composition and orientation. In Section 5.4 we provide a brief background on the mechanism of secular spin-orbit resonance, and in Section 5.5 we use N -body simulations to demonstrate that such a process could have reasonably excited the obliquity of HIP-41378 f. We explore the possibility of the other super-puffs being in high-obliquity states in Section 5.6. We conclude in Section 5.7.

5.2 Architecture and Stability of the HIP-41378 System

HIP-41378 is a roughly solar-mass F-type star which hosts five transiting planets. The relevant orbital elements and physical parameters are given by Santerne et al. (2019) and reproduced in Table 5.1. We note that recently Sulis et al. (2024) targeted HIP-41378 d with CHEOPS during the predicted transit timing and did not detect a transit, which casts some doubt on the original orbital parameters put forth by Santerne et al. (2019). They propose either a misidentified period or a large transit-timing variation to explain the missing transit. We assume the second explanation for now, and proceed with the originally determined parameters.

Most significantly, the outer three planets are very closely packed. The mutual separation of multi-planet systems is commonly parameterized by the mutual Hill radius:

$$R_H = \frac{a_i + a_{i-1}}{2} \left(\frac{m_i + m_{i-1}}{3M_*} \right)^{1/3}. \quad (5.1)$$

The mutual separations between planets d , e and planets e , f are $7.6 R_H$ and $9.3 R_H$, respectively. Systems this compact are typically dynamically unstable on timescales of around 10^7 orbits, or a few Myr (e.g. Obertas et al., 2017; Gillon et al., 2017). Given the system age of 3.1 ± 0.6 Gyr (Santerne et al., 2019) it is extremely unlikely that we are observing the system in this small stable window. Indeed, we will confirm with N -body integrations that the system is naively unstable on short timescales.

One way to stabilize these compact systems is to initialize systems in resonant configurations, which can increase the stability time by orders of magnitude (Obertas et al., 2017). In the HIP-41378 system, planets b and c lie close to a 2:1 MMR while the outer three planets lie in or near a 4:3 – 3:2 resonant chain. The fact that we are able to observe HIP-41378 in its present-day configuration points the system being in a resonant architecture. While the proportion of orbital configurations consistent with a resonance are a very small fraction of the parameter space encompassed by the observational constraints, Tamayo et al. (2017) showed that slow convergent migration preferentially places planets in these resonant configurations. This process of convergent migration has been invoked to justify the long-term stability of resonant chains such as TRAPPIST-1 (Tamayo et al., 2017), TOI-1136 (Dai et al., 2023) and HD 110067 (Lammers & Winn, 2024a).

5.2.1 Formation via Convergent Migration

We use a similar stability analysis to argue that the outer three planets in the HIP-41378 system are indeed in a 4:3–3:2 resonant chain that was created via convergent migration. We first show that systems not in resonance are overwhelmingly unstable. To do so, we have run a suite of 500 N -body simulations. We consider only the outer three planets d , e and f – these are the planets most dynamically relevant to planet f , and the distance between planets c and d render the inner two planets dynamically irrelevant to the stability of the outer three. Removing the inner two planets allows us to use a significantly larger timestep in our simulations at great computational gain. We use the WHFAST (Rein & Tamayo, 2015) integrator in REBOUND (Rein & Liu, 2012). We draw all relevant orbital parameters from the posterior distributions given in Table 5.1, using $m_d = 4.6 M_{\oplus}$. We select a timestep equal to 1/15th of planet d 's orbital period, and integrate for 10^8 years. Integrations were halted if the Hill radii of any pair of planets overlapped, a common metric for a system's instability (e.g. Obertas et al., 2017; Tamayo et al., 2020b). Our results are shown in the blue curve in Figure 5.1. We see that the vast majority of systems experience rapid instability, with approximately 90% of systems going unstable within 1 Myr. Only 7 systems are stable over the full 10^8 years.

Next, we explore initial conditions consistent with migration into resonance. We follow the prescription of Tamayo et al. (2017), which has been widely adopted in the literature (e.g. Siegel & Fabrycky, 2021; MacDonald et al., 2022; Dai et al., 2023; Lammers & Winn, 2024a). Exploiting the scale-free nature of Newtonian gravity, we set the semimajor axis of planet d to $a_d = 1$ AU. We initialize planets d , e and f on circular orbits, with consecutive planets initialized 2% wide of their present-day mean-motion resonance. The planetary masses and inclinations are randomly drawn as in the previous runs. We modelled convergent migration

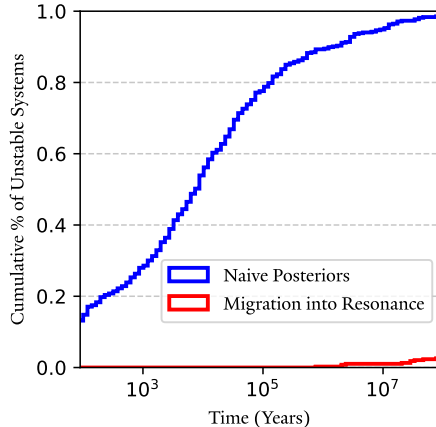


Figure 5.1. Cumulative distribution of unstable configurations of the HIP-41378 f system as a function of time. In the blue are initial configurations drawn from the posteriors reported by [Santerne et al. \(2019\)](#) and reproduced in Table 5.1. In the red are parameters consistent with resonance via convergent migration. We see that the simulations consistent with migration into resonance are overwhelmingly more stable than the naive posteriors. Given the age of the system, we consider this strong evidence that the HIP-41378 system migrated into a resonant chain.

using the `modify_orbits_forces` ([Kostov et al., 2016b](#); [Papaloizou & Larwood, 2000](#)) prescription in REBOUNDx ([Tamayo et al., 2020a](#)) as follows. Exponential semimajor axis damping was applied to planet f only with a timescale $\tau_a = 5 \times 10^6 P_d$. Eccentricity damping was applied to all planets with a timescale of $\tau_e = \tau_a/K$, where K was drawn from a log-uniform distribution $\in \{10, 10^3\}$. Each simulation was integrated for one semimajor axis damping timescale τ_a , upon which damping forces were adiabatically removed over a timescale of $5\tau_e$. We then discard any simulations that fail to lock into the desired 4:3–3:2 resonant chain. The successful simulations are rescaled such that $P_d = 278.36$ days, the present-day orbital period of planet d , and integrated for 10^8 more years. At any point, if the mutual separation between any pair of planets is less than the hill radius of the innermost planet or if any planet’s semimajor axis exceeds 3 AU, we consider the system to be unstable and halt the simulation.

We ran 500 migration simulations. 51 went unstable during the migration phase, and 1 failed to lock into the correct resonant chain. The remaining 448 simulations are shown in the red line in Figure 5.1. The initial conditions consistent with migration into the resonant chain are significantly more stable – 97% are stable over the full 10^8 years. Thus, the present-day stability of the system is strong evidence that the HIP-41378 system experienced convergent migration in its primordial history to arrive at the present-day resonant chain.

5.3 Transiting Planetary Rings

In this section we discuss how an opaque planetary ring system imprints on the transit lightcurve, as a function of its orientation and extent. We show that a realistic ring system around HIP-41378 f is capable of reproducing its transit depth, and in many cases can be detected in transit ingress/egress with the capabilities of JWST.

5.3.1 Ring Extent

The outer extent of a planetary ring system is governed by the Roche Radius ([Murray & Dermott, 2000](#); [Schlichting & Chang, 2011](#); [Piro & Vissapragada, 2020](#)):

$$R_{\text{Roche}} = 2.45 \left(\frac{3m_p}{4\pi\rho_{\text{ring}}} \right)^{1/3} \quad (5.2)$$

beyond this radius, debris which would make up a ring system will instead coalesce into a moon. The primary degree of freedom in this expression is ρ_{ring} , the density of the ring particles. Assuming zero albedo and full heat redistribution the equilibrium temperature of HIP-41378 f is 294 K ([Santerne et al., 2019](#)), which is in excess of the melting point of water ice. The rings around HIP-41378 f therefore must be rocky in composition.

Estimating a minimum reasonable density for rocky ring particles thus provides a corresponding maximum ring extent. To inform this lower limit we use the work of [Babadzhanov & Kokhirova \(2009\)](#), who find $\rho \sim 0.4 \text{ g/cm}^3$ for the most porous meteorites. Plugging in the most optimistic mass estimate for HIP-41378 f $m_f = 15 M_E$ and this fiducial lower limit into Equation (5.2), we see that HIP-41378 f is in principle capable of hosting rings that extend over $14 R_E$, well exceeding the implied $R_f = 9.2 R_E$ from the transit observations. Thus, it is in principle possible for HIP-41378 f to support a ring system large enough to reproduce the anomalous transit depth observed by [Santerne et al. \(2019\)](#). This is of course assuming the lowest possible ring particle density and the most optimistic ring configuration of directly face-on.

5.3.2 Ring Orientation

We consider now how the orientation of the ring affects the transit depth. The orbital dynamics of planetary satellites/ring particles is governed by the interplay between the solar tide and the oblateness of the host planet. In the presence of dissipation, satellites, ring particles and circumplanetary disks will damp to the

Laplace surface, with characteristic length (Tremaine et al., 2009):

$$R_L^5 = J_2 R_p^2 a_p^3 (1 - e_p^2)^{3/2} \frac{m_p}{M_*} \quad (5.3)$$

where J_2 is the quadrupole gravitational harmonic, R_p the planet's radius, a_p, e_p the semimajor axis and eccentricity of the planet's orbit around the host star, and M_* the mass of the host star. The orbital inclination of a satellite i , or the angle between the satellite's orbit normal and the planet's spin axis, is given (Tremaine et al., 2009):

$$\tan 2i = \frac{\sin 2\theta}{1 - 2R_L^5/a^5} \quad (5.4)$$

where a is the semimajor axis of the satellite's orbit about the planet, and θ is the planetary obliquity defined as the misalignment between the planet's orbit normal and its spin axis. Inspection of Equation (5.4) reveals that broadly speaking, the dynamics of a satellite or ring particle orbiting with $a < R_L$ will be dominated by the oblateness of the planet and be coupled to the planet's spin axis. Conversely, the dynamics of a satellite orbiting with $a > R_L$ is dominated by contributions from the host star and will be coupled to the planet's orbital axis. This results in a warped profile for disks that extend past R_L . Dynamics of the Laplace surface have been studied in depth by many authors (e.g. Zanazzi & Lai, 2017; Speedie & Zanazzi, 2020; Farhat & Touma, 2021).

These dynamics are significant for close-in planets, but not HIP-41378 f. For all reasonable values of J_2, R_p and ρ_{ring} , $R_L \gg R_{\text{Roche}}$, meaning the disk does not extend to the Laplace radius. Hence, to a very good approximation a putative ring system around HIP-41378 f would be completely coupled to its equator. The orientation of the ring system is thus defined completely by the planet's spin vector. The unit spin vector of the planet can be described with two angles: the obliquity θ defined previously, and the phase angle ϕ defined as the projection between the planet's spin axis projected onto the plane of the orbit, and the ascending node of the orbit.

5.3.3 Transit Depth

Consider the standard coordinate system where the z -axis points along the line of sight to the system, and the x -axis is aligned with the planet's ascending node. The area circumscribed by the outer edge of the ring seen in this frame is its projected

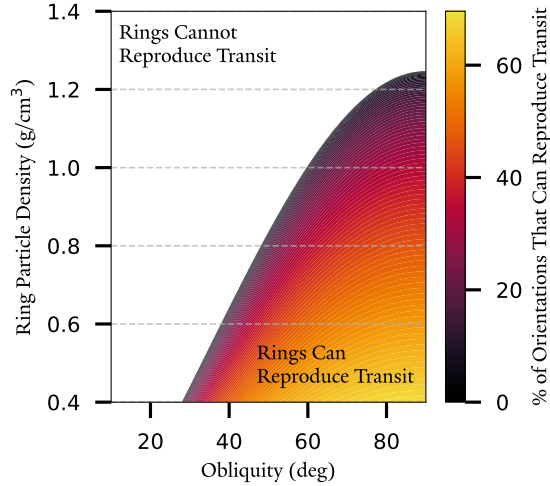


Figure 5.2. Fraction of ϕ ring orientations capable of reproducing the transit depth of HIP-41378 f as a function of planetary obliquity and ring particle density. The white area are areas of parameter space where rings cannot reproduce the transit depth observed even with the most optimistic configuration with $\phi = 0$.

area in the xy plane, and is given:

$$\begin{aligned} A_{\text{ring}} &= R_{\text{Roche}}^2 \pi \cos \phi \sin \theta \\ &= \left[2.45 \left(\frac{3m_p}{4\pi\rho_{\text{ring}}} \right)^{1/3} \right]^2 \pi \cos \phi \sin \theta \end{aligned} \quad (5.5)$$

For a given θ and ϕ , the transit extent of the ring varies inversely with ring particle density. Figure 5.2 shows, for a given planetary obliquity and ring particle density, the ring orientation necessary to reproduce the observed transit depth of HIP-41378 f. The white regions represent areas of parameter space where even for the most optimistic face-on configuration, rings are insufficient. The darkest areas of the colored contours represent the regime where a nearly face-on ring is required, and this orientation requirement is relaxed for lighter colors. We see that there is a plentiful region of parameter space where rings indeed are sufficient to reproduce the transit depth.

5.3.4 Detection in ingress/egress

Detection of planetary rings is in principle observable through various avenues, but mostly notably in artifacts during transit ingress/egress that differ from a purely spherical planet (Barnes & Fortney, 2004; Aizawa et al., 2018; Akinsanmi et al., 2018; Piro & Vissapragada, 2020). This is very similar to the procedure used

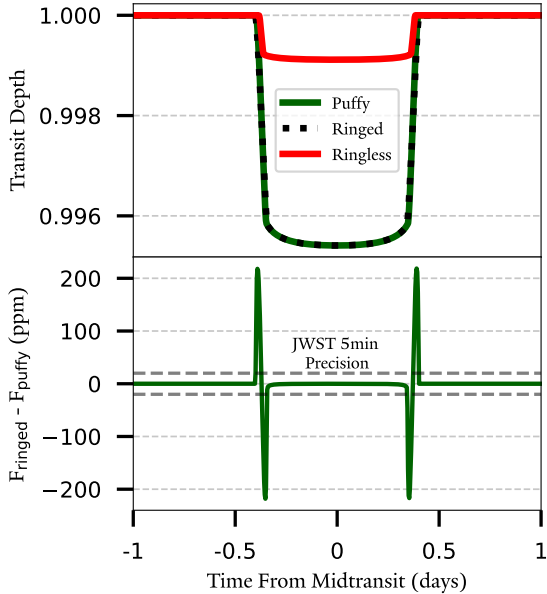


Figure 5.3. Comparison of transit lightcurves of a flat planet and a planet with an inclined ring system with identical transit depths. The ring system is modelled with $\theta = 45^\circ$, $\phi = 20^\circ$, and $R_{\text{Roche}} = 11.29 R_E$. We see that there are large deviations in ingress/egress in which a ringed system can be differentiated from a spherical planet.

to measure planetary oblateness (Seager & Hui, 2002; Barnes & Fortney, 2003; Zhu et al., 2014; Akinsanmi et al., 2024; Cassese et al., 2024a). While to date no planetary ring systems have been confirmed via this method, with the advent of JWST these measurements are imminently possible. In this subsection, we briefly demonstrate the feasibility of this method.

Figure 5.3 demonstrates the feasibility of detecting realistic ring systems around HIP-41378 f via transit ingress/egress. We use `squishyplanet` (Cassese et al., 2024a) to generate three simple transit lightcurves, which are shown in the top panel. All three lightcurves are generated assuming a circular orbit at $a = 1.37$ AU and quadratic limb darkening parameters $u_1 = 0.0678, u_2 = 0.118$. These system-specific coefficients were derived using the `ExoTIC-LD` package (Grant & Wakeford, 2024), the stellar atmosphere grids from Magic et al. (2015), and assume observations are collected in the JWST NIRSpec's G395H/F290LP bandpass. The planets are assumed to transit with an impact parameter of $b = 0$. We simulate a perfectly spherical planet with the implied measured radius of $r_f = 9.2 R_E$ (labelled "Puffy"), as well as a ring system with $\theta = 45^\circ$, $\phi = 20^\circ$ and $R_{\text{Roche}} = 11.29 R_E$ (labelled "Ringed") which requires a ring particle density of $\rho = 0.68 \text{ g/cm}^3$. The simulated ring system and planet have the same projected area, and at the scale of the first subplot the two curves appear identical. Finally, we also simulate a more

realistic spherical HIP-41378 f with a density of 1 g/cm^3 – this corresponds to a radius of $4.04 R_E$, and is labelled "Ringless". Note the large enhancement in transit depth achieved by a realistic ring system. The lower panel shows the difference in flux between the "Ringed" lightcurve and the "Puffy" lightcurve in ppm. Clear deviations in transit ingress/egress are visible. A simple estimate using PandExo (Batalha et al., 2017) suggests that JWST's NIRSpec instrument, while operating in its BOTS mode with the G395H grating + F290LP filter, is capable measuring the white light flux with a precision of $< 20 \text{ ppm/hour}$, which is in principle more than sufficient to detect this deviation and hence differentiate a ringed planet from a puffy planet with equivalent surface area.

We emphasize that these simple comparisons are designed only to demonstrate the feasibility of detecting ring systems. More detailed analysis exists elsewhere in the literature, accounting for factors such as scattered and reflected light as well (e.g. Barnes & Fortney, 2004; Sucerquia et al., 2020; Zuluaga et al., 2022). Our model does not account for these factors, nor the gap between the inner edge of the ring system and the outline of the planet. As the primary purpose of this work is to investigate the dynamics of the system, we do not extensively investigate the observational consequences.

5.4 Secular Spin-Orbit Resonance

Secular spin-orbit resonance is a well-studied phenomenon that has been shown to be a plausible origin for the nonzero obliquities of solar system bodies and exoplanets alike. In brief, a planet's obliquity (the angle between its spin axis and orbit normal) may be excited to high values if there is a near match between the precession rates of its spin axis and orbit normal.

Many examples of spin-orbit resonance are present in the solar system. Our moon is perhaps the most prominent example - its 6.68° obliquity arises as a consequence of a near match between its orbital and spin precession rates (Colombo, 1966; Peale, 1969; Touma & Wisdom, 1998). In more complex systems such as the solar system, this coupling can occur between the the precession of the spin axis and any of the fundamental frequencies contributing to the nodal precession of the orbit. This has implications for the chaotic obliquity variations of the inner planets (Ward, 1973; Touma & Wisdom, 1993; Laskar & Robutel, 1993; Zeebe, 2022; Zeebe & Lantink, 2024) as well as the 3° degree obliquity of Jupiter (Ward & Canup, 2006) and the large 89° degree obliquity of Uranus (Boué & Laskar, 2010; Millholland & Batygin, 2019; Rogoszinski & Hamilton, 2020, 2021; Lu & Laughlin, 2022; Saillenfest et al., 2022). The most well-studied and accepted case of spin-orbit resonance in our solar system is Saturn, whose 26° obliquity is almost certainly due to a near

match with a nodal frequency dominated by Neptune (Ward & Hamilton, 2004; Hamilton & Ward, 2004; Saillenfest et al., 2021a,b; Wisdom et al., 2022).

Naturally exoplanet obliquities are significantly more difficult to detect, though progress has been made on this front - see Bryan et al. (2018); Bryan et al. (2020, 2021); Poon et al. (2024a,b). However, there exists a wealth of theoretical literature suggesting that significant exoplanetary obliquities may be common via spin-orbit resonances (e.g. Shan & Li, 2018; Millholland & Batygin, 2019; Quarles et al., 2019; Su & Lai, 2020; Li, 2021; Su & Lai, 2022; Su & Lai, 2022a; Chen et al., 2023; Millholland et al., 2024). In this section, we will describe in detail the theory behind secular spin-orbit resonance.

5.4.1 Spin Axis Precession

In the presence of torques from the host star, a planet's spin axis will precess about its orbit normal. The period of precession is given (Goldreich, 1965):

$$T_\alpha = \frac{2\pi}{\alpha \cos \theta} \quad (5.6)$$

where θ is the planetary obliquity, and is defined by the angle between the planet's orbit normal and its spin axis. The precession rate is defined by α , which is primarily a function of the physical parameters the characterize the planet (Ward & Hamilton, 2004; Millholland & Batygin, 2019)

$$\alpha = \frac{3n^2 J_2}{2\Omega C} = \frac{1}{2} \frac{M_*}{m_p} \left(\frac{R_p}{a} \right)^3 \frac{k_2}{C} \Omega \quad (5.7)$$

where M_* , m_p are the masses of the star and planet respectively, n is the orbital mean motion, Ω the planet's spin frequency, J_2 the quadrupole strength of the gravitational field, R_p the planetary radius, a the semimajor axis, k_2 the tidal Love number, and C the moment of inertia normalized by $m_p R_p^2$. This precession frequency can be enhanced significantly by the presence of a circumplanetary disk (Millholland & Batygin, 2019) or a moon (Saillenfest et al., 2022; Wisdom et al., 2022).

5.4.2 Nodal Precession

In the presence of torques from the other planets in the system, the planet's orbit normal will precess about the total angular momentum of the system, or the invariant plane normal. The period of nodal precession is given by

$$T_g = \frac{2\pi}{|g|} \quad (5.8)$$

where g is the rate of change of the planet's longitude of ascending node. The dynamics governing the rate of nodal precession in a multi-planet system is quite complex and in most cases analysis is performed numerically. However, first-order conclusions and intuition can be drawn from Laplace-Lagrange secular theory (Lagrange, 1778; Laplace, 1784; Laskar, 2013; Murray & Dermott, 2000). At this level of approximation, the time evolution of the inclination I and ascending node Ω of a planet can be calculated as sum of sinusoidal contributions (Murray & Dermott, 2000; Ward & Hamilton, 2004):

$$\begin{aligned}\sin \frac{I}{2} \sin \Omega &= \sum_j \frac{I_j}{2} \sin(g_j t + \delta_j) \\ \sin \frac{I}{2} \cos \Omega &= \sum_j \frac{I_j}{2} \cos(g_j t + \delta_j)\end{aligned}\tag{5.9}$$

where I_j, g_j, δ_j are secular amplitudes, frequencies and phases that depend on the orbital architecture of the system. In a given system there may be many such terms, but for a system with N planets there are typically N large-amplitude terms that end up being significant to the dynamics of the system, with each term dominated – but not necessarily solely associated with – one of the planets. Mean motion resonances complicate this picture slightly, but an analytic solution is in principle still possible (e.g. Wisdom, 1985; Malhotra et al., 1989; Hadden & Tamayo, 2022). However, in practice these frequencies are often found numerically (e.g. Shan & Li, 2018; Millholland et al., 2024).

5.4.3 Cassini States and Resonance Capture

Cassini States are equilibrium configurations of the spin axis (Colombo, 1966; Peale, 1969; Ward & Hamilton, 2004; Fabrycky et al., 2007; Su & Lai, 2020). They correspond to configurations in which the system's invariant plane normal \hat{k} , the planet's orbit normal \hat{n} , and the planet's spin axis $\hat{\Omega}$ are coplanar, and $\hat{\Omega}$ and \hat{n} precess about \hat{k} at the same rate. Hence, in a coordinate frame centered on \hat{n} rotating with angular velocity g the Cassini States appear stationary. Defining the planetary obliquity θ as the angle between \hat{n} and $\hat{\Omega}$, the Cassini State obliquities may be expressed as a function of the ratio α/g :

$$\alpha/g \cos \theta \sin \theta + \sin(\theta - I) = 0\tag{5.10}$$

where I is the orbital inclination relative to the invariant plane, or the angle between \hat{n} and \hat{k} . There are in general 4 equilibrium solutions, but only Cassini State 2 is

characterized by high θ , which is seen for $\alpha/g > 1$.

Through linearization of the equations of motion that govern the spin axis (e.g. Ward, 1974, 1979), it can be shown that if $\alpha \cos \theta \sim |g_i|$ for some i , the amplitude of the forcing associated with this frequency grows very large and the dynamics of the spin axis are well-approximated by setting $g \sim g_i$. Hence, there exists a high-obliquity Cassini state equilibrium if there is a near match between $\alpha \cos \theta$ and any of the fundamental frequencies g_i .

Gaseous planets such as HIP-41378 f are naively expected to form with $\theta \sim 0$ as they accrete gas from the circumstellar disk. Hence, the existence of a high-obliquity equilibrium state is insufficient – there must be a mechanism to reach it. Capture into spin-orbit resonance is one such mechanism, and occurs when the ratio α/g evolves through unity from below. If this evolution is slow enough to satisfy the adiabatic criterion – that is, if the timescale of evolution is slow in comparison to the timescale of the spin-axis libration – phase-space volume will be conserved as the ratio α/g evolves. Hence, a trajectory that starts near Cassini State 2 will remain close to it as the equilibrium point grows in obliquity, and hence the spin vector itself will be excited to high obliquity. This slow change in α/g can be plausibly generated by both evolution in α (e.g. Rogoszinski & Hamilton, 2020; Saillenfest et al., 2020, 2021b,a; Wisdom et al., 2022; Saillenfest et al., 2023) or g (e.g. Millholland & Laughlin, 2019; Millholland & Batygin, 2019; Lu & Laughlin, 2022; Millholland et al., 2024).

5.5 The Obliquity of HIP-41378f

For a high-obliquity Cassini State 2 to exist for HIP 41378 f, there must be a near match between the spin axis precession rate α and one of the components of the nodal recession g_i . In this section, we first assess the likelihood of HIP-41378f presently being in a high-obliquity Cassini State. We then present a migration-driven resonance capture scenario that can plausibly excite the planetary obliquity of HIP-41378 f, and verify with N -body simulations.

5.5.1 Spin Equilibria

We first obtain the g_i frequencies of the present-day system numerically, following the procedure enumerated in Shan & Li (2018). First we construct a time-series of the orbital inclination modulated by the longitude of ascending node of planet f, $i(t)e^{\sqrt{-1}\Omega(t)}$. The initial conditions of these simulations are drawn from the set of configurations consistent with convergent migration, from Section 5.2.1. For each simulation we integrate for 3×10^6 years, recording outputs every 10 years. We then perform a Fourier Transform on the resulting time-series data, which is

displayed in black dots in the top panel of Figure 5.4. While in principle the Fourier spectrum depends on the precise orbital configuration of the system and as such will be different for each draw of the system due to the observational uncertainties, in practice these uncertainties are small enough that they do not significantly affect the power spectrum. We have marked each peak of the Fourier spectrum which exceeds an amplitude of unity with red Xs. These are taken to be the fundamental g frequencies of the present-day system. We observe 3 high-amplitude peaks.

While the nodal recession can be calculated from precise constraints on the orbital architecture, many of the physical parameters necessary to calculate the spin axis precession rate are entirely unconstrained. Thus we use the solar system bodies as fiducial estimates for α , which are plotted in the dashed colored lines in Figure 5.4. The blue and golden dashed lines represent α for an HIP-41378 f at the present-day semimajor axis of $a_f = 1.37$ AU and $C = 0.25$ with Neptune-like and Saturn-like rotation and J_2 . We see that there is a near-match with highest amplitude peak of the Fourier spectrum with $g_{\text{peak}} = 3.8 \times 10^{-4}$ rad/year for the Saturn-like case, implying an high-obliquity spin equilibrium exists if HIP-41378 f is around or slightly more oblate than Saturn (the most oblate planet in our solar system). To achieve a near-match with the other two other fundamental frequencies unrealistic values of α are required. For the low-frequency peak we require a J_2 equal to 1/5th of Neptune's while a match with the high-frequency peak requires a J_2 equal to 3× Saturn's.

5.5.2 Migration-Driven Frequency Evolution

We next explore the possibility of migration-driven evolution of the precession rates α and g exciting a spin-orbit resonance. We again emphasize the need for the ratio α/g to evolve through unity from below. The bottom subplot of Figure 5.4 depicts an example of the evolution of precession rates under the influence of planetary migration. Due to the nature of the Fourier transformation used to analyze the g frequencies it is impossible to fully track the time-evolution of the g power spectrum through the course of migration. Instead, we take a pre-migration snapshot and a post-migration snapshot of the power spectrum, which is sufficient to show the general evolution trend. The post-migration power spectrum is shown in the black dots, and is identical to the upper subplot. The pre-migration power spectrum is plotted in gray, and is analyzed from a system where planets b and c are initialized in their present-day orbits, planet d at $a_d = 2.9$ AU (approximately 3.3x its present-day semimajor axis), and planets e and f two percent wide of their respective present-day mean-motion resonances. Planets d , e and f are initialized with circular orbits and mutual inclinations drawn from a Rayleigh distribution centered on 0.5° . In contrast to the upper subplot, the x -axis

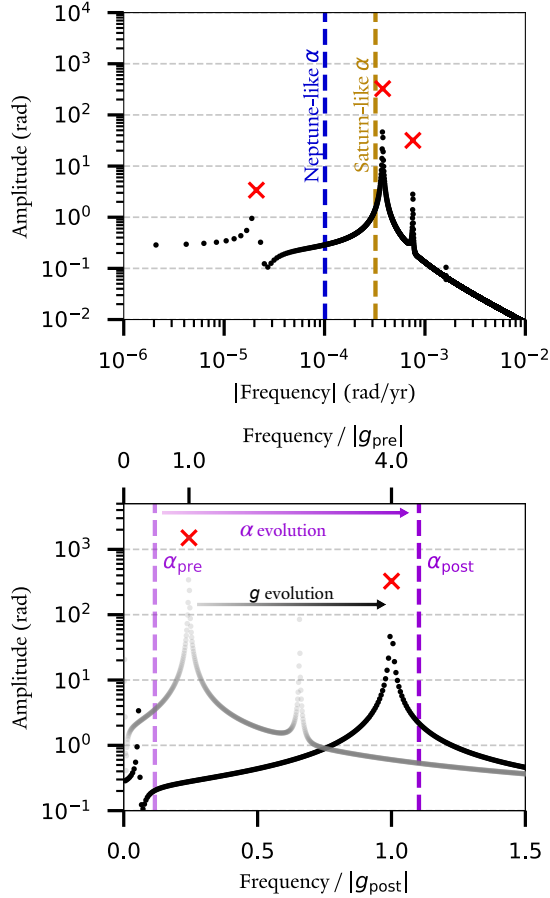


Figure 5.4. Analysis of precession rates in the HIP-41378 system, showing that capture into secular spin-orbit resonance is possible for reasonable parameters. The upper subplot shows the present-day power spectrum of the nodal recession of HIP-41378 f in black, with the peaks marked with red Xs. The spin-axis precession rates of a Neptune-like and Saturn-like planet are plotted in the vertical dashed lines, and we see that there is a near-match between the highest-amplitude peak of the nodal recession power spectrum and the Saturn-like spin axis precession rate. The lower panel shows also shows a power spectrum of a fiducial pre-migration system in the gray dots, as well as the spin-axis precession of a Saturn-like planet with slightly enhanced oblateness both pre- and post-migration in the purple vertical dashed lines. We see that $|\alpha/g|$ evolves from below unity pre-migration to above post-migration, satisfying the criteria for resonance capture and subsequent high planetary obliquity.

is now a linear scale and we zoom in near the location of the highest-amplitude peaks. The peak we consider has been marked with a red x. The x -axis has also been relabelled for convenience – the bottom labels are in units of the post-migration peak $g_{\text{post}} = 3.8 \times 10^{-4}$ rad/year, and the upper labels are in units of the pre-migration peak $g_{\text{pre}} = 9.3 \times 10^{-5}$. We see that convergent migration acts to shift the entire power spectrum towards the right, corresponding to faster nodal precession.

We also analyze the evolution of the spin axis precession rate. We consider a planet with the best-fit value for HIP-41378 f's mass $m_f = 12m_E$, dimensionless moment of inertia $C = 0.25$. We consider a relatively oblate planet with Saturn-like spin and slightly enhanced $J_2 = 1.3 J_{2,\text{Saturn}}$. This value is selected as a reasonable illustrative example as to achieve $|\alpha_{\text{post}}/g| > 1$. The pre-migration spin axis precession rate is plotted with a dotted light purple line, and the post-migration precession rate with a dotted dark purple line. Inward migration similarly pushes the spin axis precession rate to faster values. Due to the strong dependence on semimajor axis evident from inspection of Equation (5.7), the increase in precession rate is even stronger than the corresponding increase in nodal precession rate. Hence, we see that $|\alpha_{\text{pre}}/g_{\text{pre}}| < 1$ and $|\alpha_{\text{post}}/g_{\text{post}}| > 1$, satisfying the resonance capture criteria so long as migration is slow enough.

We conclude this subsection by arguing that assuming a reasonable set of physical parameters for HIP-41378 f, convergent migration is capable of capturing the planet into secular spin-orbit resonance and exciting its planetary obliquity. Hence, migration serves to simultaneously stabilize the system over Gyr timescales as discussed in Section 5.2.1, and drive the precession frequency evolution necessary to generate the high planetary obliquity needed to reproduce HIP-41378 f's anomalous transit depth with a ring system.

5.5.3 Migration Simulations

We now present a suite of 300 full N -body simulations investigating a high obliquity for HIP 41378 f caused by a spin-orbit resonance generated from primordial convergent migration, accounting for migration and self-consistent spin axis evolution. As mentioned in Section 5.2.1, the present-day stability of the system heavily implies primordial convergent migration into a resonant chain. We will show in this section that this migration serves as a natural mechanism to evolve the ratio α/g to induce spin-orbit resonance and excite a high obliquity.

The setup of our simulations closely follows that of Millholland et al. (2024). We initialize the systems in the pre-migration configurations enumerated in Section 5.5.1. We use the WHFAST integrator (Rein & Tamayo, 2015) and use a timestep equal to 1/10th of the orbital period of the innermost planet. We simulated conver-

gent migration with the `modify_orbits_forces` prescription in REBOUNDx (Tamayo et al., 2020a). In contrast to our stability simulations, we adopt a more realistic prescription used by Delisle (2017); Millholland et al. (2024). In this prescription, all three outer planets experience semimajor axis damping. The timescale of this damping for the i th planet is given

$$\tau_{a,i} = \tau_0 a_i^\beta \quad (5.11)$$

where $\tau_0 = 1 \times 10^8$ and $\beta = -1.7$. This timescale was selected by slowly increasing until the migration was slow enough to reliably capture planet f into spin-orbit resonance – as long as the migration timescale exceeds the spin-axis libration timescale the specific choice of migration timescale does not significantly impact our simulations. All three planets also experience eccentricity damping on a timescale $\tau_{e,i} = \tau_{a,i}/100$. The simulation is integrated until planet d reaches its present-day semimajor axis of $a_d = 0.88$ AU. At this point, all migration forces are turned off and we integrate for an additional 3 Myr before halting the simulation.

We account for self-consistent spin and dynamical evolution using the prescription of Eggleton et al. (1998) and Mardling & Lin (2002), implemented by Lu et al. (2023) in REBOUNDx. We endow planet f with structure and approximate the other four planets as point particles. The relevant additional parameters needed to describe the spin evolution of the planet are the initial direction and magnitude of the spin axis Ω_f , the radius of the planet r_f , the tidal Love number k_2 , and the dimensionless moment of inertia C. Note that tides are not expected to be important for the spin-axis evolution of this planet, so we do not include their effects in the interest of minimizing computation time. We vary the density of HIP-41378 f from $\rho_f \in \{0.7, 1.5\}$ g/cm³ and $J_2 \in \{4.75 \times 10^{-3}, 7.86 \times 10^{-1}\}$ – for comparison, Saturn’s J_2 moment is 1.65×10^{-2} , so our simulations range from 30% to 48x Saturn’s J_2 moment. The upper bound is unphysically high – a more physically reasonable upper bound would be $J_2 \sim 0.3$ (e.g. Wahl et al., 2021). We choose this unrealistically high upper bound to show that even for planets with extremely quick spin precession rates the spin-orbit resonance can be entered. This will be important for Section 5.5.4, when we discuss sources of α (e.g., due to a massive moon) enhancement that can mimic an unphysically oblate planet. These initial conditions are somewhat arbitrarily selected, but are designed to more than encompass a range of realistic physical parameters that would result in a near-match with the high-amplitude frequency peak identified in Section 5.5.1.

Figure 5.5 shows one of our simulations in detail. This simulation is initialized with $J_2 = 0.06641$ and $\Omega_f = 5$ hours. All three planets migrate inward and are caught into their respective mean-motion resonances at around $t \sim 1$ Myr, at which point they migrate inward in lockstep. At around $t = 8$ Myr, the spin-orbit

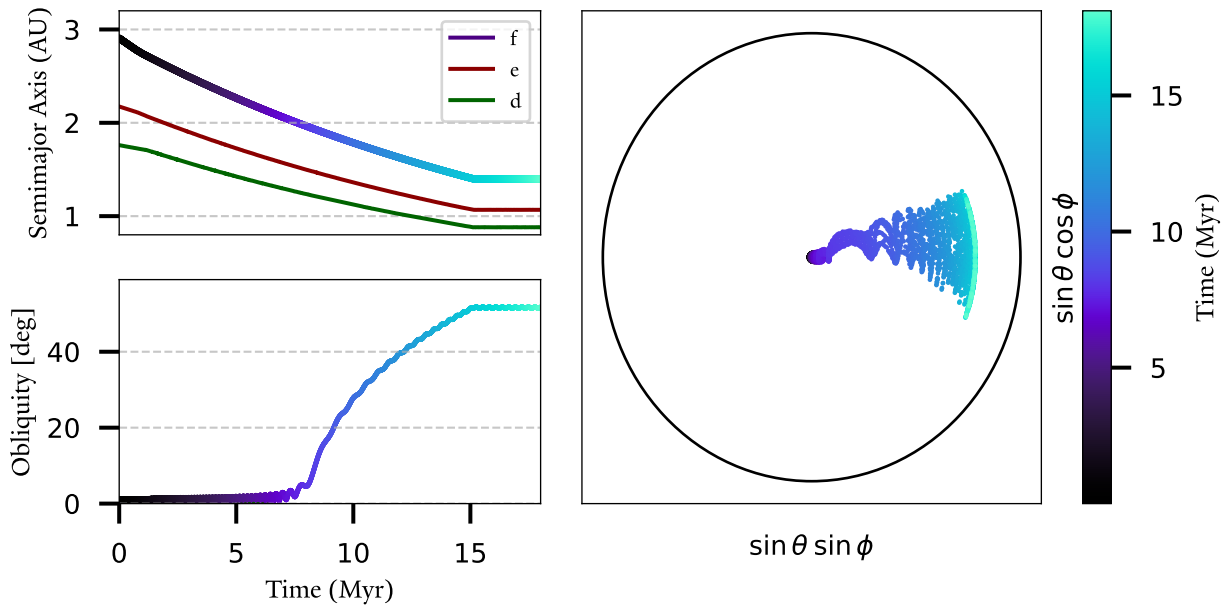


Figure 5.5. A fiducial case of the dynamical evolution of the HIP-41378 system, which leads to secular spin-orbit resonance and high planetary obliquity. The upper-left subplot shows convergent migration of the three outer planets. Each is initialized just wide of their present-day mean-motion resonances and are quickly caught into them, and migrate inward in lockstep afterwards. At around $t\sim 15$ Myr, we turn the migration force off. The bottom left plot shows the planetary obliquity evolution of HIP-41378 f. At around $t\sim 8$ Myr, the spin-orbit resonance is entered and the planetary obliquity is steadily excited until migration is turned off. The obliquity is stable at 52° . The right hand plot shows a polar view of the evolution of the planetary spin axis in a frame that precesses with the planet's orbit. The distinctive banana-like librations of capture into a Cassini State are visible.

resonance is reached and the planetary obliquity slowly grows until the migration is halted at $t \sim 15$ Myr, at which point it remains stable with small oscillations due to libration around the fixed point at around 50° .

We also report results from our entire ensemble of simulations, shown in Figure 5.6. We plot the final obliquity of planet f against its final J_2 moment for each simulation. We also ran similar suites of simulations slightly varying mutual inclination and migration speed, with no significant differences – the final planetary obliquity is mostly sensitive to the J_2 moment of HIP-41378 f. Note that the planet's spin rate does not meaningfully evolve over the course of the simulations, so this J_2 is essentially the primordial value. For reference, we have also plotted the obliquities and J_2 moments of the solar system giant planets. As predicted from our frequency analysis, starting at J_2 slightly higher than Saturn's HIP-41378 f is able enter the spin-orbit resonance and excite high planetary obliquity. The range in J_2 for capture into the spin-orbit resonance is approximately Saturn's J_2 to around 20x Saturn's J_2 – planets that are more or less oblate than this range fail to lock into the relevant frequency peak. Not all of our simulations in this range are able to attain high obliquity, which we attribute to the probabilistic nature of resonance capture (Su & Lai, 2022). The plot is color-coded with the ring particle density needed to generate a ring system with sufficient extent to reproduce the observed transit depth, assuming an orientation with ($\phi = 0$) and the final planetary obliquity. Points in black are unable to host ring systems with sufficient extent without resorting to ring particles more porous than the fiducial limit we discussed in Section 5.3.1, while the colored points are capable and heavily populate the region of J_2 parameter space where spin-orbit resonance is achieved.

Our results indicate that there is a large region of reasonable parameter space in which the convergent migration process can be expected to generate a high enough planetary obliquity in HIP-41378 f to sufficiently warp an opaque ring system out of the orbital plane to masquerade as an unusually puffy planet. We predict that if HIP-41378 f is at least as effectively oblate as Saturn then high planetary obliquities can very reasonably be attained. This assumption is not a given, but is not unrealistic. We briefly enumerate some caveats and limitations of our study. First, the evolution of planetary structure over the course of the simulation is not considered (e.g. Lu et al., 2024a). The most significant effect overlooked is the evolution of the planetary spin rate, which is not dynamically impacted by the migration process and thus remains constant in our simulations. However, as gas giant planets accrete from the circumstellar disk their spin rates are expected to form near their breakup spin rates, and then magnetohydrodynamical effects work to expel angular momentum from the system and drive the spin rates to the significantly sub-critical values we observe in the giant planets of our solar system (Batygin, 2018). This does not change the limits on the range of viable planetary

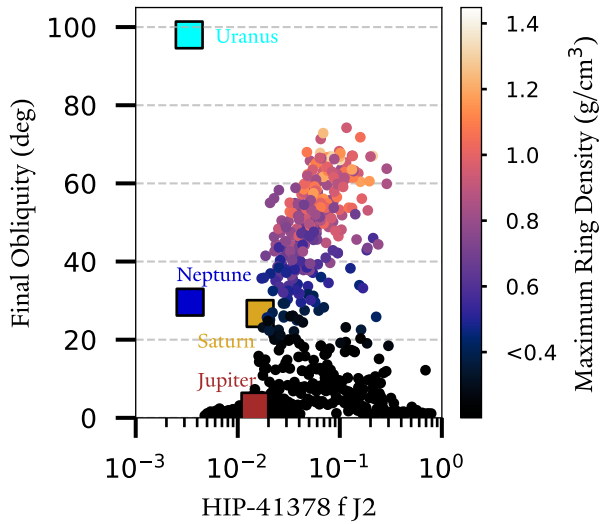


Figure 5.6. Population-level statistics of our migration simulations, plotting final planetary obliquity vs the J_2 moment of planet f. The colorbar represents the density of ring particles needed to generate a large enough ring consistent with the observed transit depth for the given final obliquity, assuming the most optimistic face-in geometry. The black points are incapable of generating the observed transit. For reference the obliquities and J_2 moments of the solar system giant planets are also plotted. We see that starting from simulations run with Saturn's J_2 , planetary obliquities capable of hosting a ring system that generates HIP-41378 f's transit profile are possible.

J_2 s that can excite obliquity, however – this limit is set by a match between the spin axis precession rate and the present-day orbital frequencies, the latter of which is well-constrained from the orbital solutions. We also did not explore a wide range of initial migration configurations, opting to arbitrarily initialize the planets at roughly twice their present-day orbits. If the migration process is significantly shorter than this, it will be more difficult to induce the requisite $|\alpha/g|$ crossing as the frequencies will evolve less. The initial formation locations of these planets are unconstrained. Finally, in our simulations we did not consider the effect of the ring on the dynamics of the spin axis itself. The only effect the ring is expected to have is a minute enhancement in α , which would be far outweighed by the uncertainties in the physical parameters of the planet.

5.5.4 The Effect of a Massive Moon

Our population-level results in Figure 5.6 predict high obliquities if a certain J_2 threshold is achieved. We have discussed J_2 thus far in the context of planetary oblateness only, but there are in fact many ways to increase the effective J_2 of the planet. One reasonable way is to include the effect of a massive moon, which were shown to be tidally stable around HIP-41378 f by [Harada et al. \(2023\)](#). In this subsection we briefly describe how a massive moon could function as a form of precession enhancement, which would allow less oblate Neptune-like planets to be caught into spin-orbit resonance.

We wish to investigate the effect a massive satellite has on the rate of spin-axis precession, given by Equation (5.7). There are two effects to consider: there are enhancements in J_2 moment and the normalized moment of inertia C . These can be written ([Tremaine, 1991](#); [Ward & Hamilton, 2004](#); [Lu & Laughlin, 2022](#)):

$$\begin{aligned} J_{2,\text{effective}} &= J_{2,\text{planet}} + \frac{1}{2} \sum_i \left(\frac{m_i}{m_p} \right) \left(\frac{a_i}{R_p} \right)^2 \\ C_{\text{effective}} &= C_{\text{planet}} + \frac{1}{m_p R_p \Omega^2} \sum_i m_i a_i^2 n_i \end{aligned} \tag{5.12}$$

where m_i is the mass, a_i is the semimajor axis and n_i is the orbital mean motion of the i th satellite in the system. It is important to note that Equation (5.12) is only valid for satellites within the Laplace radius of the planet, given by Equation (5.3). Beyond the Laplace radius, the moon may be inclined with respect to the equatorial plane of the planet, the enhancement in precession must be considered differently ([Saillenfest & Lari, 2021](#)). For the purposes of this work Equation (5.12) is a good approximation as the Laplace radius for HIP-41378 f is very large, ranging

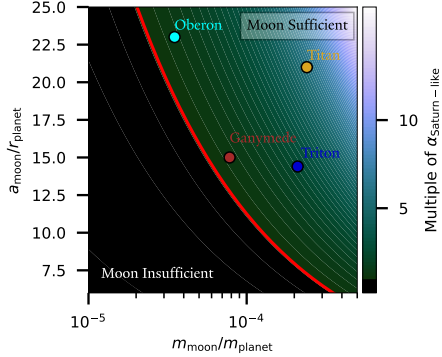


Figure 5.7. Exploration of how a massive moon enhances spin precession rate. We plot moon mass on the x -axis and moon semimajor axis on the y -axis, and the colorbar represents the spin precession rate of a planet with Neptune-like oblateness, spin rate and moment of inertia at the present-day orbit of HIP0-41378 f, enhanced by a moon of corresponding mass and orbit. The red line delineates the spin precession rate of a Saturn-like planet at the same orbit, the nominal requirement for capture into spin-orbit resonance as seen in Figure 5.6. The black region is parameter space in which the moon cannot sufficiently generate the requisite spin precession rate, with the opposite for the colored region. For reference the mass and semimajor axis ratios of the outermost major satellite of the four solar system giant planets are also plotted, and all are in the allowed parameter space. Note that all plotted moons are located significantly exterior to the Roche radius of the planet and hence the outer extent of the rings, which is typically around 3–4 R_f for our simulations.

from 37 to 122 R_f . This is beyond the orbital radius of the largest moons in our solar system, so we proceed to analyze enhancement in α under the assumption that a putative moon remains within the Laplace radius.

Figure 5.7 displays the precession enhancement a realistic moon may have. The colorbar corresponds to the precession rate α a Neptune-like planet at HIP-41378 f’s present-day orbit would exhibit if a moon of a given mass and semimajor axis was orbiting it. The red contour corresponds to the precession rate of a Saturn-like planet, the nominal cutoff for capture into secular spin-orbit resonance in our simulations, in the same location. For reference, the outermost major satellites of the four solar system planets are also plotted. We see that all four satellites are in the region of parameter space capable of sufficiently enhancing the precession rate of a Neptune-like planet to Saturn-like levels. Hence, a realistic satellite greatly expands the allowable physical parameter space of HIP-41378 f that results in capture into spin-orbit resonance.

We conclude that accounting for the existence of a realistic massive moon essentially allows all reasonable physical parameters associated with HIP-41378 f to result in capture into spin-orbit resonance. A large migrating exomoon was posited as the both the source of HIP-41378 f’s obliquity and the ring system itself

by Saillenfest et al. (2023) – in fact, the two scenarios are not incompatible with one another as a migrating exomoon acts to increase the spin precession rate. The detection of exomoon may be feasible in the near future (e.g. Kipping et al., 2022), which would represent additional credence to our theory.

5.6 Other Super-Puffs

We now briefly analyze the possibility of secular spin-orbit resonance in other super-puff systems. While the exoring hypothesis is less necessary to explain these super-puffs due to their closer-in orbits, it remains a viable solution to some of the super-puffs at farther distances (Piro & Vissapragada, 2020). In addition, for the closest super-puffs tidal heating may render obliquity tides significant (Millholland, 2019; Millholland et al., 2020). Both of these hypotheses support the intriguing results of Millholland & Laughlin (2019) and Leleu et al. (2024) who showed that sub-Neptunes near resonance tend to be puffier.

Secular spin-orbit resonance requires nodal precession of the orbit, as described in Section 5.4. One way to drive nodal precession is the J_2 moment of the host star (e.g. Brefka & Becker, 2021; Faridani et al., 2023). However, the most natural way to maintain spin-orbit resonances is companion planets. We thus restrict our attention to super-puffs in multi-planet systems. We thus consider five additional systems: Kepler-223 (Mills et al., 2016), Kepler-177 (Vissapragada et al., 2020), Kepler-359 (Hadden & Lithwick, 2017), Kepler-51 (Masuda, 2014), and K2-24 (Petigura et al., 2018). Intriguingly, a number of these systems also lie in resonant configurations, potential evidence of migration in the system’s history (e.g. Lee & Chiang, 2016).

We numerically analyze the frequency power spectra of each system as in Section 5.5. We compare the peaks of this frequency analysis to a set of physically reasonable α values for each super-puff, given by a Neptune-like oblateness and rotation rates ranging from 10 hours to 36 hours for reference. These are shown in Figure 5.8. In each subplot, the black dots are a representative frequency power spectrum for the system, and the vertical bands correspond to the reasonable α values we explored where each color corresponds to a super-puff in the system. Note that while some of these planets may be expected to be tidally locked, we did not find any near-matches for α precession rates associated with tidally locked states and thus do not depict them. We find possible matches for the following super-puffs: Kepler-51 d, Kepler-359 d, K2-24 c, Kepler-177 c, Kepler-223 e – in other words, there is a super-puff in every system which can potentially be in a spin-orbit equilibrium.

We briefly comment on the Kepler-51 system, a well-studied system that is in a 1:2:3 resonant chain (Masuda, 2014) and believed to have arrived at its present-day

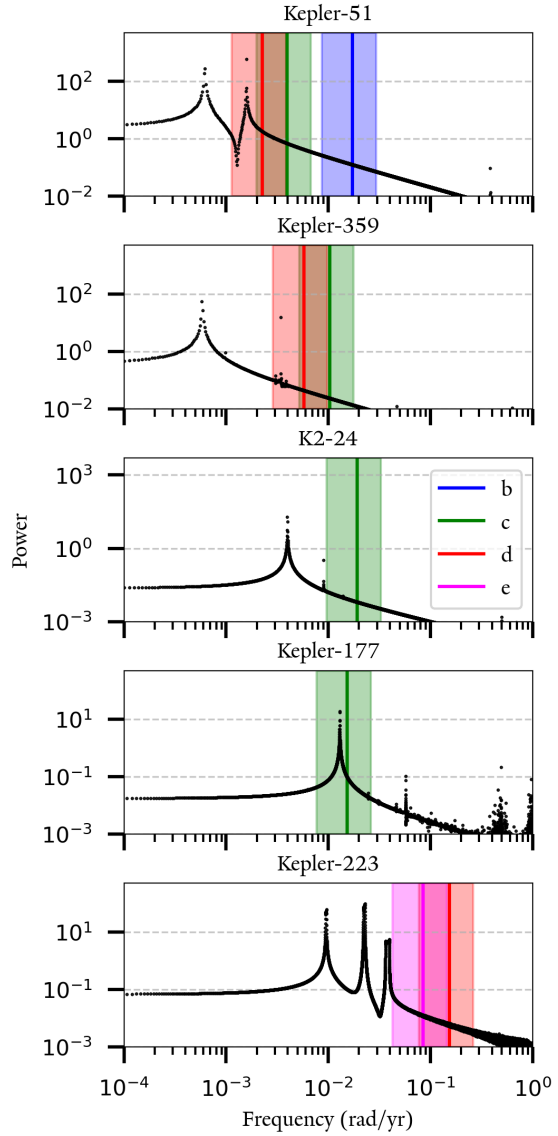


Figure 5.8. Frequency analysis of five multi-planet super-puff systems. Each subplot is analogous to the upper panel in Figure 5.4. The vertical colored bands represent reasonable present-day ranges of α for each of the super-puffs in the system, color-coded by designation. We find a near match for at least one super-puff in each system.

configuration via convergent migration (Lee & Chiang, 2016). The recent work of Lammers & Winn (2024b), who inferred an unusually slow rotation period of > 40 hours for Kepler-51 d via a measurement of the (lack of) planetary oblateness. One explanation they discussed was a high planetary obliquity, with $\theta \geq 75^\circ$, which could mask the true oblateness of the planet in the sky-projected obliquity. Their results, taken in conjunction with the near-match in frequency space for Kepler-51 d shown in Figure 5.8 and the potential migration history of the system, indicates a high-obliquity state for Kepler-51 d is a very reasonable prospect. We defer more detailed analysis of this, as well as the other super-puff systems enumerated, to future work.

5.7 Conclusion

In this work, we have investigated the dynamical history of the HIP-41378 system, motivated by the anomalous low density of the outermost planet HIP-41378 f. We find strong evidence that the system formed via convergent migration, as the outer three planets lie near a 4:3:2 resonant chain that is dynamically unstable on short timescales otherwise. We also find that if HIP-41378 f has a J_2 moment slightly greater than that of Saturn or is accompanied by a massive satellite system, this migration process likely results in capture into secular spin-orbit resonance and significant excitation of the planetary obliquity. If there is an opaque system of planetary rings around HIP-41378 f, this obliquity is in many cases able to reproduce its anomalous transit signal. Hence, we assert that a dynamical history involving convergent migration simultaneously explains both the system's long-term stability as well as in many cases generating a high planetary obliquity. This high planetary obliquity lends credence to the popular theory that HIP-41378 f is not in fact an extremely low-density planet far from its host star, but rather hosts a system of opaque rings (Akisanmi et al., 2020). We have shown that the spin-orbit configurations arising from convergent migration naturally lead to systems which can host large enough ring systems to reproduce the observed transit depth and anomalous density of HIP-41378 f. We also briefly comment on other super-puffs in multi-planet systems, and show that many of them are also plausibly in high-obliquity states.

We therefore encourage immediate additional observations targeted at HIP-41378 f to verify the true nature of the exoring hypothesis. Our work has demonstrated the first-order feasibility of differentiating between planetary rings and a puffy planet in a transit lightcurve. More nuanced modelling is certainly possible to take advantage of the vast capabilities of JWST, including accounting for the oblateness of the planet itself and rings which are not fully opaque. Scattered

(Barnes & Fortney, 2004) and reflected light (Arnold & Schneider, 2004) from ring particles may also imprint themselves on the transit lightcurve. Spectroscopic effects (Ohta et al., 2009) may also be relevant, among a host of other less obvious effects (Heller, 2018). A variety of numerical tools designed to simulate transit lightcurves of non-spherical objects are now available, including `squishyplanet` (Cassese et al., 2024a), `eclipsoid` (Dholakia et al., 2024) and `greenlturn` (Price et al., 2024). In particular, Price et al. (2024) measured constrained a low oblateness of HIP-41378 f with K2 data, which could be explained via slow rotation or nearly face-on planetary rings. In the era of JWST, such measurements will be vital in divining the true nature of HIP-41378 f’s puffiness.

Super-puffs represent one of the most intriguing unsolved mysteries in exoplanet science today. Our work has highlighted the importance of dynamics in this conversation, which until recently has been primarily a structural debate. While exorings may not be a necessary or even viable explanation for other super-puffs, planetary obliquity may still be highly relevant in the form of obliquity tides. The signatures of tidal heating are readily visible in transmission spectra (e.g. Sing et al., 2024; Welbanks et al., 2024). As most super-puffs are observed to be on circular orbits, so hence unable to be heated via eccentricity tides, tidal heating signatures would almost certainly point to significant planetary obliquity. We thus again encourage further atmospheric observations of these super-puffs as potential tests of tidal heating and signs of planetary obliquity.

5.8 Acknowledgements

We thank the anonymous referee for a productive and constructive report that greatly improved the manuscript. We thank Fei Dai, Konstantin Gerbig, Caleb Lammers, Sarah Millholland, Malena Rice, Melaine Saillenfest and Yubo Su and Josh Winn for helpful and insightful discussions. GL is grateful for the support by NASA 80NSSC20K0641 and 80NSSC20K0522. This work has benefitted from use of the GRACE computing cluster at the Yale Center for Research Computing (YCRC). Some plots in this work have made use of the colormaps in the CMasher package (van der Velden, 2020).

Part III

Coupled Planetary Structure and Dynamical Evolution

Chapter 6

The Dynamical History of the HAT-P-11 System

"Every great advance in science has issued from a new audacity in imagination."
– John Dewey

Adapted From:

Lu. T., An, Q., Li, G., Millholland, S., Rice, M., Brandt, G. M., & Brandt, T. 2025, The Astrophysical Journal, Volume 979, Issue 2

See also the companion paper:

An, Q., Lu. T., Brandt, G. M., Brandt, T. & Li, G. 2025, The Astronomical Journal, Volume 169, Issue 1

Abstract

The two planets of the HAT-P-11 system represent fascinating dynamical puzzles due to their significant eccentricities and orbital misalignments. In particular, HAT-P-11 b is on a close-in orbit that tides should have circularized well within the age of the system. Here we propose a two-step dynamical process that can reproduce all intriguing aspects of the system. We first invoke planet-planet scattering to generate significant eccentricities and mutual inclinations between the planets. We then propose that this misalignment initiated von-Zeipel-Lidov-Kozai cycles and high-eccentricity migration that ultimately brought HAT-P-11 b to its present-day orbit. We find that this scenario is fully consistent only when significant tidally-driven radius inflation is accounted for during the tidal migration. We present a suite of N -body simulations exploring each phase of evolution and show that this scenario is consistent with all observational posteriors and the reported age of the system.

6.1 Introduction

The mid-K dwarf HAT-P-11 hosts an intriguing system that has been the subject of much interest in recent years. The system has two known planets. The first, HAT-P-11 b, is a close-in ($a_b = 0.0525$ AU) eccentric ($e_b = 0.218$) super-Neptune ($m_b = 23.4 M_E$) first identified by [Bakos et al. \(2010\)](#). Follow-up Rossiter-McLaughlin ([Rossiter, 1924](#); [McLaughlin, 1924](#)) analysis of the system by [Hirano et al. \(2011\)](#) and [Sanchis-Ojeda & Winn \(2011\)](#) revealed that the orbit of HAT-P-11 b is polar ($\psi_{Ab} = 106^\circ$), which makes it a member of the potential population of perpendicular planets ([Albrecht et al., 2021](#); [Dong & Foreman-Mackey, 2023](#); [Siegel et al., 2023](#)).

HAT-P-11 b presents an interesting dynamical puzzle. Planets as close-in as HAT-P-11 b are expected to be on circular orbits due to tidal forces. The fact that HAT-P-11 b is significantly eccentric, coupled with its unusual perpendicular orbit, points to a dynamically hot history. [Yee et al. \(2018\)](#) greatly advanced our understanding of the dynamical history of the system with their discovery of the second planet in the system, HAT-P-11 c, an eccentric ($e_c \approx 0.6$) super-Jupiter ($m_c \sin i \approx 1.6 M_J$) on an $a_c \approx 4.1$ AU orbit. Their dynamical analysis of the system concluded that with this additional companion, both the eccentricity and spin-orbit misalignment of HAT-P-11 b could be explained on the condition that HAT-P-11 c was also misaligned. At the time, the orbital inclination of HAT-P-11 c was unconstrained.

The final piece of puzzle, the misalignment between the orbits of HAT-P-11 b and HAT-P-11 c, was initially explored by [Xuan & Wyatt \(2020\)](#), in which they

Table 6.1. Parameters of the HAT-P-11 System

Parameter	Value	Reference
Host Star		
Mass (M_{\odot})	$0.81^{+0.02}_{-0.03}$	Bakos et al. (2010)
Radius (R_{\odot})	$0.75^{+0.02}_{-0.02}$	Bakos et al. (2010)
Age (Gyr)	$6.5^{+5.9}_{-4.1}$	Yee et al. (2018)
HAT-P-11 b ^a		
Mass (M_{\oplus})	$23.4^{+1.5}_{-1.5}$	Yee et al. (2018)
Radius (R_{\oplus})	$4.36^{+0.06}_{-0.06}$	Huber et al. (2017)
a (AU)	$0.05254^{+0.00064}_{-0.00066}$	Yee et al. (2018)
e	$0.218^{+0.034}_{-0.031}$	Yee et al. (2018)
HAT-P-11 c		
Mass (M_J)	2.68 ± 0.41	Paper 1
a (AU)	4.10 ± 0.06	Paper 1
e	0.652 ± 0.017	Paper 1
ψ_{Ac} (°)	45 to 138 ^b	Paper 1
ψ_{bc} (°)	49 to 131 ^b	Paper 1

^aHirano et al. (2011) and Huber et al. (2017) give slightly different values for spin-orbit misalignment and eccentricity, respectively.

^bRange enclosing 95% of the (highly non-Gaussian) posterior

derived a bimodal inclination distribution for HAT-P-11 c, providing evidence of a large mutual inclination between planet b and c. An et al. (2024) (hereafter Paper 1) combined astrometry data from Hipparcos and Gaia with radial velocity data from Keck/HIRES to constrain the orbit of HAT-P-11 c, including a more precise bimodal constraint on inclination. All relevant orbital quantities of the system are well-constrained and are presented in Table 6.1. In Paper 1, the two inclination modes are treated separately, together with the projected stellar spin constrained by Sanchis-Ojeda & Winn (2011), to calculate the alignment of all three main angular momentum vectors in the HAT-P-11 system. Paper 1 reports the first measurement of the spin-orbit misalignment of HAT-P-11 c, and significantly improved measurements of the mutual inclination between HAT-P-11 b and HAT-P-11 c. A schematic view of the orbits is shown in Figure 6.1. We are now in a position to postulate the complete dynamical history of HAT-P-11.

Both planets in the HAT-P-11 system represent dynamical puzzles, and the formation history of the system has been explored by Petrovich et al. (2020); Pu & Lai (2021) among others. In this work we propose a two-step formation

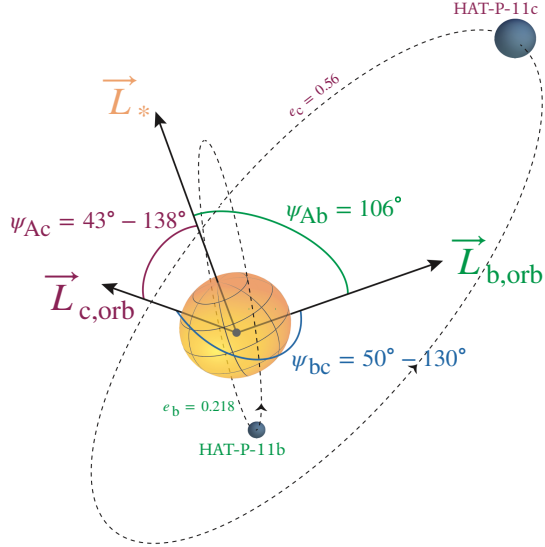


Figure 6.1. Schematic view of one possible orbital architecture of the HAT-P-11 system, based on posteriors from Table 6.1. We label the eccentricities and misalignments between each orbit and the stellar spin axis.

mechanism: we posit that both HAT-P-11 b and HAT-P-11 c initially formed in circular aligned orbits, along with two other large planets. Through dynamical instability and subsequent planet-planet scattering, both additional planets were ejected from the system. As a result, HAT-P-11 b and HAT-P-11 c were left on eccentric and misaligned orbits, which triggered von-Zeipel-Lidov-Kozai (ZLK) migration in HAT-P-11 b. Through these mechanisms, all aspects of the present-day configuration of the system are reproduced.

The paper is organized as follows. In Section 6.2 we show that planet-planet scattering results in significant eccentricities and orbital misalignments for both planets, and we reproduce the present-day orbit of HAT-P-11 c. In Section 6.3 we similarly reproduce the present close-in state of HAT-P-11 b using a series of N -body ZLK simulations accounting for both tidal and thermally driven radius evolution. We discuss implications of our study and conclude in Section 6.4.

6.2 Planet-Planet Scattering

The high eccentricity of HAT-P-11 c, coupled with the significant spin-orbit misalignment reported in Paper 1, is the first dynamical puzzle. Naively, one would expect planets to form in circular, aligned orbits, thanks to strong eccentricity damping within the protoplanetary disk. Any deviation from this paradigm is believed to be the imprint of a dynamically active history. A number of well-

understood mechanisms are known to excite the eccentricities and inclinations of planets, including but not limited to the von-Zeipel-Lidov-Kozai (ZLK) effect (von Zeipel, 1910; Lidov, 1962; Kozai, 1962) and secular chaos (Wu & Lithwick, 2011). Both of these mechanisms require an additional undetected companion in the system, something for which there is no direct evidence in the HAT-P-11 system. The existing radial velocity data are satisfactorily explained by two planets with no residual trend, and the measured astrometric acceleration is similarly consistent with the two known planets (Paper 1). To evade these constraints, an additional planet would have to be low-mass and/or very widely separated and hence be dynamically insignificant. Planet-disk interactions during planetary migration can excite eccentricities without the need for a companion, but this mechanism cannot generate the spin-orbit misalignment.

In the absence of a more distant perturber, the most promising pathway is planet-planet scattering, where close encounters between pairs of planets lead to strong gravitational interactions that produce large eccentricities and obliquities. While additional planets would be required for this mechanism, violent scattering is prone to ejecting planets or scattering them to wide orbits where they would be difficult to detect (e.g., Chatterjee et al., 2008; Carrera et al., 2019; Frelikh et al., 2019). In this section, we explore the generation of HAT-P-11 c's significant eccentricity and orbital misalignment through N-body simulations of planet-planet scattering.

6.2.1 Theoretical Background

A wealth of literature exists on the subject of planet-planet scattering. Analytic treatment of this problem is difficult, so most analyses have been performed with numerical simulations. For a comprehensive review, see Davies et al. (2014). Here we summarize some of the most relevant key results for our study.

The stability of systems involving only two planets is well-understood analytically (Gladman, 1993). Studies such as Ford et al. (2001), Petrovich et al. (2014) and Gratia & Fabrycky (2017) have shown that two-planet systems can attain a wide range of eccentricities but very rarely high mutual inclinations. Three-body scattering, on the other hand, can both excite eccentricity to arbitrarily large values and raise inclination up to 90° (Chatterjee et al., 2008; Jurić & Tremaine, 2008; Carrera et al., 2019). In the spin-orbit misalignment posterior derived in Paper 1, the 95% confidence interval is given by 45° to 138°; thus the ~40° lower limit requires three-body scattering to be invoked.

The stability of three-body systems cannot be obtained analytically. From numerical studies, system stability is both highly chaotic and dependent on mean-motion resonances (e.g., Marzari, 2014; Rath et al., 2022). However, to first-order the time to dynamical instability grows logarithmically with mutual separation

(Marzari & Weidenschilling, 2002). The mutual separation is commonly parameterized by the mutual Hill radius (though note that other criteria often offer better predictions, e.g Lammers et al. (2024)):

$$R_H = \frac{a_i + a_{i-1}}{2} \left(\frac{m_i + m_{i-1}}{3M_*} \right)^{1/3}, \quad (6.1)$$

where a_i, m_i are the semimajor axes and masses of the i th planet and M_* is the mass of the star. The Δ parameter denotes the separation in units of the mutual Hill radius,

$$\Delta = \frac{a_i - a_{i-1}}{R_H}. \quad (6.2)$$

The instability timescale grows as the separation between the planets increases (e.g., Chambers et al., 1996; Pu & Wu, 2015; Tamayo et al., 2020b).

6.2.2 N-Body Simulations

Scattering simulations are computationally expensive, and there is a large parameter space that the primordial system could inhabit. To work around this, we adopt a sequential approach.

We first use three-planet simulations, with HAT-P-11 c and two additional bodies but without HAT-P-11 b, to show that planet-planet scattering can exactly reproduce HAT-P-11 c's present-day orbit with the other bodies either ejected from the system or scattered to very wide orbits. This step assumes that we may neglect HAT-P-11 b for the purposes of reproducing HAT-P-11 c's observed parameters. We test this assumption by running an additional suite of scattering simulations with HAT-P-11 b present on an initial 0.3 AU orbit (roughly five times its present-day semimajor axis). In this suite of simulations with HAT-P-11 b, we do not seek to exactly reproduce HAT-P-11 c's orbit, given the extremely tight constraints on its semimajor axis and the large chaotic parameter space introduced by adding another surviving planet to the system. Rather, we content ourselves with showing that these simulations qualitatively match the architecture expected from the three-planet scattering simulations.

Our tiered approach to N-body simulations allows us to construct a statistical picture of the likely configurations of HAT-P-11 system after violent scattering from an initial four-planet configuration. We can then estimate the fraction of the available parameter space that can produce the high mutual inclinations and significant eccentricities that are observed for HAT-P-11 c, along with a range of plausible initial conditions for HAT-P-11 b's subsequent orbital evolution. This evolution under the influence of ZLK oscillations and tides is discussed in Section 6.3.

Three-Planet Simulations

We perform 1000 three-planet simulations using the IAS15 integrator (Rein & Spiegel, 2015) in the REBOUND N -body integrator package (Rein & Liu, 2012). We use the adaptive timestep criterion described in Pham et al. (2024). The setup of our simulations is as follows: we consider three identical planets with $m_1 = m_2 = m_3 = 2.68 M_J$, the best-fit value for HAT-P-11 c's mass. We note that our results are not sensitive to the masses of the three planets. We also ran a set of simulations with $m_1 = m_c, m_2 = m_c/2$ and $m_3 = m_c/4$ following the prescription of Anderson et al. (2020), and found no significant differences at the population level.

Three-body scattering tends to result in a single surviving planet, or additional survivors on highly eccentric/marginally unbound orbits (e.g Carrera et al., 2019). In both cases, the orbital energy of the non-innermost planets is nearly zero. Conservation of energy thus demands

$$\frac{1}{a_f} = \frac{1}{a_{1,i}} + \frac{1}{a_{2,i}} + \frac{1}{a_{3,i}}. \quad (6.3)$$

We set $a_f = 4.10$ AU, the present-day semi-major axis of HAT-P-11 c. In the interest of minimizing computation time, we set $\Delta = 3$ to induce rapid instability and scattering in our systems. This is unrealistically compact for primordial planetary systems, where separations would be expected to be around 5-10 mutual Hill radii (Raymond & Morbidelli, 2022). Changing the mutual separation of the planets does not qualitatively affect the scattering outcome, only the timescale until dynamical instability (e.g Chatterjee et al., 2008; Anderson et al., 2020). The above criterion hence informs the initial semi-major axes of the three planets: $a_{1,i} = 8.759$ AU, $a_{2,i} = 12.930$ AU, $a_{3,i} = 19.086$ AU. In each simulation, the other relevant orbital parameters for each planet are chosen at random from the following uniform distributions:

$$\begin{aligned} e &\sim \mathcal{U}(0.01, 0.05) \\ i &\sim \mathcal{U}(0^\circ, 2^\circ) \\ f, \omega, \Omega &\sim \mathcal{U}(0, 2\pi) \end{aligned} \quad (6.4)$$

Note that we do not track the motion of the stellar spin axis in our simulations. Rather, we assume that the star's initial spin axis points along the z -axis and does not evolve significantly over the course of our simulations. With this assumption, the orbital inclination i can be used as a proxy for the spin-orbit misalignment ψ_{Ac} . We account for collisions via merging planets (conserving mass, volume and momentum but not energy) using the `reb_collision_resolve_merge` collision module. We also remove particles if they exceed a distance of 10^3 AU from the

origin, using the `exit_max_distance` feature.

Figure 6.2 shows an example of one of our simulations. The system rapidly enters a regime of dynamical instability, as expected from the initialization of the planets at small mutual Hill radii. This epoch is characterized by sudden perturbations in semimajor axis, eccentricity and inclination triggered by close encounters. Within 1 Myr, one planet is completely ejected from the system. The remaining two planets continue to experience perturbations in eccentricity and inclination, until a second planet is ejected from the system around 5 Myr. At this point, HAT-P-11 c has gained significant eccentricity and inclination. The final orbital elements of HAT-P-11 c are $a_c = 4.12$ AU, $e_c = 0.639$, and $\psi_{Ac} = 65.3^\circ$, which are all time-averaged values over the last 5 Myr of the simulation.

In Figure 6.3 we report statistics from the entire ensemble of simulations. We plot histograms of the distributions in a_c , e_c and ψ_{Ac} of the innermost surviving planet in each simulation, as well as the present-day 1σ constraints (2σ for ψ_{Ac}) on the orbit of HAT-P-11 c from Paper 1. The simulation results are as expected: a_c is strongly peaked near the present-day value, and both e_c and ψ_{Ac} show a wide range of values that easily encompass the constraints. This shows that our system setup is capable of consistently producing orbits similar to that of HAT-P-11 c.

Of the 1000 simulations we ran, the number with 1, 2 and 3 surviving planets were 197, 802 and 1, respectively. The most common outcome by far is a system with two surviving planets, which would imply an external undiscovered planet in the HAT-P-11 system.

The extra planet is not in tension with observations, because the extraneous surviving planet is generally very far out and hence would be undetectable. In some cases the extra planet produces long-term secular oscillations in the orbital elements of HAT-P-11 c, but this does not impact the system's stability. In our simulations there are a total of 908 extraneous planets that survive. The 1σ semimajor axis distribution of these planets is $a_{extra} = 72^{+123}_{-37}$ AU, while the perihelion distribution of these $a_{p,extra} = 28^{+17}_{-9}$ AU. There are only 5 simulations where there is an orbit crossing between any of the extra planets and the surviving HAT-P-11 c. We do not analyze the stability of the surviving systems in-depth; an analytic criterion such as the one introduced by [Hadden & Lithwick \(2018\)](#) could be used to this end. We conclude that planet-planet scattering in a three planet system well-reproduces the unusual spin-orbit misalignment and eccentricity of HAT-P-11 c.

Four-Planet Simulations

We now consider the effect of planet-planet scattering on the orbit of HAT-P-11 b by running a suite of four-planet scattering simulations. The setup of these simulations is as follows. We perform 10,000 simulations using the new hybrid

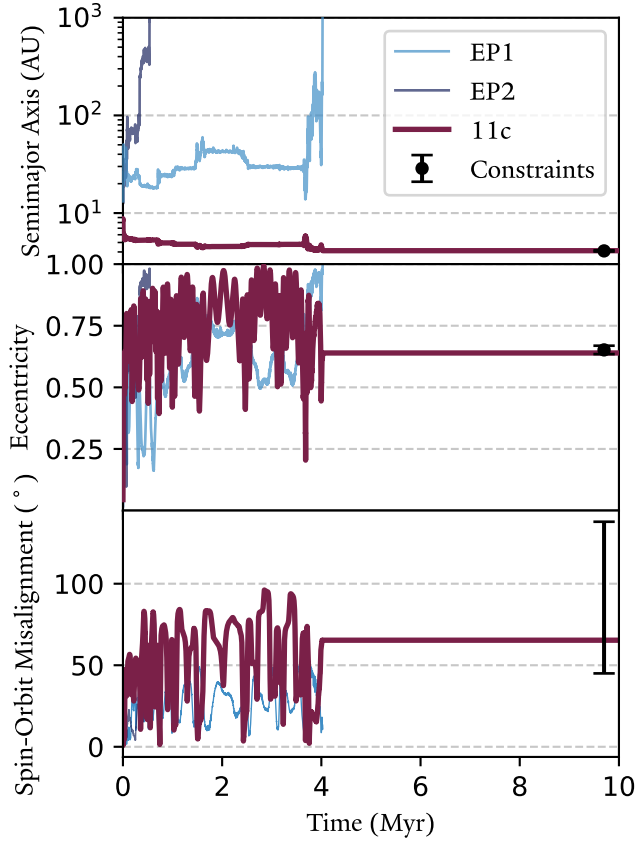


Figure 6.2. Example three-body scattering results for the origin of HAT-P-11 c. The thick maroon line and the two thin blue lines represent the orbital elements of HAT-P-11 c and the two ejected planets (EP), respectively. The subplots show the semimajor axis, eccentricity, and spin-orbit misalignment evolution of the three bodies, from top to bottom. When a planet is fully ejected from the system (heliocentric distance $> 10^3$ AU) or becomes unbound ($a < 0$), the line associated with the evolution of that planet is terminated. The black dot on the right-hand side of each subplot denotes our derived values for the present-day system, with the error bar representing the 1σ posteriors for semimajor axis and eccentricity and the 2σ posterior for spin-orbit misalignment.

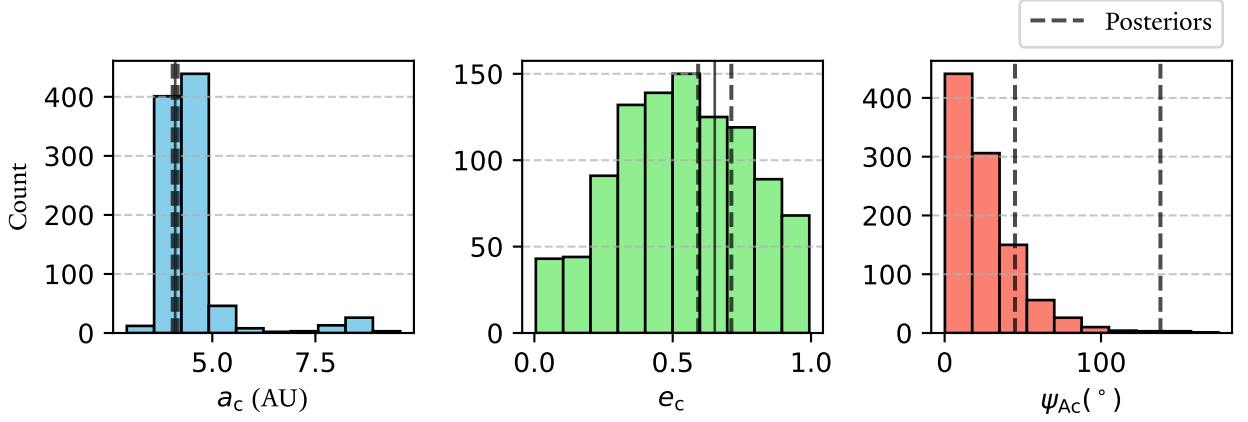


Figure 6.3. Results from our ensemble of three-body scattering simulations. We plot distributions in a , e and ψ_{Ac} for the innermost planet in our three-planet simulations. The black lines correspond to the best-fit present-day values of HAT-P-11 c from Table 6.1, with the dotted lines representing the 1σ error bars for a_c and e_c and 2σ for ψ_{Ac} . All three orbital element ranges are well-represented in our sample, showing that this system can easily be produced through planet-planet scattering without fine-tuning.

integrator TRACE (Lu et al., 2024b) in REBOUND. We initialize the outer three bodies as in the previous section. However, we now initialize HAT-P-11 b on an $a_b = 0.3$ AU orbit (roughly 5× its present-day semimajor axis), with all other orbital elements randomized in the same fashion as the three outer planets. The semimajor axis of HAT-P-11 b does not change significantly for most of our simulations. We adopt a timestep of 0.022 years, which is roughly 1/9th of HAT-P-11 b’s initialized orbit. These simulations are also integrated for 10^7 years. We also extend the maximum simulation distance to 10^4 AU. The mean fractional energy error over our 10,000 simulations is $10^{-1.43}$.

Figure 6.4 shows statistics of orbital elements from our simulations. We restrict our discussion to simulations in which HAT-P-11 b survives on an orbit within $a_b < 4$ AU; 5355 simulations satisfy this criterion. Of these simulations, the vast majority (4743, or 89%) result in three-planet systems comprised of HAT-P-11 b, HAT-P-11 c, and a very distant outer perturber. This is consistent with our results from the previous subsection, which shows that HAT-P-11 b does not play a significant role in the scattering dynamics of the giant planets. 611 simulations resulted in two-planet systems and 1 simulation resulted in a four-planet system. We plot the eccentricities and inclinations of all planets corresponding to HAT-P-11 b, HAT-P-11 c and extraneous outer planets in their respective simulations as a function of semimajor axis. The semimajor axis 1σ distributions are given by $a_b = 0.29^{+0.00001}_{-0.06}$ AU, $a_c = 4.31^{+0.40}_{-0.24}$ AU and $a_{\text{outer}} = 59^{+78}_{-24}$ AU. We also see that

HAT-P-11 b can be scattered onto a wide range of inclinations and eccentricities. These 1σ distributions are given by $e_b = 0.11^{+0.28}_{-0.07}$ and $\psi_{Ab} = 25^{+27}_{-17}$ degrees. We also ran simulations initializing additional planets between the orbits of HAT-P-11 b and HAT-P-11 c, which are overwhelmingly ejected.

We conclude that the planet-planet scattering which was likely responsible for the eccentric and misaligned orbit of HAT-P-11 c also likely resulted in HAT-P-11 b gaining an eccentric and misaligned orbit. Crucially, this creates significant misalignment between the orbits of the two planets.

6.3 ZLK Migration

The orbit of HAT-P-11 b is an even bigger puzzle than planet c. Its near-polar orbit with $\psi_{Ab} \sim 106^\circ$ (Stassun et al., 2017) is highly unusual. Most intriguingly, planets as close-in as HAT-P-11 b would naively be expected to have perfectly circular orbits, due to significant tidal effects acting quickly to circularize the orbit. Indeed, the vast majority of hot Jupiters observed do have circular orbits (Dawson & Johnson, 2018). To first order, the tidal circularization timescale is given by (Goldreich & Soter, 1966):

$$t_{\text{circ}} = \frac{4}{63} \frac{a^{13/2}}{\sqrt{GM_*^3}} Q_p m_p R_p^{-5}. \quad (6.5)$$

Plugging in the present-day values of the system and $Q_p = 10^5$, a fiducial estimate for the tidal quality factor of a Neptune-like planet (e.g Millholland, 2019), we obtain $t_{\text{circ}} = 2 \times 10^9$ years, which is compatible with the system's age of $6.5^{+5.9}_{-4.1}$ Gyr (Yee et al., 2018). However, these expressions must be used with caution. Wisdom (2008) found that the standard analytic expressions can underestimate tidal dissipation by several orders of magnitude for high eccentricities, and expressions such as Equation (6.5) significantly overpredict the circularization timescale. Given this, and the fact that tides act more efficiently at the highest eccentricities, we naively expect that HAT-P-11 b should be circularized.

However, we cannot state with certainty that the orbit should be circularized. First, we note that the default calculation of t_{circ} is not that far off from the system's age. In addition, the unconstrained tidal quality factor Q_p may well be higher than the nominal value of 10^5 as argued by Mardling (2008). In this case, HAT-P-11 b could have formed at its present-day semimajor axis and gained significant eccentricity/spin-orbit misalignment through scattering alone, without having sufficient time to fully circularize. Given the timescales and assumptions enumerated, we consider this scenario a somewhat unlikely but certainly possible scenario.

In this section, we explore a more likely alternative, where ZLK oscillations

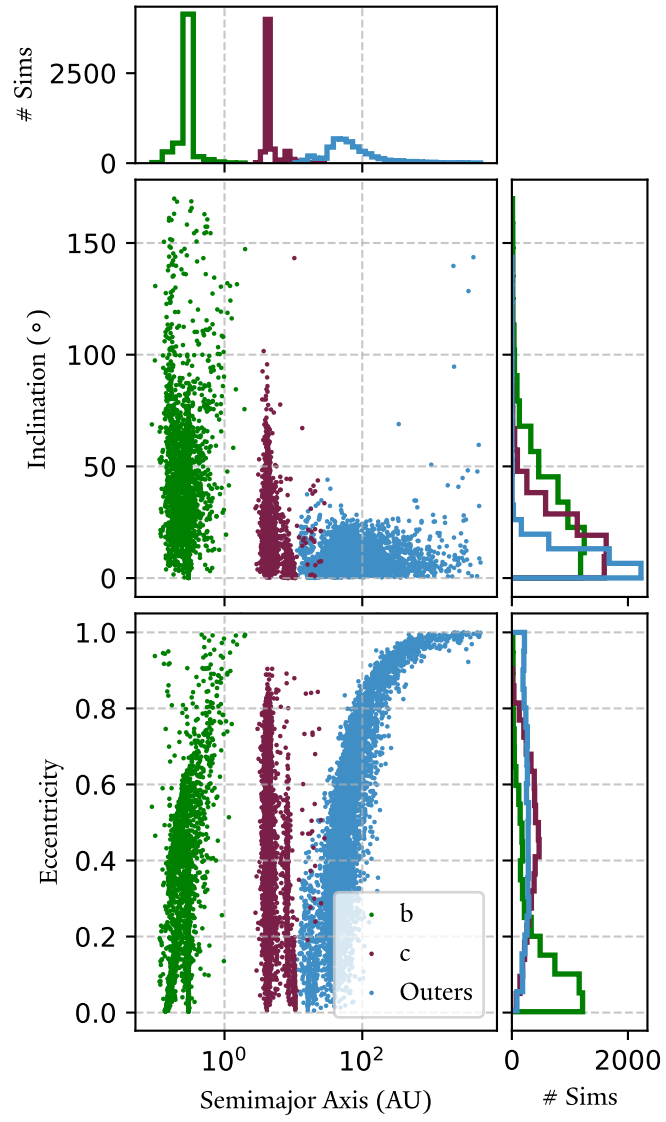


Figure 6.4. Results from an ensemble of 10,000 four-planet scattering simulations. We plot the eccentricities and inclinations of the planets representing HAT-P-11 b (green), HAT-P-11 c (maroon) and external planets (blue) as a function of semimajor axis. The points referring to HAT-P-11 b and HAT-P-11 c always correspond to the innermost planet and the innermost giant planet in our simulations, respectively. In every simulation these are distinct. The distributions of HAT-P-11 c and the outer planets are qualitatively consistent with our results from the three-planet scattering simulations. We see that HAT-P-11 b may be scattered to arbitrarily high eccentricities and very high inclinations.

(driven by HAT-P-11 c) and subsequent tidal circularization and migration act as an avenue to explain both the eccentricity and spin-orbit misalignment of HAT-P-11 b. We use initial conditions consistent with our four-body scattering simulations.

6.3.1 ZLK Oscillations

[Lidov \(1962\)](#) and [Kozai \(1962\)](#) independently identified a fascinating behavior characteristic of hierarchical three-body systems. Consider such a system, and denote the three bodies as the *star*, *b*, and *c*. If the mutual inclination between the orbits of *b* and *c* are significantly misaligned ($39.2^\circ < \psi_{bc} < 140.8^\circ$), then the orbit of *b* will experience high-amplitude coupled oscillations in eccentricity and inclination in the absence of short-range forces such as general relativity. Commonly referred to as the Kozai-Lidov effect, the initial discovery of this mechanism by [von Zeipel \(1910\)](#) has been recently brought to light by [Ito & Ohtsuka \(2019\)](#). We hence adopt the name von Zeipel-Lidov-Kozai, or ZLK effect.

For an in-depth review of the ZLK effect as well as its many applications, see [Naoz \(2016\)](#). We provide in this paper a brief overview of the analytic understanding of the ZLK effect necessary to interpret our results. The simplest way to investigate the ZLK effect analytically is in the hierarchical secular approximation, which averages over the mean motion of both *b* and *c* ([Ford et al., 2000](#)). The validity of this approximation holds as long as $a_c \gg a_b$. The initial parameter space of the HAT-P-11 system in our simulations does not always satisfy this requirement ($a_b/a_c < 0.1$), so we will use direct *N*-body simulations to explore our system to obtain more accurate results. However, good first-order understanding can still be gained from the secular approximation¹. In this approximation and assuming *b* is a test particle, *c*'s orbit remains unchanged throughout the system's evolution, and *b*'s semimajor axis remains fixed. The maximum amplitude of the eccentricity oscillations depends on the initial mutual inclination: assuming the inner begins on a circular orbit, $e_{b,\max} = \sqrt{1 - (5/3)\cos^2\psi_{bc}}$ (in the quadrupole limit). The period of the ZLK oscillations is of order (e.g., [Fabrycky & Tremaine, 2007](#)):

$$\tau_{ZLK} = \frac{2P_c^2}{3\pi P_b} \frac{m_{\text{star}} + m_b + m_c}{m_c} (1 - e_c^2)^{3/2}, \quad (6.6)$$

where P_b, P_c are the periods of the inner and outer bodies, respectively.

The genesis of these effects is the apsidal precession of *b*'s orbit, $\dot{\omega}_b$, generated by the weak perturbations of the outer. In the secular approximation, the apsidal precession rate can be explicitly calculated. The orbit-averaged Hamiltonian of

¹The extent to which the secular approximation is valid for mildly hierarchical systems is discussed in [Grishin et al. \(2018\)](#).

the system is (Ford et al., 2000; Fabrycky & Tremaine, 2007):

$$\begin{aligned} \langle \mathcal{H} \rangle = & -\frac{Gm_{\text{star}}m_b}{2a_b} - \frac{G(m_{\text{star}} + m_b)m_c}{2a_c} \\ & - \frac{Gm_{\text{star}}m_b m_c}{m_{\text{star}} + m_b} \frac{a_b^2}{8a_c^3(1 - e_c^2)^{3/2}} \\ & \times [2 + 3e_b^2 - \sin^2 \psi_{bc}(3 + 12e_b^2 - 15e_b^2 \cos^2 \omega_b)] \end{aligned} \quad (6.7)$$

where ψ_{bc} is the mutual inclination between bodies b and c . This equation can be solved for the apsidal precession rate; see Naoz et al. (2013); Naoz (2016) for an in-depth derivation:

$$\begin{aligned} \dot{\omega}_{b,\text{ZLK}} = & 6C_2 \left[\frac{1}{G_b} \left(4\cos^2 \psi_{bc} + (5\cos(2\omega_b) - 1) \right. \right. \\ & \times (1 - e_b^2 - \cos^2 \psi_{bc}) \\ & \left. \left. + \frac{\cos \psi_{bc}}{G_c} (2 + e_b^2(3 - 5\cos(2\omega_b))) \right) \right] \end{aligned} \quad (6.8)$$

where

$$C_2 \equiv \frac{G^4}{16} \frac{(m_s + m_b)^7}{(m_s + m_b + m_c)^3} \frac{m_c^7}{(m_s m_b)^3} \frac{L_b^4}{L_c^3 G_c^3} \quad (6.9)$$

where G is the gravitational constant, $L_{b/c}$ are the Delaunay action variables, and $G_c \equiv L_c \sqrt{1 - e_c^2}$. Note that this level of approximation is only strictly valid in the case of a circular outer orbit and an inner test particle, neither of which are good assumptions in our system. The next level of approximation, the octupole-level, would correctly account for both of these complications. However, the dynamics are chaotic in the octupole order (Li et al., 2014a). As we aim only to draw first-order analytical understanding from the secular model (to eventually be confirmed with full N -body simulations), we work for now in the quadrupole approximation for greater clarity into the most impactful quantities in this problem.

ZLK oscillations will persist so long as the dominant source of precession in ω_b is due to perturbations from c . As a_b becomes smaller due to tidal migration, a host of other effects become significant and may suppress the precession from c , and thus the ZLK oscillations themselves. For instance, the precession due to general relativity can be quantified (Eggleton & Kiseleva-Eggleton, 2001; Fabrycky & Tremaine, 2007):

$$\dot{\omega}_{b,\text{GR}} = \frac{3G^{3/2}(m_{\text{star}} + m_b)^{3/2}}{a_b^{5/2} c^2 (1 - e_b^2)} \quad (6.10)$$

where c here is the speed of light, not to be confused with a quantity associated with body c . [Yee et al. \(2018\)](#) ruled out the possibility of ZLK oscillations being active in the present-day HAT-P-11 system, on the basis of general relativity suppressing ZLK precession at HAT-P-11 b's present-day semimajor axis. Plugging in values associated with the present-day system, we confirm that ZLK oscillations are expected to be quenched by GR precession, with $\dot{\omega}_{b,\text{ZLK}}/\dot{\omega}_{b,\text{GR}} \sim 0.8$. Hence, HAT-P-11 b's large eccentricity cannot be attributed to it *currently* being in a high-eccentricity phase of a ZLK oscillation. However, this does not rule out the possibility of ZLK oscillations having occurred in the past. In order for this to have been the case, HAT-P-11 b must have originated at a larger semimajor axis.

6.3.2 Tidal Friction

We turn to the process of ZLK migration, which has been invoked to explain the anomalously high eccentricity and tight orbits of a number of hot Jupiters (see [Wu & Murray \(2003\)](#), [Mardling \(2010\)](#), [Beust et al. \(2012\)](#) among others). The idea behind ZLK migration is to combine the concepts of ZLK oscillations and tidal evolution. During each high-eccentricity phase of the ZLK oscillation, tidal friction becomes significant due to b's close approach with the host star.

In this work, we will consider the prescription of equilibrium tides only ([Hut, 1981](#); [Eggleton et al., 1998](#); [Mardling & Lin, 2002](#)). In this framework, the strength of tidal friction is parameterized by the constant time lag τ , which represents the time lag between the tidal bulge of a body and the line of centers connecting to the tidal perturber. τ may be related (with caution, see [Leconte et al. \(2010\)](#); [Lu et al. \(2023\)](#)) to the commonly used tidal quality factor Q via

$$\tau = (2nQ)^{-1} \quad (6.11)$$

with n the mean motion of the tidal perturber, in this case the host star. We note that more complex and nuanced tidal models are available. In particular, for the high-eccentricity ZLK epochs dynamical tides may be a more accurate prescription (e.g [Mardling, 1995](#); [Lai, 2012](#); [Fuller et al., 2014](#); [Vick et al., 2019](#); [Vick et al., 2023](#)). However, no self-consistent N -body package exists with these more complex prescriptions. Hence, we restrict ourselves to the simpler equilibrium tide model in the present work, though we encourage future works to explore the effect of more complex tidal models.

In the equilibrium tide model, bodies are no longer point particles but rather are endowed with structure. The two improvements on the point particle model are the effect of a misaligned tidal bulge and the rotational flattening of each body. Both are significant to the dynamics of ZLK migration, not only because they act

to tighten the orbit of b over time, but also because they both introduce additional precession terms. For our system, tidal precession is expected to be more relevant, so we will focus on that aspect. The precession rate associated with tides is given by (Fabrycky & Tremaine, 2007)

$$\dot{\omega}_{\text{Tide}} = \frac{15 \sqrt{G(m_{\text{star}} + m_b)} 8 + 12e_b^2 + e_b^4}{8a_b^{13/2} (1 - e_b^2)^{9/2}} \times \frac{1}{2} \left[\frac{m_b}{m_{\text{star}}} k_{\text{star}} R_{\text{star}}^5 + \frac{m_{\text{star}}}{m_b} k_b R_b^5 \right], \quad (6.12)$$

where k_{star}, k_b are the tidal Love numbers of the star and planet, respectively. Figure 6.5 demonstrates the significance of including the effects of tidal friction. In this figure we consider a system with a central object consistent with HAT-P-11A and an outer perturber consistent with HAT-P-11 c. The semimajor axis and eccentricity of HAT-P-11 b are varied, and we analyze where in semimajor axis-eccentricity space ZLK oscillations are allowed. The present-day orbit of HAT-P-11 b is also marked. The maroon and gold lines mark where $|\dot{\omega}_{\text{ZLK}}/\dot{\omega}_{\text{GR}}| = 1$ and $|\dot{\omega}_{\text{ZLK}}/\dot{\omega}_{\text{Tide}}| = 1$, respectively. Towards the upper left (lower semimajor axis and higher eccentricity) of each line, ZLK oscillations are quenched by the respective additional effect, while towards the bottom right ZLK oscillations are allowed to be active. From Equation (6.12), we see that $\dot{\omega}_{\text{Tide}}$ scales strongly with the eccentricity of b. As a result, while tides are less influential than GR at low eccentricities, the opposite is true at higher eccentricities. This is highly impactful for ZLK oscillations: a system where b is at a sufficiently high semimajor axis will be able to sustain ZLK oscillations of extremely high amplitude if only GR is considered, but if tides are accounted for as well during a high-eccentricity epoch the ZLK effect will be quenched.

Consider now the evolution of a body under the influence of tidal effects experiencing ZLK oscillations. If octupole level effects are accounted for (Naoz et al., 2013; Naoz, 2016), the maximum eccentricity of the ZLK oscillations is not constant; rather, the maxima increase slowly over the octupole timescale (Naoz et al., 2013; Li et al., 2014b). In addition, during each high-eccentricity epoch tides will shrink the orbit. The result is that over the course of ZLK oscillations, b's orbit will move towards the upper left corner of Figure 6.5. Inevitably, at some point there will be a crossing (mostly likely with the gold line), and ZLK oscillations will be quenched. Then b is marooned on a high-eccentricity orbit. This state is only temporary, however, as tides continue to be significant. Now, tidal dissipation acts efficiently to circularize and shrink the planet's orbit, until b settles into a close-in, circular orbit. Tidal circularization conserves angular momentum L_b , so

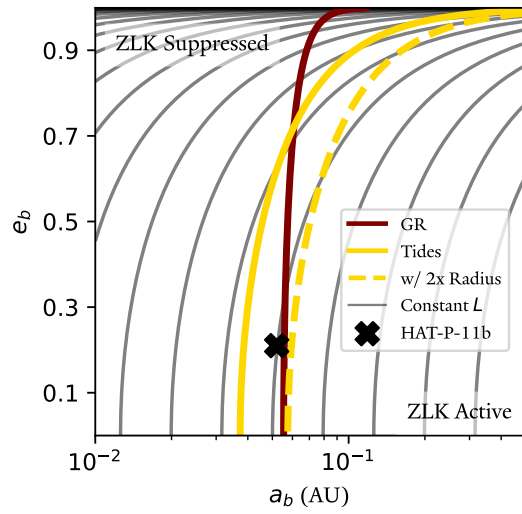


Figure 6.5. Comparison of precessions from the ZLK effect to general relativity and tides in semimajor axis-eccentricity space, using HAT-P-11's present-day configuration. The maroon line represents where the precessions due to general relativity and ZLK are exactly equal, while the gold lines represent tides with HAT-P-11 b's present day radius (solid) and tides with twice this radius (dashed). Lines of constant angular momentum are shown in gray. HAT-P-11 b's present-day position is shown as a black cross. A planet experiencing ZLK-induced high-eccentricity migration will move towards the upper left hand corner in eccentricity-semimajor axis space until it encounters one of the colored curves, at which point ZLK oscillations are quenched and it follows one of the contours of constant angular momentum to zero eccentricity.

b 's evolution through phase space will follow the contour of constant L_b (plotted in grey) intersecting the gold line until the planet reaches zero eccentricity.

Taking this together, the basic idea of our hypothesis is as follows. HAT-P-11 b initially formed at a significantly greater semimajor axis than we see today. The violent scattering events described in the previous section resulted in a significant orbital misalignment between HAT-P-11 b and HAT-P-11 c, which initiated ZLK oscillations in HAT-P-11 b's orbit. Tidal dissipation gradually tightened HAT-P-11 b's orbit until tidal precession broke the ZLK oscillations, at which point the highly eccentric HAT-P-11 b began the process of tidal circularization. We propose that HAT-P-11 b is in this final state, having not yet fully circularized. This is similar to the story proposed by [Beust et al. \(2012\)](#) to explain the orbit of the similarly eccentric close-in sub-Neptune GJ 436, but in their case the outer perturber is not well constrained.

6.3.3 Radius Evolution

It turns out that the story we just elucidated is incomplete, since simple ZLK migration alone cannot explain HAT-P-11 b's orbit. This is due to how relatively close-in HAT-P-11 c is. From Equation (6.8), the precession rate associated with the ZLK effect scales very strongly with a_c . Since a_c is small, the precession associated with ZLK oscillations is strong, and thus very high eccentricities are required for tides to break the ZLK cycles (e.g., in comparison to GJ 436). Inspection of Figure 6.5 provides a clearer picture. The contour that HAT-P-11 b presently lies on does not intersect the solid golden line in the phase space shown. While it does intersect the dark red line denoting suppression of ZLK oscillations due to GR precession, this mechanism would require suppression of ZLK oscillations at an eccentricity of just ≈ 0.5 at a semimajor axis where tidal damping is slow, and is not something that we see in our simulations. In order for HAT-P-11 b to have a constant L path from tidal quenching of ZLK oscillations to its current orbit, we would have to extend Figure 6.5 well to the right. We find that initializing HAT-P-11 b at these larger orbital separations typically results in dynamical instability, and often ejection of HAT-P-11 b. In other words, the quenching of ZLK by tidal effects in a reasonable initial parameter space cannot bring HAT-P-11 b to its present-day orbit via tidal circularization. We see that more realistic contours of constant L terminate significantly closer to the star, sometimes by up to an order of magnitude. This tendency to overshoot HAT-P-11 b's present-day orbit is insensitive to initial conditions and is confirmed with N -body simulations. Thus, the present-day configuration cannot be explained with traditional ZLK migration with fixed planet radius and equilibrium tides alone.

However, the planet's radius can be inflated due to tidal heating during ZLK

migration. Radius evolution of planets due to tidal heating is a degree of freedom that is typically unexplored in studies of the ZLK effect. During ZLK oscillations, HAT-P-11 b will reach very high eccentricities and hence experience many close pericenter approaches with the host star. During these close approaches, tidal heating becomes very significant and acts to inflate the planet’s envelope. Radius inflation from tidal heating is a well-explored concept: it has been invoked to explain the anomalously large radii of hot Jupiters (Bodenheimer et al., 2001) and sub-Saturns (Millholland, 2019; Millholland et al., 2020). These works show that the radius of a sub-Neptune or sub-Saturn can reasonably be inflated over a factor of two via this mechanism.

This effect may play a significant role in the dynamics of the system, as from Equation (6.12) tidal precession scales as $\propto R_b^5$. Indeed, we see from the dotted golden line in Figure 6.5 that increasing the radius of HAT-P-11 b by a factor of two breaks the ZLK oscillations significantly earlier, and now there does exist a reasonable contour of constant L_b that can deliver HAT-P-11 b to its present-day orbit. Coupled dynamical and thermal evolution of hot Jupiters were explored in the context of planet-planet scattering by Rozner et al. (2022); Glanz et al. (2022), who found that accounting for radius inflation significantly accelerated the formation and destruction of hot Jupiters and enhanced the production of warm Jupiters. Petrovich (2015) investigated ZLK migration for initially inflated planets which slowly shrink down. However, fully self-consistent coupled dynamical and thermal evolution in the context of ZLK migration has not been explored in detail. Given the uncertainties in our system, we employ a simplistic model for the radius inflation of HAT-P-11 b in this work, and we defer a more nuanced prescription for self-consistent thermal and orbital evolution to future work.

Millholland et al. (2020) generated 10,000 MESA models (Paxton et al., 2011), which modify and build upon the publicly available MESA models for sub-Saturns developed by Chen & Rogers (2016). These models spanned four principal parameters: mass M , envelope mass fraction f_{env} , flux from the host star F , and internal luminosity \mathcal{L} ². Each model was then evolved forward in time for 10 Gyr, after which a final radius R was reported. We fit a subset of the Millholland et al. (2020) models appropriate to HAT-P-11 b in order to construct a luminosity-radius

²Note that Millholland et al. (2020) parameterized the tidal luminosity with the factor $\Gamma \equiv \log_{10} \left[\frac{Q'(1+\cos^2 \epsilon)}{\sin^2 \epsilon} \right]$, where $Q' \equiv 3Q/2k_2$ is the reduced tidal quality factor and ϵ is the planetary obliquity. This is because both Millholland et al. (2020) and their progenitor study Millholland (2019) focused on obliquity tides. However, we are agnostic to the specific source of tides in this study, and as such require only the total luminosity deposited at the core-envelope interface.

relationship using a fourth-order polylogarithmic function:

$$\frac{R}{R_E} = A \left[\log_{10} \left(\frac{\mathcal{L}}{\mathcal{L}_\odot} \right) \right]^4 + B \left[\log_{10} \left(\frac{\mathcal{L}}{\mathcal{L}_\odot} \right) \right]^3 \\ + C \left[\log_{10} \left(\frac{\mathcal{L}}{\mathcal{L}_\odot} \right) \right]^2 + D \left[\log_{10} \left(\frac{\mathcal{L}}{\mathcal{L}_\odot} \right) \right] \\ + E \quad (6.13)$$

where $A = 5.23 \times 10^{-4}$, $B = 3.37 \times 10^{-2}$, $C = 0.801$, $D = 8.357$, and $E = 3.596 \times 10^1$. Here the orbit-averaged tidal luminosity of the planet is given by (Mardling & Lin, 2002):

$$\langle \mathcal{L} \rangle = - \mu_{b*} a_b^2 n_b \left(\frac{m_*}{m_b} \right) \left(\frac{R_b}{a} \right)^5 \left(\frac{3k_{2,b}}{2Q_b} \right) \\ \times \left[\frac{1}{2} (\Omega_e^2 h_1(e) + \Omega_q^2 h_2(e)) + \Omega_h^2 h_3(e) \right. \\ \left. - 2n_b \Omega_h h_4(e) + n^2 h_5(e) \right], \quad (6.14)$$

where Ω_e , Ω_h , Ω_q are functions of the planetary spin axis and present orbital configuration, while h_1, h_2, h_3, h_4, h_5 are functions of eccentricity. The exact expressions are given in the Appendix. Note the dependence on both orbital parameters and the spin axis. Since our code self-consistently tracks the spin and orbital evolution, this expression correctly accounts for both eccentricity and obliquity tides.

We select from the models generated by Millholland et al. (2020) as follows. Out of the 10,000 models they generated, we take a slice in mass ($20 M_E < M < 25 M_E$) appropriate for the observational constraints on HAT-P-11 b. The value of f_{env} is not at all constrained, but the present-day radius and orbital parameters of HAT-P-11 b are well-constrained (Yee et al., 2018). It is therefore vital to match these parameters at the end of our simulations. There is a degeneracy between f_{env} and the value of the tidal quality factor Q in reproducing HAT-P-11 b's radius at its present-day orbit, since the observed radius could be equally well-described by a small envelope mass with efficient dissipation (low Q) or by a large envelope mass with weaker dissipation (high Q). We assume a fiducial value of $Q = 10^5$, and then use Equations (6.13) and (6.14) to match the present-day radius of HAT-P-11 b given its present-day orbital parameters. There is some degree of uncertainty in the precise values of many of the values in Equation (6.14) at the end of our simulations, but we can make a number of simplifying assumptions to obtain a

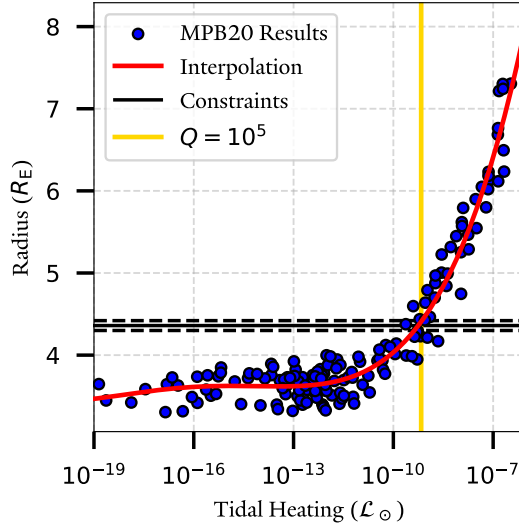


Figure 6.6. Radius-luminosity relationship derived from the models of Millholland et al. (2020). In blue are 158 of their MESA model results using the cuts described in the main text. The red line represents our best-fit to the data, using a fourth-order polylogarithmic function given in Equation (6.13). The gold vertical line shows the tidal heating at HAT-P-11 b’s present-day orbital configuration given $Q = 10^5$. The black horizontal lines show the observational constraints on HAT-P-11 b’s radius. Note that the gold and red lines intersect with the black line, meaning HAT-P-11 b’s present-day radius is reproduced.

ballpark estimate. Most of the uncertainties lie in the values of Ω_e , Ω_h and Ω_q , which are dot products of the spin vector with the Runge-Lenz vector, orbit normal, and the cross product of the two former, respectively. If we assume zero planetary obliquity as expected given significant tidal dissipation (Su & Lai, 2022b), the spin axis will be aligned with the orbital angular momentum, and $\Omega_e, \Omega_q = 0$. If we further assume that the planet rotates at the pseudo-synchronous spin rate, Ω_h can be calculated. Plugging these values and orbital parameters associated with HAT-P-11 b’s present-day orbit, along with $Q = 10^5$, gives the present-day tidal luminosity of HAT-P-11 b. We select a range of f_{env} such that there is a good match with this value. We ultimately choose $0.05 < f_{\text{env}} < 0.1$. With these slices we consider 158 models. The models we selected, as well as our best-fit line, are plotted in luminosity-radius space in Figure 6.6.

We now use our fit to the MESA models to evolve HAT-P-11 b’s radius during the simulations. In the interest of computation time and as our expression is orbit-averaged, we do not recompute the planet’s radius every timestep. Rather, radius evolution is computed once per orbit of HAT-P-11 b. Once per orbit, the orbit-averaged luminosity is calculated and fed into our luminosity-radius relation Eq. (6.13), and the radius of HAT-P-11 b is correspondingly updated. We again

emphasize that our prescription for the thermal radius evolution of the planet is a first-order approximation, where we assume the planet’s radius responds effectively instantaneously to the tidal luminosity. A more realistic prescription would include a time-delayed response to the tidal heating, and a fully self-consistent numerical prescription could involve codes that couple the dynamical evolution of the system to the planet’s thermal evolution. For example, see [Glanz et al. \(2022\)](#) who coupled outputs from MESA ([Paxton et al., 2011](#)) and AMUSE ([Portegies Zwart et al., 2009](#)). While we do not use these nuanced prescriptions in the present work, we assert that our first-order approximation qualitatively achieves similar results. As our orbital code tracks tidal luminosity self-consistently, our planet will ultimately be inflated to the same degree, and the ZLK cycles will be broken at similar times. The improvement which would likely produce the largest discrepancy between our model is our choice of equilibrium tides, but we defer treatment of the more realistic dynamical tide model to future work.

6.3.4 N-body simulations

We investigate the present-day orbit of HAT-P-11 b via ZLK migration through a suite of N -body simulations using REBOUND. The setup of our numerical simulations are as follows. We initialize HAT-P-11 A and c in their present-day orbital configurations. We select the best-fit values for the mass, semimajor axis and eccentricity of HAT-P-11 c from Table 6.1. The spin-orbit misalignment of HAT-P-11 c is less constrained; we draw from a uniform distribution $\psi_{c,i} \in \{33.3^\circ, 50.26^\circ\}$, where the lower bound is selected from the 3σ confidence interval from the observational posteriors, and the upper bound from the 2σ confidence interval of our four-body scattering simulations. The asymmetric lower bound is selected to encompass more of the highly non-Gaussian observational posterior. The nodes are randomly distributed. HAT-P-11 b is initialized with orbital elements randomly drawn from uniform distributions informed from the 2σ distributions obtained in our four-body scattering simulations: $a_b = \{0.154 \text{ AU}, 0.518 \text{ AU}\}$, $e_b = \{0.01, 0.70\}$ and $\psi_b = \{1.01^\circ, 97.0^\circ\}$. We initialize the mass with the best-fit value from Table 6.1, and the radius with Equation (6.13).

We note that our scattering simulations often include an extra surviving distant planet. The impact of distant perturbers on the classic ZLK hierarchical configuration was studied by [Best & Petrovich \(2022\)](#), who found that it generates chaotic spin-orbit evolution and makes achieving retrograde orbits easier, which would be favorable to our scenario. However, the first-order dynamics do not change, so we do not model it in our simulations. We also comment on the possibility of direct ZLK oscillations occurring between HAT-P-11 c and this surviving distant perturber. This is a fairly rare occurrence; only 653 simulations, or 14%, result in

a mutual inclination between HAT-P-11 c and the surviving outer planet greater than 40° , so ZLK oscillations are rarely triggered. However, for these simulations where the prerequisite mutual inclination for ZLK cycles is reached, $|\dot{\omega}_{\text{ZLK}}| > |\dot{\omega}_{\text{GR}}|$ so ZLK cycles are in fact active. Nevertheless, the parameter space for a surviving external planet is large and unconstrained from observation, and it doesn't change the dynamics of the inner planets qualitatively. Thus, we do not model this outer planet in our ZLK simulations.

We also model the effects of general relativity and tides. We use REBOUNDx (Tamayo et al., 2020a) to model both. For GR precession, we use the gr prescription (Anderson et al., 1975), appropriate for systems with a dominant central mass. We consider self-consistent spin, tidal and orbital evolution using the `tides_spin` effect (Lu et al., 2023), which provides the ability to evolve the evolution of the stellar spin axis for consistent spin-orbit misalignment tracking as well. For planet b, we use fiducial parameters of $k_2 = 0.5$, $I = 0.25$ appropriate for a Uranus-like planet (Yoder, 1995; Lainey, 2016), and we initialize its spin state as both pseudo-synchronized and aligned with the orbit. Planet c is considered a point particle, and the effects of structure are not accounted for. While evolution of the stellar spin axis is considered as part of the equilibrium tides model, spin-down due to stellar evolution, which would occur during the early phases of our simulations (Bouvier et al., 1997), is not modeled. These effects are not expected to be significant for our simulations. Authors such as Bolmont et al. (2012) and Faridani et al. (2023, 2024) explored the effects of stellar spin evolution on planetary orbits and only found meaningful impacts for planets within $a = 0.05$ AU, well within the hypothesized original orbit of HAT-P-11 b.

Tides on the host star and planet c are not considered, but we set the value of planet b's tidal parameter to $\tau_b = 10^{-5}$ years. This is an unrealistically high value of τ , chosen to minimize computation time: direct N-body simulations with a realistic τ value proved to be computationally infeasible. This is a common practice in numerical simulations (e.g Bolmont et al., 2015; Becker et al., 2020). Scaling τ does not change the qualitative behavior of the system. Neither the ZLK timescale nor the tidal precession rate, Equations (6.6) and (6.12) respectively, depend on the value of the tidal parameter. The only dependence on τ is the rate of orbital energy drained from tides. Thus, our scaled-up value of τ serves only to drain more energy from the planet's orbit every ZLK cycle (therefore decreasing the semimajor axis more) and increase the rate at which HAT-P-11 b circularizes once the ZLK oscillations are ultimately quenched. These both only serve to linearly modify the timescale in which the planet reaches the final stage of evolution.

We now briefly discuss what realistic values of τ may be. While the values of tidal parameters in exoplanets are very poorly constrained, estimates of Neptune's $\tau \sim 10^{-8}$ years are based on the orbit of its satellites Proteus and Larissa (Zhang

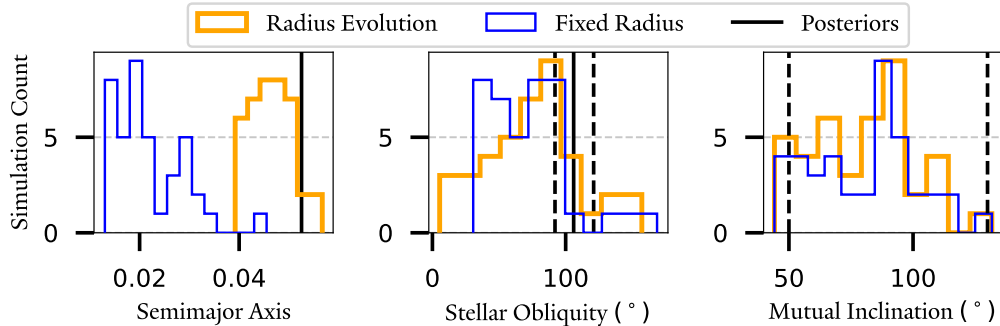


Figure 6.7. Results from a population synthesis of ZLK simulations. We consider 40 simulations with radius evolution (orange) and 40 with fixed radius (blue). We compare distributions of semimajor axis, spin-orbit misalignment and mutual inclination. We see that the fixed radius model cannot generate HAT-P-11 b's present-day semi-major axis, but the model with tidally-driven radius inflation can.

& Hamilton, 2007). Therefore, the tidal timescale in the N-body simulations is a factor $\sim 10^3$ longer than the simulation timescale.

6.3.5 Simulation Results

Figure 6.7 shows distributions of spin-orbit misalignment and eccentricity for a population synthesis of 100 systems. We initialize each simulation as described in the previous section and run until the ZLK cycles are quenched and the orbit has circularized to the present-day eccentricity $e_b = 0.218$. At this point, the simulation is halted. To illustrate the effects of radius inflation, we also run the same initial condition but fix the radius of HAT-P-11 b to its present-day value throughout the course of the simulation. We allow each simulation to run for 10 Myr, which corresponds to 10 Gyr in when time is rescaled appropriately. 40 simulations with radius inflation are able to quench ZLK oscillations and circularize in this timeframe, with the remaining 60 either never initiating ZLK oscillations or being unable to quench them in time. For the simulations with fixed radius, 40 simulations quench and circularize in time. For the population synthesis that considers radius inflation, we see that while the best-fit observational values are not the most favored there is nonetheless a high proportion of simulations that match the constraints, and we do not require fine-tuning to reproduce our posteriors. The population synthesis without radius inflation does not exhibit significant differences in the spin-orbit misalignment or mutual inclination distributions. However, as expected this model greatly underpredicts the semimajor axis of HAT-P-11 b: all simulations predict an orbit with $a_b < 0.045$ AU (consistent with the implication of Figure 6.5).

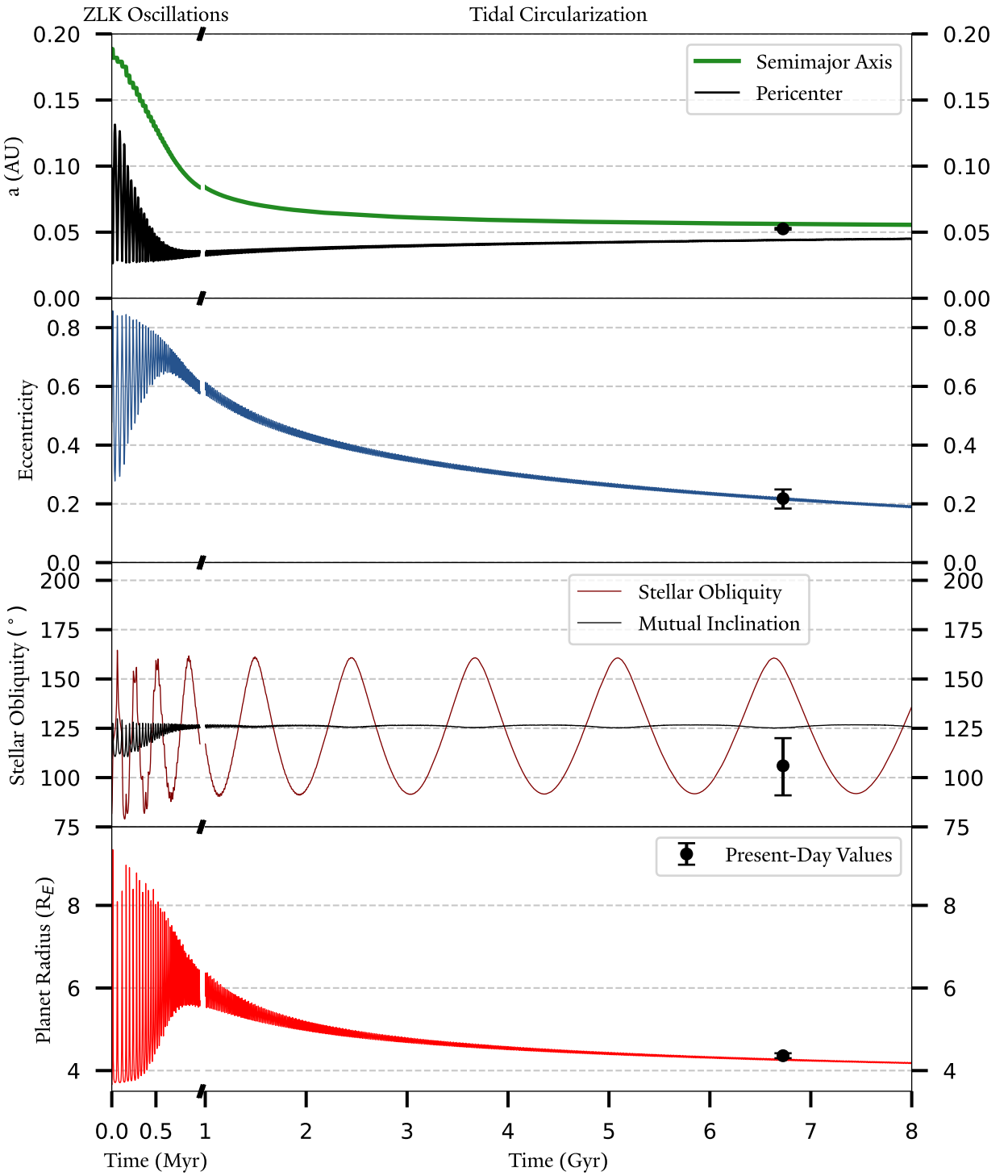


Figure 6.8. Fiducial ZLK migration of HAT-P-11 b. From top to bottom, HAT-P-11 b's semimajor axis, eccentricity, spin-orbit misalignment and radius are shown with the colored lines. The black dots represent HAT-P-11 b's measured orbital parameters, with the error bar indicating the 1σ confidence interval. We posit that HAT-P-11 b is still in the tidal circularization stage after the suppression of ZLK oscillations. There is excellent agreement between our simulation results and observed values.

Figure 6.8 shows one of our simulations in detail. Table 6.2 lists the initial orbital parameters of the simulation, as well as the final values of interest. During the first phase of the simulation, ZLK oscillations are active and the planet experiences the characteristic coupled eccentricity and inclination oscillations. At each high-eccentricity epoch, tides act on the planet to lower its semimajor axis. The radius evolution of the planet is also plotted, and we see that during each high-eccentricity epoch the planet inflates to over twice its present-day radius. Note that the minimum pericenter distance (~ 0.02 AU) is well outside twice of the tidal disruption radius ($r_t = R_p(M_*/M_p)^{1/3} \sim 0.008$ AU), so we do not include mass loss due to tidal stripping in our model, as the effects are weak (Guillochon et al., 2011). Later, the ZLK oscillations are damped during a high eccentricity epoch. Tides continue to act to circularize the planet’s orbit. In the meantime, the orbit normal of HAT-P-11 b precesses about the invariant plane of the system (essentially HAT-P-11 c’s orbit normal), as expected, resulting in periodic spin-orbit misalignment oscillations. As expected, the stellar spin axis and the orbit of HAT-P-11 c do not change significantly over the course of the integration.

We comment again on the interpretation of timescales, given our choice of τ in order to speed up computations. Please refer to Section 6.3.4 for justification regarding the choice of an enhanced dissipation rate. The enhanced dissipation rate affects the phase when tidal dissipation dominates, and thus we scale the timescales on the right-hand side of the panel to the realistic values accordingly. Note that with a more realistic tidal time-lag, we would expect to see more spin-orbit misalignment cycles on the right-hand side of the plot when tides dominate (since the orbital precession frequency does not depend on tidal dissipation and shouldn’t be scaled). In addition, we would expect to have more ZLK cycles on the left-hand side, since each cycle leads to a weaker semi-major axis decay. However, the qualitative behavior of the evolution is the same.

The age of the HAT-P-11 system is not well-constrained: Yee et al. (2018) propose an age of $6.5^{+5.9}_{-4.1}$ Gyr, while Morton et al. (2016) present an estimate of $2.69^{+2.88}_{-1.24}$ Gyr. Our results are consistent with both estimates of the system age. Note that the timescale of ZLK migration varied by around an order of magnitude, depending on initial conditions.

The present-day observational constraints on HAT-P-11 b’s orbit are also shown on Figure 6.8. Our simulation is able to match all values very well: we reproduce all observed values within 2σ other than semimajor axis, which is well-reproduced qualitatively. We propose that HAT-P-11 b is currently in this final stage of evolution and is still in the process of tidal circularization. We conclude that ZLK migration coupled with thermally driven radius evolution is capable of explaining the present-day orbit of HAT-P-11 b remarkably well. Again, we emphasize that we did not perform an exhaustive parameter space analysis of this system.

Parameter	Initial b	Final b	Initial c	Final c
$R (R_{\text{Earth}})$	3.69	4.27	N/A	N/A
$a (\text{AU})$	0.19	0.056	4.1	4.1
e	0.48	0.22	0.65	0.65
$\psi (\text{°})$	82	156	35.3	35.4

Table 6.2. Relevant input parameters and output values of the REBOUND simulation shown in Figure 6.8. The final values are the values at the time corresponding to the black dot in Figure 6.8, which is where e_b is equal to the best fit value. The orbit of HAT-P-11 c does not change significantly over the course of the simulation.

Rather, our aim is to qualitatively show that such a process is capable of reproducing HAT-P-11 b’s orbit.

We briefly comment on the sensitivity of our results to the value of the tidal parameter τ , which is almost entirely unconstrained. Of the simulations that successfully reached HAT-P-11 b’s present-day configuration, the mean evolution time is 2.44 Gyr and the 2σ range is $\{0.06, 16.96\}$ Gyr. The distribution of evolution times is sculpted by the initial configuration of the system. For instance, configurations that are initialized with a higher mutual inclination tend to reach the present-day state faster, and vice-versa. The center of the distribution is sensitive to the value of the tidal parameter τ , which shifts the distribution linearly. We provide a reasonable range of τ values that are consistent with our simulations by matching the upper limit of our simulation times with the lower limit of the age estimates provided by Yee et al. (2018), and vice versa. This gives $\tau \in \{4.84 \times 10^{-11}, 7.06 \times 10^{-8}\}$ years as the range of τ able to reconcile our results with the reported age of the system. At HAT-P-11 b’s present-day semimajor axis, this corresponds to $Q \in \{1.5 \times 10^4, 2.20 \times 10^7\}$.

6.4 Conclusions

We have proposed a two-step process of planet-planet scattering followed by subsequent ZLK migration to explain the unusual architecture of the HAT-P-11 system. A violent scattering history in which two former planets are ejected from the system is a viable explanation for the high eccentricity and spin-orbit misalignment of HAT-P-11 c. Then, the ZLK mechanism follows naturally with large mutual inclination between HAT-P-11 b and c. We find that traditional ZLK migration with fixed planetary radius cannot reproduce the orbit of HAT-P-11 b, but accounting for thermally-driven radius inflation can. Using N -body simulations, we have verified that this scenario is consistent with all observational

constraints as well as the estimated age of the system. The HAT-P-11 system is thus an excellent case study of planet-planet scattering and ZLK migration, both of which are common effects believed to sculpt the architectures of many planetary systems.

HAT-P-11 b adds to a growing census of planets on polar orbits around their host stars (Albrecht et al., 2021) – the exact significance of this peak in the stellar obliquity distribution is sensitive to detection biases and thus has not been definitively confirmed (Siegel et al., 2023; Dong & Foreman-Mackey, 2023). ZLK migration triggered by the presence of an external planetary perturber has been shown to be theoretically capable of generating the peak of perpendicular planets (Petrovich & Tremaine, 2016), and Vick et al. (2023) demonstrated that if the inner planet starts on an initially misaligned orbit, then perpendicular planets are preferentially produced. They attributed this primordial misalignment to an inclined binary companion torquing the protoplanetary disk (Spalding & Batygin, 2014; Zanazzi & Lai, 2018; Gerbig et al., 2024). We show that planet-planet scattering can lead to similar ZLK initial conditions for single star systems, and hence we demonstrate that the interplay between planet-planet scattering and ZLK migration can easily produce perpendicular planets as well. While spin-orbit misalignment measurements of close-in planets are relatively common, the same cannot be said of the longer-period giants which would constitute said external perturbers (Rice et al., 2021). The possibility of more spin-orbit misalignment measurements of these longer-period planets in the near future will allow more comprehensive analysis of systems characterized by planet-triggered ZLK migration.

Our study demonstrates the importance of considering the evolution of the physical characteristics of a planet during ZLK migration, in addition to the orbital parameters. In the high-eccentricity epochs of ZLK migration, the planet’s envelope can inflate due to tidal heating in the interior. This is highly significant, affecting not only the timescale of ZLK migration but also the equilibrium semimajor axis the planet settles at. This is particularly important in the close companion ZLK cases, since the strength of the ZLK perturbations is relatively much stronger. We show that radius inflation unlocks areas of parameter space which otherwise would be impossible to access through standard ZLK migration with fixed radius. HAT-P-11 is one of the first candidates with two confirmed planets in which ZLK migration is hypothesized to have occurred. A few other systems for which planet-planet ZLK may be possible have begun to emerge (Beust et al., 2012; Petrovich et al., 2018; Bardalez Gagliuffi et al., 2021), and as more such systems are discovered it will be crucial to consider the evolution of the physical parameters of the planet. During the preparation of this manuscript Yu & Dai (2024) performed a similar analysis on the WASP-107 system. Their study used a secular orbital evolution code and also accounted for physical processes such as tidal disruption.

This work represents another step forward into more nuanced consideration of coupled structure and orbital evolution.

While our study highlights the importance of considering physical evolution of the planet, our prescription is a first-order approximation. Given the significant uncertainties in quantities such as internal composition and tidal quality factor present in all exoplanetary systems we have not explored more sophisticated models, and assert that our first-order approximation provides sufficient qualitative insight. However, future work could more deeply consider avenues such as 1) a more sophisticated tidal model – calculating tidal heating and orbital evolution based on dynamical tides, which are more accurate for high eccentricity orbits, 2) coupling tidal heating and radius inflation during orbital evolution (e.g., implementing a lag time such that the radius does not respond instantaneously to tidal forcing, and considering the change in planetary structure when calculating tidal effects ([Ogilvie, 2009](#))) and 3) considering the effects of atmospheric mass loss ([Vissapragada et al., 2022](#)).

Finally, we note that while it may be tempting to place constraints on quantities such as the tidal quality factor with this work, this must be done with caution. The final state of HAT-P-11 b depends on the strength of tidal forcing compared to the magnitude of the precession induced by the ZLK effect. In practice, this means that it depends on a complex interplay of the initial semimajor axis, tidal quality factor, tidal love number, initial mutual inclination, and internal composition, none of which are well-constrained. To explore such a large parameter space would be a herculean task, and we again stress that this study does not claim to have done so. Rather, our work should be viewed more qualitatively as a proof-of-concept that thermally-driven radius inflation is highly significant towards the final products of planet-planet ZLK migration.

6.5 Acknowledgements

We thank the anonymous referee for comments which greatly improved the manuscript. We thank Doug Lin, Yasmeen Asali, Daniel Fabrycky, Konstantin Gerbig, Evgeni Grishen, Yurou (Nina) Liu, Rosemary Mardling, Michael Poon, Chloe Neufeld, and Yubo Su for insightful discussions. GL is grateful for the support by NASA 80NSSC20K0641 and 80NSSC20K0522. This work has benefited from use of the Grace computing cluster at the Yale Center for Research Computing (YCRC). Some plots in this work have made use of the colormaps in the CMasher package ([van der Velden, 2020](#)).

6.6 Appendix: Self-Consistent Spin, Tidal and Dynamical Equations of Motion

The ZLK migration results in Section 6.3 account for spin and tidal evolution in the equilibrium tide framework. The equations of motion used are reproduced from Egginton et al. (1998), but see also Alexander (1973); Hut (1981); Mardling & Lin (2002) for a deeper review of equilibrium tide theory. Also see Lu et al. (2023) for details on the specific implementation.

In addition to point-particle gravity, we consider the acceleration due to the quadrupole distortion of body 1, which accounts for both spin distortion and tidal perturbation from another body 2:

$$\mathbf{f}_{\text{QD}}^{(1,2)} = r_1^5 k_{L,1} \left(1 + \frac{m_2}{m_1}\right) \cdot \left[\frac{5(\boldsymbol{\Omega}_1 \cdot \mathbf{d})^2 \mathbf{d}}{2d^7} - \frac{\Omega_1^2 \mathbf{d}}{2d^5} - \frac{(\boldsymbol{\Omega}_1 \cdot \mathbf{d}) \boldsymbol{\Omega}_1}{d^5} - \frac{6Gm_2 \mathbf{d}}{d^8} \right], \quad (6.15)$$

with an analogous expression for the quadrupole distortion of body 2 due to body 1. We also consider the acceleration due to the tidal damping of body 1:

$$\mathbf{f}_{\text{TF}}^{(1,2)} = - \frac{9\sigma_1 k_{L,1}^2 r_1^{10}}{2d^{10}} \left(m_2 + \frac{m_2^2}{m_1}\right) \cdot \left[3\mathbf{d}(\mathbf{d} \cdot \dot{\mathbf{d}}) + (\mathbf{d} \times \dot{\mathbf{d}} - \boldsymbol{\Omega}_1 d^2) \times \mathbf{d} \right], \quad (6.16)$$

again, with an analogous expression for the tidal damping of body 2.

6.7 Appendix: Orbital Parameter Definitions

In Equation (6.14) several terms relating to the precise orientation of the orbit are mentioned but not defined. These are provided here. First, we define the spin vector $\boldsymbol{\Omega}$, which parameterizes both the direction and magnitude of the planet's rotation. Next, we define two vectors \mathbf{e}, \mathbf{h} . These are the Runge-Lenz vector (pointing in the direction of periastron, with magnitude equal to the eccentricity) and the orbital angular momentum vector. We define a third vector $\mathbf{q} \equiv \mathbf{e} \times \mathbf{h}$. We can thus define the following projections of the spin axis:

$$\Omega_e = \boldsymbol{\Omega} \cdot \hat{\mathbf{e}}, \Omega_h = \boldsymbol{\Omega} \cdot \hat{\mathbf{h}}, \Omega_q = \boldsymbol{\Omega} \cdot \hat{\mathbf{q}} \quad (6.17)$$

The functions of eccentricity $h_i(e)$ are also given:

$$h_1(e) = \frac{1 + (3/2)e^2 + (1/8)e^4}{(1 - e^2)^{9/2}} \quad (6.18)$$

$$h_2(e) = \frac{1 + (9/2)e^2 + (5/8)e^4}{(1 - e^2)^{9/2}} \quad (6.19)$$

$$h_3(e) = \frac{1 + 3e^2 + (3/8)e^4}{(1 - e^2)^{9/2}} \quad (6.20)$$

$$h_4(e) = \frac{1 + (15/2)e^2 + (45/8)e^4 + (5/16)e^6}{(1 - e^2)^6} \quad (6.21)$$

$$h_5(e) = \frac{1 + (31/2)e^2 + (255/8)e^4 + (185/16)e^6 + (25/64)e^8}{(1 - e^2)^{15/2}} \quad (6.22)$$

Chapter 7

Conclusion

"If I look back I am lost."
– Daenerys I Targaryen

7.1 Summary

In summary, this dissertation details my own personal contributions to the fields of numerical methods, spin-orbit dynamics and planetary structure evolution. These contributions have stood upon the shoulders of giants, and it is my hope that this work itself serves as a stepping stone for future explorations. In this Conclusion, I enumerate several exciting areas of future development that will build upon my thesis work.

7.2 The Search for Planet Nine

During the period in which this thesis was developed, various lines of evidence emerged, some supporting and others challenging the existence of Planet 9. [Batygin et al. \(2024\)](#) and [Siraj et al. \(2024\)](#) have performed detailed numerical simulations that reproduce the observed apsidal clustering of TNOs and heavily favor the presence of a distant outer planet. These results have refined the predicted orbit and on-sky position of the putative Planet 9. On the other hand, [Napier et al. \(2021\)](#) and [Bernardinelli et al. \(2022\)](#) contend that there is no need for the existence of a Planet 9. They assert that the observed TNO clustering can be explained via observational bias alone. Verifying the existence of Planet 9 is crucial to confirming the hypothesis discussed in Chapter 4.

An unambiguous detection of Planet 9 is in principle possible, and would set the debate to rest. [Rice & Laughlin \(2020\)](#) developed a promising algorithm to stack frames from the Transiting Exoplanet Survey Satellite (TESS), a method capable of directly detecting a faint Planet 9. The search is ongoing, and the astronomy community awaits the results with bated breath. Recently, [Rowan-Robinson \(2022\)](#) claimed the detection of a Planet 9 candidate in IRAS data. The candidate is inconsistent with the best-fit models of Planet 9's orbit, and thus is unlikely to be the cause of the observed apsidal alignment seen. The discovery nonetheless merits great excitement, and I am confident that many more Planet 9 candidates will be discovered in the near future. The imminent launch of the Vera Rubin Observatory will be a great asset to the hunt.

7.3 The James Webb Space Telescope

The James Webb Space Telescope (JWST) launched on December 25, 2021, and has already revolutionized the precision and quality of astronomical data. One particularly exciting prospect is JWST's ability to parse out the deviations from a perfect spherical shape of a transiting exoplanet with extraordinarily precise lightcurves.

This is an incredibly powerful probe of an exoplanet’s rotation rate and internal composition (Hellard et al., 2019). With this same technique, it is possible to detect transiting planetary rings (Akinsanmi et al., 2018) and exomoons (Cassese et al., 2024b). Regarding planetary oblateness specifically, we have previously lacked the instrumental precision to place meaningful constraints on planetary interior structure. JWST has changed that, and consequently in very recent years a number of publicly-available codes have been developed with the aim of extracting planetary oblateness from JWST lightcurves. These include `squishyplanet` (Cassese et al., 2024a), `eclipsoid` (Dholakia et al., 2024) and `greenlturn` (Price et al., 2024). The very first such oblateness measurements have been made on Kepler-51 d (Lammers & Winn, 2024a) and Kepler-167 e (Liu et al., 2024). Many more of these measurements are planned. Our understanding of exoplanetary interior structure is, at present, almost entirely unconstrained observationally. However, we stand on the precipice of a revolution – this knowledge gap will soon be shattered.

Another of JWST’s many astounding capabilities is detailed and nuanced transmission spectroscopy of exoplanetary atmospheres. Transmission spectra reveal vital information about atmospheric composition, effective temperature, and in some cases may even hold the keys to detecting biosignatures and hence life. For the work in this dissertation, the most exciting prospect is using transmission spectra as a probe of interior structure. Sing et al. (2024) and Welbanks et al. (2024) probed the atmosphere of the warm Neptune WASP-107 b, and by using disequilibrium chemistry models are able to constrain a high internal heat flux and massive core. They attribute this high internal heat to tidal heating, marking the first definitive observational detection of this phenomenon. The imprint of tidal heating on exoplanetary demographics has only been discussed theoretically – finally, the prospect of verification with real data does not seem so far-fetched.

7.4 GAIA Data Release 4

In studies that attempt to link dynamics to demographics, one massive unknown degree of freedom is the orbital architectures of distant planets. Jupiter-mass planets at orbital separations of 1-10 AU are extremely difficult to detect via any method currently available to us. Without the knowledge of outer exoplanetary system architectures, dynamicists are missing a crucial piece of the puzzle.

In the very near future, this will change. The Gaia satellite (Gaia Collaboration et al., 2016) is mapping the positions, distances, and motions of over a billion stars in the Milky Way with unprecedented precision. The next public release of Gaia Data, Data Release Four, will present the full astrometric time-series data for every star in the Gaia catalogue. According to Perryman et al. (2014), over 70,000 such

planets may be detected based on Gaia’s theoretical capabilities.

7.5 Towards a Unified Theory of System Formation

As dynamicists, our ultimate goal is to construct a truly unified theory to explain how planetary systems form. On both observational and theoretical fronts, tremendous progress has been made in the past five years by our brightest and most talented researchers. I am lucky enough to call many of them my friends and colleagues.

Measurement of the 3-D architecture of exoplanetary systems is critical to understanding their formation pathways. [Rice et al. \(2021\)](#) has spearheaded this effort with the SOLES survey, designed to comprehensively characterize the stellar obliquity distribution. As more comprehensive data streams in, the picture of planetary formation becomes more and more intriguing. For instance, [Rice et al. \(2022\)](#); [Wang et al. \(2024\)](#) find that warm Jupiters are much more aligned than hot Jupiters, suggesting that the two seemingly similar planet types in fact form through different mechanisms. [Saunders et al. \(2024\)](#) found that planets around evolved stars are rapidly re-aligned, suggesting that stellar evolution may play a crucial role in system architectures.

As the quantity and quality of the data improves, so does the nuance of theoretical models. The study of [Faridani et al. \(2024\)](#) points to the importance of stellar evolution in compact multi-planet systems. In fact, [Zanazzi et al. \(2024\)](#) shows that stellar evolution may explain many puzzles in the stellar obliquity evolution of hot Jupiters. Models of planetary interiors and tidal theory have more than kept up. [Sur et al. \(2024\)](#) have developed a next-generation numerical code for computing the internal structures of giant planets with great nuance. The quality of exoplanet data will soon reach a point where such models are necessary. Authors such as [Dewberry \(2024\)](#) and [Sun et al. \(2023\)](#) have leveraged these interior structure models to derive ever more detailed tidal theories.

Planetary obliquity is a particularly exciting field to study, as direct detection is now possible as shown by authors such as [Bryan et al. \(2018\)](#) and [Poon et al. \(2024a\)](#). These observational breakthroughs stand ready to verify the powerful theoretical predictions made in recent years. For instance, [Millholland et al. \(2024\)](#) demonstrated that resonant chain planets should very frequently be endowed with high obliquities, and [Su & Lai \(2022a\)](#) predict the same for super-Earths.

7.6 Final Thoughts

The future is bright. In the next few years, cutting-edge instruments stand poised to enact paradigm shifts in our understanding of exoplanets. Countless new problems will be raised and answered, to the end of a truly unified theory of planetary system formation. We truly are lucky to study exoplanets at this special time.

"Now, bring me that horizon"
– Captain Jack Sparrow

Bibliography

- Agol, E., Dorn, C., Grimm, S. L., et al. 2021, The Planetary Science Journal, 2, 1
- Aizawa, M., Masuda, K., Kawahara, H., & Suto, Y. 2018, AJ, 155, 206, doi: [10.3847/1538-3881/aab9a1](https://doi.org/10.3847/1538-3881/aab9a1)
- Akinsanmi, B., Lendl, M., Boué, G., & Barros, S. C. C. 2024, A&A, 682, A15, doi: [10.1051/0004-6361/202347739](https://doi.org/10.1051/0004-6361/202347739)
- Akinsanmi, B., Oshagh, M., Santos, N. C., & Barros, S. C. C. 2018, A&A, 609, A21, doi: [10.1051/0004-6361/201731215](https://doi.org/10.1051/0004-6361/201731215)
- Akinsanmi, B., Santos, N. C., Faria, J. P., et al. 2020, A&A, 635, L8, doi: [10.1051/0004-6361/202037618](https://doi.org/10.1051/0004-6361/202037618)
- Alam, M. K., Kirk, J., Dressing, C. D., et al. 2022, ApJL, 927, L5, doi: [10.3847/2041-8213/ac559d](https://doi.org/10.3847/2041-8213/ac559d)
- Albrecht, S. H., Marcussen, M. L., Winn, J. N., Dawson, R. I., & Knudstrup, E. 2021, ApJL, 916, L1, doi: [10.3847/2041-8213/ac0f03](https://doi.org/10.3847/2041-8213/ac0f03)
- Alexander, M. 1973, Astrophysics and Space Science, 23, 459
- An, Q., Lu, T., Brandt, G. M., Brandt, T. D., & Li, G. 2024, Significant mutual inclinations between the stellar spin and the orbits of both planets in the HAT-P-11 system. <https://arxiv.org/abs/2405.19510>
- Anderson, J. D., Esposito, P. B., Martin, W., Thornton, C. L., & Muhleman, D. O. 1975, ApJ, 200, 221, doi: [10.1086/153779](https://doi.org/10.1086/153779)
- Anderson, K. R., Lai, D., & Pu, B. 2020, MNRAS, 491, 1369, doi: [10.1093/mnras/stz3119](https://doi.org/10.1093/mnras/stz3119)
- Arnold, L., & Schneider, J. 2004, A&A, 420, 1153, doi: [10.1051/0004-6361:20035720](https://doi.org/10.1051/0004-6361:20035720)
- Babadzhanov, P. B., & Kokhirova, G. I. 2009, A&A, 495, 353, doi: [10.1051/0004-6361:200810460](https://doi.org/10.1051/0004-6361:200810460)

- Bailey, N., & Fabrycky, D. 2019, *The Astronomical Journal*, 158, 94, doi: [10.3847/1538-3881/ab2d2a](https://doi.org/10.3847/1538-3881/ab2d2a)
- Baker, H. F. 1905, *Proceedings of the London Mathematical Society*, 2, 24
- Bakos, G. Á., Howard, A. W., Noyes, R. W., et al. 2009, *ApJ*, 707, 446, doi: [10.1088/0004-637X/707/1/446](https://doi.org/10.1088/0004-637X/707/1/446)
- Bakos, G. Á., Torres, G., Pál, A., et al. 2010, *ApJ*, 710, 1724, doi: [10.1088/0004-637X/710/2/1724](https://doi.org/10.1088/0004-637X/710/2/1724)
- Bardalez Gagliuffi, D. C., Faherty, J. K., Li, Y., et al. 2021, *ApJL*, 922, L43, doi: [10.3847/2041-8213/ac382c](https://doi.org/10.3847/2041-8213/ac382c)
- Barnes, J. W., & Fortney, J. J. 2003, *ApJ*, 588, 545, doi: [10.1086/373893](https://doi.org/10.1086/373893)
- . 2004, *ApJ*, 616, 1193, doi: [10.1086/425067](https://doi.org/10.1086/425067)
- Baronett, S. A., Ferich, N., Tamayo, D., & Steffen, J. H. 2022, *Monthly Notices of the Royal Astronomical Society*, 510, 6001
- Batalha, N. E., Mandell, A., Pontoppidan, K., et al. 2017, *PASP*, 129, 064501, doi: [10.1088/1538-3873/aa65b0](https://doi.org/10.1088/1538-3873/aa65b0)
- Batygin, K. 2018, *The Astronomical Journal*, 155, 178
- Batygin, K., Adams, F. C., Brown, M. E., & Becker, J. C. 2019, *Physics Reports*, 805, 1–53, doi: [10.1016/j.physrep.2019.01.009](https://doi.org/10.1016/j.physrep.2019.01.009)
- Batygin, K., Bodenheimer, P., & Laughlin, G. 2009, *ApJL*, 704, L49, doi: [10.1088/0004-637X/704/1/L49](https://doi.org/10.1088/0004-637X/704/1/L49)
- Batygin, K., & Brown, M. E. 2016, *The Astronomical Journal*, 151, 22, doi: [10.3847/0004-6256/151/2/22](https://doi.org/10.3847/0004-6256/151/2/22)
- . 2021, *The Astrophysical Journal Letters*, 910, L20, doi: [10.3847/2041-8213/abee1f](https://doi.org/10.3847/2041-8213/abee1f)
- Batygin, K., Brown, M. E., & Betts, H. 2011, *The Astrophysical Journal*, 744, L3, doi: [10.1088/2041-8205/744/1/13](https://doi.org/10.1088/2041-8205/744/1/13)
- Batygin, K., Mardling, R. A., & Nesvorný, D. 2021, *The Astrophysical Journal*, 920, 148, doi: [10.3847/1538-4357/ac19a4](https://doi.org/10.3847/1538-4357/ac19a4)
- Batygin, K., Morbidelli, A., Brown, M. E., & Nesvorný, D. 2024, *ApJL*, 966, L8, doi: [10.3847/2041-8213/ad3cd2](https://doi.org/10.3847/2041-8213/ad3cd2)
- Batygin, K., & Stevenson, D. J. 2010, *ApJL*, 714, L238, doi: [10.1088/2041-8205/714/2/L238](https://doi.org/10.1088/2041-8205/714/2/L238)

- . 2013, ApJL, 769, L9, doi: [10.1088/2041-8205/769/1/L9](https://doi.org/10.1088/2041-8205/769/1/L9)
- Becker, J., Batygin, K., Fabrycky, D., et al. 2020, AJ, 160, 254, doi: [10.3847/1538-3881/abbad3](https://doi.org/10.3847/1538-3881/abbad3)
- Belkovski, M., Becker, J., Howe, A., Malsky, I., & Batygin, K. 2022, AJ, 163, 277, doi: [10.3847/1538-3881/ac6353](https://doi.org/10.3847/1538-3881/ac6353)
- Belorizky, D. 1930, Bulletin Astronomique, 6, 417
- Benisty, M., Bae, J., Facchini, S., et al. 2021, The Astrophysical Journal Letters, 916, L2, doi: [10.3847/2041-8213/ac0f83](https://doi.org/10.3847/2041-8213/ac0f83)
- Benz, W., Slattery, W. L., & Cameron, A. G. W. 1989, Meteoritics, 24, 251
- Bernardinelli, P. H., Bernstein, G. M., Sako, M., et al. 2022, ApJS, 258, 41, doi: [10.3847/1538-4365/ac3914](https://doi.org/10.3847/1538-4365/ac3914)
- Bernoulli, J. 1775, Mémoires de l'Académie des Sciences de Paris
- Best, S., & Petrovich, C. 2022, ApJL, 925, L5, doi: [10.3847/2041-8213/ac49e9](https://doi.org/10.3847/2041-8213/ac49e9)
- Beust, H., Bonfils, X., Montagnier, G., Delfosse, X., & Forveille, T. 2012, A&A, 545, A88, doi: [10.1051/0004-6361/201219183](https://doi.org/10.1051/0004-6361/201219183)
- Bodenheimer, P., Lin, D. N. C., & Mardling, R. A. 2001, ApJ, 548, 466, doi: [10.1086/318667](https://doi.org/10.1086/318667)
- Boekholt, T. C. N., Vaillant, T., & Correia, A. C. M. 2023, MNRAS, 519, 3281, doi: [10.1093/mnras/stac3777](https://doi.org/10.1093/mnras/stac3777)
- Bolmont, E., Raymond, S. N., Leconte, J., Hersant, F., & Correia, A. C. M. 2015, Astronomy & Astrophysics, 583, A116, doi: [10.1051/0004-6361/201525909](https://doi.org/10.1051/0004-6361/201525909)
- Bolmont, E., Raymond, S. N., Leconte, J., & Matt, S. P. 2012, A&A, 544, A124, doi: [10.1051/0004-6361/201219645](https://doi.org/10.1051/0004-6361/201219645)
- Borucki, W. J., Koch, D., Basri, G., et al. 2010, Science, 327, 977, doi: [10.1126/science.1185402](https://doi.org/10.1126/science.1185402)
- Borucki, W. J., Agol, E., Fressin, F., et al. 2013, Science, 340, 587, doi: [10.1126/science.1234702](https://doi.org/10.1126/science.1234702)
- Boué, G., Correia, A., & Laskar, J. 2019, EAS Publications Series, 82, 91
- Boué, G., & Laskar, J. 2010, ApJL, 712, L44, doi: [10.1088/2041-8205/712/1/L44](https://doi.org/10.1088/2041-8205/712/1/L44)
- Bouvier, J., Forestini, M., & Allain, S. 1997, A&A, 326, 1023

- Brasser, R., Duncan, M., Levison, H., Schwamb, M., & Brown, M. 2012, Icarus, 217, 1
- Brefka, L., & Becker, J. C. 2021, AJ, 162, 242, doi: [10.3847/1538-3881/ac2a32](https://doi.org/10.3847/1538-3881/ac2a32)
- Bromley, B. C., & Kenyon, S. J. 2016, The Astrophysical Journal, 826, 64, doi: [10.3847/0004-637x/826/1/64](https://doi.org/10.3847/0004-637x/826/1/64)
- Brouwer, D., & van Woerkom, A. J. J. 1950, Astronomical papers prepared for the use of the American ephemeris and nautical almanac, 13, 81
- Brown, M. E., & Batygin, K. 2021, AJ, 162, 219, doi: [10.3847/1538-3881/ac2056](https://doi.org/10.3847/1538-3881/ac2056)
- Bryan, M. L., Benneke, B., Knutson, H. A., Batygin, K., & Bowler, B. P. 2018, Nature Astronomy, 2, 138
- Bryan, M. L., Chiang, E., Morley, C. V., Mace, G. N., & Bowler, B. P. 2021, AJ, 162, 217, doi: [10.3847/1538-3881/ac1bb1](https://doi.org/10.3847/1538-3881/ac1bb1)
- Bryan, M. L., Chiang, E., Bowler, B. P., et al. 2020, AJ, 159, 181, doi: [10.3847/1538-3881/ab76c6](https://doi.org/10.3847/1538-3881/ab76c6)
- Camargo, B. C. B., Winter, O. C., & Foryta, D. W. 2018, Computational and Applied Mathematics, 37, 122–132, doi: [10.1007/s40314-018-0629-z](https://doi.org/10.1007/s40314-018-0629-z)
- Campbell, J. E. 1897, Proceedings of the London Mathematical Society, 1, 14
- Canup, R. M. 2004, ARA&A, 42, 441, doi: [10.1146/annurev.astro.41.082201.113457](https://doi.org/10.1146/annurev.astro.41.082201.113457)
- Canup, R. M., & Ward, W. R. 2002, AJ, 124, 3404, doi: [10.1086/344684](https://doi.org/10.1086/344684)
- Carrera, D., Gorti, U., Johansen, A., & Davies, M. B. 2017, The Astrophysical Journal, 839, 16, doi: [10.3847/1538-4357/aa6932](https://doi.org/10.3847/1538-4357/aa6932)
- Carrera, D., Raymond, S. N., & Davies, M. B. 2019, Astronomy & Astrophysics, 629, L7
- Cassese, B., Vega, J., Lu, T., et al. 2024a, arXiv e-prints, arXiv:2409.00167, doi: [10.48550/arXiv.2409.00167](https://doi.org/10.48550/arXiv.2409.00167)
- Cassese, B., Batygin, K., Chachan, Y., et al. 2024b, Revealing the Oblateness and Satellite System of an Extrasolar Jupiter Analog, JWST Proposal. Cycle 3, ID. #6491
- Chambers, J. E. 1999, MNRAS, 304, 793, doi: [10.1046/j.1365-8711.1999.02379.x](https://doi.org/10.1046/j.1365-8711.1999.02379.x)
- Chambers, J. E., Wetherill, G. W., & Boss, A. P. 1996, Icarus, 119, 261, doi: [10.1006/icar.1996.0019](https://doi.org/10.1006/icar.1996.0019)

- Charbonneau, D., Brown, T. M., Latham, D. W., & Mayor, M. 2000, ApJL, 529, L45, doi: [10.1086/312457](https://doi.org/10.1086/312457)
- Chatterjee, S., Ford, E. B., Matsumura, S., & Rasio, F. A. 2008, ApJ, 686, 580, doi: [10.1086/590227](https://doi.org/10.1086/590227)
- Chen, H., Li, G., Paradise, A., & Kopparapu, R. K. 2023, ApJL, 946, L32, doi: [10.3847/2041-8213/acbd33](https://doi.org/10.3847/2041-8213/acbd33)
- Chen, H., & Rogers, L. A. 2016, ApJ, 831, 180, doi: [10.3847/0004-637X/831/2/180](https://doi.org/10.3847/0004-637X/831/2/180)
- Chen, R., Li, G., & Tao, M. 2021, The Astrophysical Journal, 919, 50
- Colombo, G. 1966, AJ, 71, 891, doi: [10.1086/109983](https://doi.org/10.1086/109983)
- Correia, A. C., Boué, G., Laskar, J., & Rodríguez, A. 2014, Astronomy & Astrophysics, 571, A50
- Dai, F., Howard, A. W., Batalha, N. M., et al. 2021, The Astronomical Journal, 162, 62
- Dai, F., Masuda, K., Beard, C., et al. 2023, The Astronomical Journal, 165, 33
- Danby, J. M. A. 1992, Fundamentals of celestial mechanics
- Darwin, G. H. 1879, Philosophical Transactions of the Royal Society of London, 447
- Davies, M. B., Adams, F. C., Armitage, P., et al. 2014, in Protostars and Planets VI, ed. H. Beuther, R. S. Klessen, C. P. Dullemond, & T. Henning, 787–808, doi: [10.2458/azu_uapress_9780816531240-ch034](https://doi.org/10.2458/azu_uapress_9780816531240-ch034)
- Dawson, R. I., & Johnson, J. A. 2018, ARA&A, 56, 175, doi: [10.1146/annurev-astro-081817-051853](https://doi.org/10.1146/annurev-astro-081817-051853)
- Dehnen, W. 2017, MNRAS, 472, 1226, doi: [10.1093/mnras/stx1944](https://doi.org/10.1093/mnras/stx1944)
- Dehnen, W., & Hernandez, D. M. 2017, MNRAS, 465, 1201, doi: [10.1093/mnras/stw2758](https://doi.org/10.1093/mnras/stw2758)
- Delisle, J. B. 2017, A&A, 605, A96, doi: [10.1051/0004-6361/201730857](https://doi.org/10.1051/0004-6361/201730857)
- Dermott, S. F., & Jupp, A. H. 1984, Philosophical Transactions of the Royal Society of London. Series A, Mathematical and Physical Sciences, 313, 123. <http://www.jstor.org/stable/37678>
- Dewberry, J. W. 2024, ApJ, 966, 180, doi: [10.3847/1538-4357/ad344d](https://doi.org/10.3847/1538-4357/ad344d)
- Dholakia, S., Dholakia, S., & Pope, B. J. S. 2024, arXiv e-prints, arXiv:2410.03449, doi: [10.48550/arXiv.2410.03449](https://doi.org/10.48550/arXiv.2410.03449)

- Dittmann, A. J. 2021, MNRAS, 508, 1842, doi: [10.1093/mnras/stab2682](https://doi.org/10.1093/mnras/stab2682)
- Dong, J., & Foreman-Mackey, D. 2023, AJ, 166, 112, doi: [10.3847/1538-3881/ace105](https://doi.org/10.3847/1538-3881/ace105)
- Dong, J., Jiang, Y.-F., & Armitage, P. J. 2021, ApJ, 921, 54, doi: [10.3847/1538-4357/ac1941](https://doi.org/10.3847/1538-4357/ac1941)
- Duncan, M. J., Levison, H. F., & Lee, M. H. 1998, AJ, 116, 2067, doi: [10.1086/300541](https://doi.org/10.1086/300541)
- Efroimsky, M., & Williams, J. G. 2009, Celestial Mechanics and Dynamical Astronomy, 104, 257
- Eggleton, P. P., Kiseleva, L. G., & Hut, P. 1998, The Astrophysical Journal, 499, 853
- Eggleton, P. P., & Kiseleva-Eggleton, L. 2001, ApJ, 562, 1012, doi: [10.1086/323843](https://doi.org/10.1086/323843)
- Einstein, A. 1916, Annalen der Physik, 354, 769, doi: <https://doi.org/10.1002/andp.19163540702>
- Eriksson, L. E. J., Mustill, A. J., & Johansen, A. 2018, Monthly Notices of the Royal Astronomical Society, 475, 4609–4616, doi: [10.1093/mnras/sty111](https://doi.org/10.1093/mnras/sty111)
- Everhart, E. 1985, in Astrophysics and Space Science Library, Vol. 115, IAU Colloq. 83: Dynamics of Comets: Their Origin and Evolution, ed. A. Carusi & G. B. Valsecchi, 185, doi: [10.1007/978-94-009-5400-7_17](https://doi.org/10.1007/978-94-009-5400-7_17)
- Fabrycky, D., & Tremaine, S. 2007, The Astrophysical Journal, 669, 1298
- Fabrycky, D. C., Johnson, E. T., & Goodman, J. 2007, ApJ, 665, 754, doi: [10.1086/519075](https://doi.org/10.1086/519075)
- Fabrycky, D. C., Lissauer, J. J., Ragozzine, D., et al. 2014, ApJ, 790, 146, doi: [10.1088/0004-637X/790/2/146](https://doi.org/10.1088/0004-637X/790/2/146)
- Farhat, M. A., & Touma, J. R. 2021, MNRAS, 507, 6078, doi: [10.1093/mnras/stab2490](https://doi.org/10.1093/mnras/stab2490)
- Faridani, T., Naoz, S., Li, G., Rice, M., & Inzunza, N. 2024, arXiv e-prints, arXiv:2406.09359, doi: [10.48550/arXiv.2406.09359](https://doi.org/10.48550/arXiv.2406.09359)
- Faridani, T. H., Naoz, S., Li, G., & Inzunza, N. 2023, ApJ, 956, 90, doi: [10.3847/1538-4357/acf378](https://doi.org/10.3847/1538-4357/acf378)
- Ferraz-Mello, S. 2013, Celestial Mechanics and Dynamical Astronomy, 116, 109
- Ford, E. B., Havlickova, M., & Rasio, F. A. 2001, Icarus, 150, 303, doi: [10.1006/icar.2001.6588](https://doi.org/10.1006/icar.2001.6588)
- Ford, E. B., Kozinsky, B., & Rasio, F. A. 2000, ApJ, 535, 385, doi: [10.1086/308815](https://doi.org/10.1086/308815)

- Ford, E. B., & Rasio, F. A. 2008, ApJ, 686, 621, doi: [10.1086/590926](https://doi.org/10.1086/590926)
- Fortney, J. J., Dawson, R. I., & Komacek, T. D. 2021, Journal of Geophysical Research (Planets), 126, e06629, doi: [10.1029/2020JE006629](https://doi.org/10.1029/2020JE006629)
- Frelikh, R., Jang, H., Murray-Clay, R. A., & Petrovich, C. 2019, ApJL, 884, L47, doi: [10.3847/2041-8213/ab4a7b](https://doi.org/10.3847/2041-8213/ab4a7b)
- French, R. G., Nicholson, P. D., Cooke, M. L., et al. 1993, Icarus, 103, 163
- Fuller, J., Lai, D., & Storch, N. I. 2014, Icarus, 231, 34, doi: [10.1016/j.icarus.2013.11.022](https://doi.org/10.1016/j.icarus.2013.11.022)
- Gaia Collaboration, Prusti, T., de Bruijne, J. H. J., et al. 2016, A&A, 595, A1, doi: [10.1051/0004-6361/201629272](https://doi.org/10.1051/0004-6361/201629272)
- Gerbig, K., Rice, M., Zanazzi, J. J., Christian, S., & Vanderburg, A. 2024, ApJ, 972, 161, doi: [10.3847/1538-4357/ad5f2b](https://doi.org/10.3847/1538-4357/ad5f2b)
- Gillon, M., Triaud, A. H., Demory, B.-O., et al. 2017, Nature, 542, 456
- Gladman, B. 1993, Icarus, 106, 247, doi: [10.1006/icar.1993.1169](https://doi.org/10.1006/icar.1993.1169)
- Glanz, H., Rozner, M., Perets, H. B., & Grishin, E. 2022, ApJ, 931, 11, doi: [10.3847/1538-4357/ac6807](https://doi.org/10.3847/1538-4357/ac6807)
- Goldreich, P. 1963, MNRAS, 126, 257, doi: [10.1093/mnras/126.3.257](https://doi.org/10.1093/mnras/126.3.257)
- . 1965, AJ, 70, 5, doi: [10.1086/109673](https://doi.org/10.1086/109673)
- Goldreich, P., & Soter, S. 1966, Icarus, 5, 375, doi: [10.1016/0019-1035\(66\)90051-0](https://doi.org/10.1016/0019-1035(66)90051-0)
- Goldstein, H., Poole, C., Safko, J., & Addison, S. R. 2002, Classical mechanics, American Association of Physics Teachers
- Gomes, R., Levison, H. F., Tsiganis, K., & Morbidelli, A. 2005, Nature, 435, 466, doi: [10.1038/nature03676](https://doi.org/10.1038/nature03676)
- Grant, D., & Wakeford, H. 2024, The Journal of Open Source Software, 9, 6816, doi: [10.21105/joss.06816](https://doi.org/10.21105/joss.06816)
- Gratia, P., & Fabrycky, D. 2017, MNRAS, 464, 1709, doi: [10.1093/mnras/stw2180](https://doi.org/10.1093/mnras/stw2180)
- Greenberg, R. 2009, The Astrophysical Journal, 698, L42
- Grishin, E., Perets, H. B., & Fragione, G. 2018, MNRAS, 481, 4907, doi: [10.1093/mnras/sty2477](https://doi.org/10.1093/mnras/sty2477)
- Guillochon, J., Ramirez-Ruiz, E., & Lin, D. 2011, ApJ, 732, 74, doi: [10.1088/0004-637X/732/2/74](https://doi.org/10.1088/0004-637X/732/2/74)

- Hadden, S., & Lithwick, Y. 2017, AJ, 154, 5, doi: [10.3847/1538-3881/aa71ef](https://doi.org/10.3847/1538-3881/aa71ef)
- . 2018, AJ, 156, 95, doi: [10.3847/1538-3881/aad32c](https://doi.org/10.3847/1538-3881/aad32c)
- Hadden, S., & Tamayo, D. 2022, The Astronomical Journal, 164, 179, doi: [10.3847/1538-3881/ac8d01](https://doi.org/10.3847/1538-3881/ac8d01)
- Hairer, E., Hochbruck, M., Iserles, A., & Lubich, C. 2006, Oberwolfach Reports, 3, 805
- Hairer, E., McLachlan, R. I., & Skeel, R. D. 2009, ESAIM: Mathematical Modelling and Numerical Analysis, 43, 631. <http://eudml.org/doc/250589>
- Hamilton, D. P., & Ward, W. R. 2004, AJ, 128, 2510, doi: [10.1086/424534](https://doi.org/10.1086/424534)
- Harada, C. K., Dressing, C. D., Alam, M. K., et al. 2023, AJ, 166, 208, doi: [10.3847/1538-3881/ad011c](https://doi.org/10.3847/1538-3881/ad011c)
- Harris, A. W., & Ward, W. R. 1982, Annual review of earth and planetary sciences, 10, 61
- Hausdorff, F. 1906, Ber. Verh. Kgl. SÄ chs. Ges. Wiss. Leipzig., Math.-phys. Kl., 58, 19
- Heggie, D., & Hut, P. 2003, The Gravitational Million-Body Problem: A Multidisciplinary Approach to Star Cluster Dynamics
- Hellard, H., Csizmadia, S., Padovan, S., et al. 2019, ApJ, 878, 119, doi: [10.3847/1538-4357/ab2048](https://doi.org/10.3847/1538-4357/ab2048)
- Heller, R. 2018, in Handbook of Exoplanets, ed. H. J. Deeg & J. A. Belmonte, 35, doi: [10.1007/978-3-319-55333-7_35](https://doi.org/10.1007/978-3-319-55333-7_35)
- Heller, R., Leconte, J., & Barnes, R. 2011, Astronomy & Astrophysics, 528, A27
- Henrard, J. 1982, Celestial mechanics, 27, 3
- Henrard, J., & Murigande, C. 1987, Celestial Mechanics, 40, 345, doi: [10.1007/BF01235852](https://doi.org/10.1007/BF01235852)
- Hernandez, D. M. 2016, MNRAS, 458, 4285, doi: [10.1093/mnras/stw569](https://doi.org/10.1093/mnras/stw569)
- . 2019, MNRAS, 490, 4175, doi: [10.1093/mnras/stz2662](https://doi.org/10.1093/mnras/stz2662)
- Hernandez, D. M., & Bertschinger, E. 2015, MNRAS, 452, 1934, doi: [10.1093/mnras/stv1439](https://doi.org/10.1093/mnras/stv1439)
- . 2018, MNRAS, 475, 5570, doi: [10.1093/mnras/sty184](https://doi.org/10.1093/mnras/sty184)

- Hernandez, D. M., & Dehnen, W. 2017, MNRAS, 468, 2614, doi: [10.1093/mnras/stx547](https://doi.org/10.1093/mnras/stx547)
- . 2023, MNRAS, 522, 4639, doi: [10.1093/mnras/stad657](https://doi.org/10.1093/mnras/stad657)
- . 2024, MNRAS, 530, 3870, doi: [10.1093/mnras/stae985](https://doi.org/10.1093/mnras/stae985)
- Hernandez, D. M., Zeebe, R. E., & Hadden, S. 2022, MNRAS, 510, 4302, doi: [10.1093/mnras/stab3664](https://doi.org/10.1093/mnras/stab3664)
- Hinnov, L. A. 2018, in Stratigraphy & Timescales, Vol. 3 (Elsevier), 1–80
- Hirano, T., Narita, N., Shporer, A., et al. 2011, PASJ, 63, 531, doi: [10.1093/pasj/63.sp2.S531](https://doi.org/10.1093/pasj/63.sp2.S531)
- Holman, M. J., & Wiegert, P. A. 1999, AJ, 117, 621, doi: [10.1086/300695](https://doi.org/10.1086/300695)
- Holman, M. J., & Wisdom, J. 1993, AJ, 105, 1987, doi: [10.1086/116574](https://doi.org/10.1086/116574)
- Huber, K. F., Czesla, S., & Schmitt, J. H. M. M. 2017, A&A, 597, A113, doi: [10.1051/0004-6361/201629699](https://doi.org/10.1051/0004-6361/201629699)
- Hut, P. 1980, Astronomy and Astrophysics, 92, 167
- . 1981, Astronomy and Astrophysics, 99, 126
- Hut, P., Makino, J., & McMillan, S. 1995, ApJL, 443, L93, doi: [10.1086/187844](https://doi.org/10.1086/187844)
- Ida, S., Canup, R. M., & Stewart, G. R. 1997, Nature, 389, 353, doi: [10.1038/38669](https://doi.org/10.1038/38669)
- Ida, S., Ueta, S., Sasaki, T., & Ishizawa, Y. 2020, Nature Astronomy, 4, 880, doi: [10.1038/s41550-020-1049-8](https://doi.org/10.1038/s41550-020-1049-8)
- Ito, T., & Ohtsuka, K. 2019, Monographs on Environment, Earth and Planets, 7, 1, doi: [10.5047/meep.2019.00701.0001](https://doi.org/10.5047/meep.2019.00701.0001)
- Izidoro, A., Morbidelli, A., Raymond, S. N., Hersant, F., & Pierens, A. 2015, Astronomy & Astrophysics, 582, A99
- Jahaveri, P., Rein, H., & Tamayo, D. 2023, The Open Journal of Astrophysics, 6, doi: [10.21105/astro.2307.05683](https://doi.org/10.21105/astro.2307.05683)
- Jurić, M., & Tremaine, S. 2008, ApJ, 686, 603, doi: [10.1086/590047](https://doi.org/10.1086/590047)
- Kataria, T., Lewis, N., Mayorga, L. C., et al. 2021, A Blast From the Past: A Spectroscopic look at the Flash Heating of HD80606b, JWST Proposal. Cycle 1, ID. #2008
- Kaula, W. M. 1962, AJ, 67, 300, doi: [10.1086/108729](https://doi.org/10.1086/108729)

- Kegerreis, J., Eke, V., Gonnet, P., et al. 2019, Monthly Notices of the Royal Astronomical Society, 487, 5029
- Kegerreis, J. A., Teodoro, L. F. A., Eke, V. R., et al. 2018, The Astrophysical Journal, 861, 52, doi: [10.3847/1538-4357/aac725](https://doi.org/10.3847/1538-4357/aac725)
- Kenyon, S. J., & Bromley, B. C. 2016, The Astrophysical Journal, 825, 33
- Kinoshita, H., Yoshida, H., & Nakai, H. 1991, Celestial Mechanics and Dynamical Astronomy (ISSN 0923-2958), vol. 50, no. 1, 1991, p. 59-71., 50, 59
- Kipping, D., Bryson, S., Burke, C., et al. 2022, Nature Astronomy, 6, 367, doi: [10.1038/s41550-021-01539-1](https://doi.org/10.1038/s41550-021-01539-1)
- Knopoff, L. 1964, Reviews of Geophysics and Space Physics, 2, 625, doi: [10.1029/RG002i004p00625](https://doi.org/10.1029/RG002i004p00625)
- Knopoff, L., & MacDonald, G. J. F. 1958, Rev. Mod. Phys., 30, 1178, doi: [10.1103/RevModPhys.30.1178](https://doi.org/10.1103/RevModPhys.30.1178)
- Kokubo, E., Ida, S., & Makino, J. 2000, Icarus, 148, 419, doi: [10.1006/icar.2000.6496](https://doi.org/10.1006/icar.2000.6496)
- Kostov, V. B., Moore, K., Tamayo, D., Jayawardhana, R., & Rinehart, S. A. 2016a, ApJ, 832, 183, doi: [10.3847/0004-637X/832/2/183](https://doi.org/10.3847/0004-637X/832/2/183)
- . 2016b, ApJ, 832, 183, doi: [10.3847/0004-637X/832/2/183](https://doi.org/10.3847/0004-637X/832/2/183)
- Kozai, Y. 1962, AJ, 67, 591
- Kreyche, S. M., Barnes, J. W., Quarles, B. L., & Chambers, J. E. 2021, The Planetary Science Journal, 2, 187
- Lagrange, J. L. 1778, Mémoires de l'Académie des Sciences de Paris
- Lai, D. 1997, ApJ, 490, 847, doi: [10.1086/304899](https://doi.org/10.1086/304899)
- . 2012, MNRAS, 423, 486, doi: [10.1111/j.1365-2966.2012.20893.x](https://doi.org/10.1111/j.1365-2966.2012.20893.x)
- Lainey, V. 2016, Celestial Mechanics and Dynamical Astronomy, 126, 145, doi: [10.1007/s10569-016-9695-y](https://doi.org/10.1007/s10569-016-9695-y)
- Lainey, V., Arlot, J.-E., Karatekin, Ö., & van Hoolst, T. 2009, Nature, 459, 957, doi: [10.1038/nature08108](https://doi.org/10.1038/nature08108)
- Lainey, V., Jacobson, R. A., Tajeddine, R., et al. 2017, Icarus, 281, 286, doi: [10.1016/j.icarus.2016.07.014](https://doi.org/10.1016/j.icarus.2016.07.014)
- Lammers, C., Hadden, S., & Murray, N. 2024, ApJ, 972, 53, doi: [10.3847/1538-4357/ad5be6](https://doi.org/10.3847/1538-4357/ad5be6)

- Lammers, C., & Winn, J. N. 2024a, ApJL, 968, L12, doi: [10.3847/2041-8213/ad50d2](https://doi.org/10.3847/2041-8213/ad50d2)
- . 2024b, arXiv e-prints, arXiv:2409.06697, doi: [10.48550/arXiv.2409.06697](https://doi.org/10.48550/arXiv.2409.06697)
- Laplace, P. S. 1775, Mémoires de l'Académie des Sciences de Paris
- . 1784, Mémoires de l'Académie royale des sciences de Paris, 49
- Laskar, J. 2012, arXiv e-prints, arXiv:1209.5996, doi: [10.48550/arXiv.1209.5996](https://doi.org/10.48550/arXiv.1209.5996)
- Laskar, J. 2013, in Chaos (Springer), 239–270
- Laskar, J., Correia, A. C. M., Gastineau, M., et al. 2004, Icarus, 170, 343, doi: [10.1016/j.icarus.2004.04.005](https://doi.org/10.1016/j.icarus.2004.04.005)
- Laskar, J., Fienga, A., Gastineau, M., & Manche, H. 2011, A&A, 532, A89, doi: [10.1051/0004-6361/201116836](https://doi.org/10.1051/0004-6361/201116836)
- Laskar, J., & Robutel, P. 1993, Nature, 361, 608, doi: [10.1038/361608a0](https://doi.org/10.1038/361608a0)
- . 2001, Celestial Mechanics and Dynamical Astronomy, 80, 39, doi: [10.1023/A:1012098603882](https://doi.org/10.1023/A:1012098603882)
- Laughlin, G., Crismani, M., & Adams, F. C. 2011, ApJL, 729, L7, doi: [10.1088/2041-8205/729/1/L7](https://doi.org/10.1088/2041-8205/729/1/L7)
- Leconte, J., Chabrier, G., Baraffe, I., & Levrard, B. 2010, Astronomy & Astrophysics, 516, A64
- Lee, E. J., & Chiang, E. 2016, ApJ, 817, 90, doi: [10.3847/0004-637X/817/2/90](https://doi.org/10.3847/0004-637X/817/2/90)
- Leleu, A., Delisle, J.-B., Burn, R., et al. 2024, A&A, 687, L1, doi: [10.1051/0004-6361/202450587](https://doi.org/10.1051/0004-6361/202450587)
- Lemson, G., & Virgo Consortium, t. 2006, arXiv e-prints, astro, doi: [10.48550/arXiv.astro-ph/0608019](https://doi.org/10.48550/arXiv.astro-ph/0608019)
- Levison, H. F., & Duncan, M. J. 2000, AJ, 120, 2117, doi: [10.1086/301553](https://doi.org/10.1086/301553)
- Li, G. 2021, ApJL, 915, L2, doi: [10.3847/2041-8213/ac0620](https://doi.org/10.3847/2041-8213/ac0620)
- Li, G., & Adams, F. C. 2016, The Astrophysical Journal Letters, 823, L3
- Li, G., Naoz, S., Holman, M., & Loeb, A. 2014a, ApJ, 791, 86, doi: [10.1088/0004-637X/791/2/86](https://doi.org/10.1088/0004-637X/791/2/86)
- Li, G., Naoz, S., Kocsis, B., & Loeb, A. 2014b, ApJ, 785, 116, doi: [10.1088/0004-637X/785/2/116](https://doi.org/10.1088/0004-637X/785/2/116)
- Lidov, M. L. 1962, Planetary and Space Science, 9, 719

- Lissauer, J. J., Ragozzine, D., Fabrycky, D. C., et al. 2011, *ApJS*, 197, 8, doi: [10.1088/0067-0049/197/1/8](https://doi.org/10.1088/0067-0049/197/1/8)
- Liu, Q., Zhu, W., Zhou, Y., et al. 2024, arXiv e-prints, arXiv:2406.11644, doi: [10.48550/arXiv.2406.11644](https://doi.org/10.48550/arXiv.2406.11644)
- Lopez, E. D., & Fortney, J. J. 2014, *ApJ*, 792, 1, doi: [10.1088/0004-637X/792/1/1](https://doi.org/10.1088/0004-637X/792/1/1)
- Lu, T., An, Q., Li, G., et al. 2024a, arXiv e-prints, arXiv:2405.19511, doi: [10.48550/arXiv.2405.19511](https://doi.org/10.48550/arXiv.2405.19511)
- Lu, T., Hernandez, D. M., & Rein, H. 2024b, *MNRAS*, 533, 3708, doi: [10.1093/mnras/stae1982](https://doi.org/10.1093/mnras/stae1982)
- Lu, T., & Laughlin, G. 2022, *PSJ*, 3, 221, doi: [10.3847/PSJ/ac83c1](https://doi.org/10.3847/PSJ/ac83c1)
- Lu, T., Rein, H., Tamayo, D., et al. 2023, *The Astrophysical Journal*, 948, 41, doi: [10.3847/1538-4357/acc06d](https://doi.org/10.3847/1538-4357/acc06d)
- Luger, R., Sestovic, M., Kruse, E., et al. 2017, *Nature Astronomy*, 1, 1
- MacDonald, G. J. F. 1964, *Reviews of Geophysics and Space Physics*, 2, 467, doi: [10.1029/RG002i003p00467](https://doi.org/10.1029/RG002i003p00467)
- MacDonald, M. G., Feil, L., Quinn, T., & Rice, D. 2022, *AJ*, 163, 162, doi: [10.3847/1538-3881/ac524c](https://doi.org/10.3847/1538-3881/ac524c)
- Machida, M. N., Kokubo, E., Inutsuka, S.-i., & Matsumoto, T. 2008, *ApJ*, 685, 1220, doi: [10.1086/590421](https://doi.org/10.1086/590421)
- Magic, Z., Chiavassa, A., Collet, R., & Asplund, M. 2015, *A&A*, 573, A90, doi: [10.1051/0004-6361/201423804](https://doi.org/10.1051/0004-6361/201423804)
- Malhotra, R., Fox, K., Murray, C. D., & Nicholson, P. D. 1989, *A&A*, 221, 348
- Mamajek, E. E., Quillen, A. C., Pecaut, M. J., et al. 2012, *The Astronomical Journal*, 143, 72, doi: [10.1088/0004-6256/143/3/72](https://doi.org/10.1088/0004-6256/143/3/72)
- Mardling, R. 2010, Q-based models and their uses, https://online.kitp.ucsb.edu/online/exoplanets10/mardling/pdf/Mardling_ExoPlanets_KITP.pdf
- Mardling, R. A. 1995, *ApJ*, 450, 722, doi: [10.1086/176178](https://doi.org/10.1086/176178)
- . 2007, *MNRAS*, 382, 1768, doi: [10.1111/j.1365-2966.2007.12500.x](https://doi.org/10.1111/j.1365-2966.2007.12500.x)
- . 2008, arXiv e-prints, arXiv:0805.1928, doi: [10.48550/arXiv.0805.1928](https://doi.org/10.48550/arXiv.0805.1928)
- . 2010, *MNRAS*, 407, 1048, doi: [10.1111/j.1365-2966.2010.16814.x](https://doi.org/10.1111/j.1365-2966.2010.16814.x)
- Mardling, R. A., & Lin, D. N. 2002, *The Astrophysical Journal*, 573, 829

- Marzari, F. 2014, MNRAS, 442, 1110, doi: [10.1093/mnras/stu929](https://doi.org/10.1093/mnras/stu929)
- Marzari, F., & Weidenschilling, S. J. 2002, Icarus, 156, 570, doi: [10.1006/icar.2001.6786](https://doi.org/10.1006/icar.2001.6786)
- Masuda, K. 2014, ApJ, 783, 53, doi: [10.1088/0004-637X/783/1/53](https://doi.org/10.1088/0004-637X/783/1/53)
- Mayor, M., & Queloz, D. 1995, Nature, 378, 355, doi: [10.1038/378355a0](https://doi.org/10.1038/378355a0)
- McLaughlin, D. B. 1924, ApJ, 60, 22, doi: [10.1086/142826](https://doi.org/10.1086/142826)
- Millholland, S. 2019, ApJ, 886, 72, doi: [10.3847/1538-4357/ab4c3f](https://doi.org/10.3847/1538-4357/ab4c3f)
- Millholland, S., & Batygin, K. 2019, ApJ, 876, 119, doi: [10.3847/1538-4357/ab19be](https://doi.org/10.3847/1538-4357/ab19be)
- Millholland, S., & Laughlin, G. 2019, Nature Astronomy, 3, 424
- Millholland, S., Petigura, E., & Batygin, K. 2020, ApJ, 897, 7, doi: [10.3847/1538-4357/ab959c](https://doi.org/10.3847/1538-4357/ab959c)
- Millholland, S. C., Lara, T., & Toomlaid, J. 2024, ApJ, 961, 203, doi: [10.3847/1538-4357/ad10a0](https://doi.org/10.3847/1538-4357/ad10a0)
- Millholland, S. C., & Spalding, C. 2020, The Astrophysical Journal, 905, 71, doi: [10.3847/1538-4357/abc4e5](https://doi.org/10.3847/1538-4357/abc4e5)
- Mills, S. M., Fabrycky, D. C., Migaszewski, C., et al. 2016, Nature, 533, 509, doi: [10.1038/nature17445](https://doi.org/10.1038/nature17445)
- Morbidelli, A. 2002, Modern celestial mechanics: aspects of solar system dynamics
- Morbidelli, A., & Henrard, J. 1991, Celestial Mechanics and Dynamical Astronomy, 51, 169
- Morbidelli, A., Levison, H. F., Tsiganis, K., & Gomes, R. 2005, Nature, 435, 462, doi: [10.1038/nature03540](https://doi.org/10.1038/nature03540)
- Morbidelli, A., Tsiganis, K., Batygin, K., Crida, A., & Gomes, R. 2012, Icarus, 219, 737, doi: [10.1016/j.icarus.2012.03.025](https://doi.org/10.1016/j.icarus.2012.03.025)
- Morton, T. D., Bryson, S. T., Coughlin, J. L., et al. 2016, ApJ, 822, 86, doi: [10.3847/0004-637X/822/2/86](https://doi.org/10.3847/0004-637X/822/2/86)
- Murray, C. D., & Dermott, S. F. 2000, Solar System Dynamics (Cambridge University Press), doi: [10.1017/CBO9781139174817](https://doi.org/10.1017/CBO9781139174817)
- Mustill, A. J., Raymond, S. N., & Davies, M. B. 2016, Monthly Notices of the Royal Astronomical Society: Letters, 460, L109

- Naef, D., Latham, D. W., Mayor, M., et al. 2001, A&A, 375, L27, doi: [10.1051/0004-6361:20010853](https://doi.org/10.1051/0004-6361:20010853)
- Nagasawa, M., & Ida, S. 2011, The Astrophysical Journal, 742, 72
- Naoz, S. 2016, ARA&A, 54, 441
- Naoz, S., Farr, W. M., Lithwick, Y., Rasio, F. A., & Teyssandier, J. 2013, MNRAS, 431, 2155, doi: [10.1093/mnras/stt302](https://doi.org/10.1093/mnras/stt302)
- Naoz, S., Farr, W. M., & Rasio, F. A. 2012, ApJL, 754, L36, doi: [10.1088/2041-8205/754/2/L36](https://doi.org/10.1088/2041-8205/754/2/L36)
- Napier, K. J., Gerdes, D. W., Lin, H. W., et al. 2021, PSJ, 2, 59, doi: [10.3847/PSJ/abe53e](https://doi.org/10.3847/PSJ/abe53e)
- Newhall, X. X., Standish, E. M., & Williams, J. G. 1983, A&A, 125, 150
- Newton, I. 1687, Philosophiae Naturalis Principia Mathematica., doi: [10.3931/e-rara-440](https://doi.org/10.3931/e-rara-440)
- Obertas, A., Van Laerhoven, C., & Tamayo, D. 2017, Icarus, 293, 52, doi: [10.1016/j.icarus.2017.04.010](https://doi.org/10.1016/j.icarus.2017.04.010)
- Ogilvie, G. I. 2009, MNRAS, 396, 794, doi: [10.1111/j.1365-2966.2009.14814.x](https://doi.org/10.1111/j.1365-2966.2009.14814.x)
- Ogilvie, G. I., & Lin, D. 2004, The Astrophysical Journal, 610, 477
- Ohno, K., & Fortney, J. J. 2022, ApJ, 930, 50, doi: [10.3847/1538-4357/ac6029](https://doi.org/10.3847/1538-4357/ac6029)
- Ohta, Y., Taruya, A., & Suto, Y. 2009, ApJ, 690, 1, doi: [10.1088/0004-637X/690/1/1](https://doi.org/10.1088/0004-637X/690/1/1)
- Ossendrijver, M. 2016, Science, 351, 482, doi: [10.1126/science.aad8085](https://doi.org/10.1126/science.aad8085)
- Papaloizou, J. C. B., & Larwood, J. D. 2000, MNRAS, 315, 823, doi: [10.1046/j.1365-8711.2000.03466.x](https://doi.org/10.1046/j.1365-8711.2000.03466.x)
- Parker, R. J., Lichtenberg, T., & Quanz, S. P. 2017, Monthly Notices of the Royal Astronomical Society: Letters, 472, L75
- Paxton, B., Bildsten, L., Dotter, A., et al. 2011, ApJS, 192, 3, doi: [10.1088/0067-0049/192/1/3](https://doi.org/10.1088/0067-0049/192/1/3)
- Peale, S. J. 1969, AJ, 74, 483, doi: [10.1086/110825](https://doi.org/10.1086/110825)
- Peale, S. J., Cassen, P., & Reynolds, R. T. 1979, Science, 203, 892, doi: [10.1126/science.203.4383.892](https://doi.org/10.1126/science.203.4383.892)
- Perryman, M., Hartman, J., Bakos, G. Á., & Lindegren, L. 2014, ApJ, 797, 14, doi: [10.1088/0004-637X/797/1/14](https://doi.org/10.1088/0004-637X/797/1/14)

- Petigura, E. A., Benneke, B., Batygin, K., et al. 2018, AJ, 156, 89, doi: [10.3847/1538-3881/aaceac](https://doi.org/10.3847/1538-3881/aaceac)
- Petrovich, C. 2015, ApJ, 799, 27, doi: [10.1088/0004-637X/799/1/27](https://doi.org/10.1088/0004-637X/799/1/27)
- Petrovich, C., Malhotra, R., & Tremaine, S. 2013, ApJ, 770, 24, doi: [10.1088/0004-637X/770/1/24](https://doi.org/10.1088/0004-637X/770/1/24)
- Petrovich, C., Muñoz, D. J., Kratter, K. M., & Malhotra, R. 2020, ApJL, 902, L5, doi: [10.3847/2041-8213/abb952](https://doi.org/10.3847/2041-8213/abb952)
- Petrovich, C., & Tremaine, S. 2016, ApJ, 829, 132, doi: [10.3847/0004-637X/829/2/132](https://doi.org/10.3847/0004-637X/829/2/132)
- Petrovich, C., Tremaine, S., & Rafikov, R. 2014, ApJ, 786, 101, doi: [10.1088/0004-637X/786/2/101](https://doi.org/10.1088/0004-637X/786/2/101)
- Petrovich, C., Wu, Y., & Ali-Dib, M. 2018, The Astronomical Journal, 157, 5, doi: [10.3847/1538-3881/aaeed9](https://doi.org/10.3847/1538-3881/aaeed9)
- Pham, D., Rein, H., & Spiegel, D. S. 2024, The Open Journal of Astrophysics, 7, 1, doi: [10.21105/astro.2401.02849](https://doi.org/10.21105/astro.2401.02849)
- Piro, A. L., & Vissapragada, S. 2020, AJ, 159, 131, doi: [10.3847/1538-3881/ab7192](https://doi.org/10.3847/1538-3881/ab7192)
- Poincaré, H. 1890, Acta Math, 13, 270
- Poon, M., Bryan, M. L., Rein, H., et al. 2024a, AJ, 168, 270, doi: [10.3847/1538-3881/ad84e5](https://doi.org/10.3847/1538-3881/ad84e5)
- Poon, M., Rein, H., & Pham, D. 2024b, arXiv e-prints, arXiv:2412.05988, doi: [10.48550/arXiv.2412.05988](https://doi.org/10.48550/arXiv.2412.05988)
- Portegies Zwart, S., McMillan, S., Harfst, S., et al. 2009, NewA, 14, 369, doi: [10.1016/j.newast.2008.10.006](https://doi.org/10.1016/j.newast.2008.10.006)
- Press, W. H., Teukolsky, S. A., Vetterling, W. T., & Flannery, B. P. 2002, Numerical recipes in C++ : the art of scientific computing
- Price, E. M., Becker, J., de Beurs, Z. L., Rogers, L. A., & Vanderburg, A. 2024, arXiv e-prints, arXiv:2410.05408, doi: [10.48550/arXiv.2410.05408](https://doi.org/10.48550/arXiv.2410.05408)
- Pu, B., & Lai, D. 2021, MNRAS, 508, 597, doi: [10.1093/mnras/stab2504](https://doi.org/10.1093/mnras/stab2504)
- Pu, B., & Wu, Y. 2015, ApJ, 807, 44, doi: [10.1088/0004-637X/807/1/44](https://doi.org/10.1088/0004-637X/807/1/44)
- Qiu-Dong, W. 1990, Celestial Mechanics and Dynamical Astronomy, 50, 73
- Quarles, B., Li, G., & Lissauer, J. J. 2019, ApJ, 886, 56, doi: [10.3847/1538-4357/ab46b5](https://doi.org/10.3847/1538-4357/ab46b5)

- Quillen, A. C., Chen, Y.-Y., Noyelles, B., & Loane, S. 2018, Celestial mechanics and dynamical astronomy, 130, 1
- Rath, J., Hadden, S., & Lithwick, Y. 2022, ApJ, 932, 61, doi: [10.3847/1538-4357/ac5f57](https://doi.org/10.3847/1538-4357/ac5f57)
- Rauch, K. P., & Holman, M. 1999, AJ, 117, 1087, doi: [10.1086/300720](https://doi.org/10.1086/300720)
- Raymond, S. N., & Morbidelli, A. 2022, Demographics of Exoplanetary Systems: Lecture Notes of the 3rd Advanced School on Exoplanetary Science, 3
- Raymond, S. N., Quinn, T., & Lunine, J. I. 2006, Icarus, 183, 265, doi: [10.1016/j.icarus.2006.03.011](https://doi.org/10.1016/j.icarus.2006.03.011)
- Rein, H., & Liu, S. F. 2012, A&A, 537, A128, doi: [10.1051/0004-6361/201118085](https://doi.org/10.1051/0004-6361/201118085)
- Rein, H., & Spiegel, D. S. 2015, MNRAS, 446, 1424, doi: [10.1093/mnras/stu2164](https://doi.org/10.1093/mnras/stu2164)
- Rein, H., & Tamayo, D. 2015, MNRAS, 452, 376, doi: [10.1093/mnras/stv1257](https://doi.org/10.1093/mnras/stv1257)
- Rein, H., & Tamayo, D. 2019, Research Notes of the AAS, 3, 16, doi: [10.3847/2515-5172/aaff63](https://doi.org/10.3847/2515-5172/aaff63)
- Rein, H., Tamayo, D., & Brown, G. 2019a, MNRAS, 489, 4632, doi: [10.1093/mnras/stz2503](https://doi.org/10.1093/mnras/stz2503)
- Rein, H., Hernandez, D. M., Tamayo, D., et al. 2019b, MNRAS, 485, 5490, doi: [10.1093/mnras/stz769](https://doi.org/10.1093/mnras/stz769)
- Reinhardt, C., Chau, A., Stadel, J., & Helled, R. 2020, Monthly Notices of the Royal Astronomical Society, 492, 5336–5353, doi: [10.1093/mnras/stz3271](https://doi.org/10.1093/mnras/stz3271)
- Rice, M., & Laughlin, G. 2020, PSJ, 1, 81, doi: [10.3847/PSJ/abc42c](https://doi.org/10.3847/PSJ/abc42c)
- Rice, M., Wang, S., Gerbig, K., et al. 2023, AJ, 165, 65, doi: [10.3847/1538-3881/aca88e](https://doi.org/10.3847/1538-3881/aca88e)
- Rice, M., Wang, S., Howard, A. W., et al. 2021, The Astronomical Journal, 162, 182
- Rice, M., Wang, S., Wang, X.-Y., et al. 2022, AJ, 164, 104, doi: [10.3847/1538-3881/ac8153](https://doi.org/10.3847/1538-3881/ac8153)
- Rogers, L. A., Bodenheimer, P., Lissauer, J. J., & Seager, S. 2011, ApJ, 738, 59, doi: [10.1088/0004-637X/738/1/59](https://doi.org/10.1088/0004-637X/738/1/59)
- Rogoszinski, Z., & Hamilton, D. P. 2020, ApJ, 888, 60, doi: [10.3847/1538-4357/ab5d35](https://doi.org/10.3847/1538-4357/ab5d35)
- . 2021, PSJ, 2, 78, doi: [10.3847/PSJ/abec4e](https://doi.org/10.3847/PSJ/abec4e)

- Rossiter, R. A. 1924, ApJ, 60, 15, doi: [10.1086/142825](https://doi.org/10.1086/142825)
- Rowan-Robinson, M. 2022, MNRAS, 510, 3716, doi: [10.1093/mnras/stab3212](https://doi.org/10.1093/mnras/stab3212)
- Rozner, M., Glanz, H., Perets, H. B., & Grishin, E. 2022, ApJ, 931, 10, doi: [10.3847/1538-4357/ac6808](https://doi.org/10.3847/1538-4357/ac6808)
- Saha, P., & Tremaine, S. 1992, AJ, 104, 1633, doi: [10.1086/116347](https://doi.org/10.1086/116347)
- . 1994, AJ, 108, 1962, doi: [10.1086/117210](https://doi.org/10.1086/117210)
- Saillenfest, M., & Lari, G. 2021, A&A, 654, A83, doi: [10.1051/0004-6361/202141467](https://doi.org/10.1051/0004-6361/202141467)
- Saillenfest, M., Lari, G., & Boué, G. 2021a, Nature Astronomy, 5, 345
- Saillenfest, M., Lari, G., Boué, G., & Courtot, A. 2021b, Astronomy & Astrophysics, 647, A92
- Saillenfest, M., Lari, G., & Courtot, A. 2020, Astronomy & Astrophysics, 640, A11
- Saillenfest, M., Rogoszinski, Z., Lari, G., et al. 2022, A&A, 668, A108, doi: [10.1051/0004-6361/202243953](https://doi.org/10.1051/0004-6361/202243953)
- Saillenfest, M., Sulis, S., Charpentier, P., & Santerne, A. 2023, A&A, 675, A174, doi: [10.1051/0004-6361/202346745](https://doi.org/10.1051/0004-6361/202346745)
- Sanchis-Ojeda, R., & Winn, J. N. 2011, ApJ, 743, 61, doi: [10.1088/0004-637X/743/1/61](https://doi.org/10.1088/0004-637X/743/1/61)
- Santerne, A., Malavolta, L., Kosiarek, M. R., et al. 2019, arXiv e-prints, arXiv:1911.07355, doi: [10.48550/arXiv.1911.07355](https://doi.org/10.48550/arXiv.1911.07355)
- Saunders, N., Grunblatt, S. K., Chontos, A., et al. 2024, AJ, 168, 81, doi: [10.3847/1538-3881/ad543b](https://doi.org/10.3847/1538-3881/ad543b)
- Schlichting, H. E., & Chang, P. 2011, ApJ, 734, 117, doi: [10.1088/0004-637X/734/2/117](https://doi.org/10.1088/0004-637X/734/2/117)
- Seager, S., & Hui, L. 2002, ApJ, 574, 1004, doi: [10.1086/340994](https://doi.org/10.1086/340994)
- Shan, Y., & Li, G. 2018, The Astronomical Journal, 155, 237, doi: [10.3847/1538-3881/aabfd1](https://doi.org/10.3847/1538-3881/aabfd1)
- Siegel, J. C., & Fabrycky, D. 2021, AJ, 161, 290, doi: [10.3847/1538-3881/abf8a6](https://doi.org/10.3847/1538-3881/abf8a6)
- Siegel, J. C., Winn, J. N., & Albrecht, S. H. 2023, ApJL, 950, L2, doi: [10.3847/2041-8213/acd62f](https://doi.org/10.3847/2041-8213/acd62f)

- Sing, D. K., Rustamkulov, Z., Thorngren, D. P., et al. 2024, *Nature*, 630, 831, doi: [10.1038/s41586-024-07395-z](https://doi.org/10.1038/s41586-024-07395-z)
- Siraj, A., Chyba, C. F., & Tremaine, S. 2024, arXiv e-prints, arXiv:2410.18170, doi: [10.48550/arXiv.2410.18170](https://doi.org/10.48550/arXiv.2410.18170)
- Slattery, W. L., Benz, W., & Cameron, A. 1992, *Icarus*, 99, 167, doi: [https://doi.org/10.1016/0019-1035\(92\)90180-F](https://doi.org/10.1016/0019-1035(92)90180-F)
- Souami, D., & Souchay, J. 2012, *A&A*, 543, A133, doi: [10.1051/0004-6361/201219011](https://doi.org/10.1051/0004-6361/201219011)
- Spalding, C., & Batygin, K. 2014, *ApJ*, 790, 42, doi: [10.1088/0004-637X/790/1/42](https://doi.org/10.1088/0004-637X/790/1/42)
- Speedie, J., & Zanazzi, J. J. 2020, *MNRAS*, 497, 1870, doi: [10.1093/mnras/staa2068](https://doi.org/10.1093/mnras/staa2068)
- Spiegel, D. S., Menou, K., & Scharf, C. A. 2009, *The Astrophysical Journal*, 691, 596
- Stassun, K. G., Collins, K. A., & Gaudi, B. S. 2017, *AJ*, 153, 136, doi: [10.3847/1538-3881/aa5df3](https://doi.org/10.3847/1538-3881/aa5df3)
- Storch, N. I., & Lai, D. 2014, *Monthly Notices of the Royal Astronomical Society*, 438, 1526
- Su, Y., & Lai, D. 2020, *The Astrophysical Journal*, 903, 7
- . 2022, *Monthly Notices of the Royal Astronomical Society*, 509, 3301
- Su, Y., & Lai, D. 2022a, *MNRAS*, 513, 3302, doi: [10.1093/mnras/stac1096](https://doi.org/10.1093/mnras/stac1096)
- . 2022b, *MNRAS*, 510, 4943, doi: [10.1093/mnras/stab3698](https://doi.org/10.1093/mnras/stab3698)
- Sucerquia, M., Alvarado-Montes, J. A., Zuluaga, J. I., Montesinos, M., & Bayo, A. 2020, *Monthly Notices of the Royal Astronomical Society: Letters*, 496, L85
- Sulis, S., Borsato, L., Grouffal, S., et al. 2024, *A&A*, 686, L18, doi: [10.1051/0004-6361/202449689](https://doi.org/10.1051/0004-6361/202449689)
- Sun, M., Townsend, R. H. D., & Guo, Z. 2023, *ApJ*, 945, 43, doi: [10.3847/1538-4357/acb33a](https://doi.org/10.3847/1538-4357/acb33a)
- Sundman, K. F. 1913, *Acta mathematica*, 36, 105
- Sur, A., Su, Y., Tejada Arevalo, R., Chen, Y.-X., & Burrows, A. 2024, *ApJ*, 971, 104, doi: [10.3847/1538-4357/ad57c3](https://doi.org/10.3847/1538-4357/ad57c3)
- Szulágyi, J., Cilibrasi, M., & Mayer, L. 2018, *The Astrophysical Journal*, 868, L13, doi: [10.3847/2041-8213/aaeed6](https://doi.org/10.3847/2041-8213/aaeed6)

- Tamayo, D., Rein, H., Petrovich, C., & Murray, N. 2017, The Astrophysical Journal Letters, 840, L19
- Tamayo, D., Rein, H., Shi, P., & Hernandez, D. M. 2020a, MNRAS, 491, 2885, doi: [10.1093/mnras/stz2870](https://doi.org/10.1093/mnras/stz2870)
- Tamayo, D., Cranmer, M., Hadden, S., et al. 2020b, Proceedings of the National Academy of Science, 117, 18194, doi: [10.1073/pnas.2001258117](https://doi.org/10.1073/pnas.2001258117)
- Teyssandier, J., Lai, D., & Vick, M. 2019, Monthly Notices of the Royal Astronomical Society, 486, 2265
- Thommes, E. W., Duncan, M. J., & Levison, H. F. 1999, Nature, 402, 635
- Touma, J., & Wisdom, J. 1993, Science, 259, 1294, doi: [10.1126/science.259.5099.1294](https://doi.org/10.1126/science.259.5099.1294)
- Touma, J., & Wisdom, J. 1998, The Astronomical Journal, 115, 1653
- Tremaine, S. 1991, Icarus, 89, 85, doi: [https://doi.org/10.1016/0019-1035\(91\)90089-C](https://doi.org/10.1016/0019-1035(91)90089-C)
- Tremaine, S. 1991, Icarus, 89, 85, doi: [10.1016/0019-1035\(91\)90089-C](https://doi.org/10.1016/0019-1035(91)90089-C)
- . 2023, Dynamics of Planetary Systems
- Tremaine, S., & Davis, S. W. 2014, Monthly Notices of the Royal Astronomical Society, 441, 1408–1434, doi: [10.1093/mnras/stu663](https://doi.org/10.1093/mnras/stu663)
- Tremaine, S., Touma, J., & Namouni, F. 2009, AJ, 137, 3706, doi: [10.1088/0004-6256/137/3/3706](https://doi.org/10.1088/0004-6256/137/3/3706)
- Tremblin, P., Chabrier, G., Mayne, N. J., et al. 2017, ApJ, 841, 30, doi: [10.3847/1538-4357/aa6e57](https://doi.org/10.3847/1538-4357/aa6e57)
- Tsiganis, K., Gomes, R., Morbidelli, A., & Levison, H. F. 2005, Nature, 435, 459, doi: [10.1038/nature03539](https://doi.org/10.1038/nature03539)
- van der Velden, E. 2020, The Journal of Open Source Software, 5, 2004, doi: [10.21105/joss.02004](https://doi.org/10.21105/joss.02004)
- Vanderburg, A., Becker, J. C., Kristiansen, M. H., et al. 2016, ApJL, 827, L10, doi: [10.3847/2041-8205/827/1/L10](https://doi.org/10.3847/2041-8205/827/1/L10)
- Vick, M., Lai, D., & Anderson, K. R. 2019, Monthly Notices of the Royal Astronomical Society, 484, 5645
- Vick, M., Su, Y., & Lai, D. 2023, ApJL, 943, L13, doi: [10.3847/2041-8213/acaea6](https://doi.org/10.3847/2041-8213/acaea6)

- Vissapragada, S., Knutson, H. A., dos Santos, L. A., Wang, L., & Dai, F. 2022, ApJ, 927, 96, doi: [10.3847/1538-4357/ac4e8a](https://doi.org/10.3847/1538-4357/ac4e8a)
- Vissapragada, S., Jontof-Hutter, D., Shporer, A., et al. 2020, AJ, 159, 108, doi: [10.3847/1538-3881/ab65c8](https://doi.org/10.3847/1538-3881/ab65c8)
- Vokrouhlický, D., & Nesvorný, D. 2015, ApJ, 806, 143, doi: [10.1088/0004-637X/806/1/143](https://doi.org/10.1088/0004-637X/806/1/143)
- von Zeipel, H. 1910, Astronomische Nachrichten, 183, 345, doi: [10.1002/asna.19091832202](https://doi.org/10.1002/asna.19091832202)
- Wahl, S. M., Thorngren, D., Lu, T., & Militzer, B. 2021, ApJ, 921, 105, doi: [10.3847/1538-4357/ac1a72](https://doi.org/10.3847/1538-4357/ac1a72)
- Wang, L., & Dai, F. 2019, ApJL, 873, L1, doi: [10.3847/2041-8213/ab0653](https://doi.org/10.3847/2041-8213/ab0653)
- Wang, X.-Y., Rice, M., Wang, S., et al. 2024, ApJL, 973, L21, doi: [10.3847/2041-8213/ad7469](https://doi.org/10.3847/2041-8213/ad7469)
- Ward, W. R. 1973, Science, 181, 260, doi: [10.1126/science.181.4096.260](https://doi.org/10.1126/science.181.4096.260)
- Ward, W. R. 1974, Journal of Geophysical Research (1896-1977), 79, 3375, doi: <https://doi.org/10.1029/JC079i024p03375>
- Ward, W. R. 1975, AJ, 80, 64, doi: [10.1086/111714](https://doi.org/10.1086/111714)
- Ward, W. R. 1979, Journal of Geophysical Research, 84, 237
- Ward, W. R., & Canup, R. M. 2006, The Astrophysical Journal, 640, L91, doi: [10.1086/503156](https://doi.org/10.1086/503156)
- Ward, W. R., & Hamilton, D. P. 2004, AJ, 128, 2501, doi: [10.1086/424533](https://doi.org/10.1086/424533)
- Welbanks, L., Bell, T. J., Beatty, T. G., et al. 2024, Nature, 630, 836, doi: [10.1038/s41586-024-07514-w](https://doi.org/10.1038/s41586-024-07514-w)
- Wisdom, J. 1985, Icarus, 63, 272, doi: [10.1016/0019-1035\(85\)90011-9](https://doi.org/10.1016/0019-1035(85)90011-9)
- . 2008, Icarus, 193, 637, doi: [10.1016/j.icarus.2007.09.002](https://doi.org/10.1016/j.icarus.2007.09.002)
- . 2015, AJ, 150, 127, doi: [10.1088/0004-6256/150/4/127](https://doi.org/10.1088/0004-6256/150/4/127)
- . 2017, MNRAS, 464, 2350, doi: [10.1093/mnras/stw2598](https://doi.org/10.1093/mnras/stw2598)
- . 2018, MNRAS, 474, 3273, doi: [10.1093/mnras/stx2906](https://doi.org/10.1093/mnras/stx2906)
- Wisdom, J., Dbouk, R., Militzer, B., et al. 2022, Science, 377, 1285, doi: [10.1126/science.abn1234](https://doi.org/10.1126/science.abn1234)

- Wisdom, J., & Holman, M. 1991, AJ, 102, 1528, doi: [10.1086/115978](https://doi.org/10.1086/115978)
- Wisdom, J., Holman, M., & Touma, J. 1996, Fields Institute Communications, Vol. 10, p. 217, 10, 217
- Wu, Y., & Lithwick, Y. 2011, ApJ, 735, 109, doi: [10.1088/0004-637X/735/2/109](https://doi.org/10.1088/0004-637X/735/2/109)
- Wu, Y., & Murray, N. 2003, ApJ, 589, 605, doi: [10.1086/374598](https://doi.org/10.1086/374598)
- Xuan, J. W., & Wyatt, M. C. 2020, MNRAS, 497, 2096, doi: [10.1093/mnras/staa2033](https://doi.org/10.1093/mnras/staa2033)
- Yee, S. W., Petigura, E. A., Fulton, B. J., et al. 2018, AJ, 155, 255, doi: [10.3847/1538-3881/aabfec](https://doi.org/10.3847/1538-3881/aabfec)
- Yee, S. W., Winn, J. N., Knutson, H. A., et al. 2020, ApJL, 888, L5, doi: [10.3847/2041-8213/ab5c16](https://doi.org/10.3847/2041-8213/ab5c16)
- Yoder, C. F. 1995, Global Earth Physics: A Handbook of Physical Constants, 1, 1
- Yoshida, H. 1993, Celestial Mechanics and Dynamical Astronomy, 56, 27, doi: [10.1007/BF00699717](https://doi.org/10.1007/BF00699717)
- Yu, H., & Dai, F. 2024, ApJ, 972, 159, doi: [10.3847/1538-4357/ad5ffb](https://doi.org/10.3847/1538-4357/ad5ffb)
- Zanazzi, J. J., Dewberry, J., & Chiang, E. 2024, ApJL, 967, L29, doi: [10.3847/2041-8213/ad4644](https://doi.org/10.3847/2041-8213/ad4644)
- Zanazzi, J. J., & Lai, D. 2017, MNRAS, 464, 3945, doi: [10.1093/mnras/stw2629](https://doi.org/10.1093/mnras/stw2629)
 —. 2018, MNRAS, 478, 835, doi: [10.1093/mnras/sty1075](https://doi.org/10.1093/mnras/sty1075)
- Zeebe, R. E. 2022, AJ, 164, 107, doi: [10.3847/1538-3881/ac80f8](https://doi.org/10.3847/1538-3881/ac80f8)
- Zeebe, R. E., & Lantink, M. L. 2024, arXiv e-prints, arXiv:2403.09332, doi: [10.48550/arXiv.2403.09332](https://doi.org/10.48550/arXiv.2403.09332)
- Zhang, K., & Hamilton, D. P. 2007, Icarus, 188, 386, doi: [10.1016/j.icarus.2006.12.002](https://doi.org/10.1016/j.icarus.2006.12.002)
- Zhu, W., Huang, C. X., Zhou, G., & Lin, D. N. C. 2014, ApJ, 796, 67, doi: [10.1088/0004-637X/796/1/67](https://doi.org/10.1088/0004-637X/796/1/67)
- Zuluaga, J. I., Sucerquia, M., & Alvarado-Montes, J. A. 2022, Astronomy and Computing, 40, 100623